Cellular and circuit mechanisms of neocortical dysfunction in Fragile X Syndrome

Arjun Azhikkattuparambil Bhaskaran

université de BORDEAUX

THÈSE PRÉSENTÉE

POUR OBTENIR LE GRADE DE

DOCTEUR DE

L'UNIVERSITÉ DE BORDEAUX

École Doctorale des Sciences de la Vie et de la Santé

Neurosciences

Par

Arjun AZHIKKATTUPARAMBIL BHASKARAN

Cellular and circuit mechanisms of neocortical dysfunction in Fragile X Syndrome

Sous la direction de : Dr. Andreas FRICK

Co-directeur : Prof. Dr. Fritjof HELMCHEN

Soutenue le 22 Novembre 2018

Membres du jury:

M. Christiaan de Kock, Dr.	The Center for Neurogenomics and Cognitive Research	Président
M. James Poulet, Dr.	Max-Delbrück-Centrum für Molekulare Medizin	rapporteur
M. Christiaan de Kock, Dr.	The Center for Neurogenomics and Cognitive Research	rapporteur
Mme. Ingrid Bureau, Dr.	Institut de Neurobiologie de la Méditerranée	Examinateur
Mme. Cho Yoon, Dr.	INCIA, Bordeaux	Examinateur

Titre: Mécanismes cellulaire et circuiterie des dysfonctions néocorticales dans le syndrome du X fragile

Résumé :

Cette étude explore les réponses évoquées, l'activité intrinsèque et spontanée de deux populations neuronales différentes dans la région du cerveau correspondant à la patte arrière des souris. Dans cet article, nous nous sommes concentrés sur un modèle murin du syndrome de l'X fragile (SXF), qui est la forme la plus commune de syndrome de retard mental héréditaire et une cause fréquente de troubles du spectre autistique (TSA). SXF est un trouble à gène unique (*Fmr1*), qui peut être modélisé de manière fiable par un modèle murin transgénique : la souris *Fmr*1$^{-/y}$ déficiente pour le gène codant *Fmr1*. L'hyperexcitabilité des réseaux néocorticaux et l'hypersensibilité aux stimuli sensoriels sont des caractéristiques importantes du SXF et des TSA.Ceci est directement lié à un changement du nombre de synapses locales, de canaux ioniques, de l'excitabilité membranaire et de la connectivité des circuits de cellules individuelles. Précédemment, nous avons identifié un défaut dans les canaux ioniques, comme pouvant contribuer à ces phénotypes. Nous avons testé cette hypothèse comme un mécanisme contribuant aux défauts de traitement sensoriel chez les souris *Fmr*1$^{-/y}$. Le cortex somatosensoriel primaire de la souris (S1) traite différentes informations sensorielles et constitue la plus grande zone du néocortex, soulignant l'importance de la modalité sensorielle pour le comportement des rongeurs. Nos connaissances concernant le traitement de l'information dans S1 proviennent d'études du cortex en tonneaux lié aux moustaches, mais le traitement des entrées sensorielles des pattes postérieures est mal compris. Par l'utilisation de la technique d'enregistrement de cellule entière par patch clamp in vivo, nous avons classes les cellules en répondeurs supraliminaires (cellules qui répondaient aux stimulations de la patte arrière avec un potentiel d'action), les répondeurs subliminaires (les cellules qui répondaient sans déclencher un potentiel d'action) et les cellules non répondeuses qui ne présentaient aucune réponse. Puis, nous avons comparé les réponses évoquées sub et supraliminaires, les propriétés intrinsèques et l'activité spontanée des neurones pyramidaux de la couche 2/3 (L2/3) de la region S1 de la patte arrière (S1-HP) d'animaux anesthésiés sauvage (WT) et *Fmr*1$^{-/y}$. Nous avons identifié des altérations de réponse spontanée, intrinsèque et évoquée chez les souris *Fmr*1$^{-/y}$. L'application d'un ouvreur de canaux ioniques BKCa a restauré certaines de ces propriétés altérées chez les souris *Fmr*1$^{-/y}$.

Mots clés : Cortex somatosensoriel primaire, ouvreurs de canaux BKCa, hypersensibilité sensorielle, traitement tactile du rongeur

Title : Cellular and circuit mechanisms of neocortical dysfunction in Fragile X Syndrome

Abstract :

This study explores the evoked responses, intrinsic and spontaneous activity of two different neuronal populations in the hind paw region of the primary somatosensory cortex (S1) of mice. Initially, we explored information processing in these neurons under normal physiological conditions, and subsequently in a mouse model of Fragile X Syndrome (FXS). FXS is the most common form of inherited mental retardation syndrome and a frequent cause of autism spectrum disorders (ASD). FXS is a single gene (*Fmr1*) disorder, which can be reliably modeled by a mutant mouse model, the *Fmr1* knockout ($Fmr1^{-/y}$) mouse. Hyperexcitability of neocortical networks and hypersensibility to sensory stimuli are prominent features of FXS and ASD. We previously established a strong causal link between a channelopathy, hyperexcitability of neurons in the primary sensory region of the neocortex and sensory hypersensitivity in this mouse model. In the current study, we extended these findings, by conducting a detailed exploration of the processing of tactile sensory information (evoked by hind paw stimulation) in the neocortex of these mice.

Most of our knowledge regarding information processing in S1 comes from studies of the whisker-related barrel cortex (which processes tactile-related sensory information derived from the whiskers), yet the processing of sensory inputs from the hind-paws is poorly understood. Using *in vivo* whole-cell patch-clamp recordings, we classified the cells into suprathreshold responders (the cells which responded to the hind-paw stimulations with an action potential), subthreshold responders (the cells responded without eliciting an action potential) and non-responder cells (neurons which did not show any response). We then compared the evoked sub- and supra-threshold responses, intrinsic properties, and spontaneous activity of layer (L) 2/3 pyramidal neurons of the S1 hind-paw (S1-HP) region of anaesthetized wild type (WT) and $Fmr1^{-/y}$ mice. We identified spontaneous, intrinsic and evoked response alterations in $Fmr1^{-/y}$ mice. We probed possible mechanisms contributing to this sensory impairment in $Fmr1^{-/y}$ mice. Finally, we tested the possibility of correcting pathophysiological alterations in these neurons using specific pharmacological agents targeting the ion channel defects described previously by our team.

Keywords :

Primary somatosensory cortex, BKCa channel openers, sensory hypersensitivity, rodent tactile processing

My PhD thesis is part of Erasmus Mundus Joint PhD programme. First part of my thesis is completed in University of Bordeaux under the supervision of Dr. Andreas Frick and the second part is performed in University of Zurich under the supervision of Prof. Dr. Fritjof Helmchen.

Unité de recherche

HOME INSTITUTE

Neurocentre Magendie, Inserm U1215,
Group Cortical Plasticity,
University of Bordeaux
146 rue Léo Saignat,
33077, Bordeaux, France

HOST INSTITUTE

Brain research Institute,
Laboratory of Neural Circuit Dynamics,
University of Zurich
Winterthurerstrasse 190,
CH-8057 Zürich

TABLE OF CONTENTS

1 LIST OF FIGURES

2 ACKNOWLEDGEMENT

I would like to express my deepest appreciation and sincere gratitude to my supervisor Dr. Andreas Frick who has continually and convincingly conveyed the spirit and excitement of research. I am thankful to him for his patience, motivation, enthusiasm and immense knowledge that supported me throughout my study and research.

My deep respect and gratitude are extended to Prof. Dr. Fritjof Helmchen for his benevolence, guidance and inexorable support throughout my thesis work. I sincerely thank him for providing me with all the essential amenities during my stay at Zurich.

My sincere thanks to Dr. Marcel Oberlaender and Dr. Rajeevan. T. Narayanan for providing me an opportunity to restart my scientific career. I also thank Mr. Srinivasa Rao Marri for his financial support throughout this training.

I would like to extend my thanks to all the funding agencies, Erasmus Mundus (ENC network), FRM and EMBO for providing me a platform to build a career in Neuroscience.

I express my indebtedness to Dr. Guillaume Bony, Dr. Melanie Ginger, Dr. Katy Le Corf and Dr. Yaroslav Sych for teaching me all the valuable techniques that helped me in my research. I thank them for their sincere advice, support and enthusiasm.

Gratitude and appreciation are extended to Dr. Remi Proville, Dr. Isabel Del Pino and Dr. Xavier Leinekugel for their timely help and valuable recommendations and unflinching support. I thank all my colleagues at Frick Lab- Rafael De SA, Olivier Dubanet, Dr. Senka Hadzibegovic, Vladimir Kouskoff, Dr. Sourav Ghosh, Kamila Castro and Liangying Zhu for their selfless cooperation and suggestions. I also thank all my colleagues at Helmchen Lab- Dr. Ladan Egolf, Dr. Ariel Gilad, Dr. Asli Ayaz, Dr. Abhishek Banerjee, Fabian Voigt, Pia Silpia, Lazar Sumanovski and Yasir Gallero Salas for their support and encouragement. I would like to extend my thanks to all administrators who helped me in all the official procedures during my PhD.

I would like to thank all my friends and family members and teachers who supported and guided me throughout my life.

Above all I dedicate my PhD thesis to my better half Sreedevi for her immense love, care and support for my personal and professional well being.

3 LIST OF ABBREVIATIONS

ACC	angular cingulate cortex
ADP	afterdepolarization
AMPA	α-amino-3-hydroxy-5-methyl-4-isoxazolepropionic acid
AP	Action potential
ASD	Autism spectrum disorder
BK_{Ca}	Large Conductance, Ca^{2+}-Activated K^+ Channels
DAPI	4′,6-Diamidino-2-phenylindole
DTI	Diffusion tensor imaging
EEG	Electroencephalography
EPSC	excitatory post synaptic current
EPSP	Excitatory postsynaptic potential
Fmr1	fragile x mental retardation 1 gene
*Fmr*1$^{-/y}$	*Fmr1* gene knockout
FMRP	Fragile mental retardation protein
FP	Forepaw
FS	Fast spiking interneuron
FXG	fragile X granule
FXS	Fragile X Syndrome
GABA	gamma-Aminobutyric acid
HP	Hind paw
IPSC	Inhibitory postsynaptic current
IPSP	Inhibitory postsynaptic potential
L 2/3	Layer 2/3
LFP	Local field potential
LFS	low frequency stimulation
LTD	long-term depression
LTP	long-term potentiation
M1	primary motor sensory cortex

MEG	Magnetoencephalography
mGluR 5	metabotropic Glutamate receptor 5
NMDA	N-methyl-D-aspartate
NOS1	Nitiric oxide synthase 1
NR- cells	Non-responder cells
PBS	Phosphate buffered saline
PFA	Paraformaldehyde
PKA	Protein Kinase A
PMN	Posteromedial nucleus
PN	pyramidal neuron
PSP	Postsynaptic potential
PV	Parvalbumin
R- cells	Responder cells
ROI	region of interest
ROI	region of interest
R_{sub} cells	sub-threshold responder cells
R_{supra}- cells	suprathreshold responder cells
S1-BC	primary somatosensory barrel cortex
S1-HP	Hind paw related primary somatosensory cortex
S2	secondary somatosensory cortex
SS	Somatostatin
TBS	theta burst stimulation
VPM	Ventral posteromedial nucleus
VSD	voltage sensitive dye
WT	wild type

CHAPTER 1

4 SENSORY INFORMATION PROCESSING

Automatic integration of incoming information from different sensory modalities are essential for executing everyday tasks. Sensory information integration involves visual, auditory, somatosensory and motor cortices (Molholm et al., 2002). Sensory information processing is a complex process, with different receptors belonging to peripheral neurons in the periphery all the way to the neocortex (Nicolelis et al., 1998). The neocortex act as an adaptive processor that computes information according to the instant sensory and behavioral context. This sensory information gathering and integration by the sensory areas is possible through the interactions between feedback connections from higher cortical areas and local intrinsic cortical circuits. Both feedback and feedforward mechanisms are important for the sensory perception. Any areas included in sensory processing can be in a nonfunctional or functional mode according to the task requirement, state of the brain and neuromodulators. The function of any cerebral cortex area and functional properties of neurons at the earliest stages in cortical sensory processing is influenced by attention, expectation, and perceptual task. (Gilbert and Sigman, 2007). In addition, top-down control of neuronal activity is required for complex behavior. Consequently, top-down input inactivation alters sensory perception in mice (Manita et al., 2015).

In neurodevelopmental disorders, sensory processing is highly modified (Cascio, 2010). For instance, in Autism spectrum disorders (ASD) visual, tactile, auditory systems of the individuals are much affected. Modifications of these system cause hypersensitivity to touch, overfixation on visual details or avoidance of loud sound (Haigh, 2017) in ASD patients. These atypical experiences disrupt sensation, perception, motor behavior, emotion and cognition in ASD individuals. Therefore, it is important to study the circuit level alterations leading to sensory deficits in ASD (Robertson & Cohen, 2017).

5 AUTISM SPECTRUM DISORDER (ASD)

Donald Grey Triplett was the first person to be diagnosed with Autism (Figure 1). He showed an early abnormal appetite and social behavior (isolated) but an unusual memory for faces and names as well as repetitive behavior, attention deficit and difficulty in communication. The symptoms showed by Donald and ten other children shared common characteristics and were different in their degree of expression.

Figure 1: A picture of Donald Grey Triplett. The first person diagnosed with Autism.

Dr. Kanner identified this condition, for the first time, as a 'unique syndrome' and named it 'autism', a word previously used to describe schizophrenic symptoms (Kanner, 1968). This study was conducted among children below 11 years old and that findings were considered as a preliminary study. Even though the number of participants in the study made it statistically less significant, it became a stepping stone for the current ASD research.

ASD is a complex, heterogeneous neurodevelopmental disorder for which there is no cure and no targeted therapeutic treatment reported. It is hypothesized that autism can also be caused by environmental factors like immune dysfunction, epigenetic dysregulation, prenatal and perinatal factors drugs and toxic exposure and socioeconomic status (reviewed by Chaste & Leboyer, 2012). Another factor is the mutation of hundreds of genes which are contributing to ASD. Protein synthesis at the synapses, receptors and different ion channels are affected by these mutations and they together cause developmental synaptopathies and channelopathies (reviewed in (Ebrahimi-Fakhari and Sahin, 2015). ASD exhibit a spectrum of disorders and deficits in the behavior of affected children. They demonstrated abnormality of brain structures, impairment in sensory processing and learning disturbances (reviewed in (Trottier *et al.,* 1999, Kootz *et al.,* 1981).

The standardized criteria to help diagnose ASD provided by the American Psychiatric Association's Diagnostic and Statistical Manual, Fifth Edition (DSM-5; American Psychiatric Associationn, 2013) are as follows:

1. Persistent deficits in social communication and social interaction, currently or by history.

2. Restricted, repetitive patterns of behaviour, interests, or activities, as manifested by at least two of the following, currently or by history.
3. Symptoms must be present during the early developmental period but may not fully manifest until social demands exceed limited capacities or may be masked by learned strategies in later life.
4. Symptoms cause clinically significant impairment in social, occupational, or other important areas of current functioning.
5. These disturbances are not better explained by intellectual disability (intellectual developmental disorder) or global developmental delay. Intellectual disability and autism spectrum disorder frequently co-occur; to make comorbid diagnoses of autism spectrum disorder and intellectual disability, social communication should be below that expected for general developmental level.

5.1 SENSORY SYMPTOMS IN ASD

Recent amendments to the DSM-5 now include defects in sensory information processing as part of the diagnostic criteria for ASD. Indeed, defects in the processing of sensory information and multisensory integration are considered almost universal within the ASD population (Baranek *et al.*, 2006; Lane *et al.*, 2010; Marco *et al.*, 2011). In addition, alterations in sensory responsiveness have been strongly suggested to co-segregate with other ASD-related core symptoms and comorbidities (Green *et al.*, 2015; Uljarević *et al.*, 2017; Wigham *et al.*, 2015). Surprisingly, in spite of their widespread occurrence, there is a paucity of studies addressing this aspect of the ASD pathology, or specifically attempting to target this symptom for therapeutic rescue. Recent of research initiatives have begun to study the neurobiological underpinning of atypical sensory processing in Autism and related neurodevelopmental disorders.

The brain receives various sensory inputs from the outside and generate a response according to the specific input. In ASD, much evidence suggests that there is an altered sensitivity to sensory input (Ethridge et al., 2017, Güçlü et al., 2009, Kootz et al., 1981). Impairments in sensory processing might even cause other core symptoms such as repetitive behavior and/or social withdrawal. ASD affected children exhibit enhanced sensory discrimination and aberrant sensitivity to different sensory modalities like smell, touch, vision or sound (O'Riordan and Passetti, 2006; Scott *et al.*, 2018; Tomchek and Dunn, 2007; Zhang *et al.*, 2014). These children

overreact to a sensory stimulus and therefore try to avoid or seek that sensory stimulus (Boyd *et al.*, 2010). This hyper or hypo-sensitivity to a sensory input contributes to dysfunction of sensory information integration, processing and different behaviors in ASD (Güçlü *et al.*, 2009).

5.2 HIGH RISK GENES IN ASD

Genetic heritability of ASD is in the order of 14- 67% (Hallmayer *et al.*, 2011). There are > 250 identified high-risk genes with a strong convergence of their biological functions through network interactions. For example, identified ASD-associated protein complexesdisplay a convergent regulation of FMRP and MECP2 in ASD. ASD related genes control multiple protein-protein interactions, and any mutation of these genes leads to ASD linked behavior deficit (Li *et al.*, 2015).

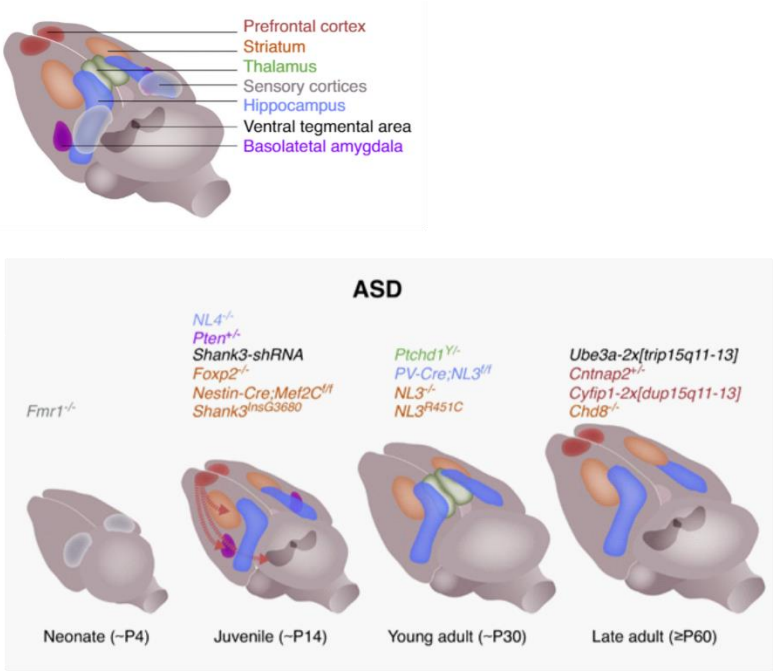

***Figure 2**: **Dysfunction of neural circuits during postnatal development in mouse models of ASD. Top**) Schematic representation of areas affected in ASD (Each area is coloured similar to the gene involved in the dysfunction of that particular brain region). **Bottom**) Illustration of specific regions which are interrupted in ASD (del Pino et al., 2018).*

The best strategy to study behavioral alterations of in ASD is to investigate factors like genetic, neural and cognitive variations linked to specific individual genes (Happé *et al.*, 2006). Manipulation of a specific gene associated with ASD enables us to study different behavioral,

functional and structural anomalies linked to the absence or overexpression of that single gene (Moy and Nadler, 2008).

5.3 SCOPE OF STUDYING FRAGILE X SYNDROME

Fragile X syndrome (FXS) is the most common inherited form of intellectual disability (Riley & Wheeler, 2017). FXS is also an attractive model for understanding the neurobiological underpinnings of ASD for the following reasons:

- FXS accounts for an estimated 3-5% of ASD cases.
- 25-50% of males with FXS meet the full diagnostic criteria for ASD (Klusek *et al.,* 2014) and most exhibit some autistic symptoms.
- FXS and other ASD genes are intertwined at the molecular level (Darnell, 2011; Parikshak *et al.,* 2013), pointing to a convergence of molecular pathways leading to cellular and circuit level changes underlying these brain disorders.
- FXS is the most common inherited form of intellectual disability and approximately 30 % of FXS patients have similar characteristics of ASD. They share common features like mental retardation, impaired social relationships, communication and repetitive behavior.
- Researchers observed that children diagnosed with autism have also shown the presence of a fragile site on the X-chromosome and characteristics of fragile X syndrome. (August and Lockhart, 1984; Brown *et al.*, 1982; Meryash *et al.*, 1982; Paul *et al.,* 1987; Pueschel *et al.,* 1985). Some of them showed no similarity between FXS and autism in behavior, but most of the studies showed an overlap or considered FXS as a subtype of autism (Bailey *et al.,* 2000; Feinstein and Reiss, 1998).
- Social withdrawal and delayed communication in FXS were significantly correlated with autism. The delay in acquiring essentials skills required to socialize were linked to verbal reasoning in both conditions (Budimirovic *et al.,* 2006). Absence or low levels of fragile X mental retardation protein (FMRP), the protein coded by the *Fmr1* gene results in compulsive, self-injurious and autistic behavior in FXS subjects (Hall *et al.,* 2008).

In addition, the overlap between these two disorders increases the relevance of screening autistic children for FXS. It will help us to understand the different x-linked alterations occur in ASDs (a detailed review by (Budimirovic and Kaufmann, 2011).

More than 250 known risk genes have been identified, most accounting for less than 1% of the genetic cause of ASD (Jeste and Geschwind, 2014). As a strategy for dealing with this genetic complexity, ASD has classically been modeled in rodents using transgenic mice presenting monogenic syndromic forms of ASD (Ghosh *et al.*, 2013; Jeste and Geschwind, 2014). Advances in transgenic technology led to development of suitable genetically modified animals for studies into the mechanisms of disease. This was made possible by silencing a targeted individual gene in situ. By silencing a gene, one can study the role of this gene in a disorder. One can introduce a transgene to eliminate or cause an abnormality by knocking out the transgene (Higgins and Cordell, 1995). The involvement of an X-linked gene in Fragile X syndrome allowed the scientists to clone the DNA sequence of X-linked fragile sites and therefore develop animal models that enable to study the neurobiological underpinning of this disorder. The *Fmr*1$^{-/y}$ mouse, in which the expression of the Fragile X Mental Retardation gene, *Fmr1* (mutated in Fragile X syndrome) is abrogated, recapitulates many of the symptoms of ASD (reviewed in (Oddi *et al.*, 2013).

5.4 FRAGILE X CHROMOSOME

The familial transmission of fragile X chromosome was described by Dr. J. Purdon Martin and Julia Bell and they suggested the involvement of a sex-linked recessive gene (Martin and Bell, 1943).

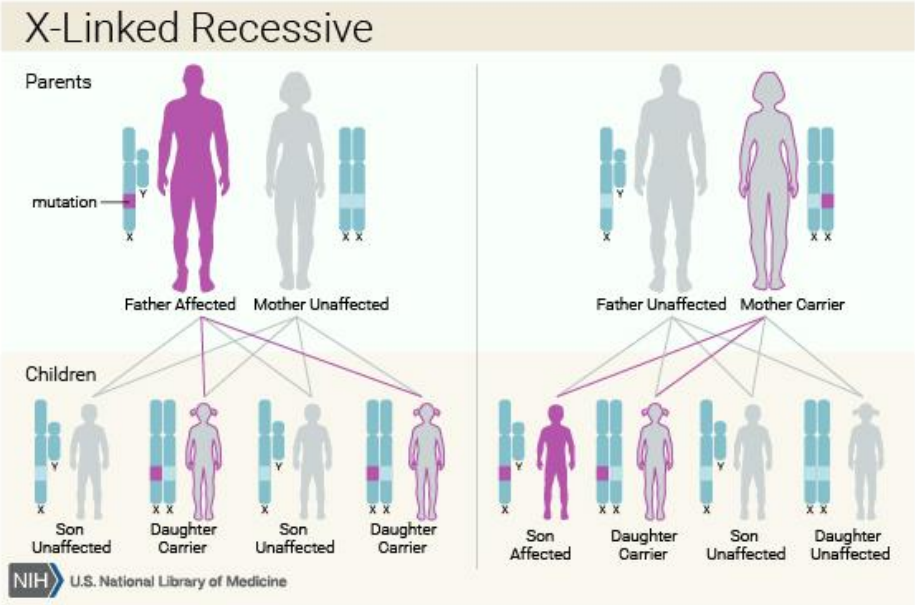

Figure 3: Inheritance pattern of X linked recessive gene.

Further studies analyzing the structure of chromosomes revealed an unusual secondary constriction towards the end of long arm of X chromosome in mentally retarded males and carrier females of a family (Lubs, 1969). This fragile site appeared to be directly related to the gene responsible for mental retardation (Moore et al., 1982). Later, the fragile site associated to the fragile X chromosome was found to be localized specifically to the band Xq27.3 (Harrison et al., 1983) and was termed FRAXA (**Fig 4**).

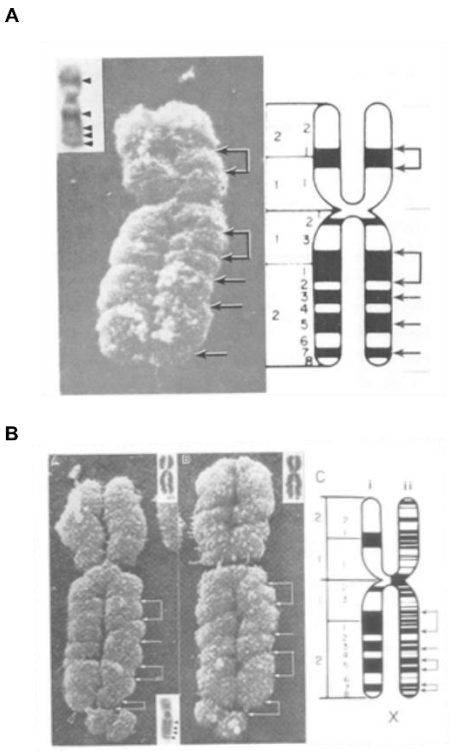

***Figure 4**: **Structure of X chromosome in Fragile X syndrome. A**) Electron microscopic view of a normal X chromosome and **B**) an X chromosome from an FXS patient (Harrison et al., 1983).*

5.5 FRAGILE X MENTAL RETARDATION 1(*Fmr1*) GENE

By 1991, the role of *Fmr1* mutations in causing fragile X syndrome was established (Verkerk et al., 1991). The *Fmr1* gene is 38kb in length and contains 17 exons (Penagarikano et al., 2007).

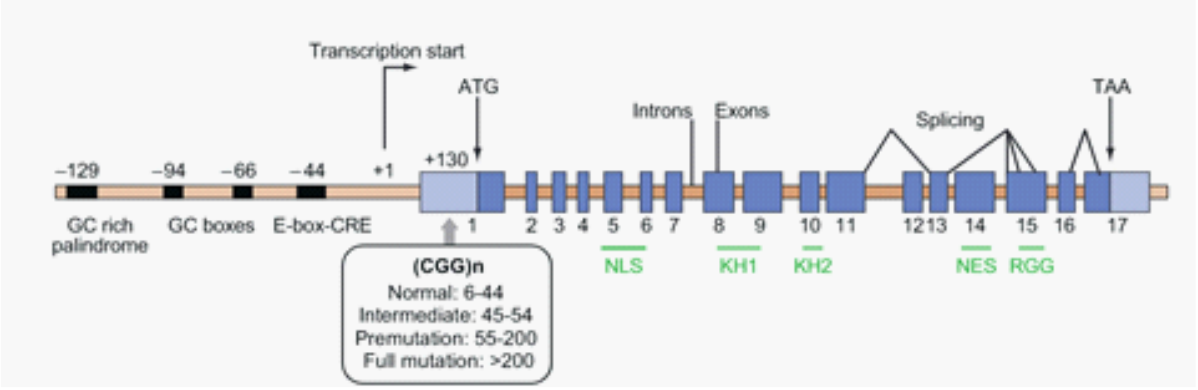

Figure 5: Schematic representation of the fragile X mental retardation 1 (Fmr1) gene *(Penagarikano et al, 2007). CGG repeat numbers in normal to full mutation is shown inside the box.*

Fmr1 harbors a CCG repeat at 5' untranslated region (UTR) within the first exon (Verkerk et al., 1991). The repeat length is polymorphic and usually range up to 55 repeats in normal individuals. When the expansion is between 55 and 200 repeats, it is called a pre-mutation and if the trinucleotide repeat length is above 200, it is termed full mutation (Fu et al., 1991; Oberle et al., 1991). The CCG trinucleotide expansion (or full mutation) in the *Fmr1*gene locus Xq27.3 leads to the hypermethylation of the gene promoter thereby silencing the gene resulting in the loss or reduced expression of fragile X mental retardation protein (FMRP) (Pieretti et al., 1991; Oberle et al., 1991). This loss of FMRP results in the clinical and cytogenetic expression of FXS.

Apart from CCG trinucleotide expansion, a few other mutations causing the fragile X phenotype have been reported. (Boulle et al., 1993) studied the *Fmr1* gene of a patient with fragile X phenotype, but without FRAXA, with normal CCG repeats and unmethylated promoter. Instead, they found a single point mutation in the *Fmr1* gene suggesting that it caused the clinical abnormalities. Also, deletions affecting part of or the entire gene resulting in FXS associated phenotype are reported (Meijer et al., 1994; Hirst et al., 1995).

5.6 FRAGILE MENTAL RETARDATION PROTEIN (FMRP)

FMRP is highly expressed in neurons of the brain and early spermatogonia in the testis in human (Devys *et al.,* 1993). FMRP expression in the cytoplasm and nucleus of neurons is slow during the early embryonic stage and increases during development. The maternal mRNAs are responsible for the expression of FMRP during the early development stage. In adult stages, FMRP protein is mainly located in the cytoplasm of the cells (Devys *et al.,* 1993; Kooy *et al.,*

2000; van Padje *et al.*, 2005). In the cytoplasm FMRP is directly associated with polyribosomes, there by regulating the translation machinery of the cell (Khandjian *et al.*, 1996). FMRP is an RNA interacting protein involved in the regulation of RNA stability, subcellular transport and translation of neural mRNAs that code for proteins involved in synapsis development, neural plasticity and brain development. FMRP is also involved in a feedback loop by controlling its own protein levels (Brown et al., 2001; Noto et al., 2016). (Zangenehpour *et al.*, 2009) reported the first 3D whole brain map of FMRP protein expressed in the old-world monkey brain and showed that certain brain structures like cerebellum, striatum and temporal lobe structure have high FMRP levels thereby supporting the notion that FMRP loss is linked to behavioural and cognitive impairment associated with these structures.

5.7 NEUROANATOMICAL, BEHAVIORAL AND PSYCHIATRIC SYMPTOMS AND RELATED CO-MORBIDITIES IN FXS PATIENTS.

5.7.1 STRUCTURAL ALTERATIONS

Initial neuroanatomical analysis of post-mortem brains of Fragile X patients suggested that there were no gross scale defects in brain structure (Hinton et al., 1991; Reyniers et al., 1999), but rather pointed to microscale changes in the brain circuitry. In particular, these early studies revealed defects in the shape of dendritic spines (Rudelli et al., 1985; Wisniewski et al 1991; Irwin et al, 2001). Indeed, dendritic spine defects are often cited as a hallmark of FXS, and ID in general (see below). However, more recent volumetric analysis based on a variety of magnetic imaging approaches has revealed a number of structural differences in specific brain areas which may be related to particular symptoms of the disease. In particular changes in grey matter and ventricular volume have been described. These studies demonstrated differences in cerebral, CSF and thalamic volumes pointing to a strong association between arise in the methylation of *Fmr1* gene and larger ventricular volume in FXS (Reiss et al., 1995, Eliez et al., 2001, Hoeft *et al.*, 2010).

A couple of studies demonstrated a deficit in white matter microstructure in FXS. For instance, (Hall et al., 2016) described an aberrant white matter structure in FXS individuals when compared to typically developing similar age group individuals. FXS individuals exhibited an

increase in fractional anisotropic values (FA) suggesting an alteration in white matter density or coherence. In girls with FXS, white matter structures were altered. In particular, FA was significantly lower in inferior longitudinal fasciculus, right internal capsule and left cerebellar peduncle (Barnea-Goraly et al., 2003; Villalon-Reina et al., 2013). Diffusion tensor imaging (DTI) showed an increased relative density of white matter fibers (left ventral fronto-striatal pathway) which is necessary for the maturation of inhibitory control (HAAS *et al.,* 2009). In general, neuroanatomical studies confirm a change in grey and white matter in FXS patients.

5.7.2 ALTERATIONS IN FUNCTIONAL CONNECTIVITY

Small world index is the balance between local and long-range network segregation and integration. Small world organization in brain networks helps to balance the network integration and segregation by maximizing the efficiency of information transfer at a low network cost. Small-worldness (ratio between normalized clustering to normalized path length) was significantly lower in the FXS group suggesting an unbalance in the circuit organization and a reduced information transfer across different neuronal connections. These deficits led to failure of proper functioning of cognition and behavior of FXS subjects (Bruno *et al.,* 2017).

Functional alterations in neuronal connectivity has been investigated using neuroimaging approaches such as functional MRI (fMRI) and electrophysiological approaches such as electroencephalography (EEG). Very few quantitative functional connectivity studies have been conducted in FXS patients. For instance, EEG recordings demonstrated an imbalance in excitatory inhibitory network, hypersensitivity, and cortico-cortical connectivity deficit in FXS patients (Wang et al., 2017). fMRI studies demonstrated an impairment in the functional and structural connectivity between thalamus and other cortical regions (Nair *et al.,* 2013, Ethridge et al., 2016; 2017). There was a long-range hyper connectivity (fronto-posterior) and a local hypoconnectivity (fronto-frontal; posterior-posterior) in FXS (van der Molen et al., 2014). EEG recordings also revealed a deficit in sensory processing. The FXS individuals showed an increase in signal to noise ratio (SNR) on presentation of an auditory stimulus suggesting hyperexcitability in FXS. Alpha oscillations, which modulate the excitation of local inhibitory circuits were downregulated in the same recordings (Ethridge *et al.,* 2017).

5.7.3 TASK-RELATED FUNCTIONAL STUDIES

Brain regions regulating *Fmr1* gene translation are much affected in FXS condition. For example, an fMRI study on FXS females during a visual memory encoding task revealed a significant low activation of left hippocampus and the basal forebrain. FXS also showed an

increased activation (hypothesized as a compensatory mechanism) of superior parietal and right precentral gyrus regions. Prefrontal regions associated with social cognition were less activated in fragile X syndrome during face encoding. In a face recognition memory task FXS individuals show significant hyposensitivity and delayed response. These subjects also avoided direct eye contacts and staring at the face (Holsen *et al.,* 2008). FXS individuals demonstrated spatial ability and attention deficit. Performance of FXS children in different cognitive tasks like visuo-construction, visuo-spatial memory, visuo-perception and visuo-motor tasks to assess their spatial ability showed a task specific deficit in spatial performance. They performed low in visuo-construction task (spatial deficit) and visuo-motor tasks (sensory motor delay). They also showed significant deficit in attention required tasks like selective attention, divided attention, sustained attention and inhibition (Cornish *et al.,* 1999; Munir *et al.,* 2000). Visual motion processing is impaired in Fragile X syndrome. FXS subjects and control groups were presented with a first order (luminance) and a second order (contrast-luminance with grey scale) stimuli. (Kogan *et al.,* 2004) reported that majority of FXS subjects were failed to discriminate the direction of motion in a visual motion processing task. But they were able to discriminate the orientation of the stimuli. Children with FXS, upon presentations of faces showing direct eye contact significantly increased the activity of left insula, left dorsal thalamus and left amygdala. Left amygdala demonstrated a negative correlation with the number of successful trials in FXS (Greicius *et al.,* 2004; Watson *et al.,* 2008).

5.7.4 INTELLECTUAL DISABILITIES

Fragile X syndrome is one of the most intensely studied neurodevelopmental disorders and has been the subject of numerous reviews (e.g. Gross et al., 2015; Hagerman et al., 2017). Intellectual disability is often regarded as one of the defining symptoms of this disorder. Affected males have mild to severe intellectual impairment (Hagerman et al., 2009; Kaufmann et al., 1999; Finelli *et al.,* 1985; Fryns *et al.,* 1984; Hanson *et al.,* 1986; Jørgensen *et al.,* 1984; Veenema *et al.,* 1987), with an IQ ranging from 35-50 (Merenstein et al., 1996). The IQ of the affected showed varied from mild to severe mental retardation. Among children with ASD, 55% displayed an intellectual disability (IQ<70). Sixteen percentage of these children had moderate to severe intellectual disability (IQ<50) and 28% exhibited average intelligence (115>IQ>85) and only 3% were of above average intelligence (IQ>115) (Charman *et al.,* 2010). Differences in intellectual ability have been correlated with FMRP levels (Kaufmann et al, 1999; Arsenault *et al.,* 2016; Theobald *et al.,* 1987; Loesch et al., Tassone et al., 1999). As it is an X-linked disorder, it generally accepted that the lower severity of intellectual and

cognitive symptoms and penetrance is observed in females (Reiss and Dant, 2003; Hagerman et al., 2009). FXS subjects typically exhibit speech and language delay, and avoidance of social/ group activities. Aberrant early gesture use is seen FXS during the early development period. FXS children used significantly less gestures. Early gesture use is an initial step to understand and develop social communication and verbal abilities. This could be a reason for the low non-verbal abilities and social impairment in FXS (Rague *et al.,* 2017).

5.8 PRECLINICAL MOUSE MODEL OF FRAGILE X SYNDROME

The first mouse model for FXS was the *Fmr1* knockout mouse. These models were generated by knocking out of *Fmr1* gene from the wild type animals through interruption of neomycin cassette in exon 5 using homologous recombination in embryonic stem cells. These mice did not have *Fmr1* RNA (the first generation still contains some remaining RNA) and the fragile mental retardation protein (FMRP). The animals were then tested for different behavioral experiments as well as organ weights. Except for the testes, the organs' weights were not significantly different from the ones in wild-type control mice. These mice exhibited FXS like characteristics including cognitive impairment, distinct social behavior and Macroorchidism. They also showed increased exploratory behavior, hyperactivity and deficit in spatial memory but showed normal fertility (Bakker *et al.,* 1994; Kooy *et al.,* 1996). *Fmr1*-Knock out mouse in many ways showed features which resembled the clinical characteristics in FXS subjects and therefore it became a reliable model of FXS for testing various phenotypes of ASDs.

Another model was created by knocking the *Fxr2*, a homologus of *Fmr1* gene. The model lacked important phenotypes like macroorchidism and loss of FMRP expression. They showed hyperactivity, impairment in open field and rotarod tests. They also showed a delayed hindpaw stimulation with a hot plate experiment (Bontekoe *et al.,* 2002). A conditioned knockout (*Fmr1 KO*2) was produced later. The crossing of *Fmr1 KO2* mice with induced recombinase expressing mice enabled them to produce a mouse that are *Fmr*1$^{-/-}$ only in specific neurons (Mientjes *et al.,* 2006). Second generation *Fmr1* knockout (*Fmr*1$^{-/-}$; *Fmr*1$^{-/y}$) mice (Mientjes *et al.,* 2006) were used in our study. These mice are distinct from the original *Fmr*1$^{-/y}$ mouse line (Bakker *et al.,* 1994) because the second-generation mice are deficient for both *Fmr1* RNA and Fragile X mental retardation protein (FMRP) (Mientjes *et al.,* 2006). These mice were generated by backcrossing 129/Sv/C57Bl/6J/FVB founders into a C57Bl/6J background (6 generations). Male wild-type and *Fmr*1$^{-/y}$ littermates were generated by crossing *Fmr*1$^{+/-}$

females with a wild-type mouse from the same background. Given that *Fmr1* is carried on the X chromosome, the resulting male progeny were either *Fmr*1$^{+/y}$ (wild-type) or *Fmr*1$^{-/y}$ (KO). Animal models are necessary to reach a better understanding of abnormal behavior, dysfunction of various brain regions, neuroanatomical pathways and molecular mechanisms in neurodevelopmental disorders such as FXS/ ASD. The phenotypes formed due to the loss of FMRP in animal models resemble the phenotypes of FXS in human (a detailed review (Kooy, 2003). This shows that they have a good construct and face validity. However, face validity is more complicated, since we are sometimes lacking robust behavioral phenotypes. Studies on *Fmr*1$^{-/y}$ mice (and in other preclinical models of the disorder such as drosophila, zebra fish and rat) have attempted to model core behavioural /cognitive aspects of the disorder. These findings have been summarized in recent comprehensive reviews (e.g. Kooy et al., 2017; Kazdoba et al., 2014; Gross et al., 2015).

5.8.1 COGNITIVE PHENOTYPES

Intellectual disability is one of the key features of Fragile X syndrome and has been examined in *Fmr*1$^{-/y}$ mice using a range of behavioral tasks including passive avoidance, fear conditioning, Morris water maze, 8 arm radial maze as well as temporal order object recognition tasks (reviewed in Kazdoba et al., 2014; Gross et al., 2015). Unfortunately, these studies have often resulted in findings that are difficult to replicate between laboratories and are variable in nature. For example, auditory-cued fear conditional paradigms have detected either deficits in the recognition of the context, or the cue, or sometimes no deficits at all (reviewed in Kazdoba et al., 2014). However, it is also possible that the tasks themselves need to be adapted to the specificities of a neurodevelopment model (Arsenault *et al.,* 2016). For instance, age of the animal. Several studies have shown that phenotypes may vary with age (Gauducheau et al., 2017). For example, an age dependent impaired development of startle response was reported in *Fmr*1$^{-/y}$ mice. Three to four weeks there was a significant increase in startle response of both *Fmr*1$^{-/y}$ and WT animals. At 8 weeks it was diminished in *Fmr*1$^{-/y}$ suggesting an immature arrest of startle response in *Fmr*1$^{-/y}$ mice (Yun *et al.,* 2006). Studies on *Fmr1* KO2 mice (second generation of *Fmr*1$^{-/y}$ mouse model, see above) suggest that behavioral phenotypes are also age-dependent. Age dependent changes of behavior was present in heterozygous *Fmr*1$^{-/y}$ female mice. In these mice, some of the behavioral abnormalities in social interactions and communication showed during juvenile stage were disappeared in adulthood. At the same time, avoidance of social novelty, hyperactivity and reduced contextual fear response were appeared during the adulthood (Gauducheau *et al.,* 2017). This led to an

important suggestion to include behavioral tasks with greater ethological relevance for testing FXS (Kazdoba et al., 2014).

To this end, a number of recent studies describe new or improved tasks, which respond to pharmacological or genetic correction and which may have improved face or predictive validity. For example, (Oddi et al., 2015) described a modified fear conditioning protocol based on classical contextual fear conditioning protocols (Frankland et al., 1998) in which the conditioned stimulus is paired with the unconditioned stimulus (shock). These mice display reduced freezing when presented with the same context 24 hours after the initial conditioning experience (Oddi et al., 2015). *Fmr*1$^{-/y}$ mice demonstrated differential learning defects in Hippocampus (dentate gyrus mediated) dependent learning paradigm where the animal had to distinguish highly similar representations (Ghilan *et al.,* 2018). Loss of FMRP impaired the functioning of prefrontal cortex (PFC). PFC specific FMRP knockout animals showed deficits in PFC-dependent learning paradigm (trace eyeblink conditioning-TEC) with a stimulus free interval between the cue and the stimulus (air puff) (Siegel *et al.,* 2017).

5.8.2 BEHAVIOR ALTERATIONS

*Fmr*1$^{-/y}$ mice exhibited higher activations of mesolimbic/ habenular circuit during the presentation of a reward stimuli (odor of almond). FXS animals did not show any preference to the reward stimuli when a mixture of stimuli presented (Kenkel *et al.,* 2016). Ultrasound vocalization (USV) was impaired in *Fmr*1$^{-/y}$ mice. (Hodges *et al.,* 2017) reported an overall lesser duration, enhanced peak and frequency and a lower amplitude USVs in *Fmr*1$^{-/y}$ mice. Changes in vocalizations represent the deficits in communication reported in fragile X syndrome. Both FXS female and male mice showed deficits in a reversal learning of Morris water maze, contextual memory linked to unexpected shocks, decreased startle response and increased social interactions (Baker *et al.,* 2010; Dobkin *et al.,* 2000; Mineur *et al.,* 2002; Nolan and Lugo, 2018). Upon introduction of simple and complex discrimination tasks and their reversal, *Fmr*1$^{-/y}$ and WT animals exhibited equal learning abilities. But WT mice showed an increased trial to criterion (TTC, 8 correct trials out of 10 consecutive trials) during the reversal tasks. It confirmed that *Fmr*1$^{-/y}$ animals were impaired in attentional set formation to previously learned dimensions (Casten *et al.,* 2011). *Fmr*1$^{-/y}$ mice demonstrated deficits in orientation tuning during a visual discrimination task. Further investigation identified a hypoactivation of PV interneurons in FXS visual cortex. Since PV interneurons receives a vast input from networks involved in different orientation and PV itself demonstrated high response probability

to all kind of orientations, the deficit in orientation tuning was hypothesized because of PV interneuron hypoactivation (Goel *et al.*, 2017).

5.8.2.1 HYPERACTIVITY

*Fmr*1$^{-/y}$ animals were hyperactive in novel environment. They showed increased locomotion, rotation and time resting at the center of an unexposed open field. The *Fmr*1$^{-/y}$ animals showed altered nest building behavior. *Fmr*1$^{-/y}$ mice failed to make nest in a time window that of WT animals when kept in a familiar open field or in new cage. These mice also exhibited excessive grooming when exposed to a novel environment (Carreno-Munoz *et al.*, 2017). Stereotypic behavior in an open field paradigm, low freezing, novelty-induced anxiety and hyperactivity were reported in different models of FXS (Ding *et al.*, 2014; Kim *et al.*, 2014; rensen *et al.*, 2015). FXS mice were highly susceptible to different types of seizures. (Ding *et al.*, 2014) reported that both juvenile female and male FXS mice exhibited significantly increased levels of audiogenic seizures. The animals were hyperactive in an open field paradigm and were shown significant hypersensitivity to a mild foot shock. They also revealed a low freezing of *Fmr*1$^{-/y}$ animals in a contextual fear conditioning paradigm (Oddi *et al.*, 2015; Restivo *et al.*, 2005). During sleep, hippocampal CA1 pyramidal neurons showed hyperactivity in *Fmr*1$^{-/y}$ animals. Low gamma power was observed in non-theta dominated neurophysiological brain states (Carr et al., 2012; Pfeiffer and Foster, 2015). The enhanced power spectral density (PSD) in low gamma power in *Fmr*1$^{-/y}$ CA1 suggested that the hyperactivity was the result of an impairment of CA3 inputs to CA1. The slow sharp-wave ripples in FXS exhibited a longer event duration, shorter oscillation frequency and a reduced CA1-PN firing rates. These changes have adverse effect on memory processing in both human and mice (Boone *et al.*, 2018). FXS mice also showed hyperactivity dependent enhancement of correct and incorrect responses during attentional learning (Kramvis *et al.*, 2013). These prefrontal cortex dependent learning deficits were also resulted from decreased synaptic functioning caused by the absence or low expression of several synaptic proteins in both OFC and PFC. Low expression of c-fos expression in the FXS mice demonstrated the lower activity of neurons in these regions during learning (Krueger *et al.*, 2011).

5.8.2.2 ANXIETY

Chronic stress had no effect on cognitive and social behavior of *Fmr*1$^{-/y}$ mice (Lemaire-Mayo *et al.*, 2017). For instance, *Fmr*1$^{-/y}$ animals exhibited low anxiety levels during chronic stress. (Qin et al., 2011) reported this change as a deficit in adaptive response of amygdala in FXS.

The disruptions in dendritic and spine morphology of amygdala neurons demonstrated an experience-driven plasticity deficit in *Fmr*1$^{-/y}$ mice. In another study (Nolan *et al.*, 2017) reported a sex specific behavior alteration following *Fmr1* deletion. They demonstrated that the FXS male mice exhibited significant hyperactivity and rearing behavior than the FXS female mice. FXS female mice showed a decreased anxiety, freezing, increased hole-poking behavior and motor coordination. Hippocampus dependent learning tasks were mainly used in detection of cognitive deficits in FXS. *Fmr*1$^{-/y}$ mice demonstrated an elevated social anxiety and a lower non-social anxiety. In a study were *Fmr*1$^{-/y}$ showed a novelty preference, but less nose contact with the stimulus mouse. The shorter period of nose contact of *Fmr*1$^{-/y}$ animals with a novel mouse, and elevated levels of grooming confirmed an increased social anxiety or arousal behavior in FXS. In an elevated zero maze, *Fmr*1$^{-/y}$ mice preferred to spend much time in open quadrants. This behavior displayed a decrease in non-social anxiety in FXS (Liu and Smith, 2009; McNaughton *et al.*, 2008).

5.8.3 CIRCUIT LEVEL ALTERATIONS

Circuit formation is depending on the neuronal activity in the brain. During early development stages, brain circuits shapes via an interplay of temporally defined gene expression patterns and spontaneous activity. Later with the development of sensory systems and experience from external stimuli, brain constitute, sharpen and better organize the neuronal circuits. A local regulatory mechanism of axonal sprouting and synaptogenesis also contribute to the new network formation (Katz and Shatz, 1996). *Fmr1* and FMRP are important for the formation of sensory cortical neuronal circuits during this 'critical period' (Doll *et al.*, 2017).

FMRP is differently expressed in various brain regions and different neuronal population. Due to this variation of expression these regions and cells act differently to the loss of FMRP. A cell with abundant FMRP is expected to have increased consequences due to the loss of this protein (Zorio *et al.*, 2017).

5.8.3.1 DISRUPTION OF NEUROGENESIS

Proper migration and maturation and distribution of neuronal subtypes across different brain layers are crucial for typical circuit formation. FMRP is important for the neurogenesis. Both FXS human and mouse showed alterations in neural stem cell early maturation. This further led to modified gene expressions in the FMRP deficient neuronal progenitor cells. A proper expression of these genes is essential for the neural development in typical human (Castrén *et al.*, 2005; Sunamura *et al.*, 2018). *Fmr*1$^{-/y}$ mouse also demonstrated impairment in

neurogenesis. Knocking FMRP out of neural stem and progenitor cells (aNSCs) upregulated the astrocyte differentiation and downregulated the neuronal differentiation in the hippocampus. Absence of FMRP caused failure of neural progenitor cell cycling and a reduction in the neural stem cells and an enhancement in number of neuroblasts. Neurogenesis in hippocampus is essential for hippocampus dependent learning. Any change in the neurogenesis in *Fmr*1$^{-/y}$ mice resulted in social anxiety impairment in hippocampus dependent learning in a delayed-nonmatching-to-place radial arm maze (DNMP-RAM) (Eadie *et al.,* 2009; Guo *et al.,* 2011; Sourial and Doering, 2017). FMRP also controls neocortical neurogenesis. FMRP is abundant in the cytoplasm of radial glial cells (RGCs) of embryonic neocortex. Specific knockdown of FMRP using shRNAs depleted the RGCs in WT as in *Fmr*1$^{-/y}$ mice. In a typical brain, FMRP prevents RGC to convert to intermediate progenitor cell (IPC) at different stages of neurogenesis in neocortex. So, a depletion led to an altered cell fate in the embryonic neocortex (Saffary and Xie, 2011). FMRP is a key player in the development of cortex. In normal condition, newly evolving progenitor cells proliferate and migrate and form new synaptic connections which are important for the circuit formation. In the absence of FMRP, N-Cadherin (Cdhr) mRNA (which controls neuronal morphology and motility) levels were decreased and these lower levels of N-Cdhr impaired cell differentiation, formation of new synaptic connections and therefore reduced the probability of establishing new circuits (both excitatory and inhibitory) (Fata *et al.,* 2014).

5.8.3.2 CHANGES IN CELL SIGNALLING

FMRP downregulate the RNA editing of neuronal mRNAs. In the absence of FMRP, synaptic protein expressions were upregulated during the early postnatal stage and downregulated in the adult. The synthesis of cerebral protein was downregulated by FMRP. *Fmr1* knockout mouse showed a significant increase of cerebral protein synthesis in various part of the brain (Filippini *et al.,* 2017; Qin *et al.,* 2005; Tang *et al.,* 2015). Decrease or absence of FMRP reduced the cAMP signal transduction mechanism, which linked to the proper regulation of cognitive functioning of the brain (Berry-Kravis and Ciurlionis, 1998). FMRP is expressed in sub populations of pyramidal neurons and form an association with nitric oxide synthase 1(NOS1) during early synaptic formation. This interaction increases the translation of NOS 1 and increase the production of nitric oxide (NO) a signaling molecule which is essential for the proper development and functioning of the nervous system (Kwan *et al.,* 2012; Lima-Cabello *et al.,* 2016). Rac1-cofilin signaling pathways that are important for the proper synaptic functioning and sensory processing were modified in FXS. These aberrant changes led to

abnormal dendritic spines and synaptic maturation in somatosensory cortex (Pyronneau *et al.*, 2017). D1 receptor signaling was impaired in prefrontal, anterior cingulate and striatum neurons of *fmr*1$^{-/y}$ mice. This in turn down regulated the phosphorylation of GluR1 receptors in FXS neurons (Wang *et al.*, 2008). Astrocyte derived factors like hiver and SPARC are important for the proper development of excitatory synapses. In *Fmr*1$^{-/y}$ cortex, there was an increase of hevin and a decrease of SPARC expression. But in hippocampus, hevin levels were significantly lower with no change in SPARC expression. It suggested the role of FMRP in astrocytic signaling and in excitatory neuronal synapse development (Wallingford *et al.*, 2017). In FXS, there was an enhancement of the Adcy1 mRNA levels. In response to the elevated levels of Adcy1 mRNA, ERK1/2 and PI3K signaling were increased in FXS mice. It contributed to different cellular abnormalities like spine density, intracellular signaling and excess protein synthesis in *Fmr*1$^{-/y}$ neurons (Sethna *et al.*, 2017).

5.8.3.3 DETERIORATION OF AXONAL GROWTH

FMRP is abundant in dendrites, axons and synapses of WT mice. Immunostaining for FMRP in *Fmr*1$^{-/y}$ neurons showed an absence of the protein in these locations. This increased the density of long, thin protrusions, 'the filopodia' in *Fmr*1$^{-/y}$ mice. Neuronal activity driven growth of dendritic protrusions including both filopodia and spines were absent in *Fmr*1$^{-/y}$ mice. FMRP loss also increased localization of filopodia in the axonal growth cone of FXS mice. The motility, of the growth cone was significantly diminished in FXS (Antar *et al.*, 2006). Fragile X granules (FXG), structures contain FMRP were widely distributed in the CNS. An elevated expression of these granules is seen in the long-range fiber tracks, thalamocortical axons and presynaptic neurons of sensory motor circuits in the *Fmr*1$^{-/y}$ mouse neocortex. Deletion of FMRP of thalamus, showed that FXG is originated by the interactions of thalamocortical and intracortical axons. This pathway specificity demonstrated the role of presynaptic FMRP in regulation of different sensory motor pathways in the brain (Akins *et al.*, 2012).

5.8.3.4 STRUCTURAL AND FUNCTIONAL CHANGES OF *FMR*1$^{-/Y}$ NEURONS

Fragile X mouse models displayed dendritic abnormalities in various regions of brain like occipital cortex, olfactory bulb and somatosensory barrel cortex (Galvez *et al.*, 2005; McKinney *et al.*, 2005). For instance, FMRP is present in newborn granules cells of olfactory bulb. Lack of FMRP increased the spine density, growth and absence of activity dependent dendritic remodeling at the olfactory cortex (Scotto-Lomassese *et al.*, 2011). FMRP is also

widely distributed across primary somatosensory cortex (S1), thalamus (Posteromedial nucleus, PMN) and striatum during early development in WT.

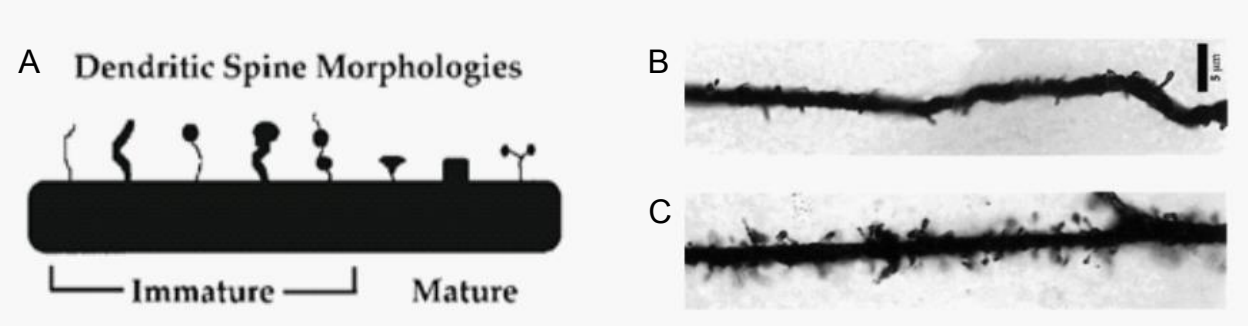

Figure 6: Dendrites in Fragile X syndrome. *A) Schematic representation of dendritic spine morphology. B) Dendritic spine morphology of control and C) Fragile X individual (Irwin et al., 2000).*

FXS neocortical neurons were characterized by long, tortuous spines with prominent terminal head. These changes contributed to modifications of intrinsic properties, spike generation or neurotransmitter release in *Fmr*1$^{-/y}$ neurons (Hinton *et al.,* 1991). CA1 pyramidal neurons in *Fmr*1$^{-/y}$ showed an increased action potential duration and firing frequency. On the other hand, the amplitude of after-hyperpolarization and after-depolarization was diminished in *Fmr*1$^{-/y}$ neurons (Luque *et al.,* 2017). L 2/3 prefrontal cortex pyramidal neurons in FXS mice showed taller and narrow action potentials in response to current injections. In this study they did not find any differences in neuronal dendritic arborization. They demonstrated the activation of a persistent long-lasting increase in the Na+ current and a fast inactivating K+ current in the soma of *Fmr*1$^{-/y}$ neurons. This elevation of sodium current could contribute to circuit level changes in FXS brain (Routh *et al.,* 2017).

Dendritic spine abnormalities and changes in synaptic plasticity in FXS are also due to failure of mGluR1 receptor dependent diacylglycerol kinase kappa (Dgkκ) activity in the absence of FMRP. *Fmr*1$^{-/y}$ mice exhibited an alteration in motor skill learning in a forelimb reaching task. Motor learning dependent synaptic strengthening of networks and dendritic spine density were significantly decreased in FXS. These changes contribute to diminished learning in motor related tasks in FXS (Padmashri *et al.,* 2013). With selective FMRP knockout in astrocytes, (Hodges *et al.,* 2017) reported an enhanced dendritic spine density during adolescence in the motor cortex. These mice showed impairment of motor-skill learning.

Even though the cortical anatomy were not changed much, the cortical maturation was disturbed by the lack of FMRP in FXS. Density of synapses and spines, synaptic protein translations and dendritic morphology changes were visible in *Fmr*1$^{-/y}$ mice (Irwin et al., 2000) (**Fig 6**). Alterations in the development and altered dendritic properties of somatosensory cortex could be a reason for the sensory hypersensitivity in Fragile X syndrome (Galvez *et al.*, 2003; Till *et al.*, 2012).

5.8.3.5 ALTERATIONS OF BASIC PROPERTIES OF SYNAPSES

Synaptic dysfunction is thought to underlie the severe intellectual disabilities in FXS. Impairment of several mechanisms in the brain together contribute to this deficit. In typically developing brain, FMRP interact with microRNA pathways. These interactions are crucial for neural development and formation of new synapses (Jin *et al.*, 2004). During the early development stage FMRP expression is crucial for the synaptogenesis (Gatto and Broadie, 2008). mGluR is one of the factors which stimulates the synthesis of FMRP at the synapses. *Fmr1* RNA positioning in dendrites also required an activation of mGluR. Different learning tasks and activation of Metabotropic glutamatergic receptors (mGluR) showed an increase of FMRP levels. Moreover, FMRP regulates scaffold proteins like Shank 1 and Gutamate receptors in the postsynaptic neurons. Absence of this protein impair all the scaffold protein and glutamate regulating cellular mechanisms in FXS mice (Antar *et al.*, 2004; Schütt *et al.*, 2009; Sidorov *et al.*, 2013). Another important example is the dysregulation of Neuroligin 1 (NL-1) which is important for the proper synaptic maturation and function in the absence of FMRP. Downregulation of NL-1 resulted in social interaction impairment and hyperactivity in FXS mice (Dahlhaus and El-Husseini, 2010). Rab3A, a presynaptic protein important for the release of neurotransmitters at the synapse is significantly down regulated in the absence of FMRP. This change reduced the neuropeptide release in the neocortex (Annangudi *et al.*, 2010).

fmr1 gene expression in presynaptic neurons regulate the number of synaptic connections to a cell (Hanson and Madison, 2007). For example, absence of postsynaptic FMRP in cochlear nucleus showed immature somato-dendritic morphology and delayed synaptogenesis (Wang *et al.*, 2018). On the other hand, excitatory synapses to auditory brain stem were increased in FXS (Garcia-Pino *et al.*, 2017). Development of both pre and postsynaptic inhibitory neurotransmission is altered in FXS differently across age. Postnatal age 10 (P10) showed a decreased inhibitory postsynaptic current (IPSC) amplitude, which was increased at P14 and

again went back to higher amplitude at P16 and then significantly decreased after P21 (Vislay *et al.,* 2013).

5.8.3.6 CHANGES IN SYNAPTIC PLASTICITY

Synaptic dysfunction is a key feature of FXS. FMRP plays a great role in regulation of these mechanisms. Single cell discharges and LFP oscillations formed by synaptic interactions of several cells exhibited aberrantly weak interactions between individual cells and neuronal networks in FXS mice (Talbot *et al.,* 2018). Studies show that there was an increase in the mGluR activation dependent long-term depression (LTD) in the absence or reduction (premutation) of FMRP. This exaggeration of LTD could contribute to the delay of synaptic maturation, development and cognitive impairment in FXS (Bear *et al.,* 2004; Huber *et al.,* 2002; Iliff *et al.,* 2013; Till *et al.,* 2011; Weiler and Greenough, 1999). Chemical induced long term potential (LTP) in hippocampus was upregulated by FMRP by regulating the phosphorylation of extracellular signal-regulated kinase (ERK)1/2. Dysfunctions of this signaling pathway actively contribute to impairment of synaptic plasticity and function, learning and memory in *Fmr*1$^{-/y}$ mice (Bassell and Warren, 2008; Desai *et al.,* 2006; Gu *et al.,* 2002; Shang *et al.,* 2009). Another study demonstrated the LTP induced by theta burst stimulation (TBS) and the LTD initiated by low frequency stimulus (LFS)were reduced in the Schaffer collateral pathway in hippocampus. In this study they also demonstrated an alteration of Alpha-amino-3-hydroxy-5-methyl-4-isoxazolepropionic acid receptor (AMPAR) mediated short term plasticity and increase in 3,5-dihydroxyphenylglycine (DHPG) induced LTD. These modifications of LTP, LTD and AMPARs significantly impaired the spatial learning and social behavior of *Fmr*1$^{-/y}$ mice (Cheng *et al.,* 2017; Huber *et al.,* 2002; Tian *et al.,* 2017). An imbalance of AMPA and NMDA ratio were visible during early postnatal development in *Fmr*1$^{-/y}$ (Pilpel *et al.,* 2009). This imbalance was resulted in enhanced development of excitatory synapses in FXS during critical period. It was associated with chloride homeostatic deficit which is caused by a chloride co-transporter NKCC1 in juvenile FXS mice. This deficit is considered as the cause of inhibitory excitatory imbalance, aberrant NMDA only silent synapses, LTP and whisker evoked responses in somatosensory cortex of *Fmr*1$^{-/y}$ mice (He *et al.,* 2017). A reduced LTP and mGluR1 expression was reported in cerebral cortex, and an increased LTP in lateral amygdala of FXS mice (Li *et al.,* 2002; Suvrathan *et al.,* 2010; Tabet *et al.,* 2016). Absence of FMRP resulted in a reduction of protein kinase A (PKA) at the synapses of Angular cingulate cortex (ACC) neurons. Impairment of PKA signaling caused a loss of pre-LTP in ACC of FXS mice (Koga *et al.,* 2015). In an experiment where the unilateral

whisker stimulations (with an artist's brush across the right vibrissal area) and motor-skill learning tasks (balance beams, chains, ladders, and other obstacles) showed an increased FMRP immunoreactivity compared to the non-trained FXS mice had strengthened the concept of association of the fragile X protein with the synaptogenesis and activity dependent plasticity (Irwin *et al.*, 2000; Todd and Mack, 2000).

5.8.3.7 ALTERATIONS OF NETWORK SYNCHRONY

Cognitive functions are regulated by the integration and segregation of different neuronal population from distinct regions of the brain. This neuronal synchrony is very crucial for the proper functioning of the brain. Different imaging techniques showed impairments of these synchrony in neurodegenerative disorders (Uhlhaas and Singer, 2006). Presence of FMRP in excitatory neurons are crucial to maintain the normal network synchrony in the neocortex. Deletion of *Fmr1* at the excitatory neurons produced longer spontaneous UP states (Hays *et al.*, 2011). *Fmr*1$^{-/y}$ mice exhibited an alteration in neuronal synchrony during early postnatal period. 2-photon calcium imaging showed that the number of neurons participated in the peaks of synchrony were significantly higher compared to WT. Single cell recordings from layer 2/3 neurons exhibited increased firing rates during the UP and DOWN states. These neuronal activity deficits were persistent across sleep and wakefulness in FXS. Under the isoflurane anesthesia, *Fmr*1$^{-/y}$ animals showed network activity and higher firing rate as similar as in unanesthetized *Fmr*1$^{-/y}$ mice. Isoflurane anesthesia is mediated by boosting the inhibitory $GABA_A$ receptors in the brain, which could be impaired in FXS mice and causing the hyperexcitability of the network (Gonçalves *et al.*, 2013). In a movement or at rest, brain networks switch between activated or inactivated states. WT and *Fmr*1$^{-/y}$ mice showed similar cortical modulations during movement and quiet rest. Multiunit activity in both WT and *Fmr*1$^{-/y}$ animals were increased during the movement. Interestingly the activated state prolonged only in *Fmr*1$^{-/y}$ across the quiet rest period. Interactions between interneurons and interneuron-excitatory neuron interactions were altered in *Fmr*1$^{-/y}$ mice. It caused a low cortical synchrony in FXS (Berzhanskaya *et al.*, 2017).

Autistic brain showed a poor synchrony and contact between the cortical regions. Circuit level underconnectivity led to alterations in sensory information processing in a task dependent manner. Correct sensory information is crucial for developing social interactions and failing this cause abnormal behavior towards a social stimulus in ASD (Just *et al.*, 2004).

5.8.3.8 HYPO-HYPER CONNECTIVITY

*Fmr*1$^{-/y}$ mice displayed a structural and functional hyper or hypoconnectivity in primary visual cortex (V1) (**Fig 7**). Structural and functional mapping in *Fmr*1$^{-/y}$ mice showed a hypoconnectivity between cortico-cortico, striatal-cortico networks from early development until the adulthood (Zerbi *et al.,* 2018). In developing barrel cortex of *Fmr*1$^{-/y}$ mice demonstrated 40 % decrease in the layer 4 (L4) excitatory neuronal projection to layer 3 (L3). Absence of FMRP did not change the average synaptic strength between L4 and L3 cells. But L4 axons were significantly more diffused in *Fmr*1$^{-/y}$ animals (Bureau *et al.*, 2008).

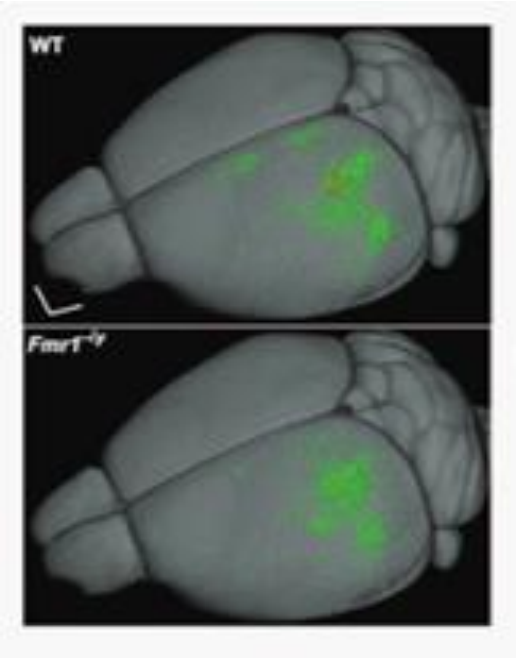

Figure 7: Reorganization of V1 inputs in Fmr1$^{-/y}$ mice*. The figure shows hyper-local connectivity and hypo-long range connectivity in Fmr1$^{-/y}$ mice (Haberl et al, 2015).*

Mesolimbic/ habenular reward circuit is altered in FXS. In the absence of FMRP, mice showed higher activations of this circuit during the presentation of a reward stimuli (odor of almond). They also exhibited higher functional activations of dorsal lateral striatum and lower activation of retro splenial cortices (Kenkel *et al.,* 2016). Furthermore, ASDs demonstrated a reduced local connectivity in prefrontal cortex and thalamus. They also displayed a reduced long-range connectivity in prefrontal cortex and an increased long-range connectivity in Thalamus (Tomasi and Volkow, 2017, Liska *et al.*, 2017).

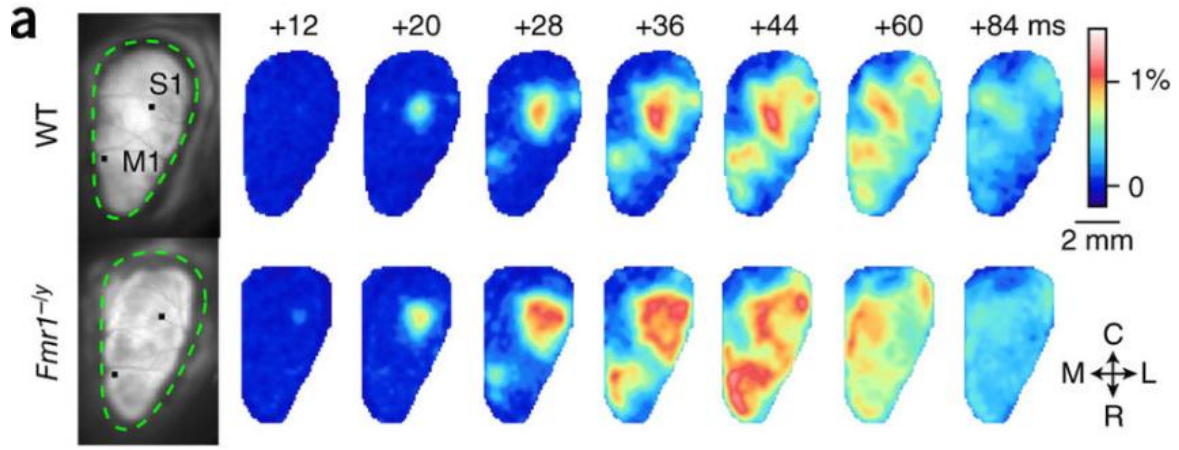

***Figure 8*: Accelerated spread of evoked neocortical activity in *Fmr1*$^{-/y}$ mice.** *The figure shows Typical cortical responses to single D2 whisker deflections monitored by VSD imaging in wild-type (WT, top) and Fmr1*$^{-/y}$ *(bottom) mice. Resting fluorescence of VSD-stained unilateral craniotomies are shown on the far left as averaged Gaussian-filtered fluorescent signals (n = 30 trials) at different times after D2 deflection. Cortical responses were measured over a large area (the green dashed line delimits the craniotomy) covering the barrel cortex (S1) and the primary motor cortex (M1). Adapted from (Zhang et al., 2014).*

Motor or somatosensory circuit impaired in *Fmr*1$^{-/y}$ mice. For instance, whisker related somatosensory cortex was highly sensitive to tactile (whisker) stimulation in FXS. *Fmr*1$^{-/y}$ mice showed exaggerated sensory response to whisker stimulations (**Fig 8**). In a gap cross task, KO animals showed reduced learning in crossing longer distance compared to WT animals. Perceptual learning required sensory motor integration (Zhang et al., 2014, Arnett *et al.*, 2014).

It is suggested that abnormal elimination or formation of synapses could be contributing to the hyper-local connectivity and a hypo-long range connectivity in ASD (Sporns *et al.*, 2000).

5.8.3.9 EXCITABILITY

Both FXS individuals and *Fmr*1$^{-/y}$ mice are hyperexcitable. The hyperexcitability in FXS emerges two to three weeks after the birth. Interestingly two days before the eye-opening, juvenile FXS rats demonstrated a hyposensitivity towards a visual stimulus coupled with low spiking rate and absence of thalamus dependent early gamma oscillations. Later stages of development there was an enhancement of excitatory neuronal activity and reduced inhibition in FXS and were resulted in hyperexcitability (Berzhanskaya *et al.*, 2016). Another aspect of hyperexcitability in FXS is the impairment of synaptic scaling. Synaptic scaling is required for the neurons to maintain the scale of synaptic strength during severe changes in neuronal activity. Absence of FMRP leads to suppression of epilepsy-associated ubiquitin e3 ligase and dephosphorylation of gene Nedd4-2 and caused a failure of ubiquitination and down-regulation of GluA1 subunit of AMPA. This failure triggered synaptic downscaling in FXS hippocampal neurons and form aberrant excitability in FXS (Geschwind, 2008; Lee *et al.*, 2018a). CaMKIIα levels were increased in the absence of FMRP. Elevated CaMKIIα enhanced the phosphorylation of Homer, a protein important for mGluR receptor signaling. Impairment of mGluR5- Homer protein interactions led to circuit hyperexcitability in in *Fmr*1$^{-/y}$ neurons (Ronesi *et al.*, 2012, Guo *et al.*, 2015). Furthermore, inhibitory $GABA_A$ receptors in the brain, which could be impaired in *Fmr*1$^{-/y}$ mice and causing the hyperexcitability of the network

(Gonçalves *et al.*, 2013). Local excitation of fast spiking interneurons (FS) in L4 was impaired in FXS. A reduction in the FS excitatory drive onto excitatory neurons were eventually led to increased intrinsic excitability in L4 pyramidal neurons. Overall, decreased inhibition and increased excitatory neuronal activity increased the UP-state duration in *Fmr*1$^{-/y}$ mice demonstrated a circuit level excitability (Gibson *et al.*, 2008).

To better understand the pathology behind the sensory information processing deficit in FXS, we focused on a wide array of methods which address changes in neurons, circuits and behavior of *Fmr*1$^{-/y}$ mice. With these we looked at different sub-types of layer 2/3 pyramidal neurons in the hind paw related primary somatosensory cortex. We studied the neocortical neuronal activity at rest and activity changes in response to intrinsic events and external stimuli.

6 MOUSE NEOCORTEX

The neocortex consists of glia and neurons that are defined by their cellular composition and defined connectivity. Mouse neocortex is composed of different layers (1, 2/3, 4, 5 and 6) (**Fig 9**). These layers are placed on top of white matter, which is a mix of axons and glia. Neuronal morphology, layer thickness, gene expression and the distribution of the cellular markers are different between cortical regions.

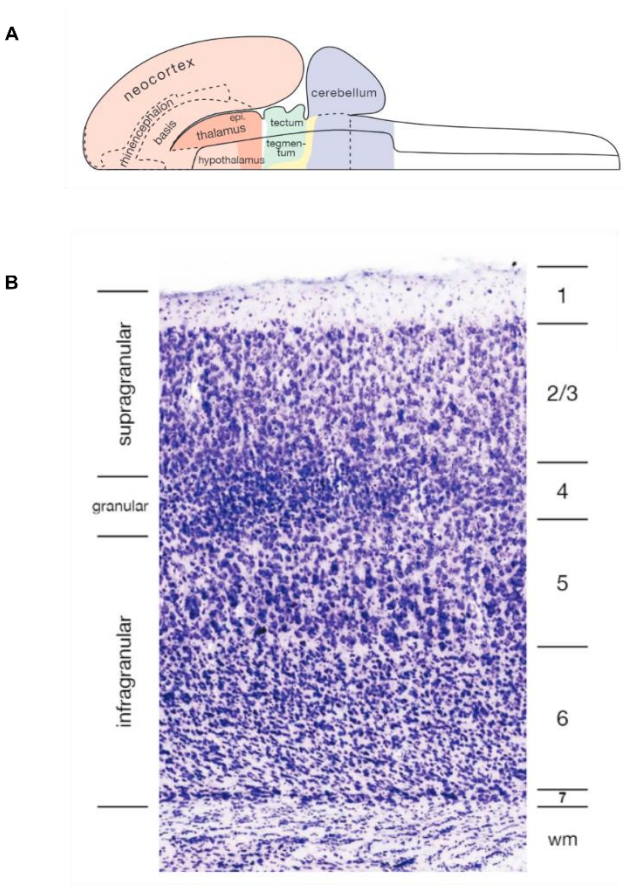

Figure 9: Mouse neocortex. A) *Map of the central nervous system (Swason et al., 2000) representing cerebral cortex and other brain regions.* ***B)*** *representation of different layers in neocortex of the mouse S1-barrel cortex (Matthew T.K, Book chapter, Neocortex).*

Layer (L) 2/3 is composed of mostly small pyramidal neurons which are mainly involved in local and long-range connectivity. L2/3 is considered as a single layer in mouse brain. Some studies showed distribution of functions within the L2/3. (Bureau et al., 2006) reported that primary somatosensory barrel cortex (S1-BC) L2/3 neurons receives inputs from thalamus via lemniscal and paralemniscal pathways from L4 and L5A. Lemniscal L4 neurons mainly projected to L3 and the paralemniscal L5A neurons projected to the superficial part of L2/3 immediately below Layer 1. Layer 2/3 contains different interneuron populations like chandelier cells and basket cells. They also contain Martinolli cells, neurogliaform cells, bitufted and bipolar cells. Each of these cells demonstrated stereotypical electrophysiological properties(Jiang et al., 2015). These interneurons form electrical and chemical synapses with excitatory neurons and other interneurons. These interactions are essential to regulate neuronal synchrony and coordinate different regions in the cortex (Galarreta and Hestrin, 2001).

7 TACTILE SYSTEM IN RODENTS

Touch is one of the most important senses in our body. In contrast to other sensory modalities like vision, audition and olfaction, somatic sensation provides both the physical nature and the spatiotemporal pattern of objects (Hartmann, 2011). The tactile system develops before all other sensory systems and it is critical for the development of motor skills, as well as social and physical relationships with other members of a society (Cascio, 2010; Mikkelsen et al., 2018). Our tactile world is rich. With the help of touch sensation, we identify, discriminate and react differently to various objects around us. Attention is required for the earliest stages of sensory processing. Tactile attention includes selective processing of the features of objects and of the spatial coordinates within which the stimuli appear. Various studies in humans collectively show that a relevant tactile information alone stimulated the activity of somatosensory-motor cortices (reviewed in (Burton and Sinclair, 2000).

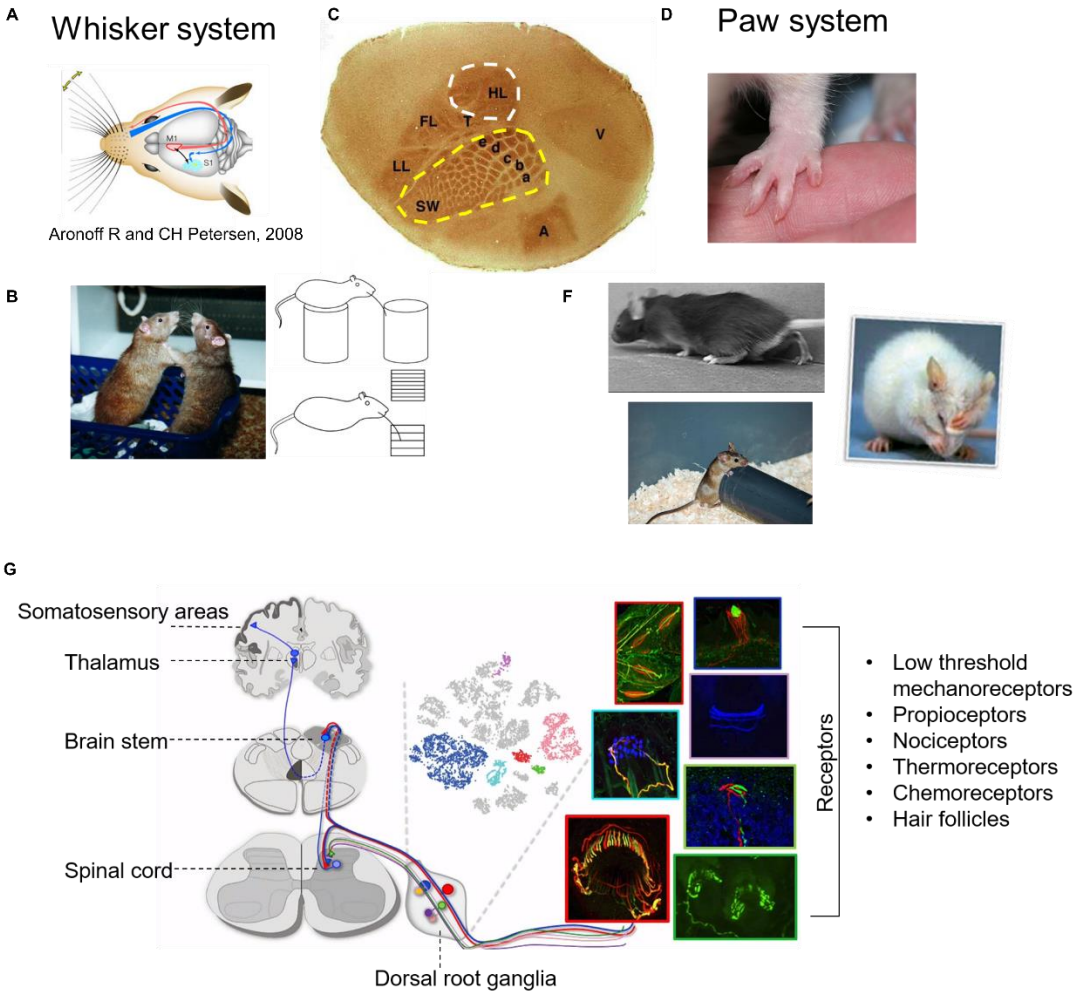

The sensory neurons of Touch, David Ginty (2018)

***Figure 10: Tactile system in rodents**. **A**) Representation of whisker system and the flow of information from the receptors (hair follicles) to sensory and motor cortices. **B**) Whiskers are mainly used for social communication, texture discrimination and object localization. **C**) Top view of the mouse brain displaying barrel cortex (SW), hind paw (HL) and fore paw (FL) cortices. **D, F**) Paws are mainly used for movement, discrimination of objects and self-grooming. **G**) schematic showing the tactile sensory information flow from the periphery (receptors) to the somatosensory integration areas.*

Rodents tactile system mainly consisting of a well-defined whisker system and paw system (hind paw and forepaw). Mice use the whiskers for social communication, texture discrimination and object recognition. On the other hand, paws are used mainly for the movement, discrimination of objects and self-grooming (Aronoff R and CH Petersen, 2008; Hirasawa et al., 2016; Carlson and Burton, 1988) (**Fig 10**).

The hind paw of the mice consists of low threshold mechanoreceptors like Merkel cells and Pacinian corpuscles under the glabrous skin of the hind paw of mice. The information reaches the peripheral receptors and from there this information is carried into brain stem dorsal column nuclei (DCN) via dorsal horn. A second order neuron carry sensations from DCN to the thalamus and provide excitatory input into the thalamus via the lemniscal pathway. The excitatory-inhibitory balance within the thalamus shapes the responses to tactile stimuli. Finally, a third order thalamocortical neuron forwards the stimulus to the somatosensory cortex (Abraira and Ginty, 2013; Aguilar et al., 2008, Orefice et al., 2016) (**Fig 10**). In some cases, sensory information will be sent from neocortex to other brain regions. For instance, tactile sensations associated with discriminative touch from whiskers also relayed to CA1 regions of hippocampus (Pereira et al., 2007). Furthermore, sensory evoked responses measured using fMRI demonstrated a wide range of functional connectivity of S1-HP to anterior, medial, parietal cortices, and motor, cingulate and prefrontal cortices (Schroeter et al., 2016). WT mice were able to discriminate two different foot stimuli (electrical and mechanical) and associate these with somatosensory discrimination learning (Hirasawa et al., 2016). Removal of SI and SII in adult macaque produced severe and irreversible impairment on a variety of tactile tasks like texture and size discrimination (Carlson and Burton, 1988).

In this study I focused on Layer 2/3 pyramidal neurons of hind paw related primary sensory cortex. We classified the neurons according to their response towards a tactile sensory stimulation of hind paw (**Fig 11**) of mouse. We further studied different parameters including

spontaneous activity, intrinsic properties and characteristic features of hind paw evoked sensory responses.

8 AIM OF THE CURRENT STUDY

Fragile x syndrome (FXS) is the most common heritable form of intellectual disability and the best-known cause of autism, and is caused by hypermethylation of a single gene, *Fmr1* (Brown et al., 1982a; 1982b; Penagarikano et al., 2007). It is well characterized by changes in structural and functional connectivity in the developing brain (Cascio, 2010; Lai et al., 2016; Zerbi et al., 2018). In FXS patients, there is a high prevalence of sensory information processing defects – a feature shared with ASD (Haigh, 2017; Posar and Visconti, 2017; Robertson and Baron-Cohen, 2017). FXS mice display a higher cortical network synchrony, local and long-range connectivity deficits. These changes affect the circuits and pathways associated with sensory perception and integration in FXS and are considered an important cause of cognitive and behavioural impairment in ASD (Contractor et al., 2015; Gonçalves et al., 2013; Haberl et al., 2015; del Pino et al., 2018; Zerbi et al., 2018). Modifications of excitatory circuits lead to changes in spontaneous cortical network activity and impairment of functional properties and connectivity of individual neurons. These alterations of circuits and individual neuronal structural and functional properties together contribute to the aberrant sensory processing in FXS (Baum et al., 2015; Bhakar et al., 2012; Cornish et al., 2004; Fata et al., 2014; Hays et al., 2011; Juczewski et al., 2016).

During the early development, there seems to be a reduced connection probability of glutamatergic inputs between different layers in the primary somatosensory cortex of *Fmr1*$^{-/y}$ mice (Bureau et al., 2008). It is known that the hypermethylation of the *Fmr1* gene affects different protein interactions, receptors and ion channels which are crucial for neuronal intrinsic excitability in the brain (Brown et al., 2010; Deng et al., 2013; Ferron, 2016; Frick et al., 2017; Johnston et al., 2016; Sunamura et al., 2018; Zhang et al., 2014). In a normal brain, cortical excitatory neurons show a difference in input-output connectivity to neuronal subtypes of various layers. This dissimilarity creates diverse intrinsic electrophysiological properties and aberrant sensory responses to different sensory stimuli. (Douglas and Martin, 2004; Estebanez et al., 2015; Milenkovic et al., 2014; Pinto and Dan, 2015).

Consistent with clinical studies, (Dahlhaus, 2018; Puts et al., 2014; Tavassoli et al., 2016) *Fmr1*$^{-/y}$ mice display sensory hypersensitivity and hyperexcitability to multiple sensory modalities (Ethridge et al., 2017; Gibson et al., 2008; Rotschafer and Razak, 2014; Takarae

and Sweeney; Zhang et al., 2014; 2018). In FXS, there is an overall effect on the number of local synapses, ion channels, membrane excitability and circuit activities of the cell types. Individual neurons in different brain regions as well as within the same brain region are affected in FXS. These changes in neuronal properties could be the cause of hypersensitivity and hyperexcitability in FXS (Gibson et al., 2008; Kalmbach et al., 2015; Sinclair et al., 2017). Thus, it is important to do measurements from identified neuronal subtypes in the neocortex. Study of intrinsic properties and sensory evoked responses of individual excitatory neurons are important to understand sensory outputs, integration of information, sensory perception, learning and cognition in FXS (Arieli et al., 1996; Katz and Shatz, 1996; Zhang et al., 2014).

Previous studies from our laboratory (Zhang et al., 2014; Haberl et al., 2015, Zerbi,…… Arjun A Bhaskaran et al., 2018) and others demonstrated an increased hyperexcitability and dysfunctions in neocortical circuits and behavioral deficits in FXS mice. Therefore, we propose an alteration in spontaneous, intrinsic and circuit level alterations in hind paw related primary cortex layer 2/3 in FXS mice leading to atypical sensory information processing in FXS mice.

Here we addressed various questions. First, examined if a cortical excitatory neuron (in a typically developing brain), which responds to a sensory stimulus is different in their functional properties from a neighboring cortical excitatory neuron which do not respond to the same stimulus. Second, we verified if these neurons are altered functionally and structurally in a mouse model of fragile X syndrome. Third, what could be the possible mechanisms involved in these alterations. Finally, we tested whether targeting ion channels (previously known to have deficits in FXS) pharmacologically could rescue some of these defects.

To answer these questions, we used whole cell patch clamping *in vivo* coupled with a hind paw sensory stimulation and recorded spontaneous, intrinsic properties and the evoked responses to the stimulus. we identified three sub-types of neurons in the hind paw related primary somatosensory cortex (S1-HP) of wild type littermate. We classified them as suprathreshold responders (neurons responded with action potentials, APs), subthreshold responders (neurons responded with no APs) and non-responders (neurons did not show any response). We explored spontaneous, intrinsic and sensory stimulus evoked activities of these neuronal sub-types. We then probed the properties of the same sub-types of neurons in *Fmr*1$^{-/y}$ mice. We looked at the cortico-cortical and thalamocortical connectivity in these mouse model. Later we tested the sensory motor ability of *Fmr*1$^{-/y}$ mice in an adhesive removal test.

CHAPTER 2

9 MATERIALS AND METHODS

9.1 ETHICAL STATEMENT

All experimental procedures were performed in accordance with the EU directive 2010/63/EU and French law following procedures approved by the Bordeaux Ethics Committee (CE2A50). Mice were housed in a SPF animal facility before experiments, kept on a 12 h: 12 h light: dark cycle and always had ad libitum access to food and water. All experiments were performed in the light phase.

9.2 ANIMAL BACKGROUND

A Second generation *Fmr1* knockout (*Fmr1*$^{-/-}$; *Fmr1*$^{-/y}$) mice (Mientjes *et al.*, 2006) were used in our study. These mice are distinct from the original *Fmr*$^{1-/y}$ mouse line (Bakker *et al.*, 1994) because they are deficient for both *Fmr1* RNA and Fragile X mental retardation protein (FMRP) (Mientjes *et al.*, 2006). These mice were generated by backcrossing 129/Sv/C57Bl/6J/FVB founders into a C57Bl/6J background (6 generations). Male wild-type and *Fmr*1$^{-/y}$ littermates were generated by crossing *Fmr*1$^{+/-}$ females with a wild-type mouse from the same background. Given that *Fmr1* is carried on the X chromosome, the resulting male progeny were either *Fmr*1$^{+/y}$ (wild-type) or *Fmr*1$^{-/y}$ (KO).

9.3 ELECTROPHYSIOLOGY EXPERIMENTS

9.3.1 INTRACELLULAR SOLUTION

The major content of our solution is potassium methane-sulfonate ($KMeSO_3$). Ethylene glycol-bis (β-aminoethyl ether)-N,N,N',N'-tetraacetic acid (EGTA) is added to the solution to stabilize the intracellular free calcium ion concentration. HEPES [4-(2-hydroxyethyl)-1-piperazineethanesulfonic acid)] helped to maintain the pH of the solution. Energy molecules like Magnesium/Sodium ATPs (adenosine triphosphate) are added to the solution to promote

sodium potassium gradients across the cell membrane. Sodium GTP (Guanosine triphosphate) is added to maintain G-protein mediated responses.

1x intracellular solution was freshly prepared every day prior to the experiments. A proper mix of internal solution (2x) and ddH_2O resulted in an osmolarity of 280 to 290 mmol. The final intracellular solution was filtered using a 0.22-µm pore-size centrifuge filter (Costar Spin-X).

9.4 PHARMACOLOGICAL TREATMENT

To study the cause of alterations in spontaneous, intrinsic and evoked responses, different ion channels and receptors were targeted.

To target BKca channels, mice were treated with BMS- 191011. A stock of 50 mM of BMS191011 was prepared in DMSO and were stored as 20 µL aliquots at -20°C. For the cortical application of the drug, it was diluted to a final concentration of 100 µM in PBS (dilution 1:500).

Cortical applications of BMS-191011 was performed at least 30 minutes prior to the whole cell patch clamp experiments.

9.5 ANIMAL PREPARATION

About 4-5 weeks old male *Fmr*1$^{-/y}$ mice and their WT littermates were chosen randomly for the experiment. Animals were kept in the experiment room and allowed to habituate for at least 30 minutes prior to the anesthesia. It helped us to reduce the stress and respiratory events partially during the experiments.

Mice were anesthetized with a mixture of ketamine (100 mg.kg−1) and xylazine (10 mg.kg−1) and administered via intraperitoneal injections. After 5 minutes, the absence of reflex was verified with a gentle air puff to the eyes and pinches on the tail and toes (upper and lower limbs). If the reflexes were absent, experimental protocols were started. The head of the animal

was shaved and cleaned properly. Mice were head-fixed using non-puncture ear-bars and a nose-clamp (SR-6M, Narishige). The head of the animal was kept not too low or high to avoid abnormal breath and heart rate. In all the experiments, temperature was maintained at 37°C. Conductive adhesive strips (~1 cm2) were placed on and under the hind-paw (HP) and in some experiments, above and below the fore-paw (FP). For local anesthesia, a few drops of lidocaine were injected under the skin covering the skull and waited at least for 2 minutes. The skin was cut with a scalpel or scissors and exposed the skull. The surface of the skull was cleaned well to get rid of tissues and muscles. The target region (1 mm posterior to bregma, 1.5 mm lateral) was marked using the stereotactic manipulator. The stereotaxic coordinates were previously assessed in a set of control experiments using intrinsic optical imaging. The surface (1mm x 1mm) around the marking was thinned carefully using a dental drill (World Precision Instruments). Phosphate buffered saline (1X PBS) was supplemented to cool down the surface during the drill. With forceps, the thickness of the thinned skull was observed. Four sides of the thinned skull were scratched without damaging the cortex and the bone flap was carefully flipped and removed. Immediately PBS was applied on the craniotomy to prevent drying and bleeding. Using a sponge, the blood (if bleeding) and the PBS solution were removed. The surface was let to dry briefly until a slight shiny dura appeared. With a needle (always a new needle) tip, a small hole was made on the dura. Using fine tipped forceps, the hole was expanded, and the dura was completely removed. PBS was applied again to prevent surface drying. In some cases where blood vessels were encountered, the dura hole expansion was restricted to a smaller region to avoid bleeding.

For thalamic stimulation experiments, a small hole (300 µm approx.) was drilled (1.95 mm posterior to bregma, 1.5 mm lateral) to fix the electrode.

9.6 WHOLE CELL PATCH CLAMP *in vivo*

All signals were acquired using a Multiclamp 700B amplifier and Clampex 10.4 software (Axon Instruments). Data were low-pass filtered at 3 kHz and sampled at 20 kHz.

Pipettes with an open-tip resistance of 4–6 MΩ were pulled from borosilicate glass using a PC-10 puller (Narishige) and filled with intracellular solution (1x). The pipette was attached to the head stage. The PBS solution was removed completely from the skull surface. Then the pressure inside the pipette was increased (> 200 mBar). Pipette was lowered until it touched the surface of the brain and that point was taken as zero. PBS was applied again. In current clamp, the offset was set to zero. Then the system was switched to voltage clamp to monitor the test pulse (+10 mV, 5-10 ms, repetition rate > 10 Hz). To perform recordings in layer 2/3, the electrode was lowered until 125 mm at an angle of 30º. At this level the pressure was lowered to 30-50 mBar and changed to STEP mode. Further the pipette was lowered at 2 µm steps until the presence of a cell was detected. The cell-pipette interactions were identified by a rapid bouncy reduction in the test pulse (≥ 20%). Once the cell contact was confirmed, the pipette was advanced to one or two steps and the pressure was released immediately. A tremendous reduction in the pulse was visible and immediately the holding voltage was changed to -70 mV. Most of the cells were sealed immediately. In some cases, a suction was required for the giga seal (>1GΩ). After attaining the giga seal, a sharp suction pulse was used to achieve a whole cell mode. After recording the pipette was gently removed (slow steps). Each experiment ranged from 2 to 3 hours.

9.7 HIND PAW (HP) AND FOREPAW (FP) STIMULATIONS

Sensory responses were evoked by applying current pulses (2 ms, 100 V, 30 mA) via conductive adhesive strips (~1 cm^2) placed on and under the HP and FP, as described previously (Palmer *et al.*, 2012). These electrodes covered the entire paw (toes and palm, both

glabrous and hairy skin). Once the whole cell was achieved, the HP was stimulated 40 times with at least 3 sec of interval (~0.3 Hz) and recorded evoked responses of the attached cell. After, we stimulated the FP and tested if the same cell responds to both HP and FP. In a few experiments the cells were filled with biocytin for post-hoc neuronal labeling (Fig, **A, B**).

9.8 VENTRAL POSTERIOR MEDIAL NUCLEUS (VPM) OF THALAMUS STIMULATIONS

VPM (1.955 mm posterior to bregma, 1.5-1.75 mm lateral and 3-4 mm depth) was stimulated (200µs, 200 µA, 10 s interval, 20 trials per stimulation session) using a concentric bipolar electrode (FHC, CBARC 50) (Viaene *et al.*, 2011). First, a stimulation of HP (as previously explained) was done. Later VPM was stimulated and the thalamus evoked responses were recorded from the same neuron. After the completion of the experiment, a lesion was made at VPM using injection of current pulses (2 mA, 2 ms, 40 trials)

9.9 ADHESIVE REMOVAL TEST

We performed the adhesive removal test as explained in (Bouet *et al.*, 2009). Briefly, adhesive removal test is used to study the sensory motor deficits related to the paw and mouth. Mice were habituated to the new environment at least 30 minutes prior to the experiment (experiment room is different from that of housing). Then the animals were kept in a testing box (new regular transparent box used to house the mice) for another 60 seconds. Rectangular similar sized adhesive tapes were applied to the plantar surface of right and left hind paws of the animal with equal pressure. Each animal was always held by similar experimenter and the other experimenter stick the adhesive tapes on the paws. After the adhesive tape placement, the animals were gently kept in the testing box. Direct observations were made by two experimenters standing on each side of the testing box. Contact time (the time point where the mouse sensed the presence of adhesive strips on the paw) to right and left paws, ‘Start of

removal' time and the 'end of removal' were measured with the help of timers. With these values we also calculated the 'total duration' (from contact time to the finish of removal).

9.10 PERFUSION

Following biocytin filling (1- 5mg/ ml Biocytin) of the recorded neurons, the brains were fixed by transcardial perfusion with 4% paraformaldehyde in PBS and post-fixed for 2h at room temperature (RT). Subsequently, 80-µm-thick tangential slices were cut using a vibratome (Leica).

9.11 IMMUNOHISTOCHEMISTRY

9.11.1 BIOCYTIN STAINING FOR RECONSTRUCTION

After the perfusion, biocytin filled neurons were detected using streptavidin-Alexa Fluor 555 (1:1,000, 2h at RT).

9.11.1.1 REAGENTS

The slices were washed 3 to 5 times with 0.1M PB. Then the slices were treated with permeabilization solution (0.7% triton X in 1x PBS), incubation at RT for 2 hours. The slices were stained with Streptavidin-Alexa 555, 1:1000 + 0.3% tritonX in 1x PBS, incubation at RT in dark for 2.5 hours. After the staining, the slices were washed 3 to 5 times with 0.1M PB. The slices positive for biocytin were mounted in Mowiol and allowed to dry for semi-automated Neurolucida reconstructions.

9.11.2 DAPI (4,6 – diamidino-2-phenylindole dihydrochloride)

DAPI was mainly used to identify the layers and the target regions. A stock solution 5mg/mL of DAPI was prepared in ddH2O and stored at -20ºC. The slices were left in DAPI (1: 10000) for 15-20 minutes on a shaker. The slices were then washed three times (10 minutes interval) with 1x PBS and mounted in Mowiol for further identifications.

9.12 DATA ANALYSIS

9.12.1 SPONTANEOUS AND INTRINSIC PROPERTIES

To determine the AP threshold, we measured the membrane potential at the beginning of the rising phase of the first AP occurring during the IV curve protocol. AP half-width was determined by measuring the duration of these first APs at half-amplitude (from threshold to the peak). For recording/analysis of the afterdepolarization (ADP), trains of three APs at various frequencies were generated by brief somatic current injections (1 nA, 1.08 ms), and those AP trains occurring during down states were selected for the analysis. Three to six trials were averaged, and the ADP amplitude (from baseline) was measured 5 ms after the peak of the last AP. AP half-width ratio was measured as the ratio between the third and first AP. To measure input resistance, we injected 500-ms-long hyperpolarizing (-100 pA) current and measured the membrane potential deflection at 300 ms relative to baseline after bridge balance correction. We determined average up- and down-state membrane potentials by plotting the distribution of membrane potential values. Up-state frequency and duration analysis were adapted from (Beltramo et al. 2013). Briefly, the spontaneous down- to up-state transitions were identified as membrane depolarization crossing a threshold set at 1/3 of the amplitude down- to up-state. Only transitions in which the signal remained for more than 150 ms above the threshold were considered. All analysis was performed using ClampFit 10.4 software (Axon Instruments).

9.12.2 EVOKED RESPONSE ANALYSIS

Parameters of evoked sub-threshold synaptic potentials were calculated from an averaged trace of 40 successive trials. Onset was computed as the earliest point, less than 50 ms after stimulation, at which Vm crossed a baseline +3 standard deviation thresholds. Sweeps for which an onset less than 50 ms could not be detected were counted as failures. Peak latency was calculated as the time from the onset of the stimulus to the maximum peak of the averaged

response. The duration of the synaptic responses was calculated by measuring the width of the averaged response at half-maximal amplitude. The duration of the synaptic responses was calculated by measuring the width of the averaged response at half-maximal amplitude. Noise is calculated as the standard deviation measured within a 200 ms time window just before the stimulus onset. Signal to Noise ratio is represented as the ratio between mean response amplitude and the standard deviation of the baseline.

The calculation of evoked supra-threshold responses and their coefficient of variation were adapted from (de Kock et al., 2007). Briefly, the number of APs was quantified within a 200-ms-long time window following the stimulus onset and averaged over 40 stimulus trials. The average spontaneous activity (0–200 ms window before stimulus) was then subtracted from this value. The coefficient of variation was calculated by dividing the number of APs within 200 ms following the stimulus by the standard deviation on a trial-by-trial basis. AP jitter is analysed by plotting trials in function of time to peak of spikes within a 100 ms time window just after the stimulus onset. All analysis was performed using Clampfit 10.4 software (Axon Instruments) and Python.

9.12.3 STATISTICAL TESTS USED

All the values were first tested for outliers (Grubb's outlier test) followed by normality check using Shapiro-Wilk normality test. If the values were normally distributed an unpaired t-test is used. For non-normally distributed parameters we used Mann-Whitney's U-test. To compare three or more groups, we used two-way repeated ANOVA (GraphPad Software) followed by Bonferroni post-hoc analysis. P values < 0.05 were considered significant (* $P < 0.05$, ** $P < 0.01$, *** $P < 0.001$). Boxplots indicated the median value (middle line), the 25^{th} and 75^{th} percentiles (box), and the highest and lowest values (whiskers).

CHAPTER 3

10 RESULTS 1

10.1 DEFECTS IN TACTILE STIMULUS EVOKED RESPONSES OF LAYER 2/3 PYRAMIDAL NEURONS IN THE *FMR*1$^{-/Y}$ MOUSE MODEL OF FRAGILE X SYNDROME

The three main aims of my PhD thesis were (1) the characterization of hind paw (HP) stimulus elicited sensory responses in layer (L) 2/3 pyramidal neurons of the corresponding primary somatosensory cortex (S1-HP) in mice (**Fig 11**), (2) the identification of the circuit alterations underlying atypical sensory information processing in *Fmr*1$^{-/y}$ mice, and (3) the testing of a pharmacological approach for the correction of sensory defects.

To address these aims, I performed *in vivo* whole-cell patch-clamp recordings from individual L2/3 pyramidal neurons (PN) to measure their intrinsic properties, spontaneous activity, and paw stimulus evoked responses in anaesthetized wild type (WT) and *Fmr*1$^{-/y}$ mice. In addition, I used direct electrical stimulation of the thalamic projections from the ventral posteromedial nucleus (VPM) to the S1-HP to probe alterations in this pathway to the sensory deficits in *Fmr*1$^{-/y}$ mice. Finally, I utilized a HP dependent behavioral task to evaluate a possible link between atypical sensory processing and a behavioral outcome.

10.1.1 CLASSIFICATION OF LAYER 2/3 PYRAMIDAL NEURONS ACCORDING TO THE PRESENCE OF SENSORY STIMULUS EVOKED RESPONSES

Stimulation of the HP elicited either no response in L2/3 PN of the contralateral S1-HP region, a sub-threshold response (EPSP only), or in few neurons supra-threshold responses (action potentials) in some of the trials (**FIG 11**). Accordingly, we classified the recorded neurons into two main groups. Those responding to the hind-paw stimulation were classified as 'responder' (R) cells (including both sub- and supra-threshold responders), and those that did not respond as 'non-responder' (NR) cells (**Fig 11, C**).

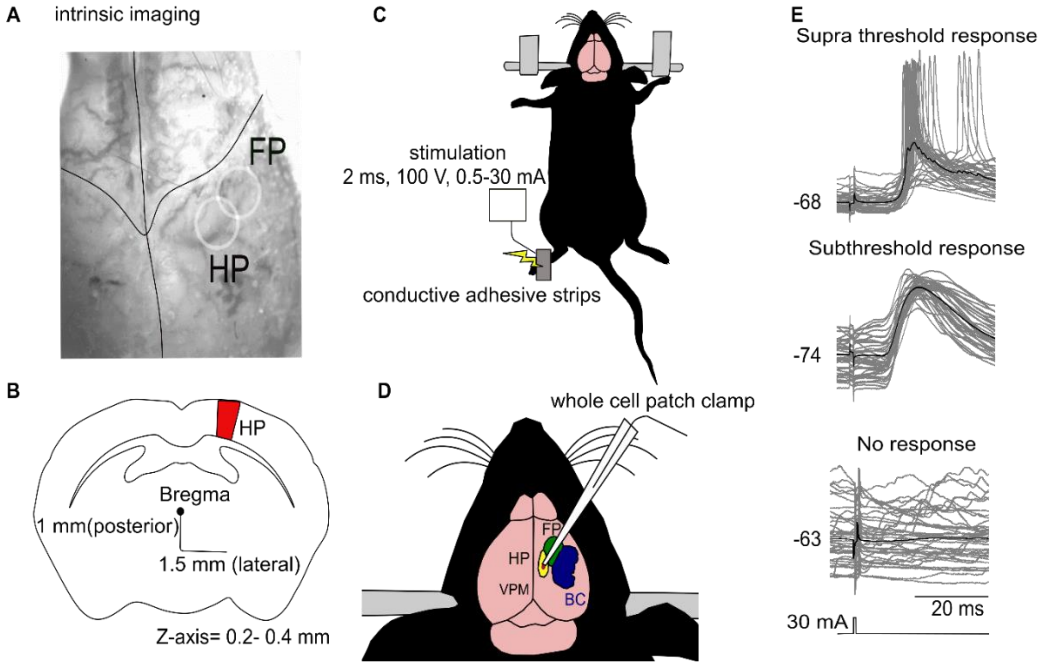

Figure 11: Hind paw related primary somatosensory cortex (S1-HP) layer 2/3 (L2/3) pyramidal neurons (PN) showed distinct responses to HP stimulations. ***A)*** *Intrinsic imaging showing region of interest (ROI), HP.* ***B)*** *Co-ordinates according to the Allen brain mouse connectivity atlas (in red, HP).* ***C)*** *Schematic representation of hind-paw stimulation. Each stimulation session consisted of 40 trials. A 2-ms long current stimulus of 30-mA was given via attached conductive adhesive strips (top).* ***D)*** *Whole cell patch clamp recording at hind-paw*

region of the cortex were performed during the stimulation in anesthetized mice. ***E****) Example traces from three neurons representing supra-threshold responses (top), sub-threshold responses (middle) and no response to sensory stimulus (bottom).*

In WT mice, 43.48 % (20 out of 46 cells) of L2/3-PN were sub-threshold R-cells, and 41.3 % (19/46) NR-cells. There was no significant difference in this distribution between *Fmr*1$^{-/y}$ and WT mice (*Fmr*1$^{-/y}$ R-cells, 44.4 % (32/72); NR-cells, 45.8 % (33/72); $p > 0.05$, Fisher's exact test). Approximately 15.21 % (7/ 46) of R cells in WT and 9.7% (7/72) in *Fmr*1$^{-/y}$ mice were supra-threshold R-cells (WT-R_{supra} vs *Fmr*1$^{-/y}$ R_{supra}, $p > 0.05$). Overall, there was no difference in the average depth of recording of L2/3 PN between WT (R, 227.7 ± 64.9 µm; NR, 228 ± 73 µm) and *Fmr*1$^{-/y}$ mice (R, 245 ± 71 µm; NR, 252. 73 ± 68.14 µm). Interestingly, however, there was a significant shift in the presence of supra-threshold R-cells from L2 towards L3 in *Fmr*1$^{-/y}$ mice (WT-R_{supra} = 175.84 ± 51.7 µm; *Fmr*1$^{-/y}$ R_{supra} = 250 ± 53.26 µm, $p < 0.01$) (**Fig 24**).

The result section is structured in the following way. First, I describe the spontaneous firing properties of NR- and R-cells in WT mice and compare these properties to those of neurons from *Fmr*1$^{-/y}$ animals (**Section 10.2, 10.2.1** to **10.2.3**). Similarly, I will then analyze the intrinsic properties of these neurons (**Section 10.3, 10.3.1** to **10.3.3**) and their dendritic morphology (**Section 10.4, 10.4.1** to **10.4.5**) for both neuronal populations and genotypes. The main part will be devoted to the characterization of HP stimulus evoked responses in WT mice and their alterations in *Fmr*1$^{-/y}$ mice (**Section 10.5-10.8**). Next, I used a sensory motor behavior paradigm (**Section 10.9**) to test the impact of these cellular/circuit deficits for the behavioral output. Finally, **Section 10.10** will describe the effects of pharmacological targeting of BK_{Ca} channels on sensory stimulus evoked responses.

In some of the chapters we included the properties of NR-cells in our analysis. These neurons might either respond to tactile stimulation of the hind-paw digits (rather than the palm) or

encode sensory modalities such as temperature or pain. Nonetheless, we think it is interesting to describe some of their properties in WT mice, as well as their alterations in *Fmr*1$^{-/y}$ mice.

10.2 SPONTANEOUS FIRING ACTIVITY IN WT AND *FMR*1$^{-/Y}$ MICE.

10.2.1 SPONTANEOUS FIRING ACTIVITY OF NR- AND R_{sub}- CELLS IN WT MICE

Ongoing spontaneous activity in the brain is important for encoding information about our surrounding environment (Arieli et al., 1996). This spontaneous firing activity is intrinsically produced in the cortex and critical for sensory perception, learning and cognition (Gilbert and Sigman, 2007).

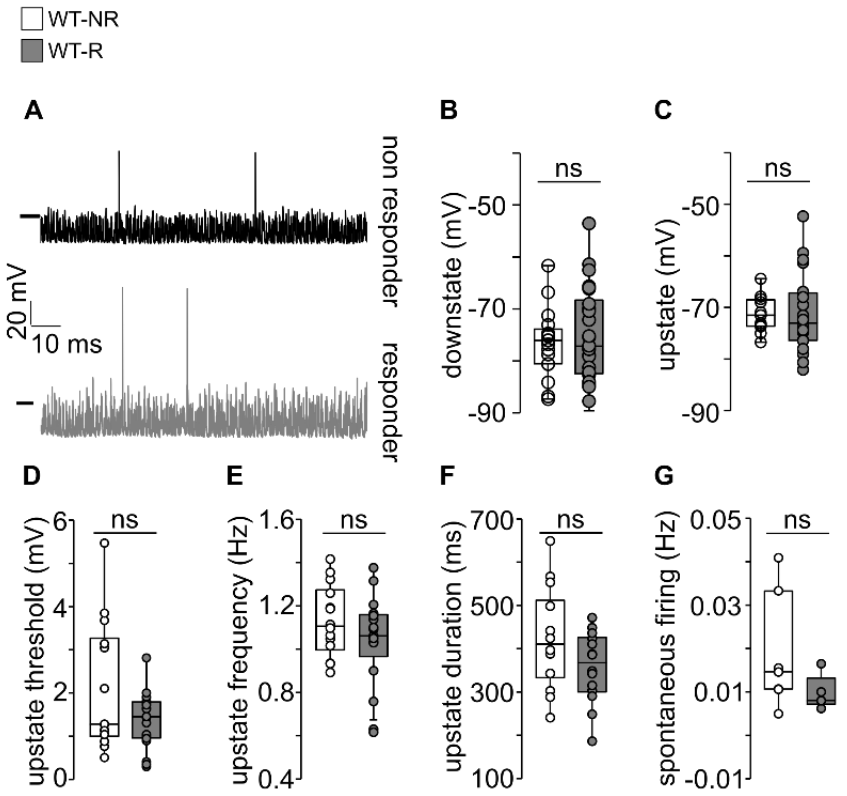

***Figure 12*: Spontaneous firing activity in WT mice. A)** *Example traces of spontaneous firing activity of NR- and R_{sub}- neurons in anesthetized WT mice. Horizontal marks indicate -60 mV.*

B) *Down-state (WT-NR, median = -76.04 mV, n = 17; WT-R_{sub}, median = -77.17 mV, n = 26; p > 0.05, unpaired t-test)* ***C)*** *and Up-states (WT-NR, median = -71.49 mV, n = 12; WT-R_{sub}, median = -73.03 mV, n = 20; p > 0.05, unpaired t-test) were comparable between NR- and R_{sub}- cells.* ***E)*** *Upstate threshold (WT-NR, median = 1.27 mV, n = 14; WT-R_{sub}, median = 1.45 mV, n = 26; p > 0.05, unpaired t-test),* ***F)*** *Upstate frequency (WT-NR, median = 1.1 Hz, n = 14; WT-R_{sub}, median = 1.06 Hz, n = 17; p > 0.05, unpaired t-test) and* ***G)*** *Upstate duration(WT-NR, median = 410.55 ms, n = 14; WT-R_{sub}, median = 367.2 ms, n = 14; p > 0.05, unpaired t-test) were unchanged.* ***H)*** *NR- cells demonstrated a non-significant but higher spontaneous firing rate than WT- R_{sub}- cells (WT-NR, median = 0.0146 Hz, n = 7; WT-R_{sub}, median = 0.008 Hz, n = 5; p > 0.05, Mann-Whitney U-test). Boxplots show the median, interquartile, range and individual values. P > 0.05, non-significant (Fmr1$^{-/y}$ compared to wild type). Statistical significance was calculated by unpaired student t-test (for normal distribution) and Mann-Whitney U-test (Not normal distribution).*

To learn more about this ongoing activity in L2/3 PN of the S1-HP region and to probe its alteration in *Fmr*1$^{-/y}$ mice, we measured the spontaneous firing rate, and the frequency and amplitude of Up-/ Down-states. In WT mice, we found that NR-cells displayed a non-significant spike rate when compared to R_{sub}- cells (WT-NR-, 0.0185 ± 0.012 Hz; WT- R_{sub}-, 0.011 ± 0.005; p > 0.05) (**Fig 12, G**). The membrane potential (Vm) at Up-/ Down-states was comparable between WT-NR- and WT- R_{sub}- cells (Down-state; WT-NR-, -76.60 ± 6.53 mV; WT- R_{sub}-, -75.05 ± 8.77 mV; p > 0.05) (Up-state; WT-NR-, -71.28 ± 3.42 mV; WT- R_{sub}-, -71.16 ± 7.75 mV; p > 0.05) (**Fig 12**, **B, C**). Similarly there was no difference for the Up-states with respect to their threshold (WT-NR-, 2.09 ± 1.49 mV; WT- R_{sub}-, 1.38 ± 0.62 mV; p > 0.05), frequency (WT-NR-, 1.13 ± 0.16 Hz; WT- R_{sub}-, 1.039 ± 0.209 Hz; p > 0.05), and duration (WT-NR-, 418.64 ± 116.02 ms; WT- R_{sub}-, 357.09 ± 81.8 ms, p > 0.05) (**Fig 12, D, E, F**).

10.2.2 SPONTANEOUS FIRING ACTIVITY OF NR- AND R_{sub}- CELLS IN *FMR1*$^{-/Y}$ MICE

Previous studies reported alterations in Up/- Down-states and network hyperexcitability for layer 4 cells of the S1-barrel cortex in *Fmr1*$^{-/y}$ mice (Gibson et al., 2008; Hays et al., 2011). We tested whether these phenotypes were also present in the L2/3 network of S1-HP of *Fmr1*$^{-/y}$ mice.

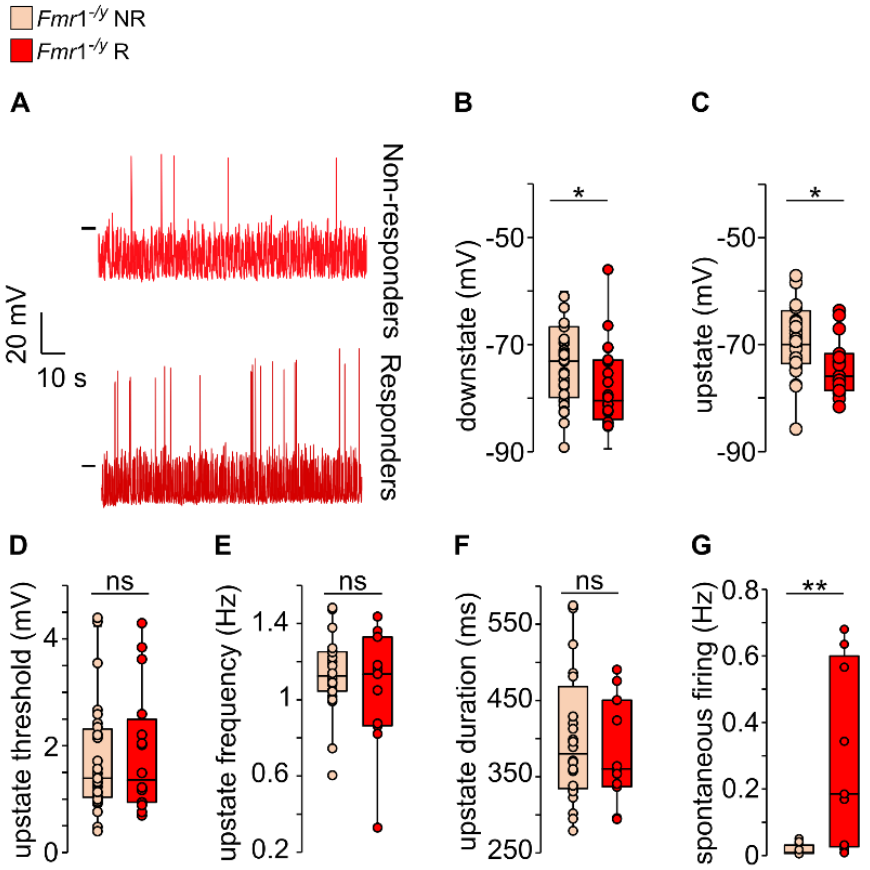

***Figure 13**: **Differences in spontaneous firing rate and UP-/Down-states between NR- and R_{sub}- cells in Fmr1$^{-/y}$ mice. A)** Example traces of spontaneous firing activity of NR- and R_{sub}-neurons in anesthetized Fmr1$^{-/y}$ mice. Horizontal marks indicate -60 mV. **B)** Down-state (Fmr1$^{-/y}$-NR, median = -61.03 mV, n = 33; Fmr1$^{-/y}$-R_{sub}, median = -56.02 mV, n = 19; $p < 0.05$, Mann-Whitney U-test) **C)** and Up-states (Fmr1$^{-/y}$-NR, median = -69.97 mV, n = 29; Fmr1^{-}*

$^{/y}$-R_{sub}, median = -75.94 mV, n = 15; p < 0.05 , unpaired t-test) were significantly different between NR- and R_{sub}- cells. ***E****) Upstate threshold (Fmr1$^{-/y}$-NR, median = 1.39 mV, n = 28; Fmr1$^{-/y}$-R_{sub}, median = 1.358 mV, n = 16; p > 0.05, Mann-Whitney U-test),* ***F****) Upstate frequency (Fmr1$^{-/y}$-NR, median = 1.125 Hz, n = 24; Fmr1$^{-/y}$-R_{sub}, median = 1.135 Hz, n = 11; p > 0.05, unpaired t-test) and* ***G****) Upstate duration (Fmr1$^{-/y}$-NR, median = 380.11 ms, n = 12; Fmr1$^{-/y}$-R_{sub}, median = 360.135 ms, n = 11; p > 0.05, Mann-Whitney U-test) were unchanged.* ***H****) NR- cells demonstrated a significant increase in spontaneous firing rate than R_{sub}- cells (Fmr1$^{-/y}$-NR, median = 0.009 Hz, n = 12; Fmr1$^{-/y}$-R_{sub}, median = 0.185 Hz, n = 9; p < 0.01, Mann-Whitney U-test). Boxplots show the median, interquartile, range and individual values. *p < 0.05, **p < 0.01, ^{ns}p > 0.05 (Fmr1$^{-/y}$ compared to wild type). Statistical significance was calculated by unpaired student t-test (for normal distribution) and Mann-Whitney U-test (Not normal distribution).*

We first compared the Up-/ Down-states of NR- and R_{sub}- cells in *Fmr*1$^{-/y}$ mice. We found that the Down-state was significantly more depolarized in NR-cells compared to R_{sub}-cells (*Fmr*1$^{-/y}$ NR, -74.4 ± 6.64 mV; *Fmr*1$^{-/y}$ R_{sub}-, -78.89 ± 5.89 mV; Mann-Whitney U-test; p < 0.05) (**Fig 13, B**), while Upstate was significantly more hyperpolarized in R_{sub}-cells (*Fmr*1$^{-/y}$ NR-, -70.17 ± 5.91 mV; *Fmr*1$^{-/y}$ R_{sub}-, -74.16 ± 5.50 mV; Unpaired t-test; p < 0.05) (**Fig 13, C**). Interestingly, and in contrast to WT mice, the spontaneous firing pattern of R_{sub}-cells in *Fmr*1$^{-/y}$ mice was significantly increased when compared to NR-cells (*Fmr*1$^{-/y}$ NR, -0.019 ± 0.015 Hz; *Fmr*1$^{-/y}$ R_{sub}-, 0.293 ± 0.273 Hz; Mann-Whitney U-test; p < 0.01) (**Fig 13, G**). Upstate threshold (*Fmr*1$^{-/y}$ NR, 1.75 ± 1.03 mV; *Fmr*1$^{-/y}$ R_{sub}-, 1.87 ± 1.16 mV; Mann-Whitney U-test; p > 0.05), frequency (*Fmr*1$^{-/y}$ NR, 1.136 ± 0.196 Hz; *Fmr*1$^{-/y}$ R_{sub}-, 1.05 ± 0.316 Hz; Unpaired t-test; p > 0.05) and duration (*Fmr*1$^{-/y}$ NR, 403.59 ± 88.6 ms; *Fmr*1$^{-/y}$ R_{sub}-, 380.65 ± 68.85 ms; Mann-Whitney U-test; p > 0.05) were unchanged in *Fmr*1$^{-/y}$ mice (**Fig 13, D, E, F**).

10.2.3 SPONTANEOUS ACTIVITY IS ALTERED IN *FMR1*$^{-/-Y}$ MICE

In the previous two chapters I described specific differences in Up-/Down-states and spontaneous firing rates between R_{sub}- and NR-cells in WT mice. Interestingly, these cell-type dependent differences disappeared in *Fmr1*$^{-/-y}$ mice, reflecting cell-type- and circuit specific alterations in this disorder (**Fig 12, 13**).

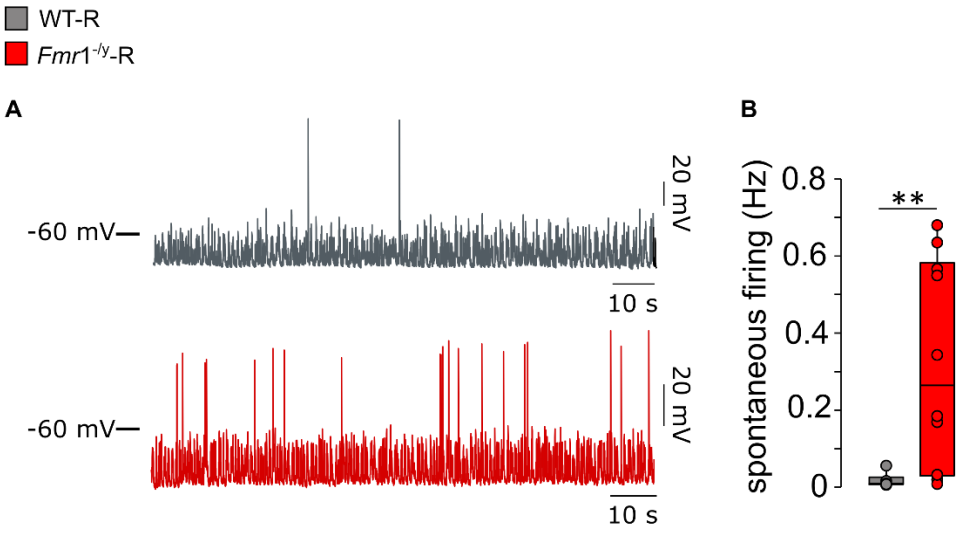

***Figure 14**: **Spontaneous firing rate of R_{sub}-cells was significantly increased in Fmr1$^{-/y}$ compared to WT mice**. **(A)** Example traces of Up-/Down-states subthreshold responder cells in WT (top) and Fmr1$^{-/y}$ mice (bottom). (**B**) Spontaneous firing rate of subthreshold responder cells were significantly enhanced in Fmr1$^{-/y}$ mice (WT-R_{sub}, median = 0.008 Hz, n = 5; Fmr1$^{-/y}$-R_{sub}, median = 0.185 Hz, n = 9; p < 0.01, Mann-Whitney U-test). Boxplots show the median, interquartile, range and individual values. **p < 0.01 (Fmr1$^{-/y}$ compared to wild type). Statistical significance was calculated by unpaired student t-test (for normal distribution) and Mann-Whitney U-test (Not normal distribution).*

Next, I will compare the genotype dependent variations for R_{sub}- and NR-cells. First, we measured a significant difference in the UP-/Down-states between R_{sub}-and NR-cells in *Fmr1*$^{-/-y}$ mice (**Fig, 13**), which was not observed for WT mice. Across genotypes, however, there was no difference in this feature for R_{sub}-cells (unpaired t-test, p > 0.05). There was no genotype

effect on Up-state for either cell type (cf. WT mice, Mann-Whitney U-test, $p > 0.05$). Second, we found that the spontaneous firing of R_{sub}-cells was significantly increased in *Fmr*1$^{-/y}$ mice (cf. WT mice, Mann-Whitney U-test, $p < 0.01$) (**Fig 14, B**), while there was no difference for NR-cells across genotypes.

In conclusion, we observed cell-type specific alterations in spontaneous activity in *Fmr*1$^{-/y}$ mice, which might give rise to changes in the ongoing activity and the processing of sensory information within the L2/3 network of S1-HP.

10.3 INTRINSIC EXCITABILITY PROPERTIES OF NR- AND R_{sub}- CELLS

We then asked if these genotype specific changes in the spontaneous activity of NR-/ R_{sub} neuronal populations are caused by an alteration in their intrinsic excitability properties. The intrinsic properties of neurons crucially regulate their input/ output function due to the presence of ion channels in the membrane of neurons. Thus, any change in the functional properties or expression levels of ion channels will alter the integration of information in neurons- for example as a consequence of plasticity or in disorders (reviewed in Frick & Johnston, 2005; Szlapczynska et al., 2014, Johnston et al., 2016).Our lab and others previously reported an increase in the intrinsic excitability of S1-L5 pyramidal neurons in *Fmr*1$^{-/y}$ mice (Zhang et al., 2014, Zhang et al., 2016; reviewed in Johnston et al., 2016; Frick et al., 2017).

Here, we probed if similar alterations in the intrinsic properties were also present in L2/3 PN of S1-HP in *Fmr*1$^{-/y}$ mice. First, we investigated the intrinsic properties of NR- and R_{sub}- cells in WT mice, and then compared these measurements with those from neurons in *Fmr*1$^{-/y}$ mice.

10.3.1 INTRINSIC PROPERTIES OF NR- AND R_{sub}- CELLS IN WT MICE

Characterization of the action potential firing properties in response to current injections showed significant differences between NR- and R_{sub}-cells in WT mice (**Fig. 15**). The

number of APs as function of current injected was not different between the two groups (**Fig 15, E**; $p > 0.05$). Accordingly, the maximum number of evoked APs (WT-NR, 20.63 ± 10.60; WT- R_{sub}-, 18.59 ± 5.45; unpaired t-test $p > 0.05$) (**Fig 15, F**), and the number of APs fired at 2 times rheobase (WT-NR, 7.38 ± 4.87; WT- R_{sub}-, 9.53 ± 3.22; $p > 0.05$) (**Fig 15, G**) were comparable.

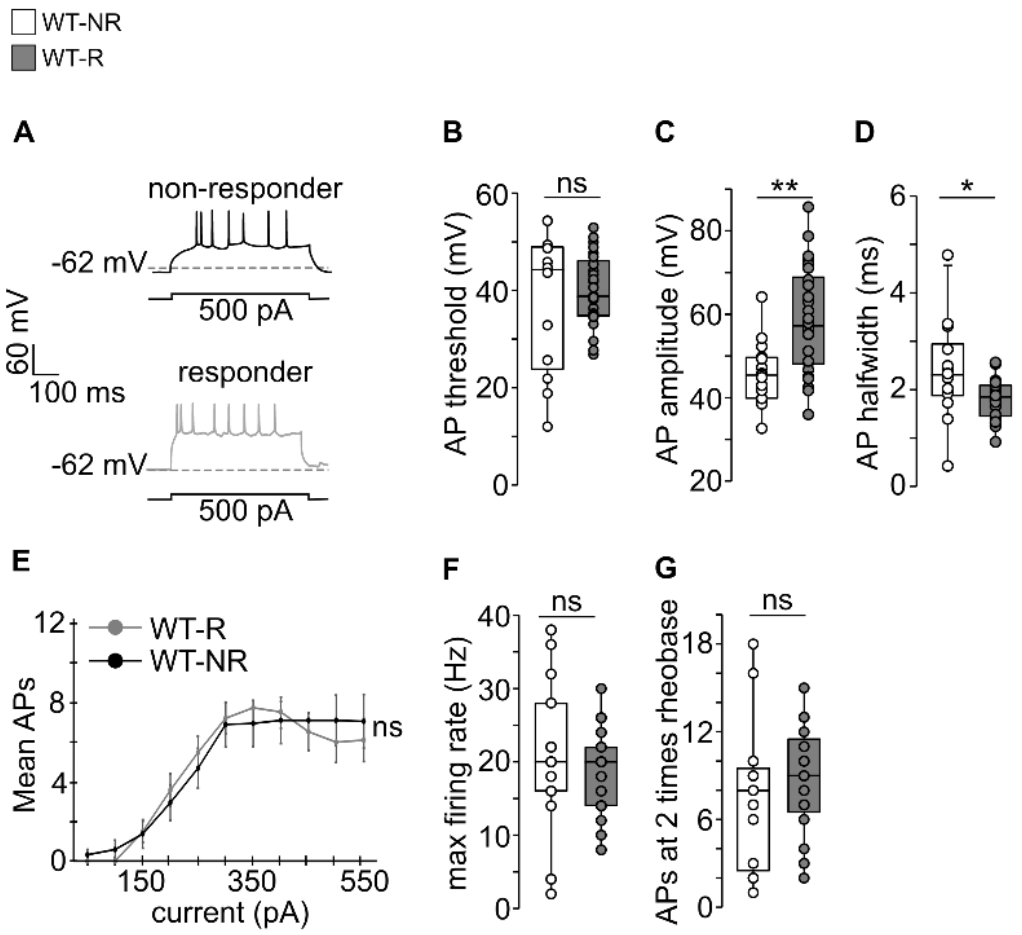

***Figure 15**: **Increase in AP amplitude of R_{sub}-versus NR-cells in WT mice. A**) Example traces of voltage responses to steps of current injection (500 pA) in one NR- and R_{sub}-cell. **B)** There was no difference in AP threshold of WT- NR and WT- R_{sub}- cells WT-NR, median = 44.295 mV, n = 13; WT-R_{sub}, median = 39.38 mV, n = 25; $p > 0.05$, unpaired t-test). **C)** WT-R_{sub} cells demonstrated a significantly larger AP amplitude than NR-cells (WT-NR, median = 45.42 mV, n = 15; WT-R_{sub}, median = 57.235 mV, n = 26; $p < 0.01$, unpaired t-test). **D)** WT-NR cells*

showed an increased AP halfwidth (WT-NR, median = 2.30 ms, n = 14; WT-R_{sub}, median = 1.82 ms, n = 24; p < 0.05, unpaired t-test) ***E****) Average number of APs as a function of current injected was not different between both neuronal populations (repeated measurements two-way ANOVA, p > 0.05). Maximum number of evoked APs (WT-NR, median = 20, n = 19; WT-R_{sub}, median = 20, n = 27; p > 0.05, unpaired t-test)* ***F****), and, spikes at 2 times rheobase (WT-NR, median = 8, n = 17; WT-R_{sub}, median = 9, n = 21; p > 0.05, unpaired t-test)****G****) were similar for both groups. Boxplots show the median, interquartile, range and individual values. *p < 0.05, **p < 0.01, ^{ns}p >0.05 (Fmr1$^{-/y}$ compared to wild type). Statistical significance was calculated by unpaired student t-test (for normal distribution) and Mann-Whitney U-test (Not normal distribution).*

The amplitude of the first AP within a train of WT- R_{sub}- cells was significantly higher compared to WT-NR-cells (WT-NR-, 45.83 ± 7.62 mV; WT- R_{sub}-, 58.53 ± 12.6 mV; unpaired t-test; p < 0.01) (**Fig 15, C**). WT- NR-cells exhibited an increase in AP halfwidth (WT-NR-, 2.39 ± 1.01 ms; WT- R_{sub}-, 1.825 ± 0.43 ms; p > 0.05) (**Fig 15, D**). AP-threshold did not show any differences between the two population of neurons (WT-NR-, 38.17 ± 14.24 mV; WT-R_{sub}-, 40.49 ± 7.27 mV; Unpaired t-test; p > 0.05).

In conclusion, except for the amplitude of APs, NR- and R_{sub}-cells of WT mice showed similar firing properties in response to step current injections.

10.3.2 INTRINSIC PROPERTIES OF NR- AND R_{sub}-CELLS IN *FMR*1$^{-/-Y}$ MICE

*Fmr*1$^{-/y}$ NR- and R_{sub}- cells showed a larger average number of spikes (8-10 spikes/ step current) at the maximal current injection steps (450-550 pA) compared with WT neurons (**Fig 16, E**), suggesting an increase in intrinsic excitability and a concomitant change in the firing properties. Furthermore, *Fmr*1$^{-/y}$ NR- and R_{sub}- cells showed a higher maximum evoked number of spikes compared to the WT animals. Within the genotype *Fmr*1$^{-/y}$ NR- and R_{sub}-

cells did not display any differences their maximum evoked responses (*Fmr1*$^{-/y}$ NR-, 23.15 ± 8.2; *Fmr1*$^{-/y}$ R_{sub}-, 23.68 ± 6.5; Mann-Whitney U-test; p > 0.05) (**Fig 16, F**).

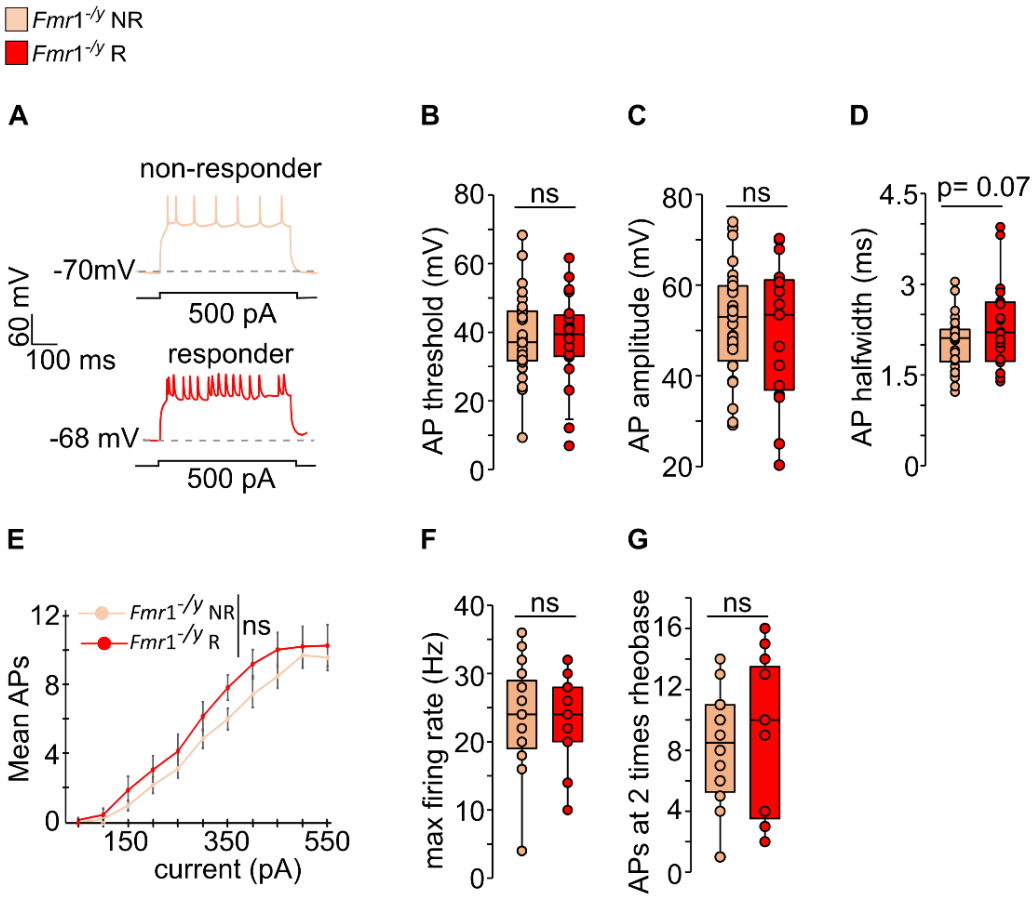

***Figure 16**: **Decrease in AP duration of NR-versus R_{sub}- cells in Fmr1$^{-/y}$ mice. A, B**) Example traces of voltage responses to 500 pA current injection in NR- and R_{sub}- cells of Fmr1$^{-/y}$ mice. **B)** There was no difference in AP threshold of Fmr1$^{-/y}$-NR and Fmr1$^{-/y}$ - R_{sub}- cells (Fmr1$^{-/y}$-NR, median = 37.10 mV, n = 32; Fmr1$^{-/y}$ - R_{sub}, median = 39.48 mV, n = 20; p > 0.05, unpaired t-test). **C)** There were no differences in AP amplitude between these cells (Fmr1$^{-/y}$-NR, median = 53.02 mV, n = 32; Fmr1$^{-/y}$ - R_{sub}, median = 52.22 mV, n = 20; p > 0.05, unpaired t-test). **D)** Fmr1$^{-/y}$-R_{sub} cells showed a trend of increase AP halfwidth (Fmr1$^{-/y}$-NR, median = 2.11 ms, n = 30; Fmr1$^{-/y}$ - R_{sub}, median = 2.20 ms, n = 20; p = 0.07, unpaired t-test) **E)** Average number of APs as a function of current injected was not different between both neuronal populations*

(repeated measurements two-way ANOVA, p > 0.05). Maximum number of evoked APs (Fmr1$^{-/y}$-NR, median = 24, n = 33; Fmr1$^{-/y}$ - R_{sub}, median = 24, n = 19; p > 0.05, unpaired t-test) ***F)****, and, spikes at 2 times rheobase (Fmr1$^{-/y}$-NR, median = 8.5, n = 20; Fmr1$^{-/y}$ - R_{sub}, median = 10, n = 13; p > 0.05, unpaired t-test)* ***G)*** *were similar for both groups. Boxplots show the median, interquartile, range and individual values. ^{ns}p > 0.05 (Fmr1$^{-/y}$ compared to wild type). Statistical significance was calculated by unpaired student t-test (for normal distribution) and Mann-Whitney U-test (Not normal distribution).*

The number of APs fired at 2 times rheobase was not distinct within the two *Fmr*1$^{-/-y}$ populations (*Fmr*1$^{-/y}$ NR-, 7.85 ± 3.91; *Fmr*1$^{-/y}$ R_{sub}-, 8.69 ± 4.99; Unpaired t-test; p > 0.05) (**Fig 16, G**). There were also no differences in AP threshold (*Fmr*1$^{-/-y}$ NR-, 39.26 ± 12.32 mV; *Fmr*1$^{-/y}$ R_{sub}-, 37.96 ± 13.42 mV; p > 0.05) and AP amplitude within *Fmr*1$^{-/y}$ mice (*Fmr*1$^{-/-y}$ NR-, 48.29 ± 7.94 mV; *Fmr*1$^{-/y}$ R_{sub}-, 49.67 ± 15.44 mV; p > 0.05) (**Fig 16, B, C**). In contrast, the AP halfwidth was altered in *Fmr*1$^{-/y}$ NR- and R_{sub}-cells showed an increased spike halfwidth compared to the WT population. *Fmr*1$^{-/y}$ NR- cells showed a trend of increased AP halfwidth compared to *Fmr*1$^{-/y}$ R_{sub}-cells (*Fmr*1$^{-/y}$ NR-, 2.019 ± 0.43 ms; *Fmr*1$^{-/y}$ R_{sub}-, 2.315 ± 0.72 ms; Unpaired t-test; p = 0.07) (**Fig 16, D**).

Overall, the NR- and R_{sub}-cells demonstrated a variation from the properties of similar cell population in WT mice. For instance, the number of APs evoked as a function of current injected and the AP firing were higher in both NR- and R_{sub}-cells of *Fmr*1$^{-/y}$ mice. Also, the spike amplitude difference of NR- and R_{sub}-cells no longer existed in *Fmr*1$^{-/y}$ mice. Another key characteristic that we noticed was the increase of AP halfwidth in both NR- and R_{sub}-cells of *Fmr*1$^{-/y}$ mice. This confirms the previous finding pointing towards the role of FMRP in regulation of AP duration in hippocampus and other cortical regions (Zhang et al., 2014, Deng et al., 2013).

10.3.3 INTRINSIC PROPERTIES WERE CHANGED IN *FMR1*$^{-/Y}$ COMPARED TO WT MICE

The average number of APs as a function of current injected was significantly increased in *Fmr1*$^{-/y}$ R_{sub}- cells (Unpaired t-test p< 0.05) (**Fig 17, C**). Thus, the maximum number of APs was approximately increased by 66 % in *Fmr1*$^{-/y}$ R_{sub} cells (point-by-point comparison using unpaired t-test; current steps between 450 and 550 pA) ($p < 0.05$) cells (**Fig 17, C**). The maximum evoked firing was significantly increased in *Fmr1*$^{-/y}$ R_{sub}- cells when compared with WT- R_{sub}- cells ($p < 0.01$) (**Fig 17, D**).WT- NR-cells did not show any difference in the average number of spikes at maximal current steps when compared with *Fmr1*$^{-/y}$ NR- cells (not shown, $p > 0.05$).

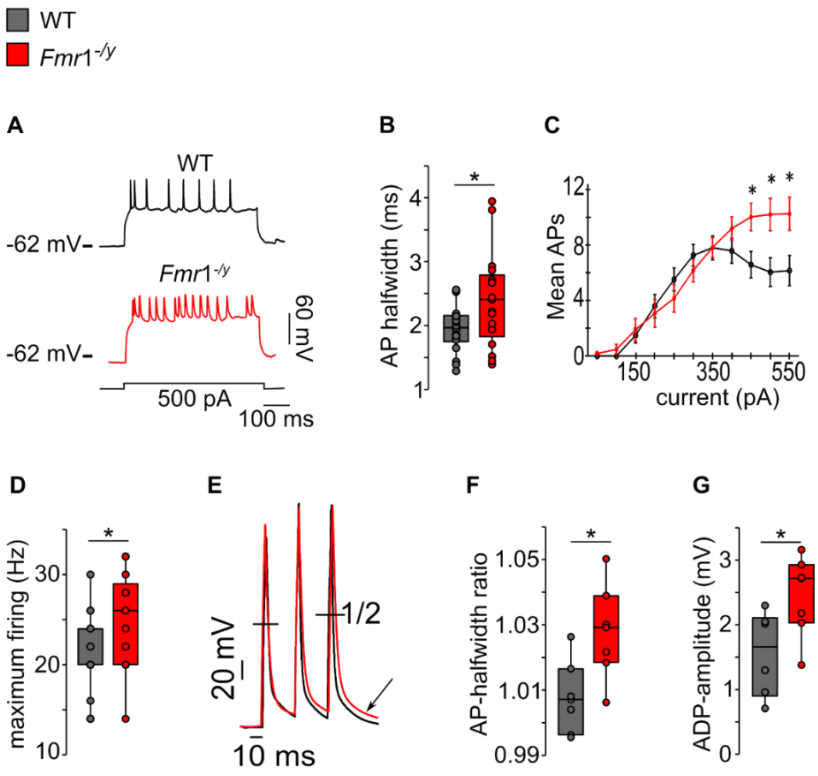

***Figure 17*: Intrinsic properties of R_{sub} cells were modified in *Fmr1*$^{-/y}$ mice.** *(**A**) Example traces of voltage responses to steps of current injection (500 pA) in individual WT-R_{sub} (top) and Fmr1*$^{-/y}$*-R_{sub} (bottom) neuron. **(B)** Fmr1*$^{-/y}$*-R_{sub} cells significantly increased the spike*

*halfwidth (WT-R_{sub}, median = 1.85 ms, n = 24; $Fmr1^{-/y}$-R_{sub}, median = 2.205 ms, n = 20; p < 0.01, unpaired t-test). (**C**) There was no difference in AP firing for current injections up to 350 pA (repeated measurements two-way ANOVA). But there was a significant increase of AP firing in $Fmr1^{-/y}$-R_{sub} cells in at the maximum current steps (450-550 pA). (**D**) Maximum evoked firing rate was significantly increased in $Fmr1^{-/y}$-R_{sub} cells (WT-R_{sub}, median = 20, n = 27; $Fmr1^{-/y}$-R_{sub}, median = 24, n = 19; p < 0.01, unpaired t-test). **(E)** Grand average of injection of 3 consecutive current pulses of 1 nA (pulse width of 1 ms, intra-pulse interval of 23 ms and 1 s duration). ADP-amplitude is represented with an arrow **(F)** Averaged AP-halfwidth ratio (third/ first AP) in the 40 Hz frequency range was significantly higher in $Fmr1^{-/y}$-R_{sub} cells (WT-R_{sub}, median = 1.007, n = 7; $Fmr1^{-/y}$-R_{sub}, median = 1.029, n = 7; p < 0.05, unpaired t-test). **(G)** Average ADP-amplitude at 40 Hz was significantly greater in $Fmr1^{-/y}$-R_{sub} cells (WT-R_{sub}, median = 1.66 mV, n = 6; $Fmr1^{-/y}$-R_{sub}, median = 2.72 mV, n = 7; p < 0.05, unpaired t-test). Boxplots show the median, interquartile, range and individual values. *p < 0.05 ($Fmr1^{-/y}$ compared to wild type). Statistical significance was calculated by unpaired student t-test (for normal distribution) and Mann-Whitney U-test (Not normal distribution).*

When we compared the AP amplitudes of WT and *Fmr*$1^{-/y}$ neurons, there was a significant decrease of amplitude of *Fmr*$1^{-/y}$ R_{sub}- cells (data did not show; Unpaired t-test; $p < 0.05$). When the AP halfwidth values obtained from *Fmr*$1^{-/y}$ R_{sub}- and NR- cells were compared with the WT- R_{sub}- and NR- cells we found a significant increase in AP halfwidth of *Fmr*$1^{-/y}$ R_{sub}- cells (WT- R_{sub}- vs *Fmr*$1^{-/y}$ R_{sub}-, $p < 0.05$) (**Fig 17, B**)and a trend of increase in *Fmr*$1^{-/y}$ NR- cells (Unpaired t-test; $p = 0.09$; data did not show). The AP-threshold was not different in any comparison ($p > 0.05$).

To probe a change in the afterdepolarization (ADP) in *Fmr*$1^{-/y}$ mice we evoked a train of three APs by injection of three 1 nA current pulses (pulse width of 1 ms, intra-pulse interval of 23 ms and 1 s duration). We observed an increase in ADP amplitude in *Fmr*$1^{-/y}$ R_{sub}- neurons (WT-

R_{sub}-, 1.148 ± 1.23 mV; *Fmr*1$^{-/y}$ R_{sub}-, 2.44 ± 0.61 ms; Unpaired t-test; $p < 0.05$) (**Fig 17, E, G**). The first AP halfwidth (WT- R_{sub}-, 1.055 ± 0.058 ms; *Fmr*1$^{-/y}$ R_{sub}-, 1.091 ± 0.103 ms; Mann-Whitney U-test; $p > 0.05$) and third AP halfwidth (WT- R_{sub}-, 1.064 ± 0.06 ms; *Fmr*1$^{-/y}$ R_{sub}-, 1.121 ± 0.10 ms; Mann-Whitney U-test; $p > 0.05$) were not different within and between the genotype. Interestingly AP halfwidth ratio (3rd AP halfwidth/ 1st AP halfwidth) was significantly increased in *Fmr*1$^{-/y}$ R_{sub}- neurons (WT- R_{sub}-, 1.007 ± 0.01 ms; *Fmr*1$^{-/y}$ R_{sub}-, 1.027 ± 0.014 ms; Unpaired t-test; $p < 0.05$) (**Fig 17, F**).

Above results suggest alterations of spontaneous and intrinsic properties of NR- and R_{sub}- cells within and between the genotypes. These data confirm the network dysfunction and intrinsic hyperexcitability in *Fmr*1$^{-/y}$ mice.

10.4 MORPHOLOGY OF NR- AND R_{sub}- CELLS

Next, we examined if there is any correlation between the functional and structural properties of these neurons. Neuronal excitability is crucial for the proper development of dendrites and an hyperexcitability could lead to abnormal dendritic development (Frangeul et al., 2017; Galves et al., 2003, 2005; Irwin et al., 2002, Amatrudo et al., 2012).

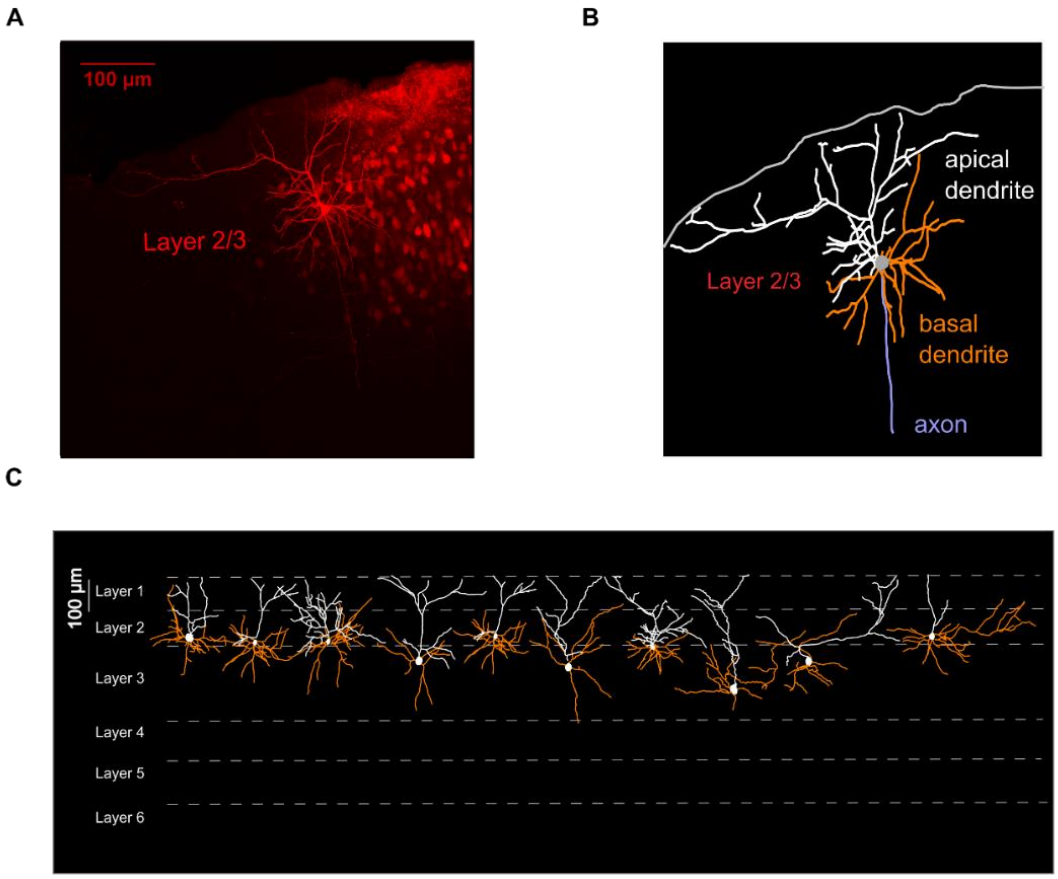

***Figure 18**: **Morphology of neuron subtypes in WT and Fmr1$^{-/y}$ mice**. **A)** Example of a biocytin filled neuron stained with streptavidin-Alexa 555. **B)** Manual reconstruction of the same neuron using Neurolucida. Apical dendrites are shown in black and basal dendrites in orange. **C)** A gallery of reconstructed L2/3 pyramidal neurons showing location and depth of recordings, structural diversity.*

NR- and R_{sub}- cells from WT mice differed in their spontaneous and intrinsic properties and we probed differences in their neuronal morphology. In *Fmr*1$^{-/y}$ mice alterations of morphology of dendrites and axons are well established (Irwin et al., 2002; Neuhofer et al., 2015; Till et al., 2012). The hyperexcitability of NR- and R_{sub}- cells of *Fmr*1$^{-/y}$ mice from our study is also pointing towards a potential alteration of neuronal morphology of *Fmr*1$^{-/y}$ mice. To investigate any changes in morphology of these neurons, biocytin labelled NR- and R_{sub}- neurons (refer methods and **Fig 18, A, B, C**), were reconstructed using Neurolucida (MBF) and then analyzed

in Neuroexplorer software (MBF). The parameters describing Apical and basal dendrites were quantified (Marx et al., 2012).

10.4.1 APICAL DENDRITIC MORPHOLOGY OF NR- AND R_{sub} CELLS IN WT MICE.

Mean length of apical dendrite segments was significantly higher in WT- R_{sub}- cells (WT-NR-, 32.95 ± 3.99 µm; WT- R_{sub}-, 46.43 ± 9.38 µm; Unpaired t-test; $p < 0.05$) (**Fig 19, A**).

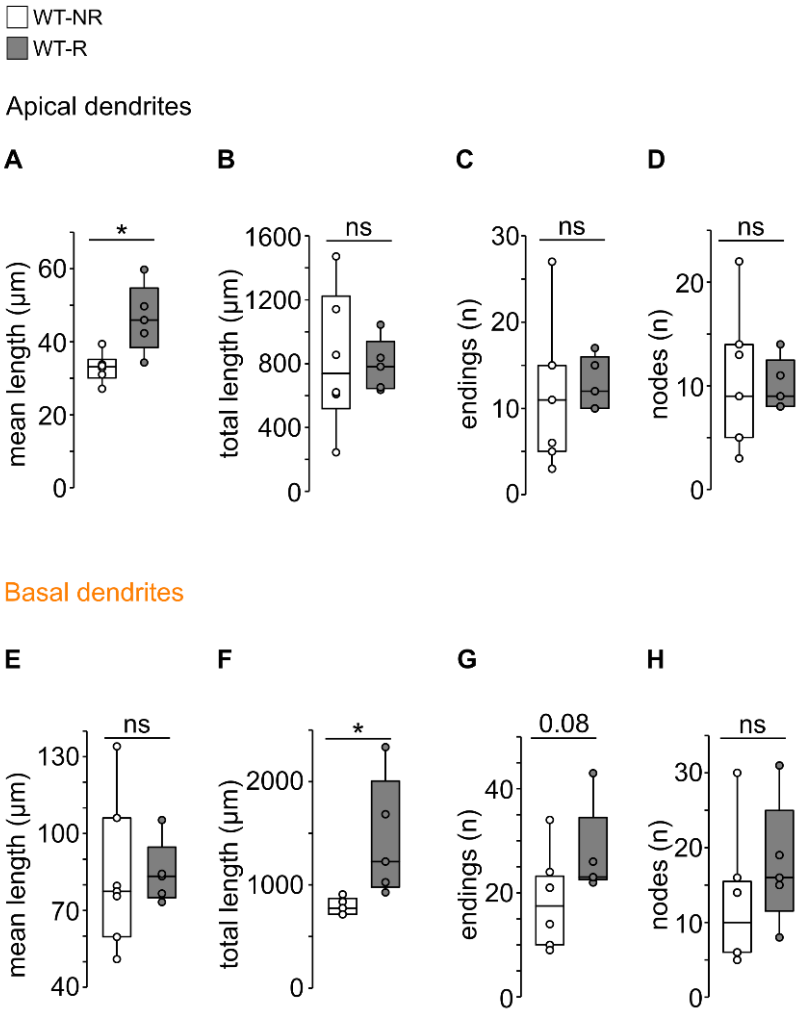

***Figure 19**: **Dendritic morphology of NR- and R_{sub}- cells of WT mice. Apical dendritic features- (A- D). A)** Mean apical dendritic segment length in WT mice was significantly higher in R_{sub} cells (WT-NR, median = 33.16 µm, n = 6; WT-R_{sub}, median = 45.94 µm, n = 5; $p < 0.05$, unpaired t-test). **B)** Total apical dendritic length was not different between NR and R_{sub}*

*cells in WT mice (WT-NR, median = 737.85 µm, n =7; WT-R_{sub}, median = 781 µm, n = 5; p > 0.05, Mann-Whitney U-test).**C**) Number of endings (WT-NR, median = 11, n = 7; WT-R_{sub}, median = 12, n = 5; p > 0.05, unpaired t-test) and **D**) Number of nodes of WT-NR- and WT-R_{sub}- were unchanged (WT-NR, median = 9, n = 7; WT-R_{sub}, median = 9, n = 5; p > 0.05, unpaired t-test).* ***Basal dendritic features (E-H)****. **E**) Mean basal dendritic segment length in WT mice showed no difference between NR and R_{sub}cells (WT-NR, median = 77.43 µm, n = 7; WT-R_{sub}, median = 83.32 µm, n = 5; p > 0.05, unpaired t-test). **F**) Total apical dendritic length was significantly higher in R_{sub} cells in WT mice (WT-NR, median = 774.3 µm, n = 5; WT-R_{sub}, median = 1225.4 µm, n = 5; p < 0.05, unpaired t-test).**G**) Number of endings were higher in WT-R_{sub} cells (WT-NR, median = 17.5, n = 8; WT-R_{sub}, median = 23, n = 5; p = 0.08, unpaired t-test) and **H**) Number of nodes of WT-NR- and WT- R_{sub}- were unchanged (WT-NR, median = 10, n = 8; WT-R_{sub}, median = 16, n = 5; p > 0.05, Mann-Whitney U-test).Boxplots show the median, interquartile, range and individual values. *p < 0.05, ^{ns}p > 0.05 ($Fmr1^{-/y}$ compared to wild type). Statistical significance was calculated by unpaired student t-test (for normal distribution) and Mann-Whitney U-test (Not normal distribution).*

We did not observe any differences in total apical dendritic length (WT-NR, 1148.03 ± 945.208 µm; WT- R_{sub}-, 790.04 ± 165.6 µm; Mann-Whitney U-test; p > 0.05), number of endings (WT-NR, 11.71 ± 8.26; WT- R_{sub}-, 12.8 ± 3.11; Unpaired t-test; p > 0.05) and nodes (WT-NR, 10.14 ± 6.69; WT- R_{sub}-, 10 ± 2.55; Unpaired t-test; p > 0.05)between the WT sub-types (**Fig 19, B, C, D**).

Morphology of NR- and R_{sub}- in WT mice showed a difference in their apical dendritic properties. WT- NR- cells showed a higher mean apical dendritic length. We then examined the basal dendritic morphology of WT mice.

10.4.2 BASAL DENDRITIC MORPHOLOGY OF NR- AND R_{sub} CELLS IN WT MICE.

Total basal dendritic length was significantly higher in WT-R_{sub}-cells (WT-NR-, 789.34 ± 82.38 µm; WT- R_{sub}-, 1439.02 ± 578.3 µm; Unpaired t-test; $p < 0.05$) (**Fig 19, F**). Mean basal dendritic length were comparable in WT mice (WT-NR, 83.34 ± 28.29 µm; WT- R_{sub}-, 84.54± 12.46 µm, $p < 0.05$) (**Fig 19, E**). We noticed a trend of increase in number of endings of basal dendrites of WT-R_{sub} cells (WT-NR-, 17.88 ± 8.74; WT- R_{sub}-, 27.4 ± 8.85; Unpaired t-test; $p = 0.08$) (**Fig 19, G**). No change in number of nodes of basal dendrites of (WT mice WT-NR-, 12.13 ± 8.49; WT- R_{sub}-, 17.8 ± 8.41; Unpaired t-test; $p > 0.05$) (**Fig 19, H**).

In summary, we demonstrated a promising trend of morphological differences of apical and basal dendrites between NR- and R_{sub}- cells in WT mice. Next, we probed the morphology of NR and R cells in *Fmr*1$^{-/y}$ mice.

10.4.3 APICAL DENDRITIC MORPHOLOGY OF NR- AND R_{sub} CELLS IN *FMR*1$^{-/Y}$ MICE.

We observed a general decrease of mean apical dendritic length (*Fmr*1$^{-/y}$ NR-, 35.65 ± 14.07 µm; *Fmr*1$^{-/y}$ R_{sub}-, 21.3 ± 3.59 µm; Unpaired t-test; $p < 0.05$) (**Fig 20, A**). We did not see any difference in total apical dendritic length in *Fmr*1$^{-/y}$ R_{sub}- cells (*Fmr*1$^{-/y}$ NR-, 825.97 ± 569.9 µm; *Fmr*1$^{-/y}$ R_{sub}-, 445.7 ± 223.34 µm; Unpaired t-test; $p < 0.05$) (**Fig 20, B**). Furthermore, *Fmr*1$^{-/y}$ NR-cells demonstrated a trend of increase of apical dendritic endings (*Fmr*1$^{-/y}$ NR-, 11.71 ± 8.26; *Fmr*1$^{-/y}$ R_{sub}-, 13.5 ± 10.88; Mann-Whitney U-test; $p = 0.09$) (**Fig 20, C**) and no difference in number of nodes (*Fmr*1$^{-/y}$ NR-, 10.14 ± 6.69; *Fmr*1$^{-/y}$ R_{sub}-, 7.13 ± 3.72; Unpaired t-test; $p > 0.05$) (**Fig 20, D**).

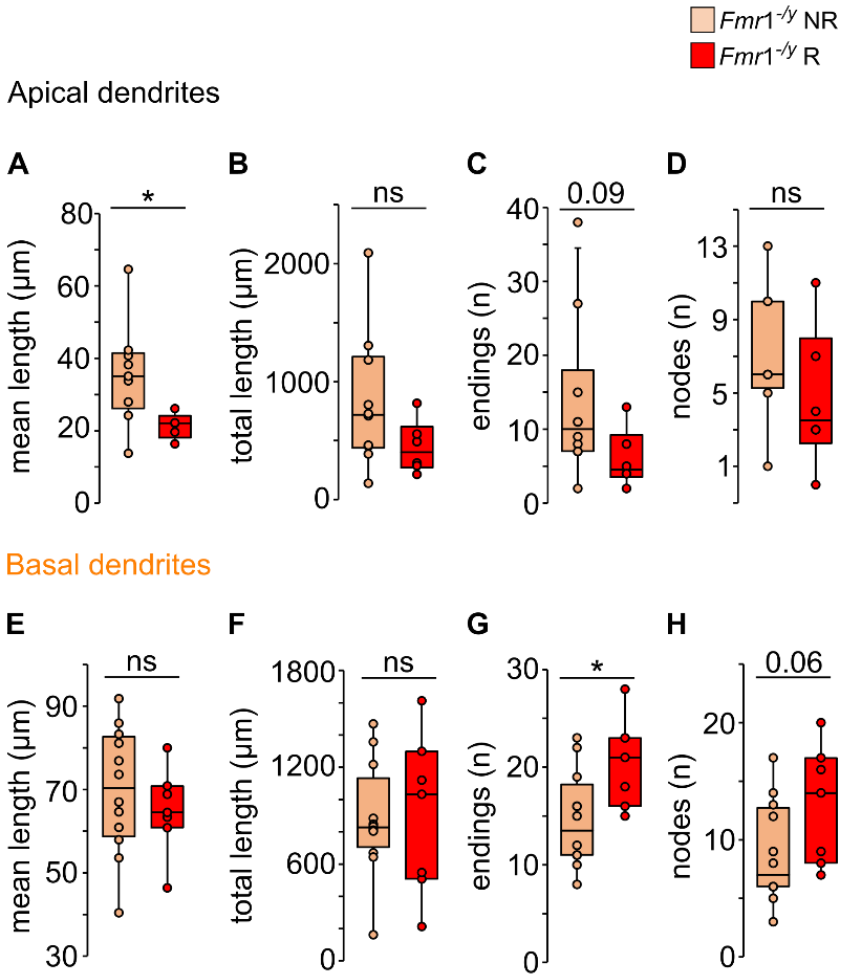

***Figure 20**: **Dendritic morphology of NR- and R_{sub}- cells of $Fmr1^{-/y}$ mice. Apical dendritic features- (A- D). A)** Mean apical dendritic segment length in $Fmr1^{-/y}$ mice was significantly higher in NR cells ($Fmr1^{-/y}$ -NR, median = 35.1 µm, n = 9; $Fmr1^{-/y}$-R_{sub}, median = 22.1 µm, n= 5; $p < 0.05$, unpaired t-test). **B)** Total apical dendritic length was not different between NR and R_{sub} cells in $Fmr1^{-/y}$ mice ($Fmr1^{-/y}$ -NR, median = 719 µm, n = 9; $Fmr1^{-/y}$-R_{sub}, median = 400.3 µm, n = 5; $p > 0.05$, unpaired t-test).**C)** Number of endings showed a trend of increase in $Fmr1^{-/y}$-R_{sub} cells ($Fmr1^{-/y}$ -NR, median = 10, n = 10; $Fmr1^{-/y}$-R_{sub}, median = 4.5, n = 6; $p = 0.09$, Mann-Whitney U-test) and **D)** Number of nodes of $Fmr1^{-/y}$ -NR- and $Fmr1^{-/y}$- R_{sub}- were unchanged ($Fmr1^{-/y}$ -NR, median = 6, n = 8; $Fmr1^{-/y}$-R_{sub}, median = 3.5, n = 6; $p > 0.05$, unpaired t-test). **Basal dendritic features (E-H). E)** Mean basal dendritic segment length*

*(Fmr1$^{-/y}$ -NR, median = 70.32 µm, n = 12; Fmr1$^{-/y}$-R$_{sub}$, median = 64.5 µm, n = 75; p > 0.05, unpaired t-test)and **F**) Total basal dendritic length was not different between NR and R$_{sub}$ cells in Fmr1$^{-/y}$ mice (Fmr1$^{-/y}$ -NR, median = 826.65 µm, n = 12; Fmr1$^{-/y}$-R$_{sub}$, median = 1032.7 µm, n = 7; p > 0.05, unpaired t-test).**G**) Number of endings showed a significant increase in Fmr1$^{-/y}$-R$_{sub}$ cells (Fmr1$^{-/y}$ -NR, median = 13.5, n = 12; Fmr1$^{-/y}$-R$_{sub}$, median = 21, n = 7; p < 0.05, unpaired t-test) and **H**) Number of nodes of Fmr1$^{-/y}$- R$_{sub}$- showed a trend of increase but not significantly different from Fmr1$^{-/y}$- NR cells (Fmr1$^{-/y}$ -NR, median = 7, n = 12; Fmr1$^{-/y}$-R$_{sub}$, median = 14, n = 7; p = 0.06, unpaired t-test). Boxplots show the median, interquartile, range and individual values. *p < 0.05, ^{ns}p > 0.05 (Fmr1$^{-/y}$ compared to wild type). Statistical significance was calculated by unpaired student t-test (for normal distribution) and Mann-Whitney U-test (Not normal distribution).*

In summary, apical dendritic morphology of R$_{sub}$- cells in *Fmr*1$^{-/y}$ mice demonstrated a decrease in mean apical lengthand a trend of decrease in number of endings.

We further investigated the changes of basal dendrites of NR- and R$_{sub}$- cells within *Fmr*1$^{-/y}$ mice.

10.4.4 BASAL DENDRITIC MORPHOLOGY OF NR- AND R$_{sub}$- CELLS IN *FMR*1$^{-/Y}$ MICE.

In contrast with WT data, we did not find any differences in mean basal dendritic length (*Fmr*1$^{-/y}$ NR, 69.77 ± 15.06 µm; *Fmr*1$^{-/y}$ R$_{sub}$-, 64.97 ± 10.32 µm; Unpaired t-test; p > 0.05) and total basal dendritic length (*Fmr*1$^{-/y}$ NR, 876.39 ± 346.6 µm; *Fmr*1$^{-/y}$ R$_{sub}$-, 904.55 ± 497.39 µm; Unpaired t-test; p > 0.05) (**Fig 20, E, F**) in *Fmr*1$^{-/y}$ mice. Number of endings was significantly higher in *Fmr*1$^{-/y}$ R$_{sub}$- cells (*Fmr*1$^{-/y}$ NR, 14.5 ± 4.85; *Fmr*1$^{-/y}$ R$_{sub}$-, 20.57 ± 4.58; Unpaired t-test; p < 0.05) (**Fig 20, G**). We also noticed a trend of increase of number of nodes in basal dendrites of *Fmr*1$^{-/y}$ R$_{sub}$- cells (*Fmr*1$^{-/y}$ NR, 8.75 ± 4.29; *Fmr*1$^{-/y}$ R$_{sub}$-, 13 ± 5.03; Unpaired t-test; p = 0.06) (**Fig 20, H**).

We noticed differences of basal dendritic morphology in *Fmr*1$^{-/y}$ mice which were not like the morphological distinctions that we saw in WT mice. These results together confirm that the NR- and R_{sub}- cells are morphologically separated in WT mice in various apical and dendritic properties. These morphological features are disappeared in *Fmr*1$^{-/y}$ mice. Notably, new morphological changes that were not present in WT mice appeared in *Fmr*1$^{-/y}$ mice.

10.4.5 ALTERATIONS IN STRUCTURAL MORPHOLOGY OF R_{sub} CELLS IN *FMR*1$^{-/Y}$ COMPARED TO WT MICE

We first examined the mean and total length of Apical dendrites between WT and *Fmr*1$^{-/y}$ mice. Apical dendrites of *Fmr*1$^{-/y}$ R_{sub}- cells showed a significant decrease in mean (Unpaired t-test; $p < 001$) and total length (Unpaired t-test; $p < 0.05$) (**Fig 21, E, F**).

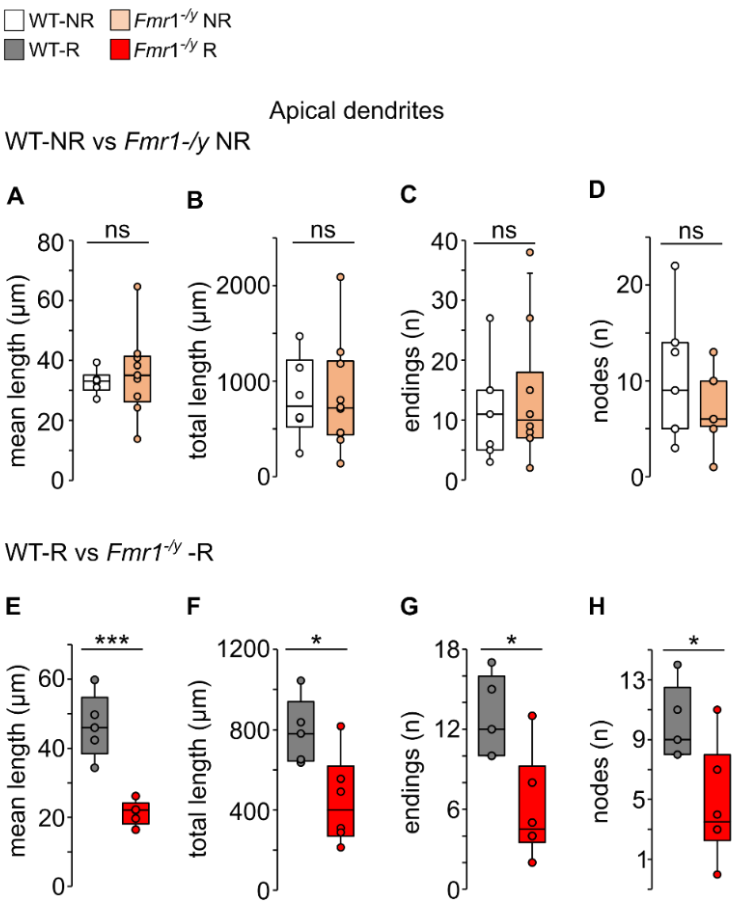

Figure 21: ***Decreased mean, total apical dendritic length, number of endings and nodes in Fmr1$^{-/y}$-R$_{sub}$ cells. Comparison of Apical dendritic features between WT-NR and Fmr1$^{-/y}$-NR cells (A-D).*** ***A)*** *Mean apical dendritic segment length (WT-NR, median = 33.16 µm, n = 6; Fmr1$^{-/y}$-NR, median = 35.1 µm, n = 9; p > 0.05, unpaired t-test),* ***B)*** *Total apical dendritic length (WT-NR, median = 737.85 µm, n = 6; Fmr1$^{-/y}$-NR, median = 719 µm, n = 10; p > 0.05, Mann-Whitney U-test),* ***C)*** *Number of endings (WT-NR, median = 11, n = 7; Fmr1$^{-/y}$-NR, median = 10, n = 10; p > 0.05, Mann-Whitney U-test) and* ***D)*** *Number of nodes of Fmr1$^{-/y}$ -NR- and Fmr1$^{-/y}$- R$_{sub}$- cells (Fmr1$^{-/y}$ -NR, median = 6, n = 8; Fmr1$^{-/y}$-R$_{sub}$, median = 3.5, n = 6; p > 0.05, unpaired t-test) were unchanged.* ***Comparison of Apical dendritic features between WT-R$_{sub}$ and Fmr1$^{-/y}$-R$_{sub}$ cells (E-H).*** *Fmr1$^{-/y}$-R$_{sub}$ cells showed a significant decrease in* ***E)*** *Mean apical dendritic segment length (WT-R$_{sub}$, median = 45.94 µm, n = 5; Fmr1$^{-/y}$-R$_{sub}$, median = 22.1 µm, n = 5; p < 0.001, unpaired t-test),* ***F)*** *Total apical dendritic length (WT-R$_{sub}$, median = 781 µm, n = 5; Fmr1$^{-/y}$-R$_{sub}$, median = 400.3 µm, n = 6; p < 0.05, unpaired t-test),* ***G)*** *Number of endings (WT-R$_{sub}$, median = 12, n = 5; Fmr1$^{-/y}$-R$_{sub}$, median = 4.5, n = 6; p < 0.05, unpaired t-test) and* ***H)*** *Number of nodes (WT-R$_{sub}$, median = 9, n = 5; Fmr1$^{-/y}$-R$_{sub}$, median = 3.5, n = 9; p < 0.05, unpaired t-test). Boxplots show the median, interquartile, range and individual values. *p < 0.05, **p < 0.01, ***p < 0.001, ^{ns}p > 0.05 (Fmr1$^{-/y}$ compared to wild type). Statistical significance was calculated by unpaired student t-test (for normal distribution) and Mann-Whitney U-test (Not normal distribution).*

Furthermore, comparison between WT and *Fmr*1$^{-/y}$ mice demonstrated a significant decrease of apical dendritic endings (Unpaired t-test; $p < 0.05$) and nodes of of R-cells in *Fmr*1$^{-/y}$ (Unpaired t-test; $p < 0.05$) (**Fig 21, G, H**).

Next, we compared the basal dendrites of WT and *Fmr*1$^{-/y}$ mice to see if any morphological alteration occurred in the mutant NR- and R$_{sub}$- cells.

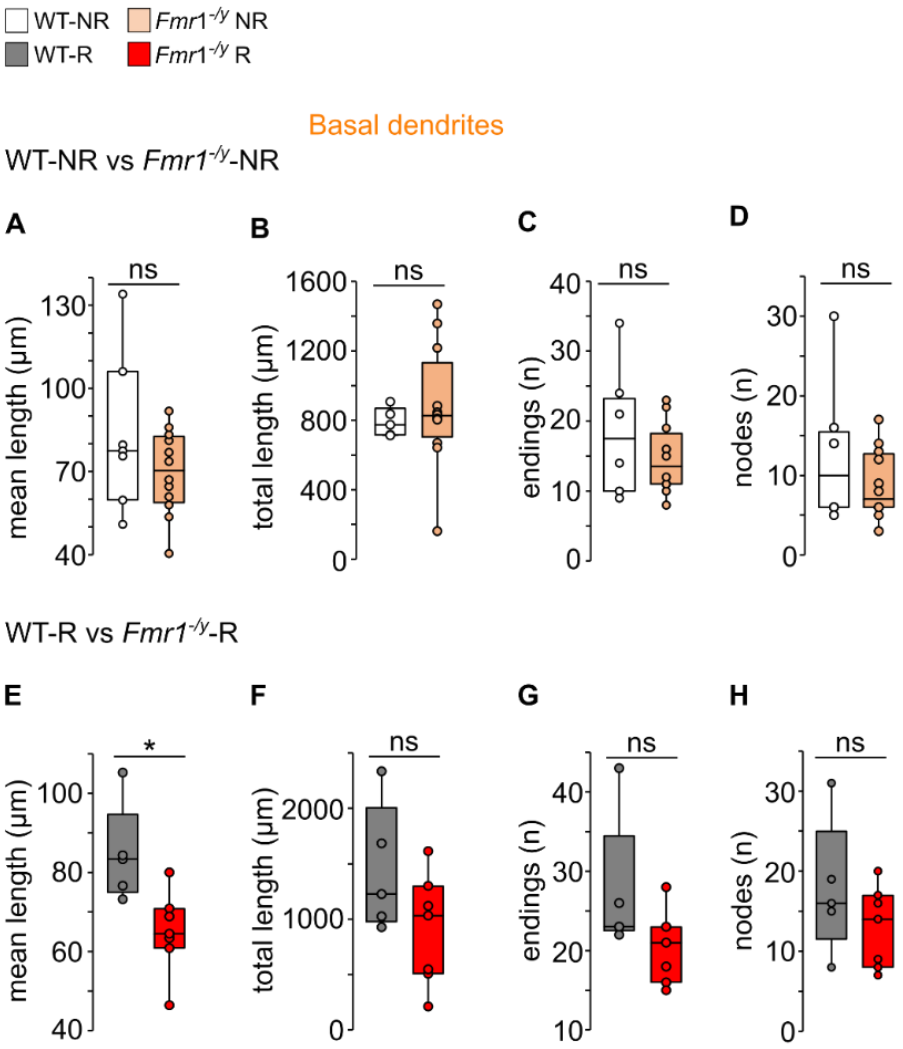

Figure 22: Mean basal dendritic length is decreased in Fmr1$^{-/y}$ R$_{sub}$ cells. Comparison of basal dendritic features between WT-NR and Fmr1$^{-/y}$-NR cells (A-D). ***A)*** *Mean basal dendritic segment length (WT-NR, median = 77.43 µm, n = 7; Fmr1$^{-/y}$-NR, median = 70.32 µm, n = 12; p > 0.05, unpaired t-test),* ***B)*** *Total basal dendritic length (WT-NR, median = 774.3 µm, n =5; Fmr1$^{-/y}$-NR, median = 826.65 µm, n = 12; p > 0.05, unpaired t-test),* ***C)*** *Number of endings (WT-NR, median = 17.5, n = 8; Fmr1$^{-/y}$-NR, median = 13.5, n = 12; p > 0.05, unpaired t-test) and* ***D)*** *Number of nodes (Fmr1$^{-/y}$ -NR, median = 10, n = 8; Fmr1$^{-/y}$-R$_{sub}$, median = 7, n = 12; p > 0.05, Mann-Whitney U-test) of Fmr1$^{-/y}$ -NR- and Fmr1$^{-/y}$- R$_{sub}$- cells were unchanged.* ***Comparison of basal dendritic features between WT-R$_{sub}$ and Fmr1$^{-/y}$-R***

cells (E-H). ***E)*** *$Fmr1^{-/y}$-R_{sub} cells showed a significant decrease in Mean apical dendritic segment length (WT-R_{sub}, median = 83.32 µm, n = 5; $Fmr1^{-/y}$-R_{sub}, median = 64.5 µm, n = 7; p < 0.05, unpaired t-test).* ***F)*** *Total apical dendritic length (WT-R_{sub}, median = 1225.4 µm, n = 5; $Fmr1^{-/y}$-R_{sub}, median = 1032.7 µm, n = 7; p > 0.05, unpaired t-test),* ***G)*** *Number of endings (WT-R_{sub}, median = 23, n = 5; $Fmr1^{-/y}$-R_{sub}, median = 21, n = 7; p > 0.05, unpaired t-test) and* ***H)*** *Number of nodes (WT-R_{sub}, median = 16, n = 5; $Fmr1^{-/y}$-R_{sub}, median = 14, n = 7; p > 0.05, unpaired t-test) were unchanged. Boxplots show the median, interquartile, range and individual values. *p < 0.05, ^{ns}p > 0.05 ($Fmr1^{-/y}$ compared to wild type). Statistical significance was calculated by unpaired student t-test (for normal distribution) and Mann-Whitney U-test (Not normal distribution).*

Mean basal dendritic length of both R_{sub}- cells showed a trend of decrease in *Fmr*$1^{-/y}$ mice (Unpaired t-test; p > 0.05) (**Fig 22, E**). We did not see any differences in other parameters in any cell sub-types between genotypes.

Overall, comparison of morphology of NR- and R_{sub}- cells of WT and *Fmr*$1^{-/y}$ mice showed a significant alteration of apical and dendritic morphology. This trend of increase could explain the changes in network, intrinsic properties that we observed in *Fmr*$1^{-/y}$ mice. Considering the low number of neurons in each group, in future we require a greater number of neuronal reconstructions to support the trend.

In conclusion, NR-cells were distinguishable from R_{sub}-cells in a number of properties, including spontaneous firing activity, intrinsic excitability, and dendritic arborization, supporting the idea they belong to a different population within the L2/3 network of S1-HP. In addition, we found that some of these measures were altered in *Fmr*$1^{-/y}$ mice. In the current study, we did not attempt to characterize the functional role of NR-cells under normal

physiological, or pathological, conditions. We presume that these neurons process information related to other sensory modalities, such as thermoregulation or pain (Milenkovic et al., 2014) or other higher order functions (Casas-Torremocha et al., 2017).

The next chapters focus on sensory information processing in R_{sub}-cells, and their alterations in *Fmr*1$^{-/y}$ mice. We have shown that R_{sub}-cells in *Fmr*1$^{-/y}$ mice display an increased spontaneous firing rate and intrinsic excitability (and also some differences in the morphology of apical dendrites) when compared to those of WT mice. It is well known that the ongoing spontaneous activity (Petersen et al., 2003) and intrinsic properties of neurons have an important role in determining the characteristics of sensory responses to various stimuli. For example, an identical sensory stimulus can evoke different neuronal responses dependent on the pre-stimulus intrinsic activity levels (Bolt et al., 2017). Next, we explored sensory stimulus evoked responses in light of our findings of altered excitability and spontaneous activity.

10.5 HINDPAW STIMULATIONS EVOKED RESPONSES IN S1-HP L2/3 PYRAMIDAL NEURONS

As stated at the beginning of the Results section, stimulation of the HP elicited either no response in L2/3 PN of the contralateral S1-HP region, a sub-threshold response (EPSP only), or supra-threshold responses (action potentials) (**Fig 11, C**).

Hyperexcitability to sensory stimulus is a key component in FXS. Previous studies showed that both FXS individuals and *Fmr*1$^{-/y}$ mice are hypersensitive to auditory and tactile stimuli (Zhang et al., 2014, Knoth et al., 2014; Rotschafer and Razak, 2014; Scott et al., 2018). We measured HP stimulated evoked sensory responses in contralateral S1-HP L2/3 pyramidal neurons in WT and in *Fmr*1$^{-/y}$ mice and then analyzed the suprathreshold (AP) responses and sub-threshold responses (postsynaptic potential, PSP) responses evoked by the hind paw stimulations. Second, in some mice we also stimulated the contralateral forepaw to probe changes in the

receptive field properties in *Fmr*1$^{-/y}$ mice. Third, we directly stimulated VPM and recorded from S1-HP L2/3 neurons to probe any circuit deficit in these mice. Finally, we demonstrated pharmacological correction of some of these identified alterations in *Fmr*1$^{-/y}$ mice.

10.5.1 HIND PAW STIMULATION EVOKED RESPONSES IN R_{SUPRA} CELLS WERE ALTERED IN *FMR*1$^{-/Y}$ MICE

As stated before, there was no difference in the average depth of recording of L2/3 PN between WT (R_{sub}-, 227.7 ± 64.9 µm; NR-, 228 ± 73 µm) and *Fmr*1$^{-/y}$ mice (R_{sub}-, 245 ± 71 µm; NR-, 252. 73 ± 68.14 µm). Interestingly, however, there was a significant shift in the presence of supra-threshold R-cells from L2 towards L3 in *Fmr*1$^{-/y}$ mice (WT-R_{supra}, 175.84 ± 51.7 µm; *Fmr*1$^{-/y}$ $R_{supra,}$ 250 ± 53.26 µm; $p < 0.01$). Most of the sub-threshold responders in WT mice were in L 3 of S1-HP (WT-R-, 227.7 ± 64.9 µm; WT-R_{supra}, 175.84 ± 51.7 µm; Mann-whitney U test; $p < 0.05$) (**Fig 23, A**). We measured the ongoing spontaneous firing before the sensory stimulus, and the combined sensory stimulus evoked and spontaneous activity within a time window of 200 ms duration following the sensory stimulus. *Fmr*1$^{-/y}$ mice showed no difference in average pre-stimulus APs compared to WT- mice (WT-R_{supra} cells, 0.007 ± 0.012 Hz; *Fmr*1$^{-/y}$ R_{supra} cells, 0.095 ± 0.158 Hz; $p > 0.05$) (**Fig 23, B, C**). In contrast, we found that the post-stimulus APs fired per trial were significantly higher in *Fmr*1$^{-/y}$ R_{supra} cells (WT-R_{supra} cells, 0.332 ± 0.77 Hz; *Fmr*1$^{-/y}$ R_{supra} cells, 0.77 ± 0.349 Hz; $p < 0.05$) (**Fig 23, B, C**). We also observed an increased AP firing per trial during the post-stimulation period compared to pre-stimulation period in both WT and *Fmr*1$^{-/y}$ mice (WT- R_{supra} cells = $p < 0.05$; *Fmr*1$^{-/y}$ R_{supra} cells = $p < 0.0001$) (**Fig 23, B, C**).

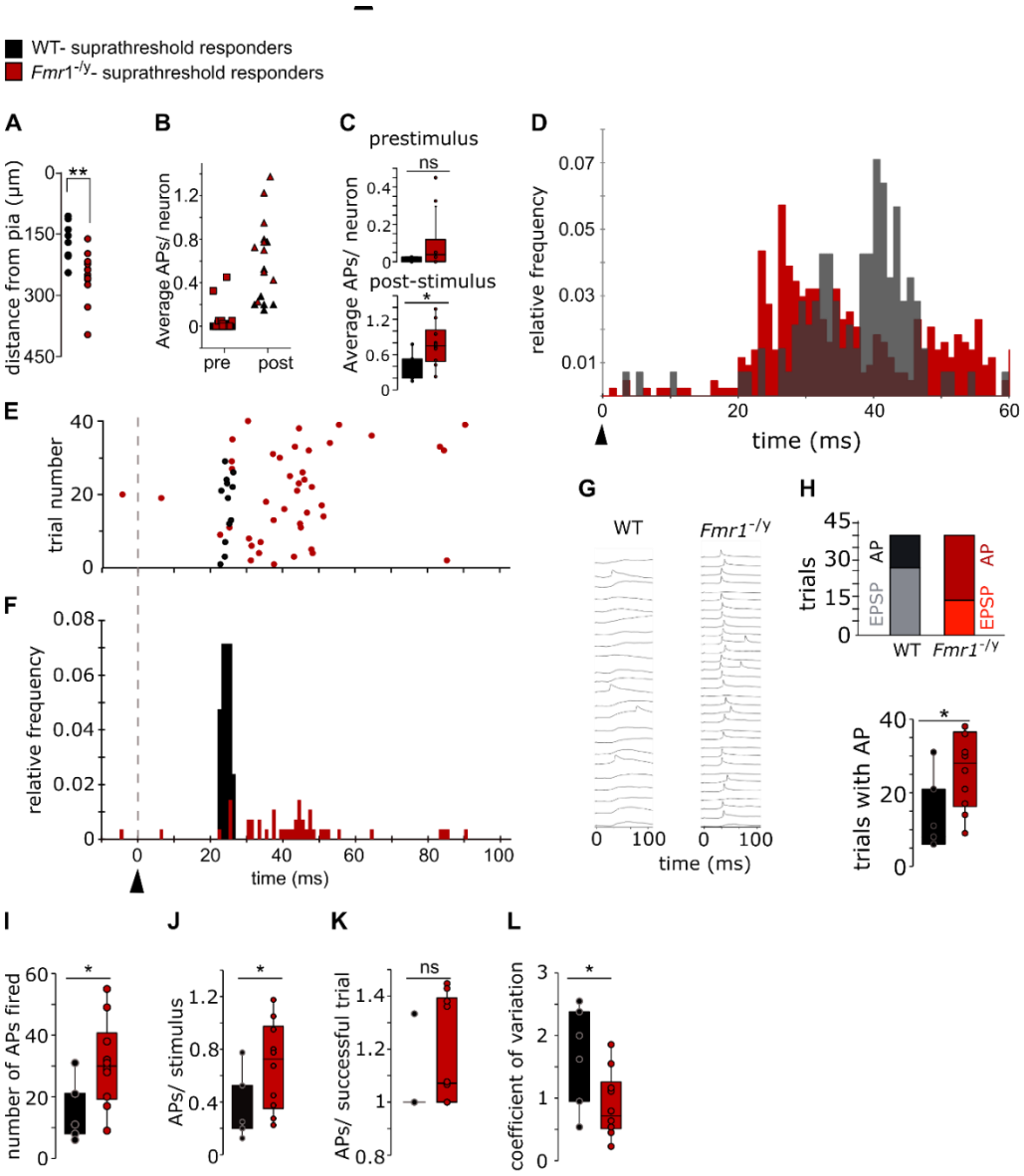

Figure 23: Increased AP firing and altered AP Jitter in suprathreshold responders of Fmr1$^{-/y}$ mice. ***(A)*** *Depth of recording in WT and Fmr1$^{-/y}$ mice. The majority of WT-R$_{supra}$ cells were recorded from L2 of S1-HP (calculate from the angle of pipette and recording depth). In contrast Fmr1$^{-/y}$ cells were localized in L3 of S1-HP (Fisher's exact test, $p < 0.01$).* ***(B and C)*** *Averaged spontaneous APs (Pre-stimulus, 0- 200 ms window before the stimulus) in WT (represented as black square) was not different from Fmr1$^{-/y}$ mice (symbolized as brown square). APs elicited following the stimulus (post-stimulus, 200 ms duration after the stimulus) was significantly increased in Fmr1$^{-/y}$ mice (showed in brown triangles) compared to WT*

(presented as black triangles) (post-stimulus APs; WT, median = 0.2, n = 7; Fmr1$^{-/y}$, median = 0.75, n = 10; p < 0.05, unpaired t-test). ***(D)*** *Overlaid Peristimulus time histogram (PSTH) showing difference in post stimulus AP timing in WT (black) and Fmr1$^{-/y}$ suprathreshold responders. Onset of stimulus (marked with a black arrow) is represented as 0 ms.* ***(E)*** *Number of APs fired by individual WT (black) and Fmr1$^{-/y}$ (brown) neurons after the stimulus was provided (black arrow denotes stimulus onset).* ***(F)*** *PSTH of AP firing show an increased jitter in Fmr1$^{-/y}$ neurons (WT in black, Fmr1$^{-/y}$ in brown). The time window shows 50 ms (post-stimulus) and the black arrow shows the onset of stimulus.* ***(G)*** *Example traces of evoked APs presenting 40 trials in WT (left) and Fmr1$^{-/y}$ cells (right).* ***(H)*** *Fmr1$^{-/y}$ cells show a significantly altered proportion of number of APs and EPSPs eliciting trials (top). We observed a Significantly higher probability of evoking an AP in Fmr1$^{-/y}$ cells (bottom left, Fisher's exact test, p < 0.0001). Each data point is a neuron and are corresponding to number of trials with a sensory stimulus evoked AP.* ***(I)*** *Total number of APs fired per session (40 trials) was significantly elevated in Fmr1$^{-/y}$ cells (WT, median = 8, n = 7; Fmr1$^{-/y}$, median = 30, n = 10; p < 0.05, Mann-Whitney U-test).* ***(J)*** *Number of stimulus evoked APs were increased in Fmr1$^{-/y}$ cells (WT, median = 0.2, n = 7; Fmr1$^{-/y}$, median = 0.725, n = 10; p < 0.05, Mann-Whitney U-test).* ***(K)*** *Number of APs per successful trial (trial eliciting an AP) was not different between the genotypes (WT, median = 1, n = 7; Fmr1$^{-/y}$, median = 1.07, n = 10; p > 0.05, Mann-Whitney U-test).* ***(L)*** *A significant reduction of coefficient of variation (standard deviation/ mean AP) was observed in Fmr1$^{-/y}$ cells (WT, median = 2, n = 7; Fmr1$^{-/y}$, median = 0.716, n = 10; p < 0.05, unpaired t-test). Boxplots show the median, interquartile, range and individual values. *p < 0.05, **p < 0.01, ^{ns}p > 0.05 (Fmr1$^{-/y}$ compared to wild type). Statistical significance was calculated by unpaired student t-test (for normal distribution) and Mann-Whitney U-test (Not normal distribution).*

We then measured the mean number of APs per stimulus (average pre-stimulus APs were subtracted from the average post-stimulus APs). We observed an increased mean evoked activity with APs per stimulus in *Fmr*1$^{-/y}$ R_{supra} cells (WT- R_{supra} cells, 0.325 ± 0.23 Hz; *Fmr*1$^{-/y}$ R_{supra} cells, 0.675 ± 0.33 Hz; $p < 0.05$) (**Fig 23, J**). We then examined the coefficient of variation in WT and *Fmr*1$^{-/y}$ R_{supra} cells. The *Fmr*1$^{-/y}$ R_{supra} cells showed a significantly reduced coefficient of variation (WT- R_{supra} cells,1.72 ± 0.739; *Fmr*1$^{-/y}$ R_{supra} cells, 0.886 ± 0.52; $p < 0.05$) (**Fig 23, L**). Interestingly, none of these 17 R_{supra} cells (both WT and *Fmr*1$^{-/y}$) demonstrated any response failure. WT- R_{supra} and *Fmr*1$^{-/y}$ R_{supra} cells displayed a combination of EPSP and AP responses in each session (40 trials). We further measured the proportion of EPSPs and APs per session in response to the hind paw stimulus. WT- R_{supra} cells responded with APs in 32.5% of the stimulation trials, while *Fmr*1$^{-/y}$ R_{supra} cells exhibited responses with APs in 65% of the trials (WT- R_{supra} number of trials with AP = 91/ 280 trials, *Fmr*1$^{-/y}$ R_{supra} number of trials with AP = 260/400, $p < 0.0001$) (**Fig 23, G, H**). This finding was in agreement with the total number of spikes per each session. The total number of APs elicited in each session (40 trials) was significantly elevated in *Fmr*1$^{-/y}$ R_{supra} cells (WT- R_{supra} cells, 13.29 ± 9.27; *Fmr*1$^{-/y}$ R_{supra} cells, 30.8 ± 14; $p < 0.05$) (**Fig 23, I**).

Next, we investigated whether the properties of sub-threshold responses evoked by the hind paw stimulation differed between neurons from *Fmr*1$^{-/y}$ and WT mice.

10.5.2 HIND PAW STIMULATION EVOKED EXCITATORY POSTSYNAPTIC POTENTIALS (EPSPS) WERE ALTERED IN *FMR*1$^{-/Y}$ MICE

We analyzed the subthreshold responses of R_{sub} cells in WT and *Fmr1*$^{-/y}$ animals. Responses had an onset latency of ~25 ms in WT mice, which tended to be increased, albeit non-significantly, in *Fmr1*$^{-/y}$ neurons (WT- R_{sub}, 25.52 ± 8.78 ms; *Fmr*1$^{-/y}$ R_{sub}, 28.31 ± 12.10 ms; $p > 0.05$). **Figure 24 A** displays raw traces from an individual WT and *Fmr1*$^{-/y}$ subthreshold

responder cell and **Figure 24 B** represent the grand average (including failures) of all EPSPs for both genotypes, illustrating the major alterations for neurons of *Fmr1*$^{-/y}$ mice.

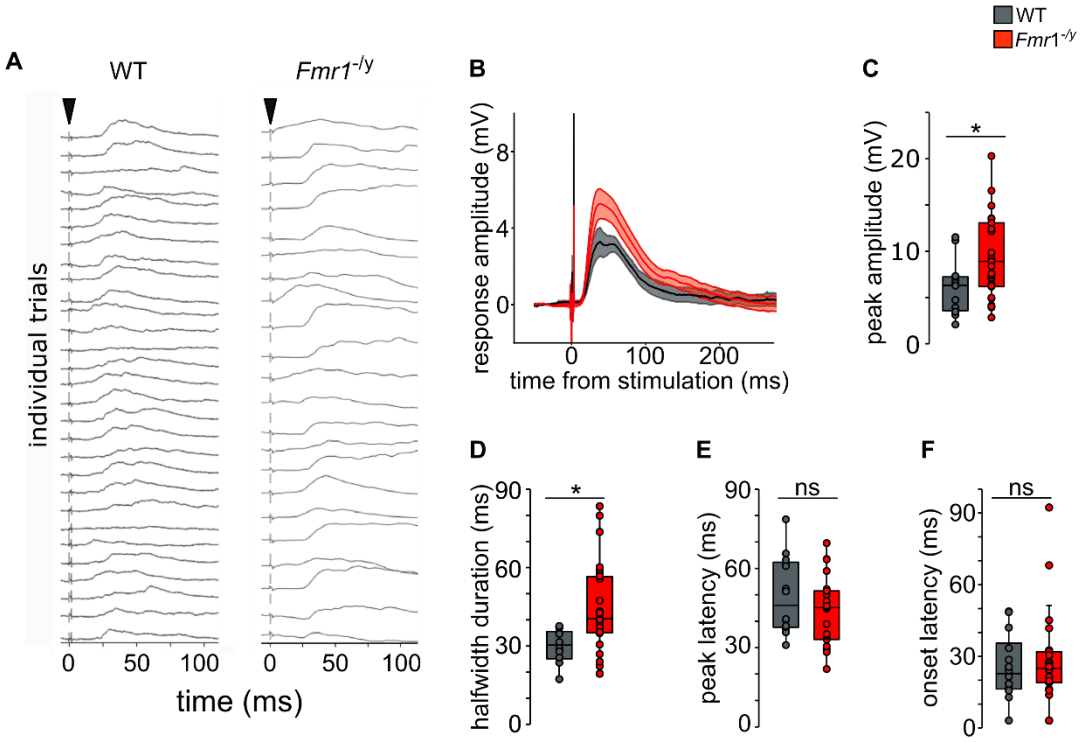

***Figure 24**: **Hind paw stimulation evoked subthreshold responses in WT and Fmr1*$^{-/y}$ *mice in vivo**. **(A)** Example of sensory stimulation evoked responses of a single neuron from WT (left) and Fmr1*$^{-/y}$ *(right)mice. (**B**) Average responses of all trials evoking an EPSP of the WT and Fmr1*$^{-/y}$ *L2/3 PN population. Fmr1*$^{-/y}$ *cells show an increased. (**C**) peak amplitude (WT, median = 6.29 mV, n = 12; Fmr1*$^{-/y}$*, median = 8.89 mV, n = 27; p < 0.05, unpaired t-test). (**D**) halfwidth duration (WT, median = 30.36 ms, n = 10; Fmr1*$^{-/y}$*, median = 40.37 ms, n = 28; p < 0.05, unpaired t-test) and, (**E**) no change in peak latency (WT, median = 46.06 ms, n = 14; Fmr1*$^{-/y}$*, median = 45.1 ms, n= 23; p > 0.05, Mann-Whitney U-test) and, **(F)** onset latency(WT, median = 22.8 ms, n = 14; Fmr1*$^{-/y}$*, median = 25.02 ms, n = 24; p > 0.05, Mann-Whitney U-test) of the response. Boxplots show the median, interquartile, range and individual values. *p < 0.05, *^{ns}*p > 0.05 (Fmr1*$^{-/y}$ *compared to wild type). Statistical significance was calculated by unpaired*

student t-test (for normal distribution) and Mann-Whitney U-test (Not normal distribution). All average values include failure traces.

EPSP amplitude of *Fmr*1$^{-/y}$ R_{sub}-cells was significantly larger compared to WT-R_{sub}-cells (WT-R_{sub}-, 6.3 ± 2.95 mV; *Fmr*1$^{-/y}$ R_{sub}-, 9.05 ± 4.03 mV; Unpaired t-test; $p < 0.05$) (**Fig 24, C**). Responses of *Fmr*1$^{-/y}$ mice also displayed an increased half-amplitude duration (WT-R, 29.25 ± 6.71 ms; *Fmr*1$^{-/y}$ R_{sub}-, 49.34 ± 20.13 ms; Unpaired t-test; $p < 0.05$) (**Fig 24, D**). We did not see any differences in latency between the genotypes (**Fig 24, E, F**).

These changes in sub-threshold responses support the notion that neocortical L2/3 pyramidal neurons of S1-HP are hyperexcitable in response to a hind paw tactile stimulation in *Fmr*1$^{-/y}$ mice. Together with changes in their spontaneous activity, intrinsic excitability and morphology, this points to a substantial hyperexcitability of somatosensory neocortical circuits that may underlie tactile sensory hypersensitivity in *Fmr*1$^{-/y}$ mice.

Cortico-cortical interactions are crucial for the integration of information within and across sensory modalities (Hodkinson et al., 2016). Alterations in synaptic inputs might induce reorganization of cortex (Humanes-Valera et al., 2014). We previously demonstrated a reorganization in the local and brain-wide connectivity impinging on the primary visual cortex, V1 (Haberl et al., 2015). An enlargement of receptive fields of neurons and networks has been demonstrated in ASD individuals (Schauder et al., 2017; Schwarzkopf et al., 2014).

To test whether the connectivity of S1-HP is reorganized leading to alterations in receptive fields, we stimulated the contralateral forepaw (FP) while recording in S1-HP.

10.6 HP-FP CONNECTION WAS REORGANIZED IN *FMR1*$^{-/Y}$ MICE

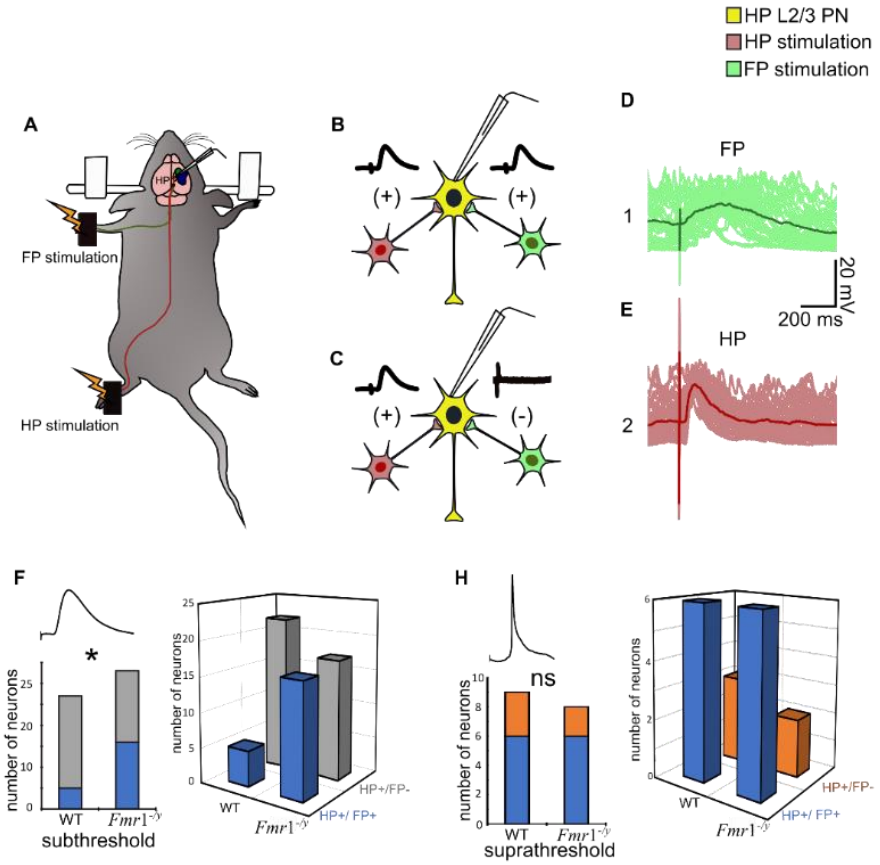

Figure 25: Increased occurrence of HP L2/3 PN responding to both HP and FP stimulations in Fmr1$^{-/y}$ mice. ***A)*** *Schematic representation of sequential stimulation of HP and FP.* ***B)*** *Representation of a cell responding to both HP and FP stimulation (HP^{+}/ FP^{+}).* ***C)*** *Representation of a cell responding to HP but not FP stimulation (HP^{+}/ FP^{-}). Example traces of a single neuron responding to FP (**D**) and to HP (**E**)stimulation.* ***F)*** *Number of R_{sub} cells responding to both HP and FP was increased in Fmr1$^{-/y}$ mice.* ***H)*** *Distribution of R_{supra} cells responding to both HP and FP stimulations was not changed. Fisher's exact test (Graphpad), *p < 0.05.*

We noticed is the long onset latency of the FP stimulation evoked sub-threshold responses in S1-HP L 2/3 pyramidal neurons of WT and *Fmr*1$^{-/y}$ mice (WT, 33.8 ± 8.6 ms; *Fmr*1$^{-/y}$, 36.45 ± 8 ms; Mann-Whitney U test; $p > 0.05$). We performed HP and FP stimulations while measuring the responses in the same HP L2/3 PN (WT = 36 cells, *Fmr*1$^{-/y}$ = 41 cells) (**Fig 25, A**). FP stimulation evoked both supra (WT-R_{supra}= 9, *Fmr*1$^{-/y}$ R_{supra} = 8) and sub-threshold responses (WT- R_{sub}- =27, *Fmr*1$^{-/y}$ R_{sub}- = 33) in the S1-HP L2/3 pyramidal neurons. Accordingly, we classified the cells into cells that responded to both stimuli (HP^+/FP^+) and those that responded only to HP stimulation (HP^+/ FP^-) (**Fig 25, B, C, D, E**). In WT 30.5 % of R-cells (both sub and supra) responded to both HP and FP stimuli, whereas in *Fmr*1$^{-/y}$ mice this ratio was substantially increased (53.65%; Mann-Whitney U test; $p = 0.07$).

66.66 % (n = 6/ 9) of WT-R_{supra} cells responded to both stimuli and 75 % of *Fmr*1$^{-/y}$ R_{supra} cells (n= 6/ 8) were responded to both stimuli. We did not see any difference between the distribution of HP^+/FP^+ and HP^+/FP^- suprathreshold responders among the genotype ($p > 0.05$, Fisher's exact test) (**Fig 25, H**).

Interestingly 48.48 % (n= 16/ 33) of *Fmr*1$^{-/y}$$R_{sub}$-cells responded to both HP and FP stimulations. We discovered that only 18.5 % of WT- R_{sub}-cells (n = 5/ 27) responded to HP and FP stimulations. There was a significant increase of number of *Fmr*1$^{-/y}$ R cells responded to HP and FP stimuli (Fisher's exact test, $p < 0.05$) (**Fig 25, F**).

10.7 VENTRAL POSTEROMEDIAL NUCLEUS (VPM) OF THALAMUS STIMULATIONS

Peripheral tactile receptors are connected to the cortex via lemniscal and paralemniscal pathways. These pathways relay information via the thalamus (Mo et al., 2017, Bureau et al., 2006). Thalamocortical interactions are very important in regulating sensory perception and motor control (Manita et al., 2015; Petersen and Crochet, 2013; Sreenivasan et al., 2017).

Thalamocortical networks undergo functional and structural changes in ASDs in human and rodents (Nair et al., 2013; Tomasi and Volkow, 2017, Bureau et al., 2008).

Next, we investigated the contribution of the thalamocortical projection to the observed alterations in HP stimulus evoked responses by directly stimulating the projection from ventral posteromedial nucleus (VPM) while recording in S1-HP. We then compared the responding neuronal populations in wild type and *Fmr*1$^{-/y}$ mice S1-HP to those obtained by HP stimulation (**Fig 26, A, B, C, D)**.

10.7.1 THALAMIC VPM EVOKED EPSPs WERE ALTERED IN *FMR*1$^{-/Y}$ MICE

Variability between individual trials (a total membrane potential shift) were higher in *Fmr*1$^{-/y}$ mice.

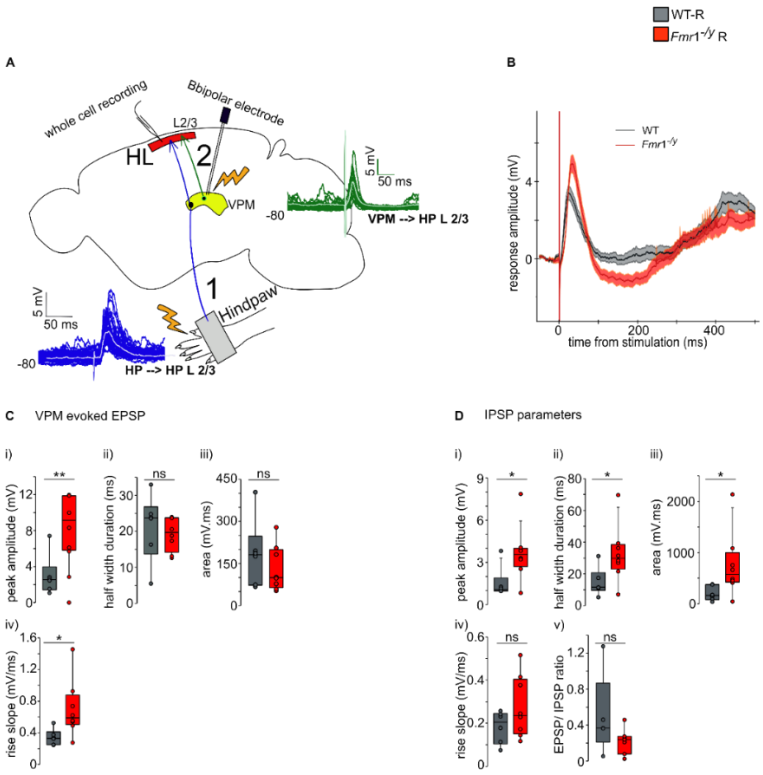

***Figure 26**: **VPM stimulation evoked EPSPs in HP L2/3 PN were altered in Fmr1$^{-/y}$ mice. A)** Schematic representation of HP and VPM stimulations while recording from S1-HP L2/3 PN.*

A bipolar electrode was placed in the VPM. The numbers indicate the sequence of stimulation. Example traces (40 trials) of a neuron responding to hind paw stimulation in blue and VPM evoked responses of the same neuron in green is represented. ***B****) Average VPM evoked responses of all recorded neurons (without failure traces) in WT and* $Fmr1^{-/y}$ *mice (data represented as mean ± SD).* ***VPM evoked EPSP response features (C, i- iv). (C, i)*** *VPM evoked EPSP responses in* $Fmr1^{-/y}$ R_{sub} *cells showed an increased peak amplitude (WT-*R_{sub}*, median = 2.54 mV, n = 6;* $Fmr1^{-/y}$*-*R_{sub}*, median = 9.15 mV, n = 8; p < 0.01, Mann-Whitney U-test). There were no differences in halfwidth duration (WT-*R_{sub}*, median = 23.74 ms, n = 6;* $Fmr1^{-/y}$*-*R_{sub}*, median = 19.64 ms, n = 8; p > 0.05, unpaired t-test) (****C, ii****) and area under the curve (WT-*R_{sub}*, median = 181.07 mV.ms, n = 6;* $Fmr1^{-/y}$*-*R_{sub}*, median = 99.41 mV.ms, n = 8; p > 0.05, unpaired t-test) (****C, iii****). (****C, iv****) Rise-slope (20-80%) was significantly increased in* $Fmr1^{-/y}$ *mice (WT-*R_{sub}*, median = 0.332 mV/ ms, n = 6;* $Fmr1^{-/y}$*-*R_{sub}*, median = 0.587 mV/ ms, n = 8; p < 0.05, Mann-Whitney U-test).* ***Features of IPSPs preceded by the VPM evoked EPSPs (D, i- iv). (D, i)*** *IPSPs in* $Fmr1^{-/y}$ R_{sub} *cells demonstrated signficantly increased peak amplitude (WT-*R_{sub}*, median = 11.483 mV, n = 6;* $Fmr1^{-/y}$*-*R_{sub}*, median = 29.90 mV, n= 8; p < 0.05, unpaired t-test), halfwidth duration (WT-*R_{sub}*, median = 1.013 ms, n = 5;* $Fmr1^{-/y}$*-*R_{sub}*, median = 3.565 ms, n = 8; p < 0.05, unpaired t-test) (****D, ii****) and area under the curve (WT-*R_{sub}*, median = 199.62 mV.ms, n = 6;* $Fmr1^{-/y}$*-*R_{sub}*, median = 554.69 mV.ms, n =7; p > 0.05, unpaired t-test) (****D, iii****). (****D, iv****) There was no difference in rise-slope (20-80%) (WT-*R_{sub}*, median = 0.204 mV/ ms, n = 6;* $Fmr1^{-/y}$*-*R_{sub}*, median = 0.236 mV/ ms, n = 8; p > 0.05, unpaired t-test). (****D, v)*** $Fmr1^{-/y}$ R_{sub} *cells displayed a lower, but not significant EPSP/IPSP ratio (WT-*R_{sub}*, median = 0.37, n = 6;* $Fmr1^{-/y}$*-*R_{sub}*, median = 0.24, n = 8; p > 0.05, unpaired t-test). Boxplots show the median, interquartile, range and individual values. *p < 0.05,* $^{ns}p > 0.05$ *(*$Fmr1^{-/y}$ *compared to wild type). Statistical significance was calculated by unpaired student t-test (for normal*

distribution) and Mann-Whitney U-test (Not normal distribution). All average values include failure traces.

The peak amplitude of EPSPs evoked by VPM stimulations were not different between WT and *Fmr*1$^{-/y}$ (WT- R_{sub}-, 2.98 ± 2.48 mV; *Fmr*1$^{-/y}$ R_{sub}-, 8.59 ± 3.43 mV; Mann-Whitney U-test; $p < 0.01$) (**Fig 26, C, i)**. Half amplitude duration was not different between the genotype (WT- R_{sub}-, 21.19 ± 9.32 ms; *Fmr*1$^{-/y}$ R_{sub}-, 19.25 ± 4.63 ms; $p > 0.05$) (**Fig 26, C, ii)**.

Rise slope (20-80 %) of *Fmr*1$^{-/y}$ R_{sub}- neurons were significantly higher compared to WT- R_{sub}- neurons (WT- R_{sub}-, 0.343 ± 0.102 mV.ms; *Fmr*1$^{-/y}$ R_{sub}-, 0.7 ± 0.358 mV.ms; $p < 0.05$) (**Fig 26, C, iv**).

10.7.2 INCREASED INHIBITION FOLLOWING EPSPs DURING VPM STIMULATION IN *FMR*1$^{-/Y}$ MICE

VPM stimulation evoked an EPSP, followed by a pronounced inhibitory post synaptic potential (IPSP) in HP-L2/3 PN of *Fmr*1$^{-/y}$ mice. Fig. 28A shows the average responses for all recorded neurons (WT R_{sub}-, n = 6; *Fmr*1$^{-/y}$ R_{sub}-, n = 13). Analysis showed that the *Fmr*1$^{-/y}$ EPSPs were accompanied by stronger IPSPs (**Fig 26, D**).

Inhibitory like response in *Fmr*1$^{-/y}$ animals demonstrated a larger peak amplitude (WT- R_{sub}-, 1.073 ± 0.133 mV; *Fmr*1$^{-/y}$ R_{sub}-, 3.684 ± 1.98 mV; Unpaired t-test; $p < 0.05$) (**Fig 26, D, i**). These IPSPs in *Fmr*1$^{-/y}$ mice had larger area under the curve (WT- R_{sub}-, 199.62 ± 145.01 mV.ms; *Fmr*1$^{-/y}$ R_{sub}-, 554.69 ± 324.34 mV.ms; Unpaired t-test; $p < 0.05$) (**Fig 26, D, iii**). The half-width duration was significantly higher in *Fmr*1$^{-/y}$ R_{sub-} cells (WT- R_{sub}-, 14.65 ± 8.97 ms; *Fmr*1$^{-/y}$ R_{sub}-, 32.58 ± 17.95 ms; Unpaired t-test; $p < 0.05$) (**Fig 26, D, iii**). We did not find any difference in the Excitatory/ Inhibitory (E/I) ratio (WT- R_{sub-}, 0.503 ± 0.46; *Fmr*1$^{-/y}$ R_{sub-}, 0.22 ± 0.14; $p > 0.05$) between the genotype (**Fig 26, D, v**).

10.8 INCREASED INTRA-TRIAL VARIATIONS AND FAILURE RATES OF EPSP RESPONSES IN *FMR1*$^{-/Y}$ MICE

There was a significantly higher number of failure traces in HP evoked responses in *Fmr1*$^{-/y}$ mice (WT-R_{sub} HP = 79/520; *Fmr1*$^{-/y}$ -R_{sub} HP = 203/984; $p < 0.01$, Fisher's exact test) (**Fig 27, B**). We measured the trial-to-trial variation (noise) in responses evoked by HP stimulation (**Fig 27, D**).

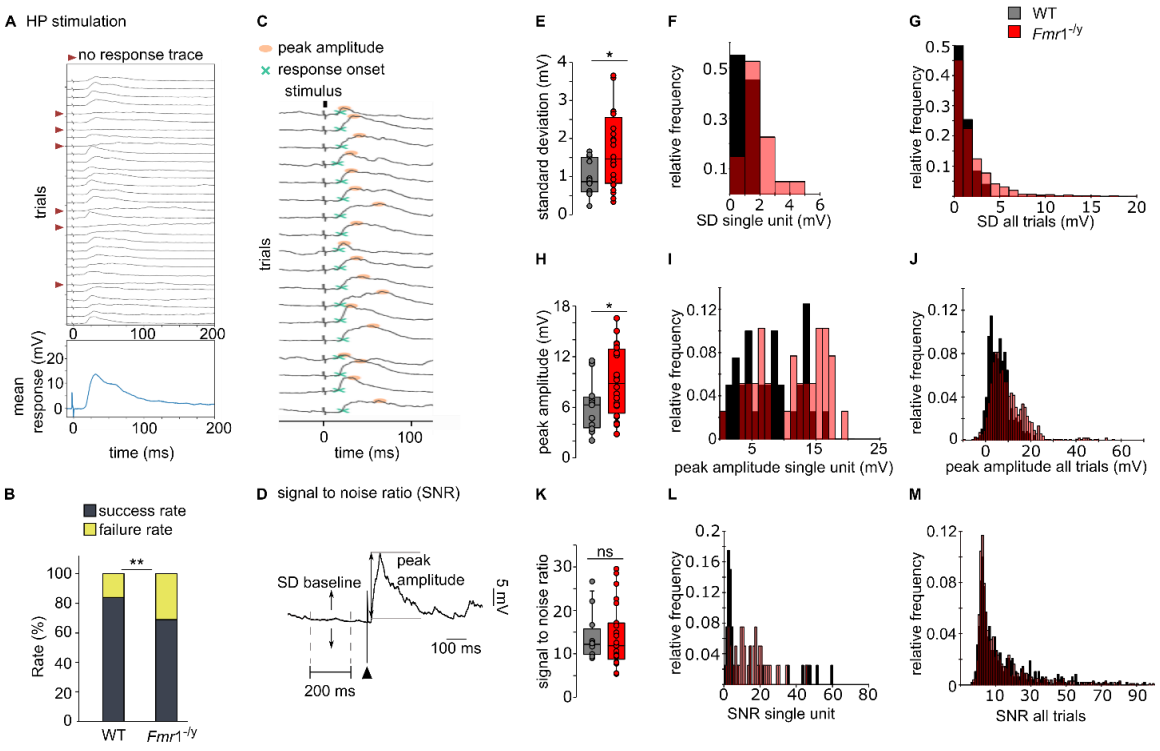

Figure 27*: Increased trial-to-trial variability in *Fmr1*$^{-/y}$ mice.** *(**A**)Example traces from a WT-R_{sub} neuron presenting both failure (marked with red arrow) trials that did not elicit a response when a stimulus was given and successful trials that resulted in a response during a session of 40 successive hind paw (HP) stimulations (top). Average response of the same neuron including failures (bottom).* ***(B) *HP stimulation evoked responses in Fmr1*$^{-/y}$ *cells show a significant decrease in failure rates (WT* $_{success}$ *= 84 %; Fmr1*$^{-/y}$ $_{success}$ *= 75 %) (Fisher's exact test, p< 0.01).* ***(C)*** *Example traces from a Fmr1*$^{-/y}$ *neuron showing variations in responses*

during a session of 40 successive hind paw (HP) stimulations (at '0' the stimulus was given). Onset of the stimulus (green cross) and peak amplitude (in orange circle) are presented for each trial. ***(D)****representation of the components involved in the calculation of signal to noise ratio of the evoked response. SD (standard deviation) of baseline, stimulus onset (black arrow) and the peak response amplitude are shown.* ***(E)*** *Average standard deviation of the baseline is significantly increased in Fmr1$^{-/y}$ cells (WT, median = 0.87 mV, n = 12; Fmr1$^{-/y}$, median = 1.45 mV, n = 24; p < 0.05, unpaired t-test). Relative frequency of standard deviation of 40 trials of a single neuron* ***(F)****, and whole population distribution* ***(G)****.* ***(H)*** *Average response amplitude was significantly greater in Fmr1$^{-/y}$ cells (WT, median = 6.29 mV, n = 12; Fmr1$^{-/y}$, median = 8.81 mV, n = 24; p < 0.05, unpaired t-test). Relative frequency of response amplitudes from 40 trials of a single neuron* ***(I)*** *and all neurons* ***(J)****.* ***(K)*** *No significant differences in Signal to Noise Ratio (response amplitude/ variance of the baseline) between the genotypes (WT, median = 12.18, n = 12; Fmr1$^{-/y}$, median = 11.86, n = 24; p > 0.05, unpaired t-test). Boxplots show the median, interquartile, range and individual values. Relative frequency of SNR of single unit* ***(L)*** *and all the trials* ***(M)****. *p < 0.05, **p < 0.01, ^{ns}p > 0.05 (Fmr1$^{-/y}$ compared to wild type). Statistical significance was calculated by unpaired student t-test (for normal distribution) and Mann-Whitney U-test (Not normal distribution).*

We found that the noise (standard deviation of the baseline within a 200 ms time window before the onset of stimulus) was significantly increased in *Fmr*1$^{-/y}$ -R_{sub} cells (WT-$R_{sub,}$ 0.97 ± 0.466 mV; *Fmr*1$^{-/y}$ -$R_{sub,}$ 1.689 ± 0.956 mV; p < 0.05) (**Fig 27, E, F, G**). Response amplitude was higher in *Fmr*1$^{-/y}$ -R_{sub} cells (WT-$R_{sub,}$ 6.11 ± 2.95 mV; *Fmr*1$^{-/y}$ -$R_{sub,}$ 9.047 ± 4.03 mV; p < 0.05) (**Fig 27, H, I, J**). We did not see any difference in signal to noise ratio between the genotypes (WT-$R_{sub,}$ 13.76 ± 5.45; *Fmr*1$^{-/y}$ -$R_{sub,}$ 13.93 ± 6.93; p > 0.05).

Overall, we noticed an increased trial to trial variability (noise) and increase signal (response amplitude) in *Fmr*1$^{-/y}$ -R_{sub} cells compared to WT-R_{sub} cells.

10.9 ALTERED SENSORY MOTOR FUNCTIONS OF *FMR1*$^{-/Y}$ MICE IN AN ADHESIVE REMOVAL TEST

The aforementioned alterations in the intrinsic properties of L2/3 S1 neurons, in their dendritic morphology, spontaneous firing activity, and in their responses to tactile sensory stimulation may all be expected to impact on the way in which *Fmr*1$^{-/y}$ mice respond to their environment. To explore this question, we used a simple test of sensory-motor function which examines the ability of the animal to detect and remove a piece of adhesive tape placed on the plantar surface of the paw. We modified this test, compared to published protocols in mice, to test sensory motor function related to hind paw in *Fmr*1$^{-/y}$ mice.

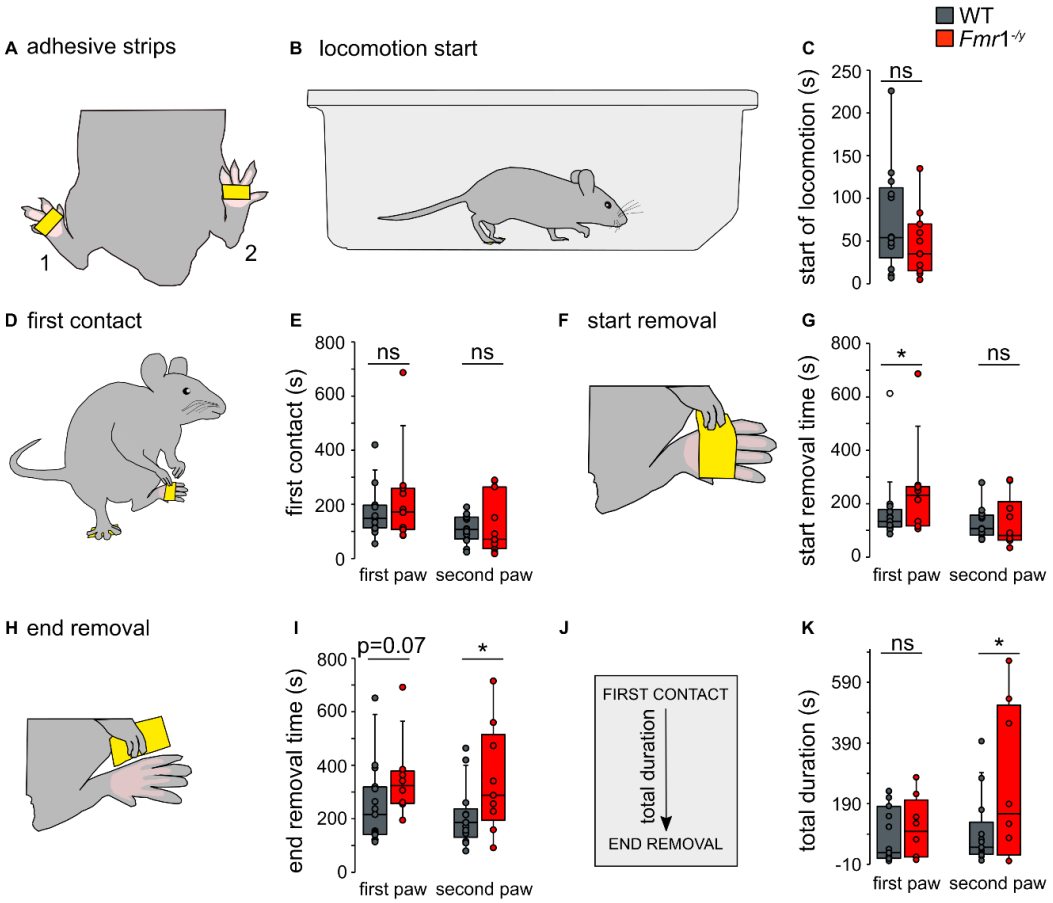

***Figure 28**: **Fmr1**$^{-/y}$ **mice displayed sensory motor deficits in an adhesive removal test for measuring sensory motor ability**. **(A)** Two equal sized adhesive tape strips are applied to the*

*plantar surface of the hind paws. Number 1 shows the 1st paw and number 2 denotes 2nd paw. (**B**) After the application of the adhesive strips, the animal is released into the testing box. Start of locomotion is observed and noted. (**C**) Both WT and Fmr1-/y mice started locomotion in similar fraction (WT, median = 53.5 s, n = 12; Fmr1-/y, median = 35 s, n = 11; p > 0.05, unpaired t-test). (**D**) Schematic representation of the 'first contact'. The first touch on the adhesive strips on any one of the paws with mouth or forepaw is considered as 'first contact'. (**E**) The first contact time of the first paw or second paw were not different between WT and Fmr1-/y mice (first paw;WT, median = 141 s, n = 14; Fmr1-/y, median = 171 s, n = 10; p > 0.05, unpaired t-test; second paw;WT, median = 107 s, n = 15; Fmr1-/y, median = 70 s, n = 11; p > 0.05, unpaired t-test). (**F**) Schematic representation of 'start of removal' phase of the testing procedure. (**G**) The latency for start of removal of the adhesive strips from the first paw was significantly shorter in WT mice when compared with Fmr1-/y littermate mice. Though there was a delay in Fmr1-/y mice in the start of removal of the strips from the second paw for the Fmr1-/y mice, it was not significant(first paw;WT, median = 127 s, n = 12; Fmr1-/y, median = 215 s, n = 9; p < 0.05, unpaired t-test; second paw;WT, median = 106 s, n = 12; Fmr1-/y, median = 80.5 s, n = 10; p > 0.05, Mann-Whitney U-test). (**H**) Schematic representation of final phase of the testing procedure in which the adhesive strip is completely removed from the paw (end removal time). (**I**) End removal time of adhesive strips from the first paw showed a trend of delay in Fmr1-/y mice. End removal time of adhesive strips from second paw was significantly delayed in Fmr1-/y mice (first paw;WT, median = 185.5 s, n = 14; Fmr1-/y, median = 307 s, n = 7; p = 0.07, unpaired t-test; second paw;WT, median = 186 s, n = 13; Fmr1-/y, median = 314.5 s, n = 8; p < 0.05, Mann-Whitney U-test). (**J**) Total duration of interaction with adhesive strip (time from the first contact to the end of removal). (**K**) Total duration of the task, notably the removal of adhesive strips from the second paw was significantly delayed in Fmr1-/y mice (first paw;WT, median = 28 s, n = 15; Fmr1-/y, median = 98.5 s, n = 8; p > 0.05,*

*unpaired t-test; second paw;WT, median = 31 s, n = 13; Fmr1$^{-/y}$, median = 156.5 s, n = 8; p < 0.05, unpaired t-test). Boxplots show the median, interquartile, range and individual values. *p < 0.05, ^{ns}p > 0.05 (Fmr1$^{-/y}$ compared to wild type). Statistical significance was calculated by unpaired student t-test (for normal distribution) and Mann-Whitney U-test (Not normal distribution).*

We scored the latency to the first contact (the moment the animal first senses and reacts to the adhesive strips attached to the paws; (**Fig 28 D, E**), the start of the 'removal' phase (**Fig 28 F, G**) and the end of the 'removal' phase (**Fig 28 H, I**) and the total duration of the first contact (**Fig 28 J, K**). We evaluated these interactions separately for first paw (in the illustrative example, the right hind paw) or the remaining hind paw (second paw). In general, the mouse used either its fore paw, or its mouth, to remove the adhesive strip (both types of interactions were scored). We did not observe any difference in the latency to first contact with either first paw (WT, 146.93 ± 56.14 s; *Fmr*1$^{-/y}$,168.7 ± 70.21 s; Unpaired t-test; p > 0.05) and or the second paw (WT, 110.67 ± 49.69 s; *Fmr*1$^{-/y}$, 122.91 ± 107.72 s; Mann-Whitney U-test; p > 0.05) (**Fig 28, E**).

Even though we did not observe any difference in latency to contact, *Fmr*1$^{-/y}$ mice showed a significant delay in the starting phase of the strip removal compared to WT mice (WT,136.83 ± 35.30 s; *Fmr*1$^{-/y}$, 192.11 ± 72.57 s; p < 0.05). The start of the removal from the second paw was not significantly different between WT and *Fmr*1$^{-/y}$ mice (WT,115.83 ± 40.02 s; *Fmr*1$^{-/y}$,129.9 ± 94.71 s; Mann-Whitney U-test; p > 0.05) (**Fig 28, G**).

WT mice finished the removal of adhesive strips much faster than *Fmr*1$^{-/y}$ mice (first paw; WT, 220.29 ± 101.54 s; *Fmr*1$^{-/y}$, 301.29 ± 67.64 s; Unpaired t-test; p = 0.07; second paw; WT, 209.77 ± 114.25 s; *Fmr*1$^{-/y}$,377.50 ± 189.18 s; Mann-Whitney U-test; p < 0.05) (**Fig 28, I**).

Lastly, we calculated the total time (duration) required from the point of first contact until the complete removal of both strips. We observed that the WT animals completed the task within

a shorter timeframe compared to *Fmr*1$^{-/y}$ mice (first paw; WT, 83.87 ± 91.61 s; *Fmr*1$^{-/y}$,109.38 ± 102.02 s; Mann-Whitney U-test; $p > 0.05$; second paw; WT, 39.8 ± 27.64 s; *Fmr*1$^{-/y}$, 225.5 ± 258.02 s; Unpaired t-test; $p < 0.05$) (**Fig 28, K**).

10.10 PHARMACOLOGICAL RESCUE APPROACH USING AN OPENER OF BK_{Ca} CHANNELS

Absence of FMRP is strongly associated with sensory hypersensitivity both in patients with FXS and in the *Fmr*1$^{-/y}$ mouse (Dahlhaus 2018, Deng et al., 2013, reviewed in Contractor et al., 2015). In addition to its canonical role as a modulator of mRNA translation, stability and transport, FMRP also fulfills non-canonical functions via direct protein-protein interactions. For example, FMRP binds to, and regulates the functional properties of several ion channels, such as potassium (K^+) channels like Slack and BK (big potassium Ca^{2+} and voltage activated), and calcium (Ca^{2+}) channels. Thus, the loss of FMRP causes channelopathies and thereby abnormal dendritic and cellular function (Brown et al., 2010; Deng et al., 2013; Ferron, 2016; Ferron et al., 2014; reviewed in Frick et al., 2017) in the CNS of *Fmr*1$^{-/y}$ mouse. Previously, we identified a dysfunction of BK_{Ca} channels as a mechanism to underlie neuronal/dendritic hyperexcitability of L5 pyramidal neurons of S1-BC in *Fmr*1$^{-/y}$ mice *in vitro* (Zhang et al., 2014). We thus decided to target these ion channels pharmacologically to determine whether our observed pathophysiological changes are linked to dysfunction of BK_{Ca} channels.

10.10.1 BK_{Ca} CHANNEL OPENER RESCUED SOME OF THE PROPERTIES OF *FMR*1$^{-/Y}$ NEURONS

Our initial characterization of the spontaneous firing properties of NR- and R_{sub}- cells in *Fmr*1$^{-/y}$ and WT littermates demonstrated a number of significant alterations in these properties (**Fig 12-14**). We explored whether direct neocortical S1-HP application of BMS191011 can correct these alterations. BMS treatment significantly depolarized the Down-state of *Fmr*1$^{-/y}$ R_{sub}- cells (*Fmr*1$^{-/y}$ R_{sub}-, -78.32 ± 5.85 mV; BMS- *Fmr*1$^{-/y}$ R_{sub}-, -70.04 ± 4.50; $p < 0.001$) (data not

shown). As a consequence, the difference in Down-states between NR- and R_{sub}-. cells of *Fmr1*$^{-/y}$ mice (**Fig, 14**) was not observed following BMS191011 application (BMS- *Fmr1*$^{-/y}$ NR-, -73.15 ± 8.07 mV; BMS- *Fmr1*$^{-/y}$ R_{sub}-, -70.04 ± 4.50 mV; $p > 0.05$).

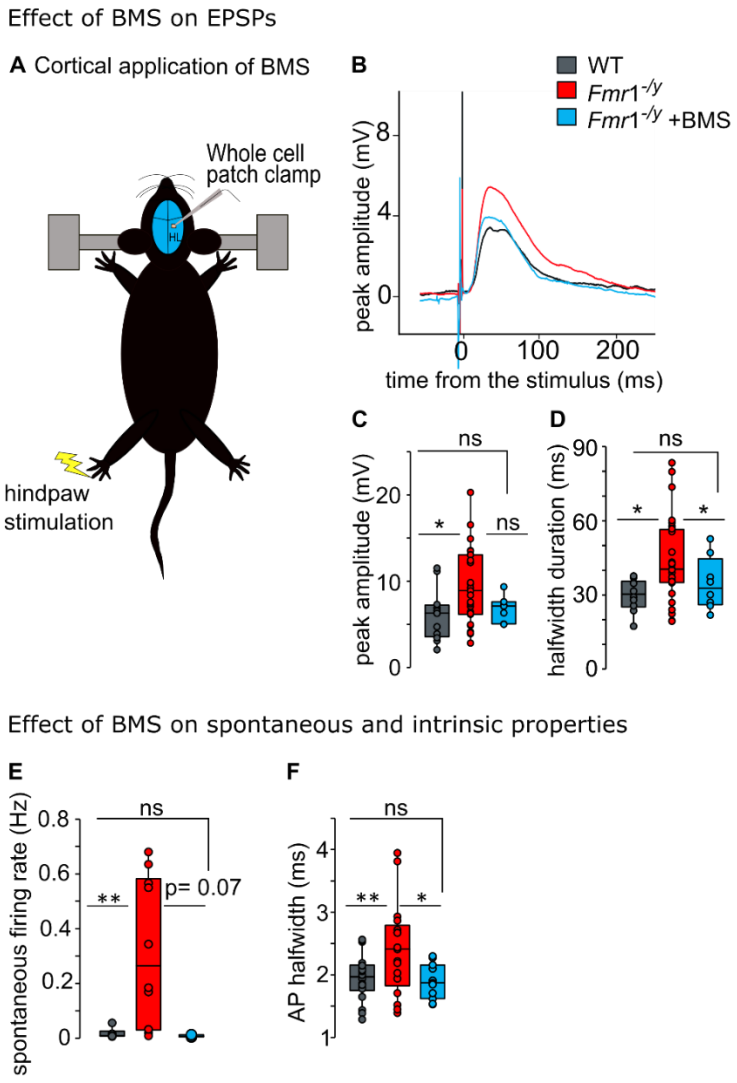

***Figure 29**: **BMS191011 rescued some of the altered evoked response, spontaneous and intrinsic properties in Fmr1*$^{-/y}$ *mice. A**) Schematic representation of administration of BMS via direct cortical application. **B**) Grand average evoked responses (with failures) of WT, Fmr1*$^{-/y}$*, and BMS treated Fmr1*$^{-/y}$ *mice. BMS treatment reduced peak amplitude ($p < 0.001$) (**C**), and half amplitude duration ($p < 0.05$) (**D**) in Fmr1*$^{-/y}$ *mice. **(E)** BMS treatment significantly*

decreased spontaneous firing rate ($p < 0.05$) and, ***(F)*** *AP halfwidth in $Fmr1^{-/y}$ neurons ($p < 0.05$). In BMS-treated $Fmr1^{-/y}$ mice, these parameters were not significantly different from control (WT) animals. Boxplots show the median, interquartile, range and individual values. $*p < 0.05$, $**p < 0.01$, $^{ns}p > 0.05$ ($Fmr1^{-/y}$ -treated mice compared to wild type and $Fmr1^{-/y}$ mice). Statistical significance was calculated using One-way ANOVA (analysis of variance) followed by Bonferroni multiple comparison post-hoc test.*

Even though we did not observe any difference in upstate threshold, frequency and duration in non-treated *Fmr*$1^{-/y}$ R_{sub}- and NR cells (**Fig, 13**), we found significant change in the upstate frequency in BMS-treated neurons (BMS- *Fmr*$1^{-/y}$ NR-, 1.183 ± 0.14 Hz; BMS- *Fmr*$1^{-/y}$ R_{sub}-,1.35 ± 0.13 Hz; $p < 0.05$) (data not shown). BMS treatment significantly reduced the upstate frequency of *Fmr*$1^{-/y}$ R_{sub}- cells (*Fmr*$1^{-/y}$ R_{sub}- vs BMS- *Fmr*$1^{-/y}$ R_{sub}-, $p < 0.05$) (data not shown). Upstate duration and threshold were not different (data not shown).

Previously we demonstrated that in WT mice NR- cells showed more spontaneous firing activity compared to R_{sub}-cells (**Fig, 12**). In contrast *Fmr*$1^{-/y}$ R_{sub}- cells were exhibited more firing rate compared to NR- cells (**Fig, 13**). BKca channel treatment resulted in a pattern that was similar to WT animals (**Fig 29, E**). BMS-191011- treated *Fmr*$1^{-/y}$ R_{sub}- and NR- cells demonstrated no difference in spontaneous firing (BMS- *Fmr*$1^{-/y}$ NR-, 0.0273 ± 0.05; BMS- *Fmr*$1^{-/y}$ R_{sub}-, 0.002 ± 0.004; $p > 0.05$). BMS-treated *Fmr*$1^{-/y}$ R_{sub}- cells showed a trend towards a decrease of the spike rate compared to non-treated *Fmr*$1^{-/y}$ R_{sub}- cells ($p = 0.09$) (data not shown).

10.10.2 BK_{Ca} CHANNEL OPENER, BMS191011 RESCUED SOME OF THE INTRINSIC PROPERTIES OF *FMR*$1^{-/Y}$ CELLS

In FXS, loss of FMRP reduces the activity of BK channels, and thereby causes AP broadening, an increase in presynaptic calcium influx and elevated neurotransmitter release (Deng et al., 2013). We previously demonstrated some of these alterations in neocortical L5 pyramidal

neurons of S1-BC in *Fmr*1$^{-/y}$ mice (Zhang et al., 2014). In agreement with the latter study we found that in L2/3 pyramidal neurons of S1-HP the AP halfwidth was significantly increased in both non-treated *Fmr*1$^{-/y}$ R_{sub}-and NR- cells when compared to WT neurons. Bath application of BMS191011 reduced the spike halfwidth of *Fmr*1$^{-/y}$-R_{sub}- cells in *Fmr*1$^{-/y}$ mice. BMS-*Fmr*1$^{-/y}$-R_{sub}- ($p < 0.05$) cells demonstrated significantly reduced AP halfwidth values that of non-treated *Fmr*1$^{-/y}$ mice (**Fig 29, F**). After the treatment R_{sub}- and NR- cells of *Fmr*1$^{-/y}$ mice did not show any difference in AP halfwidth when compared to the same cell types in WT mice (Mann-Whitney U test; $p > 0.05$). There were no differences between the R_{sub}- and NR- cells of treated *Fmr*1$^{-/y}$ mice (BMS- *Fmr*1$^{-/y}$ NR-, 1.99 ± 0.44 ms; BMS- *Fmr*1$^{-/y}$ R_{sub}-, 1.896 ± 0.28 ms; $p > 0.05$).

We did not observe any difference in the rheobase after the treatment. The average number of spikes at 2 times rheobase was increased for both treated NR and R cells (BMS- *Fmr*1$^{-/y}$NR-, 9.06 ± 4.15; BMS- *Fmr*1$^{-/y}$ R_{sub}-, 9.86 ± 2.41; $p > 0.05$) (data not shown). Maximum number evoked spikes were not changed with the treatment. Treated *Fmr*1$^{-/y}$ R_{sub}-and NR- cells showed similar firing rates with the non-treated *Fmr*1$^{-/y}$ cells (Mann-Whitney U test; $p > 0.05$). BMS-*Fmr*1$^{-/y}$ R_{sub}-cells were showed a significant increase in maximum evoked firing compared to WT-R- cells ($p < 0.01$) (data not shown). Average spikes fired at the maximal current steps (500, 550 pA) were significantly different between BMS-KO NR and R cells ($p < 0.05$). BMS-KO_R were also fired spikes significantly higher compared to WT R cells ($p < 0.05$). BMS191011 treatment reduced the average number of spikes in *Fmr*1$^{-/y}$ NR cells at the maximal current steps (data not shown).

10.10.3 EFFECT OF BK_{Ca} CHANNEL OPENER ON ALTERED EPSPs OF *FMR*1$^{-/Y}$ CELLS

Since sensory disturbances are one of the most reliably measured and prominent features of FXS, we decided to measure the effect of pharmacological intervention on sensory-evoked

responses in the L2/3 S1 neurons. BMS191011 was administered (refer Methods) via direct cortical application.

EPSP peak amplitude was significantly higher in non-treated *Fmr*1$^{-/y}$ mice compared with their WT littermates. BMS1901011 treatment substantially reduced the EPSP amplitude of *Fmr*1$^{-/y}$ mice. There was no significant difference between treated *Fmr*1$^{-/y}$ mice with either WT nor non-treated *Fmr*1$^{-/y}$ mice (WT-R_{sub}-, 6.11 ± 2.95 mV; *Fmr*1$^{-/y}$ R_{sub}-,9.047 ± 4.03 mV, BMS-*Fmr*1$^{-/y}$ R_{sub}-,7.16 ± 1.38 mV; $p > 0.05$) (**Fig 29, C**). Half amplitude duration of non-treated *Fmr*1$^{-/y}$ R_{sub}- cells was significantly broader compared with WT-R_{sub}- cells. BMS treatment reduced the half amplitude duration in *Fmr*1$^{-/y}$ R_{sub}- cells. We did not see any significant differences between WT and treated *Fmr*1$^{-/y}$ mice (WT-R_{sub}-, 29.25 ± 6.71 ms; BMS- *Fmr*1$^{-/y}$ R_{sub}-, 38.55 ± 11.17 ms; $p > 0.05$) also between treated and non-treated *Fmr*1$^{-/y}$ mice (*Fmr*1$^{-/y}$ R_{sub}-, 49.17 ± 20.54; BMS- *Fmr*1$^{-/y}$ R_{sub}-, 38.55 ± 11.17 ms; $p > 0.05$) (**Fig 29, D**).

CHAPTER 4

11 DISCUSSION

11.1 OUR FINDINGS

Sensory hypersensitivity, hyperexcitability and defects in sensory perception have been demonstrated in both human patients with ASD (reviewed in Robertson and Baron-Cohen, 2017; Tavassoli et al., 2018) and, in Shank2 and *Fmr*1$^{-/y}$ mice (Aloisi et al., 2017, Zhang et al., 2014, reviewed in Contractor et al., 2015, and Sinclair et al., 2017, Schmeisser et al., 2012). The neocortex of *Fmr*1$^{-/y}$ mice was shown to be hyperexcitable under basal conditions (Gibson et al., 2008; Gonçalves et al., 2013; Hays et al., 2011), but so far only few studies have investigated the neurobiological mechanisms underlying these defects (e.g. Zhang et al., 2014). In my thesis work, I studied the intrinsic/morphological properties and spontaneous activity, as well as the processing of hind-paw related sensory information in different L2/3 pyramidal neuron sub-types of the hind-paw related primary somatosensory cortex. I then probed alterations in the neocortical circuit in *Fmr*1$^{-/y}$ mice. To do this, I combined *in vivo* whole cell patch clamp recordings with hind-paw stimulation in anesthetized WT and *Fmr*1$^{-/y}$ littermates. We found a wide spectrum of cell-type specific spontaneous and intrinsic excitability changes, which in turn resulted in hyperexcitability of neocortical circuits in *Fmr*1$^{-/y}$ mice (**Fig 12-17**). Notably, we identified an enhanced spontaneous firing and action potential output in response to intrinsic excitability (**Fig 14, 17**) in R_{sub} cells of *Fmr*1$^{-/y}$ mice. We also showed difference in the dendritic morphology of these neuronal sub-types in *Fmr*1$^{-/y}$ mice (Fig **18-22**). We demonstrated that these changes correlated with cellular level hyperexcitability to a tactile sensory stimulus in *Fmr*1$^{-/y}$ R_{sub} and R_{supra} cells (**Fig 23-24**). Further investigation on thalamocortical projections to these neurons showed a circuit level deficit in *Fmr*1$^{-/y}$ mice (**Fig 26**). We also confirmed that these changes in intrinsic excitability and sensory hypersensitivity resulted in in sensory motor behavior deficits in *Fmr*1$^{-/y}$ mice (**Fig 28**). Hyperexcitability in *Fmr*1$^{-/y}$ mice was previously attributed partly to BK_{Ca} channel dysfunction (Zhang et al., 2014).

We demonstrated that direct cortical application of BK_{Ca} opener (BMS-191011) pharmacologically rescued some of the altered parameters in *Fmr*1$^{-/y}$ mice (**Fig 29**).

11.1.1 CELL TYPES IN SENSORY INFORMATION PROCESSING

The neocortex contains many different neuron types with diverse structural and functional characteristics. In my study, I identified three main subtypes of pyramidal neurons (NR-, R_{sub}- and R_{supra}- cells) within layer 2/3 of S1-HP (**Fig, 11**). These neuronal populations were distinguished by their spontaneous, intrinsic and morphological properties. In a typically developing brain, the neuronal diversity gives rise to the complexity of neocortical circuits and their manifold functions (Fishell and Heintz, 2013). It is generally accepted to classify neocortical neurons into two broad categories: Pyramidal neurons that provide excitation and form local and long-ranging connections, and inhibitory interneurons primarily modulating local circuits. Within these neuronal classes there are many neuronal sub-types (Cembrowski and Menon, 2018; Zaitsev et al., 2012, Nelson et al., 2006). Cell to cell variability is a critical feature of complex biological systems. Heterogeneity in intrinsic properties is essential for efficient representation of sensory information. An intrinsically heterogenous population of neurons encodes a richer array of stimuli compared to homogenous neuronal population (Tripathy et al., 2013). Recent advances in RNA sequencing (RNA-seq) of single cells revealed a continuum of gene expression patterns even within a neuronal population. A combination of transcriptome information with other higher-order properties like intrinsic, morphological, connectivity and response properties will help us to gain a more complete understanding of the rich diversity of cell types within a particular brain region (Cembrowski and Menon, 2018; Mo et al., 2015; Sugino et al., 2017; Tasic et al., 2016; Zeng and Sanes, 2017). Overall, all neurons serving the same function that differs from functions of other neurons are viewed as members of the same type. These neurons have unique functions and properties as an individual and homogenous functions and properties as members within a population. Classification of

distinct neurons within and across populations is important to understand how the brain works under normal conditions and fails to work in physiopathological conditions (Sharpee, 2014; Zeng and Sanes, 2017).

We found that neurons that responded to HP stimulus (i.e. in a sub-threshold manner), and those that did not respond, demonstrated differences in spontaneous firing rates, dendritic morphology, and intrinsic properties. NR-cells were spontaneously (not significant) more active (**Fig 12**). Spontaneous activity is essential to connect neurons with cellular specificity and to refine these connections with subcellular precision in developing excitatory neurons (Winnubst et al., 2015). Spontaneous activity together with intrinsic properties are also involved in working memory, arousal and synaptic homeostasis during sleep (Kanth, Ramaswamy and Muller, 2015).

In *Fmr*1$^{-/y}$ mice we found changes in the spontaneous activity, intrinsic properties, and HP evoked sensory responses in both L2/3 populations. For example, NR- and R_{sub}-cells showed abnormal spontaneous and intrinsic properties compared to the corresponding WT populations. Most of these changes differentially affected these two populations, attesting to modality specific alterations of these neocortical circuits. In contrast to the spontaneous firing rate in WT mice, *Fmr*1$^{-/y}$ mice R_{sub}-cells showed higher spontaneous firing rates than NR-cells (**Fig 13, 14**). In my study I focused on stimulation of the tactile receptor system of the paws, and not on other sensory modalities such as temperature or pain (Milenkovic et al., 2014). We therefore did not investigate the functional consequences of alterations in NR-cells for sensory information processing in *Fmr*1$^{-/y}$ mice.

In *Fmr*1$^{-/y}$ mice, alterations in the number of synapses, ion channel function, concomitant membrane excitability and overall circuit activity have been described. Deletion of *Fmr1* in excitatory neurons produces longer spontaneous UP states (Hays *et al.*, 2011). The neocortex

showed functional connectivity changes. For example, alterations in the synaptic properties were demonstrated for the projection from L4 to L2/3 pyramidal neurons of S1-BC during the development. In addition, the excitatory drive to fast spiking (FS) interneurons in L4 was reduced in *Fmr*1$^{-/y}$ mice. This led to an overall decrease in the local feedback inhibition in neocortical layer 4. Furthermore, impairment in FS mediated disynaptic inhibitition together with an increase in the intrinsic membrane excitability of excitatory neurons increased the excitability of neocortical networks (Gibson et al., 2008). These changes in neuronal properties could contribute to neocortical hyperexcitability and sensory hypersensitivity in FXS (Zhang et al., 2014; Haberl et al., 2015; Aloisi et al., 2017; Gibson et al., 2008; Kalmbach et al., 2015; Sinclair et al., 2017).

In agreement with our previous study on L5 pyramidal neurons of S1-BC and S1-HP (Zhang et al., 2014), we found that L2/3 pyramidal neurons of S1-HP were also hyper-excitable. The maximum number of action potentials fired (following current injection) was significantly increased in both NR- and R_{sub}-cells of *Fmr*1$^{-/y}$ mice (**Fig 16, 17**). Changes in Na^+ and K^+ channels contributing to enhanced action potential firing in response to current injections had also been demonstrated for L2/3 neurons of the prefrontal cortex (PFC) of *Fmr*1$^{-/y}$ mice (Routh et al., 2017). Even though we did not notice any difference in the amplitude of the first AP, we found a significant increase in AP halfwidth in both NR- and R_{sub}-cell populations in *Fmr*1$^{-/y}$ mice. This finding is in agreements with a previous study on CA3 hippocampal pyramidal neurons showing an increased AP duration following the loss of FMRP (Deng et al., 2013). We also demonstrated that the ADP amplitude and the AP-halfwidth ratio in response to a train of 3 current pulses were significantly increased in *Fmr*1$^{-/y}$ R_{sub}- cells (**Fig, 17**). These results agree with a previous finding from our lab where experiments were conducted in L5 neurons and dendrites (Zhang et al., 2014). The broadening of action potential and the increased ADP

resulted from a dysfunction of large-conductance calcium activated potassium (BK) channels (Deng et al., 2013; Zhang et al., 2014).

11.1.2 IMPORTANCE OF CELLULAR MORPHOLOGY IN SENSORY PERCEPTION

Dendritic and axonal length, diameter and branching patterns are the most informative among morphological properties for defining a cell (Zeng and Sanes, 2017). In our study, the NR- and R_{sub}-cells in WT animals showed differences in morphological features. The average apical dendritic length and total apical dendritic length was different between these two population. NR-cells have a shorter basal and apical dendrite (**Fig 18-22**). This differences in morphological features could correlate with differences in the brain-wide projections of neurons (Matsubara et al., 1996). Morphological and functional characteristics of dendrites influence signal integration and propagation, and thus sensory perception. Sensory information processing in the brain takes place within the neuronal dendrites performing complex computations (London and Häusser, 2005). For instance, dendrites of L 2/3 visual cortex neurons consist of dendritic hotspots which code for multiple sensory stimuli. The dendritic hotspots for similar stimulus were widely scattered over different dendrites. On the other hand, the dendritic hotspots coding for different stimuli are distributed within a dendritic tree among neighboring dendritic segments. Neurons that demonstrated a highly tuned output signal receive heterogeneous input signals. This shows that the sensory integration involves distributed inputs across dendrites which later summated to form a reliable output (Jia et al., 2010).

Electrophysiological properties of neurons can be modified as a consequence of changes in dendritic morphology (Amatrudo et al., 2012; Mainen and Sejnowski, 1996). Both apical and basal dendritic total length and average segment length of NR- and R_{sub}-cells were substantially decreased in *Fmr*1$^{-/y}$ mice. *Fmr*1$^{-/y}$ R_{sub}-cells also displayed a reduced number of endings and

nodes (**Fig, 20-22**). Dendritic abnormalities have been demonstrated in various brain regions, including the occipital cortex, olfactory bulb and somatosensory barrel cortex (Galvez et al., 2005; McKinney et al., 2005). FMRP is widely distributed across primary somatosensory cortex (S1), thalamus (posteromedial nucleus, PMN) and striatum during early development in WT. In the absence of FMRP, cortical maturation is disturbed, leading to a change in the density of synapses and spines, synaptic protein translation and dendritic morphology in *Fmr*1$^{-/y}$ mice. These alterations during development might underlie sensory hypersensitivity in Fragile X syndrome (Galvez et al., 2003; Till et al., 2012).

Even though we found significant differences in morphology of NR and R_{sub} cells within and between genotypes, we might require a greater number of reconstructions for the final conclusion.

11.1.3 TOUCH- A POTENTIAL SENSORY SYSTEM FOR STUDYING SENSORY PROCESSING

Most of the tactile response studies so far have been performed utilizing the primary whisker barrel cortex (S1-BC) of rodents. Few studies have addressed processing of other touch sensation information such as the one transmitted by the glabrous skin of the primate hand or the rodent paw (Abraira and Ginty, 2013, Orefice et al., 2016). In my study I used electric stimulations of HP to simulate and study the characteristics of tactile sensory responses evoked in HP-S1 L2/3 pyramidal neurons (**Fig, 11**). Using mild stimuli applied via conducting adhesive strips on and below the glabrous skin of hind paw of the mouse. In our study we showed a deficit in HP stimulation evoked tactile sensory responses of S1-HP L2/3 neurons. We observed a substantial increase of number of AP firing neurons in *Fmr*1$^{-/y}$ mice compared to the WT littermates. These *Fmr*1$^{-/y}$ R_{supra} neurons exhibited increased number of APs per session as well per stimulus (**Fig, 23**). We also found that HP stimulation evoked sub-threshold sensory responses of *Fmr*1$^{-/y}$ mice that are significantly different in peak amplitude and

halfwidth duration when compared to WT neurons (**Fig, 24**). We also noticed several changes in VPM evoked responses in S1-HP pyramidal neurons in L2/3. We observed differences in EPSP peak amplitude and a substantial increase of half-width duration (**Fig, 26**). It suggests that in *Fmr*1$^{-/y}$ mice, both AP and EPSP eliciting responses are highly altered.

The utility of the *Fmr*1$^{-/y}$ model for studying atypical sensory experience/sensory hypersensitivity is supported by additional studies in the first generation *Fmr*1$^{-/y}$ mutant. For example, single unit extracellular recordings performed in the auditory cortex of anesthetized mice following the presentation of acoustic stimuli of different frequency demonstrated sensory hyperresponsiveness in *Fmr*1$^{-/y}$ mice, compared with WT controls (Rotschafer and Razak, 2013). In the whisker barrel cortex, intrinsic optical imaging combined with C2 whisker stimulation demonstrated that a larger cortical area is excited in *Fmr*1$^{-/y}$ compared to the WT mice (Arnett et al., 2014). Similarly, a previous study from our lab pointed to an increased activation of the S1 barrel region, following D2 whisker stimulation using the same *Fmr*1$^{-/y}$ model as the present study (Zhang et al., 2014). In particular, the authors showed that in *Fmr*1$^{-/y}$ mice hyperexcitability implicated not only the large-scale network but also the way information is processed at the subcellular level in individual S1 neurons. Abnormally enhanced spontaneous network activity and hyperexcitability might contribute to exaggerated responses to sensory stimuli in *Fmr*1$^{-/y}$ mice. An additional study from our lab suggested that at the network level, atypical sensory responsiveness might also be caused by a local hyper-connectivity and a long range hypoconnectivity impinging on the primary visual cortex of *Fmr*1$^{-/y}$ mice (Haberl et al., 2015). Similarly, the defects we observed in the VPM evoked responses in S1-HP L2/3 pyramidal neurons suggest a possibility of a long-range circuit level dysfunction in *Fmr*1$^{-/y}$ mice (**Fig, 26**). This is supported by functional mapping studies (e.g. Bureau et al., 2008, Haberl et al., 2015, Zerbi et al., 2018). For example, in *Fmr*1$^{-/y}$ mice connections from L4 to L3 were weak. In contrast, L5A and L5B projections to L3 was

maintained. At the same time, *Fmr*1$^{-/y}$ mice showed a balance between synaptic depression and an enhancement of intra-cortical connectivity (Bureau et al., 2008). As these layers actively receive inputs from thalamus, we assumed these changes could have resulted from a network deficit which includes thalamus and other cortical layers which send information to L2/3 neurons. For instance, during the first 10 postnatal days, in *Fmr*1$^{-/y}$ mice displayed aberrant cortical neuronal properties. In WT during this period, the thalamocortical network undergoes a coordinated developmental refinement, which is essential for proper tactile coding. Examination of the physiological properties of L4 neurons in acute brain slices of these mice, showed elevated intrinsic excitability, increased feedforward inhibitory drive and altered thalamocortical synaptic kinetics. This data suggested cortical hypersensitivity to thalamocortical inputs (Domanski A, 2013). Another feature we observed in VPM evoked responses was the strong IPSP following the EPSP (**Fig 26**). Excitatory inhibitory imbalance is present in *Fmr*1$^{-/y}$ mice. During development intracellular chloride were maintained by Na^+-K^+-Cl-co-transporter (NKCC1) (Kaila et al., 2014). NKCC1 is highly expressed in *Fmr*1$^{-/y}$ mice neocortex at p10. This high expression of NKKC1 induces a prolonged depolarization of excitatory GABA neurons in L4 neurons of *Fmr*1$^{-/y}$ mice (He et al., 2014, 2018).

11.1.4 SPARSENESS IN NEOCORTEX

Sensory information processing in the neocortex is very complex. To reach a better understanding of this process, one needs to identify the cellular components of the respective neocortical circuits and their properties. In my thesis, I classified two types of neurons with respect to whether they responded to hind paw stimulation in anesthetized mice. Approximately 50 % of the neurons responded to the stimulation while the remainder of the population did not respond at all (neither in a sub- nor in supra-threshold manner). Amongst the responder cells, only ~16 % responded with an action potential at some of the trials. Similar sparse action potential firing was reported in S1-BC of mice, (Crochet et al., 2011; Kock et al., 2007) rat

visual cortex of (Medini, 2011) and oral somatosensory cortex (Clemens et al., 2018). The number of AP firing in S1-HP L2/3 pyramidal neurons in *Fmr*1$^{-/y}$ mice was comparable with WT. But we found a decrease of 6 % of sub-threshold responder cells in *Fmr*1$^{-/y}$ mice. That suggest an increased proportion of silent cells (NR-) in *Fmr*1$^{-/y}$ mice (**Fig 23**). These sparse firing could be a result of scattered excitatory inputs or, synaptic properties or lower intrinsic neuronal excitability. Other reasons for the sparse firing in the cortex might be a low fraction of neurons firing action potentials response to sensory stimulus or few action potentials fired per responding neuron, and stimulus specificity/ inappropriate stimulus. Firing sparseness has previously been demonstrated for, supra-granular layers when compared to infragranular layers (Barth and Poulet, 2012). In our data, we did not see any difference in recording depth for sub-threshold responders of WT and *Fmr*1$^{-/y}$ mice. Notably, we discovered a significant difference of recording depth of suprathreshold responders in WT and *Fmr*1$^{-/y}$ mice (**Fig, 23**).

The sparse firing could be a result of change in the brain state from anesthetized to alert or motivated could increase the number of neurons firing an AP (Barth and Poulet, 2012). For instance, in layer 2/3 S1-BC in anesthetized head fixed mice, the majority of pyramidal neurons fired very little or not at all following tactile sensation evoked in the principal whisker. But in a non-anesthetized head fixed mouse exploring objects at close proximity elicited APs in 22-25 % of the total L2/3 cells recorded with a probability of 10 % per contact. (Crochet et al., 2011; Lee and Brecht, 2018).

11.1.5 BIMODAL NEURONS IN NEOCORTEX

Perception is considered a multisensory process. It involves the integration of visual, auditory, tactile, gustatory and olfactory information. Different neocortical circuits processing these various sources of information interact and form a multisensory percept (Choi et al., 2018). Neocortical neurons might specifically code for a single modality or integrate two or several types of stimuli. In my thesis, I have shown that there are at least two main neuronal populations

in S1-HP. For example, I found a set of neurons which respond (R-) to hind paw stimulation and another group of neurons (NR-) that did not (**Fig, 11**). These NR-cells likely code for a different sensory modality. Amongst the R-cell population, we showed that ~30 % (Rsub- and Rsupra- cells together) responds not only to hind paw stimulation, but also to forepaw sensory stimulus in WT mice (**Fig, 25**), suggesting an inter-limb connectivity in L2/3 S1-HP. This proportion of cells is matching with the bimodal responses of neurons of the somato-visual area, which is located between V1 and S1 of mice. Most of the latter neurons were located in layer 5 rather than layer 2/3. The majority of these neurons display bimodal PSP responses and less those containing APs, and only few responded with an AP when V1 and S1 stimuli are presented simultaneously (Olcese et al., 2013). The same neocortical regions can code for two different stimuli that are part of a common receptive field. For instance, intrinsic imaging of forepaw S1 during cooling and tactile stimulation showed an overlapping response signal to both cool and tactile stimulus (Milenkovic et al., 2014). These sensory inputs carried by distinct sensory organs convey important information about the environment. Our brain integrates these multisensory modalities to identify if there are matching or if the incoming information must be considered and processed separately (Senkowski et al., 2008).

Multiple sources of sensory information converge onto, and are being integrated by, individual neocortical neurons. After this initial integration, these neurons interact with neurons from other neocortical brain regions (van Atteveldt et al., 2014). Distinct regions behave differently to the same stimulus. For example, an arousal state caused by free running of a mouse on a treadmill causes a depolarization followed by hyperpolarization in primary visual and auditory cortices. In contrast, in somatosensory and secondary visual areas arousal produces hyperpolarization. In all these areas, trains of sensory stimuli initiate similar sensory responses. These results show that in normal conditions these brain areas behave differently towards arousal but act similarly to a sensory stimulus (Shimaoka et al., 2018). Multimodal integration

takes place in different regions of brain. Integration of tactile and auditory stimuli within the auditory cortex was previously shown in macaque monkeys using fMRI-BOLD measurements. The constant arrival of signals and their latencies are vital in shaping sensory processing and integration (Rohe and Noppeney, 2016). The brain needs to determine which signals originate from the same sources based on their co-occurrence in time and space (Wallace et al., 2004). The sensory processing of auditory stimulus in the auditory cortex was disrupted by the simultaneous activation of the tactile stimulus, and tactile stimulus alone induced depolarization in auditory cortex (Kayser et al., 2005). In a recent study, neurons of the primary visual cortex (V1) L2/3 of mouse were shown to encode tactile stimuli (whisker) during active exploration of a controlled tactile environment (Kandler et al., 2018). Behavior goals determine the relevance of the input information and the appropriate actions to be chosen. Attention helps to choose these inputs and actions. Many integrative processes are adaptive to this behavior goal. The sensory stimulus arriving first in a sensory area (with a faster latency) can reset the phase of oscillations before the arrival of another sensory stimulus (van Atteveldt et al., 2014). Addition of a supporting input (double input stimulation) enhances the multisensory responses in single neurons (Chabrol et al., 2015).

11.1.6 FOREPAW-HINDPAW NETWORK

In our study we showed that 18 % of the R_{sub} cells (75% of the total R-cell population) and 66 % of the R_{supra} cells (25% of the total R-cell population) responding to hindpaw stimulation also responded to forepaw stimulus in WT mice (**Fig, 25**). Coordinated hind limb movement is required for the locomotion. A precise yet flexible control of interlimb coordination allows an animal to maintain dynamic stability in a continuously changing environment. Inputs from both limbs activate all the pathways that project to the spinal cord. Somatosensory feedback from the limbs activates parallel excitatory and inhibitory descending and ascending pathways

that project to a specific network which control specific limb or in parallel project to the network that control the other limb (reviewed in Frigon, 2017).

The sensory neocortex consists of topographic representations or maps of receptor surfaces representing the sensory environment. These orderly representations of sensory surfaces have been demonstrated for auditory, visual, tactile and other sensory modalities. Representation of multiple maps helps to process distinct stimulus features. For example, multiple small maps promote the formation of more efficient connections between frequently interacting neurons. These maps are amenable and can be refined by neuronal activity. They are, in turn, important for modulating the sensory perception (Kaas, 1997). In *Fmr*1$^{-/y}$ mice, I demonstrated an approximate 50 % increase in the R-cell population (~24 % increase from WT population) in S1-HP L2/3 responding to both HP and FP stimulus. The R_{supra} cells did not show a difference in the proportion compared to the WT. 75% of the R_{supra} cells (19.5 % of the total R- population) responded to both HP and FP in a suprathreshold manner. Subthreshold responders demonstrated a huge difference that of WT littermates. 48.8 % of *Fmr*1$^{-/y}$ R_{sub}- cells (39 % of the total R- population) responded to both HP and FP (**Fig, 25**). There is an overlap between the HP and FP region in S1 (Morales et al., 2012). These interconnected somatosensory areas could reorganize during a central or peripheral deafferentation or injury. For instance, a complete deafferentation of hind paw induced by injury or pharmacological blocks could increase the sensory responses at forepaw cortex (Humanes-Valera et al., 2014). In rodents, tactile information can be considered extremely important given the size of the neocortical sheet devoted to this information. Even a simple manipulation of early tactile experience in mice (trimming of whisker) resulted in enlarged receptive field properties, reduced angular tuning, enhanced responsiveness and a change in the temporal patterns of stimulus evoked discharges of cortical neurons (Simons and Land, 1987).

11.1.7 SENSORY MOTOR BEHAVIOUR

Adhesive removal test has been used for testing sensory-motor deficits in rodents (Bouet et al., 2009; Komotar et al., 2007). We found that *Fmr*1$^{-/y}$ mice showed a delay in sensory as well as motor response. For instance, *Fmr*1$^{-/y}$ mice demonstrated a delayed first contact with the adhesive strips. We also observed that the *Fmr*1$^{-/y}$ mice were started removal of the strips very late compared to WT littermates. WT animals finished removal of both strips before *Fmr*1$^{-/y}$ mice (**Fig, 28**). The total time taken by WT mice were significantly lesser than *Fmr*1$^{-/y}$ mice. This test involves both HP and FP and rarely the mouth. A deficit in cortical-cortical (**Fig, 25**) or thalamocortical network (**Fig, 26**) or aberrant tactile sensory responses (**Fig, 23-24**) and hyperexcitability of the neurons (**Fig, 16, 17**) can impair the sensory-motor coordination of the mice. Similar tactile impairments were demonstrated in *Fmr*1$^{-/y}$ mice on whisker dependent sensory learning paradigm (gap cross task). The exaggerated cortical responses to whisker stimuli correlated with the deficit in learning. S1-BC of *Fmr*1$^{-/y}$ mice showed an expansion of somatosensory map in L2/3. *In vivo* showed an impairment in frequency encoding of somatosensory tactile information (Juczewski et al., 2016). The delay in response to a sensory stimulus (here the adhesive strips) could be the tactile defensiveness of *Fmr*1$^{-/y}$ mice. For instance, adult *Fmr*1$^{-/y}$ mice actively avoided a stimulus (harmless whisker stimulus) (He et al., 2017).

11.1.8 IMPLICATIONS OF BK_{CA} CHANNELS

BK_{Ca} (big conductance Ca^{2+} and voltage-activated K^{+}) channels are important regulators of neuronal/dendritic excitability and synaptic transmitter release. They contribute to the fast after-hyperpolarization during AP trains by repolarizing the membrane potential, thus regulating AP width and firing rate, and consequently neurotransmitter release (Faber and Sah, 2003a, 2003b; Salkoff et al., 2006). BK_{Ca} channels co-exist with calcium channels, the

postsynaptic protein PSD95, NMDA receptors (Sailer et al., 2006), amongst others, enabling their various roles in regulating calcium influx, transmitter release and excitability.

In my study, I demonstrated alterations in the intrinsic firing properties of neocortical L2/3 pyramidal neurons in *Fmr*1$^{-/y}$ mice. For instance, *Fmr*1$^{-/y}$ NR- and R_{sub} neurons showed increased number of APs in response to a depolarization current injection (**Fig 17**). The first AP measurements showed an increased AP halfwidth compared with their WT littermates (**Fig, 17**). A similar AP broadening was observed in L5 pyramidal neurons of the somatosensory and entorhinal cortex in the absence of FMRP due to BK_{Ca} channel dysfunction (Deng et al., 2013; Zhang et al., 2014). Similarly, the abnormal broadening of APs in L2/3 pyramidal neurons was caused by a dysfunction of BK_{Ca} channels. In our study, a direct cortical application of the BK_{Ca} channel agonist, BMS191011, significantly reduced the AP halfwidth in *Fmr*1$^{-/y}$ neurons. We also revealed an increased ADP-amplitude and AP-halfwidth ratio in *Fmr*1$^{-/y}$ R_{sub} neurons (**Fig 17**). Even though we have not done any experiment to show a rescue of these properties *in vivo*, previous findings from our lab showed an application of BMS191011 *in vitro* rescued these aberrant properties in the dendrites and soma of L5 neurons in *Fmr*1$^{-/y}$ mice (Zhang et al., 2014). We further demonstrated an exaggerated evoked sensory response in *Fmr*1$^{-/y}$ mice. *Fmr*1$^{-/y}$ R_{sub} showed an increased peak amplitude, and halfwidth duration (**Fig, 24**). Cortical application of BMS191011 rescued the peak amplitude and halfwidth duration (**Fig 29**). This shows that BMS has both peripheral and local effect.

11.2 A NOISY BRAIN IN FRAGILE X SYNDROME

Variability is one of the noticeable features of behavior. Change of the state of neural circuits and the noise (fluctuations or disturbances that are not part of the signal) contribute to this variability in the behavior. Noise is an important determinant of transfer of information in the brain (Faisal et al., 2008). In our study we calculated the baseline fluctuation (calculated as SD

of baseline) in WT animals. These fluctuations (noise) were significantly larger in *Fmr*1$^{-/y}$ mice (**Fig E, F, G**). Noise is essential for the cortical neurons to produce precise spike sequences from synaptic input and therefore for processing of information within the neocortex (Mainen & Sejnowski, 1995). Increased noise in the system can modify the spike timing and thus increase trial-to-trial variability (Faisal et al., 2008). Opening and closing of ion channels (75 % of the total neuronal membrane noise at rest is coming from K^+ channel fluctuations) create intrinsic electric noise for the neuron (Donnell & Rossum, 2014). This contributes to fluctuations in membrane potential and an increase in the spontaneous firing of the neuron (Donnell & Rossum, 2014). The increase of noise of neuronal activity in *Fmr*1$^{-/y}$ mice could be due to the channelopathies, defects in circuit level deficits (thalamo-cortical or FP-HP network) identified in our study (**Fig 12-28**) and previous work (Zhang et al., 2014, Haberl et al., 2015, Zerbi et al., 2018, Contractor et al., 2015). Furthermore, a change in any protein production and degradation, synaptic vesicle fusion, and signaling molecule- receptor interactions could contribute to the noise. A minute change (fluctuations) in the system will alter the whole cell response (Faisal et al., 2008).

Using fMRI, evoked responses in visual, somatosensory and auditory cortices have recently been investigated in Autism individuals (Dinstein et al., 2012, Haigh et al., 2015). In these studies, an increase in noise (response standard deviation) and no change in the signal (mean amplitude of the response) was found in ASD patients. As a result, the signal-to-noise ratio was significantly weaker in ASD individuals, decreasing the reliability of the responses. In our experiments in the somatosensory cortex of *Fmr*1$^{-/y}$ mice we found an increase in both the signal and the noise compared to WT littermates. Thus, on average the signal-to-noise ratio was unaltered between genotypes. We noticed a negative correlation between the noise and signal amplitude in individual WT and *Fmr*1$^{-/y}$ neurons (data not shown). This could be explained as a strategy of brain to detect and transmit weak signals. For example, at low noise

levels, sensory signal does not cross the threshold, and a higher noise could completely mask the signal (Faisal et al., 2009).

11.3RELEVANCE OF CURRENT STUDY IN TRANSLATIONAL RESEARCH

Animal ASD models are powerful tools for studying dysfunctions in ASD. Investigations into sensory behaviors provide strong translational tools for the autism research (reviewed in Robertson & Cohen 2017). For translational research three objectives are important.

1.**Construct validity**: The cause behind the deficit should be similar in origin (for example, *Fmr1* gene mutation)

2. **Face validity**: behavior of the animal must show a strong resemblance to human behavior (for example, sensory hypersensitivity)

3.**Predicitive validity**: the results obtained by pharmacological treatment should be able to translate to human (for example: rescue using BKca openers)

(reviewed in Robertson & Cohen 2017).

Previous studies demonstrate similarities between FXS human and mice (reviewed in Dahlhaus, 2018). We found that *Fmr1*$^{-/y}$ mice were extremely relevant for the study of deficits in human. For example, the changes that we observed in spontaneous activity and intrinsic properties (increased AP output) match with findings from EEG recordings in humans. Wang et al., 2017 showed that there is an increased Gamma power (intrinsic excitability and disrupted E/I balance) in FXS individual compared to healthy control. FXS individuals on presentation of an auditory stimulus displayed a gradual decrease in habituation of spikes suggested an elevation of sensitivity towards sensory stimulus (Ethridge et al., 2016). Our data also demonstrated an increase in response amplitude (EPSPs) and AP firing (suprathreshold)

conforming hypersensitivity in both FXS human and mice (**Fig 23-24**). Less reliable evoked responses have been reported previously in ASD individuals (Dinstein et al., 2012, Haigh et al., 2015, reviewed in Robertson & Cohen, 2017). We found that WT individual neurons demonstrated more precise AP firing timing compared to *Fmr*1$^{-/y}$ mice. In *Fmr*1$^{-/y}$ cells AP timing was significantly more scattered over a time window of 0-60 ms following the stimulus (a combination of early and very late AP jitter). In contrast WT cells mainly fired between 20-45 ms (**Fig 23**), suggesting WT sensory responses are much reliably locked to the stimulus. Another striking similarity that we noticed is the defect in thalamocortical network. For example, Nair et al., 2013 reported a decreased functional connectivity between thalamus to prefrontal, parieto-occipital, motor and somatosensory regions. Another study displayed a reduced local but increase long range functional connectivity in ASD individuals (Tomasi et al., 2017). We found an increase in peak amplitude and an increased IPSP like signal following VPM stimulation (**Fig 26**). Even though we did not make further experiments to prove if there is a circuit deficit between thalamus and HP-S1 region, we presume that circuit dysfunction could be one of the reasons contributing to this change. In *Fmr*1$^{-/y}$ mice we identified a receptive field expansion (functionally) between hind paw and forepaw region (**Fig 25**). In ASD individuals increased receptive fields have been reported in the visual cortex (Schauder et al., 2017). Finally, we identified sensory motor impairment in *Fmr*1$^{-/y}$ mice (**Fig 28**), which has been previously reported in ASD human literature (Cascio et al., 2010, Friefeld et al., 1994, Güçlü et al., 2007). Apart from the aforementioned similarities, we are the first to describe trial-to-trial variability and noise in the *Fmr*1$^{-/y}$ mouse model, which has so far only been studied in Autism individuals.

12 CONCLUSION

The processing of hind paw related tactile information in mice is a poorly studied topic. In my project I investigated this question in L2/3 pyramidal neurons (PN) of the S1-HP region using whole-cell patch-clamp recordings in head fixed, anesthetized mice. The analysis of spontaneous firing, intrinsic excitability, morphological and evoked response properties of S1-HP L2/3 neurons in WT suggests the existence of several PN sub types in this layer, namely neurons that do not respond to tactile stimulation of the HP palm, those that respond in a sub-threshold fashion, and those that fire action potentials in some stimulation trials. Our investigation of these aforementioned properties revealed a variety of specific alterations in these different sub-types in *Fmr*1$^{-/y}$ mice (mouse model of fragile X syndrome). We found that the spontaneous activity of neurons in WT and *Fmr*1$^{-/y}$ neurons are very low. But, a comparison between WT and *Fmr*1$^{-/y}$ neurons demonstrated a significant increase of spontaneous firing in *Fmr*1$^{-/y}$-R_{sub} neurons. Intrinsic excitability properties of NR and R_{sub} cells revealed that L 2/3 neurons in *Fmr*1$^{-/y}$ mice are hyperexcitable. Furthermore, we found that the hyperexcitability and change in spontaneous firing rate contribute to an exaggerated tactile sensory response. Apart from the aforementioned alterations, *Fmr*1$^{-/y}$ neurons displayed an increased failure rate, trial-to-trial variability, a cortico-cortical network reorganization and an altered thalamocortical functional connectivity. We also demonstrated that these modifications together contributed to a noisy brain and an impairment in sensory motor behavior in a simple sensory-motor task. Direct cortical application of a BK_{Ca} channel opener pharmacologically corrected the main excitability phenotype, spontaneous firing rate, and evoked response properties including peak amplitude and halfwidth duration of *Fmr*1$^{-/y}$ neurons.

Overall our study reveals some of the neurobiological underpinnings of atypical sensory information processing within the S1-HP L2/3 network of *Fmr1*$^{-/y}$ mice. These alterations might give rise to altered sensorimotor behavior. Finally, our findings support the idea that

BK_{Ca} channels might be suitable targets for ameliorating neocortical hyperexcitability and sensory processing deficits in fragile x syndrome and autism spectrum disorder.

CHAPTER 5

13 FUTURE PERSPECTIVE AND PRELIMINARY DATA

My work to date (Bony, Bhaskaran et al and Bhaskaran et al, in preparation) and that of my colleagues (Zhang et al. 2014; Haberl *et al.*, 2015) provide strong evidence that neocortical circuits are altered in the *Fmr*1$^{-/y}$ mouse. At this point our findings are based on studies in anesthetized animals. Since these circuit-based changes are likely to have profound consequences for cortical signal flow underlying behavior and, importantly behavioral abnormalities are the main indicators of autistic pathology. It will therefore be important to evaluate the role of circuit alterations in an appropriate behavioral context. Manipulations of specific pathways and local circuits during a texture discrimination task will permit me to do this in the context of sensory-based decision-making. The ongoing project in the host lab of Prof Helmchen (Zurich) provides me with the experience and tools to now address these questions in the *Fmr*1$^{-/y}$ model.

This chapter is structured in the following way. First, I will talk about different viral approaches for targeting local circuits (here, M1 and S1-BC) and a specific pathway (M1 → S1). Second, I will explain the validation of injected viral vectors using an Optotetrode. Third, I will talk about the texture discrimination task that we used in the experiment. Finally, I will talk about the preliminary data that we obtained from the project.

13.1METHODS AND MATERIALS

13.1.1 VIRAL INJECTIONS

To carry out inhibition on the population level we expressed a redshifted Channelrhodopsin called JAWS in pyramidal neurons of primary somatosensory and motor cortices (**Fig 30, A**). Illumination of light causes an increase in chloride pump activity, inducing an increased hyperpolarization and inhibition of the neuronal activity (Chuong *et al.*, 2014).

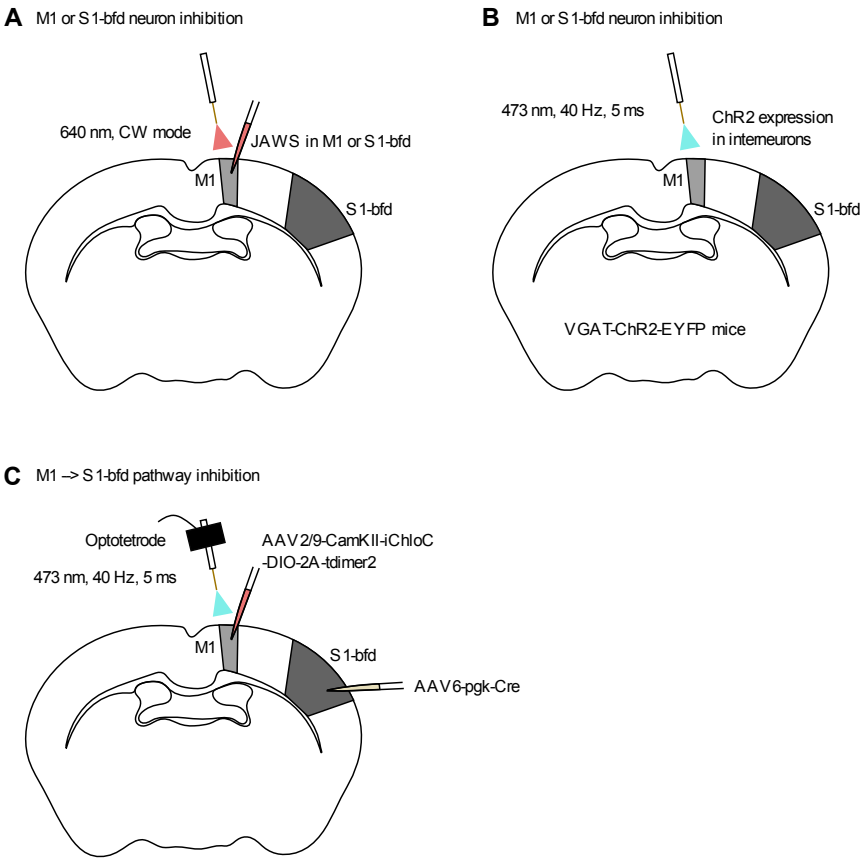

***Figure 30. Viral injection for manipulation of neurons during behaviour**. **A)** JAWS injection in M1 of wild-type mice and inhibition using red light (640 nm, CW mode (continuous illumination). All pyramidal neurons expressing JAWS are inhibited. We repeat this in S1-BF for another set of experiments where we inhibit all S1 pyramidal neurons expressing JAWS. **B)** ChR2 expression in interneurons (VGAT-ChR2-EYFP mouse line). Inhibition of all pyramidal neurons via activation of interneurons using a blue light (473 nm, 40 HZ, 5 ms). We target M1 and S1-BF in different experiments. **C)** Pathway targeted expression of iChloC*

(M1→ S1bf). Using a blue light (473 nm, 40 Hz, 5 ms) pathway specific inhibitions are achieved.

In another set of experiment, we used genetically modified V-GAT mice. The vesicular γ-aminobutyric acid (GABA) transporter (VGAT) is specifically expressed in GABAergic neurons. In this mouse model, Channelrhodopsin (ChR2)-YFP is specifically expressed in GABAergic neurons (**Fig 30, B**). Upon blue light illumination, ChR2 expressing interneurons are activated and induced an inhibition of excitatory neurons (Zhao *et al.,* 2011).

For pathway specific inhibitions we injected an improved version of Cre dependent chloride-conducting Channel rhodopsin (AAV2/9-CamKII-iChloC-DIO-2A-tdimer2) in M1. We then injected a retrograde adenovirus (AAV6-pgk-Cre) in S1bf (primary somatosensory barrel cortex). All the neurons which express this retrograde virus in M1 (primary motor cortex) were labelled with iChloC (Wietek *et al.,* 2015). Later with blue light the chloride pump in these neurons were enhanced pathway specific inhibitions were achieved (M1→ S1bf) (**Fig 30, C**).

13.1.2 ANIMALS AND SURGICAL PROCEDURES

All procedures of animal experiments were carried out according to the guidelines of the Veterinary Office of Switzerland and approved by the Cantonal Veterinary Office in Zurich. A total of 7 male mice (2-6 months age) were used in this study. To implant fiber and optotetrode, mice were anesthetized with 2% isoflurane (mixed in pure oxygen). Body temperature was maintained at 37ºC. To prevent inflammation and pain during anesthesia, a 0.1µl/g bw of Metacam was injected subcutaneously. Prior to implantation, connective tissue was removed from the skull bone. The bone was additionally polished, dried and iBond (Kulzer, Total Etch) was applied to ensure best adhesion of the skull to the connective dental cement. To further stabilize the implant on the skull we used Charisma (Kulzer, A1) to produce a thin ring on the skull rim. Both iBond and Charisma require UV light curing. Small slit-like craniotomies were made to allow for virus injections and implantation of fiber (carried out on the same day).

First, using intrinsic imaging, we mapped S1bf, S1-hindlimb (HL) and S1 forelimb (FL). Later ~120 nl of a retrograde adenovirus (AAV6-pgk-Cre) were delivered into S1bf at a rate of 20 nl/min. Coordinates for primary motor cortex were determined using the Allen brain atlas and previous studies (Chen *et al.,* 2015). To specifically tag the M1 neurons projecting to S1bf, an improved version of Cre dependent chloride-conducting Channel rhodopsin (AAV2/9-CamKII-iChloC-DIO-2A-tdimer2) was injected in M1. A custom setup with a syringe and a barometer was used to control pressure injections. To allow for local diffusion and to avoid

possible refluxes, the glass injection pipettes (10-15 µm diameter) were kept in place after injection for 10 min.

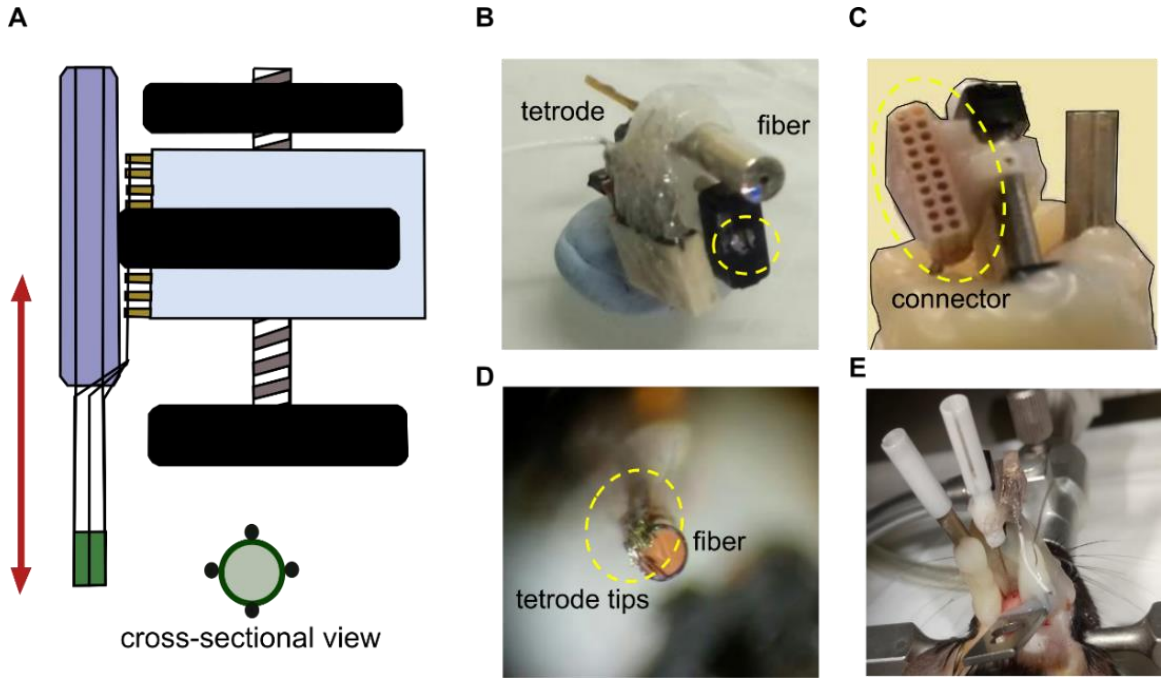

Figure 31. Optotetrode preparation*. **A)** Schematic of custom-designed optotetrode. Cross section of optotetrode tip comprising the UM22-100 fiber surrounded by four tetrodes. **B)** The screw to control the depth of fiber tip. **C)** Connector with 16 channels to record multiple neurons extracellularly. **D)** Optic fiber and the tetrode tips. **E)** Placement of optotetrode in the target region.*

All the implantations were done superficially (100-200 µm from the pia surface). Prior to fiber implantation we slightly scratched the dura surface using a fine needle. The opto-tetrode was implanted at around 200 µm depth in M1 and a ground screw was placed contralateral to the implant hemisphere. After, the craniotomy was sealed with Vaseline, which melts at body temperature and completely covers the craniotomy. Next, we applied dental cement (Tetric EvoFlow A1) on the skull and around the implant followed by UV light curing. A light-weight metal head post was additionally cemented to the skull, allowing for painless head-fixation during the behavioral experiments. After two weeks of recovery, the mice were habituated to head-fixation and trained in the texture discrimination task.

13.1.3 TEXTURE DISCRIMINATION TASK

Mice were first injected with different viral constructs for various inhibition experiments. The target areas were primary motor cortex (M1), primary somatosensory barrel cortex (S1bf) and secondary somatosensory cortex (S2) (**Fig 32, B, C**).

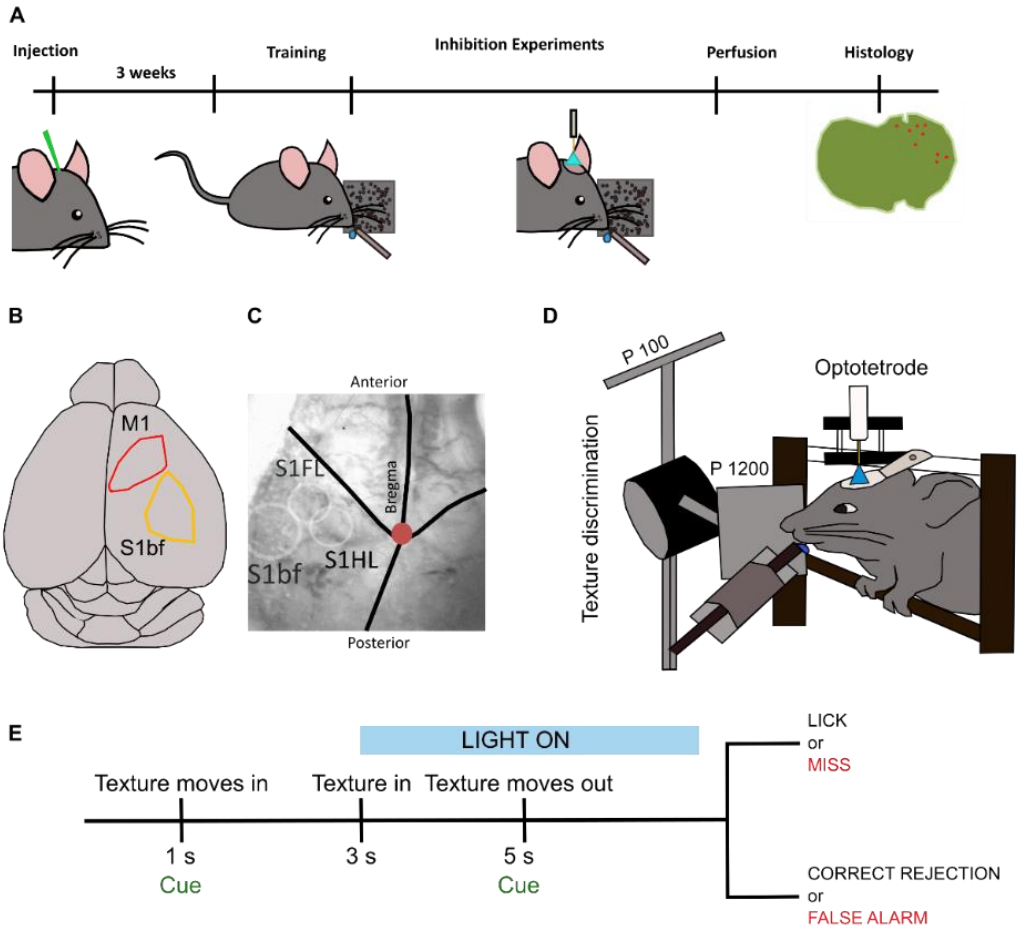

Figure 32. Texture discrimination task and experiment outline. ***A)*** *Experimental time window.* ***B, C)*** *Area of interest and intrinsic mapping of S1bf, S1 HL and S1 FL.* ***D)*** *texture discrimination task.* ***E)*** *schematic representation of texture discrimination task and inhibition protocol.*

We waited at least three weeks for sufficient expression of the injected virus. Then we started the texture discrimination experiment (**Fig 32**, **A**). Mice were first accommodated to head fixation through a series of short-duration head fixations. After starting water scheduling, each mouse was first trained to lick upon a texture presentation (**Fig 32, D**). After this shaping period we added presentations of either the go-texture (sandpaper grit size P100) or the no-go texture (sandpaper grit size P1200) and trained the mouse to discriminate the two texture types (Chen

et al., 2013). For the go-texture the mouse had to lick at a waterspout to receive a water droplet as reward (Hit trial). Failure to lick was considered a Miss trial. For the nogo-texture the mouse had to refrain from licking so that lick/no-lick events were interpreted as false alarm (FA) and correct reject (CR) responses, respectively.

The two texture types were presented with 50% probability. Each trial started with a TTL pulse to synchronize the calcium recording with the behaviour setup. One second after trial start, a first 2-kHz auditory tone (2 pulses of 100-ms duration at 50-ms interval) signalled the start of the texture approach (~90º to the whisker pad). It took 2 s for the texture to reach the end position so that the first whisker-to-texture touch occurred in the interval 2–3 s after trial start. Textures stayed in contact with the whiskers for 2 seconds and were retracted afterwards. Upon texture retraction a second 4-kHz auditory tone (4 pulses of 50 ms duration at 25-ms interval) signalled the start of 2-s report period, during which a water drop was delivered if the mouse licked correctly for the go-texture (Hit trial). A loud white noise sound stimulus of 4-s duration was presented as punishment if the mouse licked for the nogo-texture (FA trial). Both reward and punishment were omitted if the mouse did not lick (CR and Miss trials for nogo-texture and go-texture presentations, respectively). The lick detector was reachable throughout the entire session. Textures were presented pseudo-randomly with no more than 3 presentations of the same texture type in 3 consecutive trials. After learning the texture discrimination task mice reported their decision by starting to lick during the late period of a texture presentation (3.5-4 s after trial start) and then during the response period (5-7 s after trial start). Lick rate and whisker movements (video recording) were also calculated (**Fig 32, E**).

The proximal end of the optic fiber is connected to the optical set up for the optogenetic illumination. Omicron LuxX 473-nm laser is used to activate ChR2-tagged interneurons of V-GAT mouse line and iChloC expressing pyramidal neurons to target specific pathways. For the activation of JAWS expressing pyramidal neurons we used Coherent BioRay 640 laser. To achieve stable CW operation, lasers were run at 80% of maximal output power. A variable neutral density filter (NDC-25C-4M; Thorlabs) was used to control the fluorescence excitation power at the fiber tip.

Inhibition trials were set to a probability of 25% of the total session. We applied a 4-s long period of light stimulation from 2-6 s after trial start using a waveform generator (Agilent 33500B; TTL-triggered from the DAQ board for behavior control). Optogenetic protocols were adapted from (Sych *et al.,* 2018) with permission. Experiments were continued until the mice

stop licking. After each experiment they were provided with a few drops of normal water (limited to keep them thirsty for the next day).

13.1.4 POST-HOC IMMUNOHISTOCHEMISTRY

One to two months after the training, mice were anaesthetized (100 mg /kg body weight (bw) ketamine and 20 mg /kg bw xylazine) and perfused transcardially with 4% paraformaldehyde in phosphate buffer, pH 7.4. After perfusion, tissue was removed from the skull and the head including the multi-fiber implant was additionally fixated in 4% paraformaldehyde for one week. Then, the ventral (bottom) side of the skull bone was removed and the brain was carefully extruded. Coronal sections (75 – 100 µm thickness) were cut with a vibratome (VT100, Leica). Sections were mounted onto glass slides and confocal images were acquired with Olympus FV1000.

13.1.5 DATA ANALYSIS

Overall performance across normal condition and with photoinhibition were calculated in per cent.

Performance = (Hit + CR)/ (Hit + CR + Miss + FA)) *100 and

Performance with photoinhibition = (iHit + iCR)/ (iHit + iCR+ iMiss + iFA)) *100

Where Hit and Miss are the number of correct Hit trials and Miss trials (wrong rejection) respectively, among all trials in a session without photoinhibition. Likewise, FA is the number of false alarms (wrong licks) and CR is the number of correct rejections. iHit, iMiss, iFA, and iCR denote the same variables for the trials with photoinhibition.

For analysis of the performance change, we calculated the d' measure as described in (Chen *et al.*, 2015) previously. Briefly,

d' (control) = Z (Hit/ (Hit + Miss))- Z (FA/ (FA + CR)),

d' (photoinhibition) = Z (iHit/ (iHit + iMiss))- Z (iFA/ (iFA + iCR)),

The effect of photoinhibition was quantified as the difference of d' values for each session

Δd' = d'(photoinhibition) – d'(control)

We also calculated the FA rate in % and Miss rate in %: -

FA rate (%) = (FA/ (FA+ CR)) *100

FA rate with inhibition, (iFA rate) (%) = (iFA/ (iFA + iCR)) *100

Miss rate is calculated as below,

Miss rate (%) = (Miss/ (Hit+ Miss)) *100

Miss rate with inhibition (iMiss rate) (%) = (iMiss/ (iHit+ iMiss)) *100

Spikes recorded with optotetrode were sorted in Tint software. Whisker angle, lick rate and spike parameters were processed and analysed using MATLAB.

13.1.6 STATISTICAL TESTS

Across mice we have recorded different number of sessions and trials. Furthermore, mice had individual performance levels, some could discriminate textures with above 90% correct trials while others were close to 75%. To account for variations in sample number (that is, the number of trials and samples from which the performance, FA and Miss rates are calculated) and mouse-to-mouse variations in performance levels we used a random draw of same amount of trials into sessions to estimate performance. Total number of draws and consequently total number of trials which contribute to the calculation of performance levels was the same across all mice. For each of these session performances (performance %, dprime and Δd'), fa and miss rates is calculated for each mouse. As changes in performance during optogenetic perturbation followed non-normal distribution we have used Wilcoxon signed rank test to calculate significance levels. All graphs are made using MATLAB. Appropriate modifications and arrangement of the figures without the manipulation of the data were done using Inkscape.

13.2RESULTS 2

13.2.1 JAWS MEDIATED INHIBITION OF S1-BF PYRAMIDAL NEURONS DID NOT AFFECT THE OVERALL PERFORMANCE IN TEXTURE DISCRIMINATION TASK

Texture discrimination task is whisker dependent in mice. In this experiment whisker plays a crucial role in touch, sense and detection of different textures to make a choice. S1bf is one of the important areas corresponding to the control of sensory inputs and outputs to the whisker regions. We tested this by expressing JAWS, a redshifted channel rhodopsin enhancing chloride pump in S1 bf pyramidal neurons. With the help of light (**Fig 30, A**) we inhibited the activity of JAWS expressing neurons with a red light (650 nm) from 2 s to 6s after the trial started. A total of 25 % inhibition trials were provided during each session. We performed the experiment on two animals for a total of 10 days. The average performance of the animals was not altered with JAWS mediated inhibition in S1 (Performance in %; NoLight = 91.65 ± 1.04; Light = 89.48 ± 0.87; mean ± SEM; Wilcoxon signed rank test; p = 0.109) (**Fig 33, A**).

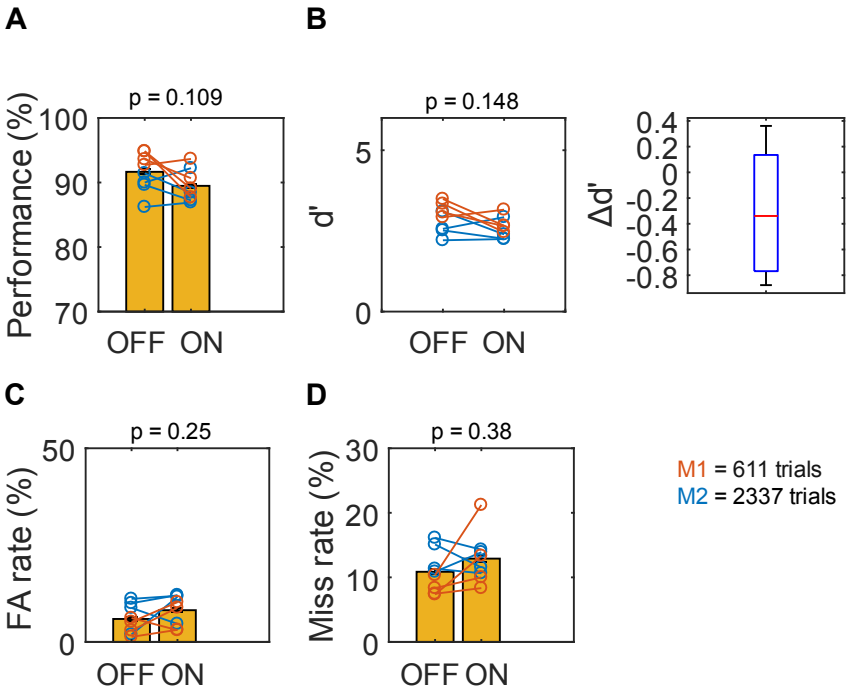

Figure 33. JAWS mediated S1 pyramidal neuron inhibition decreased the overall performance and increased FA and MISS rates. ***A)*** *Inhibition of JAWS expressing S1bf pyramidal neurons showed no impact on average performance. Each data point denotes an individual session performance percentage. Each animal and the corresponding data points are similarly colour coded (M1, M2).* ***B)*** *Overall performance, d' was not changed with*

*inhibition. Each data point represents d'prime of an individual session (**B,** left). Mean d'prime change (Δd') is -0.307 ± 0.17 (**B**, right). **C**) False rate and **D)** Miss rate were not changed with S1 pyramidal neuron inhibition. Data presented as mean ± SEM for panels (**A, C and D**), Boxplot (**B**, right) show the median, interquartile, and range. Animals n = 2; sampled 200 trials without replacement, 4 independent draws followed by Wilcoxon signed rank test.*

The overall performance d' is not changed during the inhibition (d'performance; NoLight = 2.90 ± 0.15; Light = 2.59 ± 0.11, mean ± SEM; Wilcoxon signed rank test; p = 0.1484) (**Fig 33, B**). There were no differences in the rate of FA (FA rate in %; NoLight = 5.92 ± 1.32; Light = 8.18 ± 1.40; mean ± SEM; Wilcoxon signed rank test; p = 0.25) and MISS (MISS rate in %; NoLight = 10.86 ± 1.16; Light= 12.9 ± 1.39; mean ± SEM; Wilcoxon signed rank test; p = 0.38) showed a substantial but a non-significant increase (**Fig 33, C and D**).

13.2.2 ACTIVATION OF INTERNEURONS IN S1-BF ALTERED THE OVERALL PERFORMANCE OF THE MOUSE IN TEXTURE DISCRIMINATION TASK

With the JAWS, we restricted our inhibition to a smaller population of pyramidal neurons. To see a better and wider inhibitory effect, we used V-GAT mice.

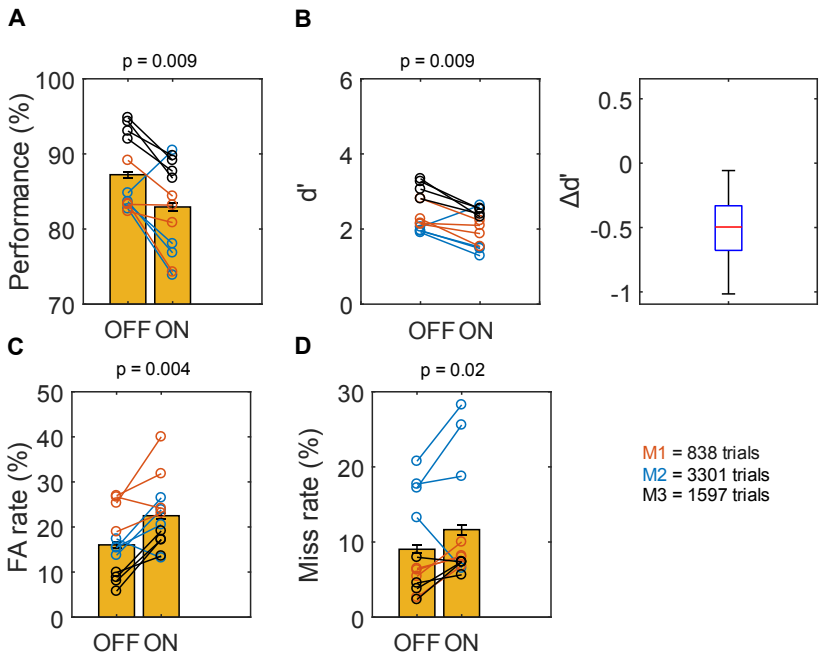

***Figure 34. Inhibition of S1 pyramidal neurons via interneuron excitation in VGAT mice reduced the overall performance and increased FA and MISS rates. A)** Interneuron driven inhibition of S1bf pyramidal neurons led to a significant drop of average performance. Each*

data point denotes an individual session performance percentage. Each animal and the corresponding data points are similarly colour coded (M1, M2, M3). ***B****) Overall performance, d' was reduced with inhibition. Each data point represents d'prime of an individual session (****B,*** *left). Mean d'prime change (Δd') is -0.43 ± 0.116 (****B****, right).* ***C****) FA rate and* ***D)*** *MISS rate were significantly increased with inhibition. Data presented as mean ± SEM for panels (****A, C and D****), Boxplot (****B****, right) show the median, interquartile, and range. Animals n = 3; sampled 400 trials without replacement, 4 independent draws followed by Wilcoxon signed rank test.*

These are genetically modified mice where all the interneurons in the brain are expressed with ChR2 (**Fig 30**, **B**). With this mouse model we can excite the interneurons expressing ChR2 at the reach of the light and therefore producing a stronger inhibition on S1bf pyramidal neurons. We performed the experiment on 3 animals for a total of 12 days. As expected, the average performance (**Fig 34**, **A**) was dropped significantly with the illumination (Performance in %; NoLight = 87.23 ± 1.44; Light = 82.93 ± 1.74; mean ± SEM; Wilcoxon signed rank test; p = 0.009). The overall performance d' is significantly decreased with the inhibition (d' performance; NoLight = 2.47 ± 0.15; Light = 2.037 ± 0.138; mean ± SEM; Wilcoxon signed rank test; p = 0.009) (**Fig 34, B**).

We then measured the incorrect responses of the animal. We found that both false alarms (FA rate in %; NoLight = 16.03 ± 2.11; Light = 22.5 ± 2.22; mean ± SEM; Wilcoxon signed rank test; p = 0.004) and misses (MISS rate in %; NoLight = 9.03 ± 1.8; Light= 11.65 ± 2.28; mean ± SEM; Wilcoxon signed rank test; p = 0.02) were significantly increased with interneuron mediated inhibition of S1bf pyramidal neurons (**Fig 34**, **C, D**).

13.2.3 JAWS MEDIATED INHIBITION OF M1 PYRAMIDAL NEURONS HAD NO IMPACT ON THE OVERALL PERFORMANCE OF THE MOUSE IN THE TEXTURE DISCRIMINATION TASK

Sensory motor cortices together initiate and execute the whisker movements. We examined the effect of inhibition of M1 (300 µm posterior to bregma; 1250 µm lateral; 200 µm depth) by activating chloride pump in pyramidal neurons expressing JAWS-ChR2 with illumination (**Fig 30, A**). We examined the effect of inhibition on behaviour over 10 days. We observed that an inhibition of M1 pyramidal population showed no effect on the overall performance of the animal (Performance in %; NoLight = 85.13 ± 0.69; Light = 84.03 ± 0.77; mean ± SEM; Wilcoxon signed rank test; p = 0.25) (**Fig 35, A**).

The overall performance d' was unchanged with the inhibition (d' performance; NoLight = 2.19 ± 0.06; Light = 2.12 ± 0.07, mean ± SEM; Wilcoxon signed rank test; p = 0.64) (**Fig 35, B**).

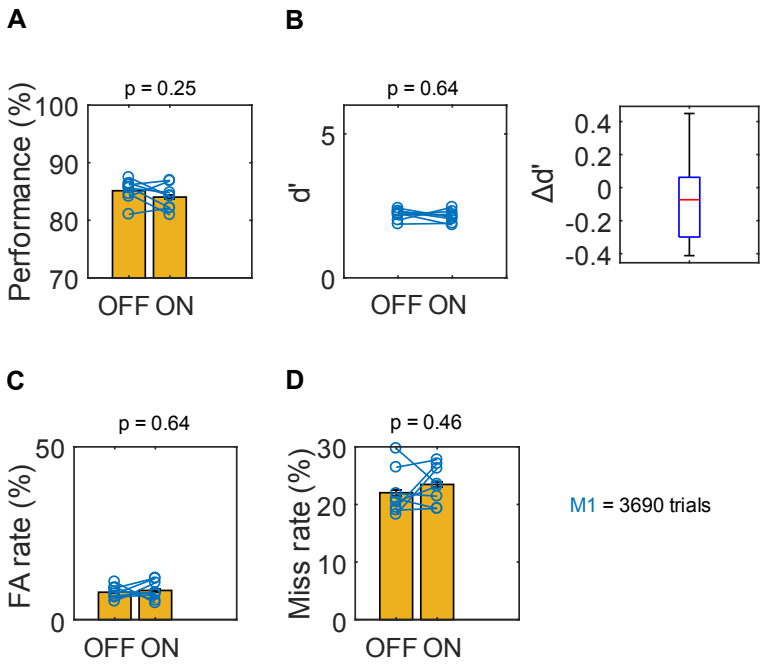

Figure 35. JAWS mediated M1 pyramidal neuron inhibition dropped the overall performance and increased FA and MISS rates. ***A)*** *Inhibition of M1 pyramidal neurons did not change the average performance of the animals. Each data point denotes an individual session performance percentage. Each animal and the corresponding data points are similarly colour coded (M1).* ***B)*** *Overall performance, d' also not modified with the inhibition. Each data point represents d'prime of an individual session (**B,** left). Mean d'prime change (Δd') is -0.072 ± 0.09 (**B**, right).* ***C)*** *FA rate and* ***D)*** *Misses are not affected with inhibition. Data presented as mean ± SEM for panels (**A, C and D**), Boxplot (**B**, right) show the median, interquartile and range. Animals n = 1; sampled 400 trials without replacement, 8 independent draws followed by Wilcoxon signed rank test.*

We then measured incorrect responses of the animal during and after the inhibition trials. We found that both false alarms (FA rate in %; NoLight = 7.93 ± 0.63; Light = 8.45 ± 0.98; mean ± SEM; Wilcoxon signed rank test; p = 0.64) and misses (MISS rate in %; NoLight = 22.03 ± 1.41; Light = 23.47 ± 1.18; mean ± SEM; Wilcoxon signed rank test; p = 0.46) were comparable with interneuron mediated inhibition of S1bf pyramidal neurons (**Fig 35, C, D**).

13.2.4 INTERNEURON DRIVEN INHIBITIONS OF M1 PYRAMIDAL ACTIVITY DECREASED THE OVERALL PERFORMANCE OF THE ANIMAL IN THE TEXTURE DISCRIMINATION TASK

Next, we measured the performance of the V-GAT mice while inhibiting M1 partially (**Fig 30, B**). We performed the experiment on 3 animals across 11 days. We found a significant reduction in the average performance of the animal with M1 inhibition (Performance in %; NoLight = 92.54 ± 0.83; Light = 89.12 ± 1.24; mean ± SEM; Wilcoxon signed rank test; p = 4.88 e-04) (**Fig 36, A**).

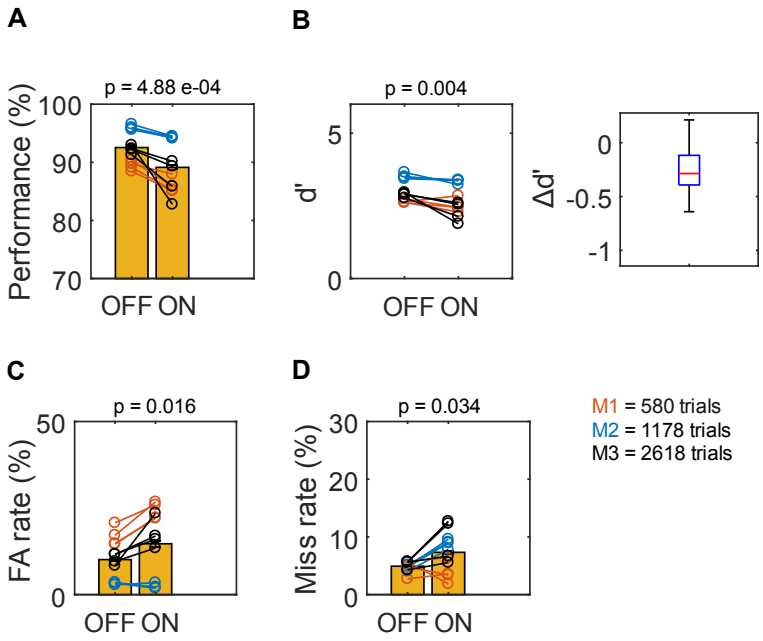

Figure 36. Inhibition of M1 pyramidal neurons of VGAT mice decreased the performance and increased both FA and MISS rates. ***A)*** *Interneuron driven inhibition of M1 pyramidal neurons is significantly dropped the average performance. Each data point denotes an individual session performance percentage. Each animal and the corresponding data points are similarly colour coded (M1, M2, M3).* ***B)*** *Overall performance, d' is reduced with inhibition. Each data point represents d'prime of an individual session (**B,** left). Mean d'prime change (Δd') is -0.304 ± 0.09(**B**, right).* ***C)*** *False alarm and* ***D)*** *Misses are increased with inhibition. Data presented as mean ± SEM for panels (**A, C and D**), Boxplot (**B**, right) show the median, interquartile, and range. Animals n = 3; sampled 400 trials without replacement, 4 independent draws followed by Wilcoxon signed rank test.*

The overall performance d' is significantly reduced with M1pyramidal neuron inhibition (d' performance; NoLight = 3.019 ± 0.11; Light = 2.715 ± 0.15; mean ± SEM; Wilcoxon singed rank test; p = 0.004) (**Fig 36, B**). We then measured errors made by the animal during and after the inhibition trials. We discovered that both false alarms (FA rate in %; NoLight = 10.12 ± 1.74; Light = 14.69 ± 2.85; mean ± SEM; Wilcoxon signed rank test; p = 0.016) and misses (MISS rate in %; NoLight = 4.92 ± 0.25; Light = 7.33 ± 0.98; mean ± SEM; Wilcoxon signed rank test; p = 0.034) were significantly higher with interneuron mediated inhibition of S1bf pyramidal neurons (**Fig, 36 C, D**).

13.2.5 PATHWAY SPECIFIC (M1 PYRAMIDAL NEURONS PROJECTING TO S1-BF) INHIBITIONS INCREASED THE NUMBER OF FALSE ALARMS NOT THE MISSES

Later, with the help of a retrograde AAV6-pgk-Cre in S1bf and AAV2/ 9-CamKII-iChloc-DIO-2A-tdimer 2 in M1, we specifically targeted the M1 pyramidal neurons projecting to S1bf.

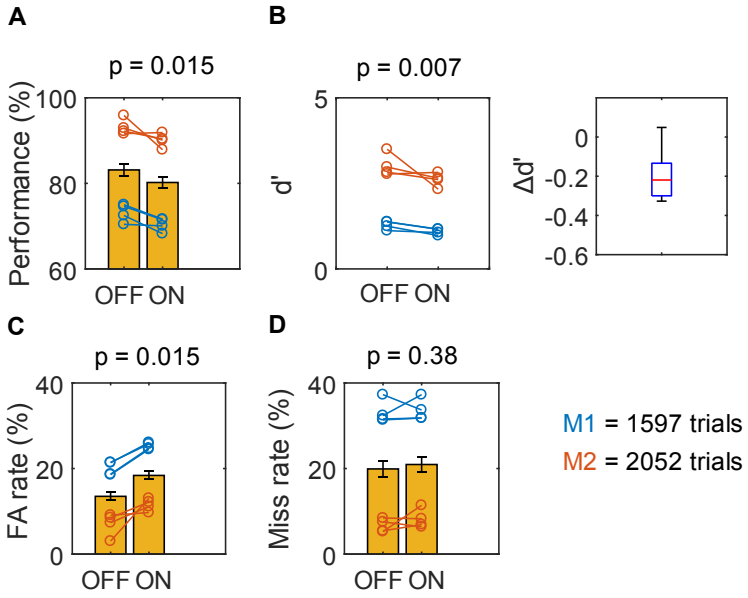

Figure 37. M1→S1 pathway specific inhibition reduced the overall performance through increased FA rate modulations. ***A)*** *Pathway specific inhibition (M1 pyramidal neurons projecting to S1bf) significantly dropped the performance. Each data point denotes an individual session performance percentage. Each animal and the corresponding data points are similarly colour coded (M1, M2).* ***B)*** *Overall performance, d' is reduced with inhibition. Each data point represents d'prime of an individual session* ***(B,*** *left). Mean d'prime change*

*(Δd') is -0.302 ± 0.13 (**B**, right). **D)** False alarm is increased with the pathway specific inhibition. **E)** Number of misses are not changed with the pathway specific inhibition. Data presented as mean ± SEM for panels (**A, C and D**), Boxplot (**B**, right) show the median, interquartile, and range. Animals n = 2; sampled 400 trials without replacement, 4 independent draws followed by Wilcoxon signed rank test.*

We then implanted an Optotetrode in M1 to validate the effect of the opsin (inhibition effect) and record the neuronal activity during the texture discrimination task. Optotetrode enabled us to record extracellular activity of single unit neurons and inhibited the activity of iChloc expressed pyramidal neurons via illumination (**Fig 30, C**). We performed the pathway specific inhibitions in 2 animals and collected Optotetrode recordings from one animal across 15 days. Inhibition of M1 pyramidal neurons projecting to S1bf decreased the overall performance of the animal (Performance in %; NoLight = 83.14 ± 3.84; Light = 80.20 ± 3.76; mean ± SEM; Wilcoxon signed rank test; p = 0.015) (**Fig 37, A**). d' for the overall performance is significantly lowered by this pathway inhibition (d' performance; NoLight = 2.148 ± 0.33; Light = 1.845 ± 0.29 mean ± SEM; Wilcoxon signed rank test; p = 0.007) (**Fig 37, B**). M1→ S1 pathway inhibition significantly increased the rate of false alarm (FA rate in %; NoLight = 13.49 ± 2.56; Light = 18.36 ± 2.62; mean ± SEM; Wilcoxon signed rank test; p = 0.015) (**Fig 37, C**). Interestingly we did not find any significant difference in the rate of misses with the inhibition (MISS rate in %; NoLight = 19.90 ± 5.05; Light = 20.94 ± 4.86; mean ± SEM; Wilcoxon signed rank test; p = 0.38) (**Fig 37, D**).

13.2.6 INHIBITION OF M1 PYRAMIDAL NEURONS PROJECTING TO S1BF SIGNIFICANTLY MODULATED THE ACTIVITY OF NEURONS DURING TEXTURE PRESENTATION OR LICK PERIOD

M1 pyramidal neurons projecting to S1bf showed interesting characteristics obtained from the spike data recorded with Optotetrode. Single units recorded were very diverse in their response to different textures and differently behaved during distinct time points in the task. Some cells responded only to Go trials and others responded only to NoGo trials. Some cells did not or did respond to both stimuli (**Fig 38, B** (**a, b, c, d**)). This silence of cells to both stimuli may be due to longer distance from the tetrode tips or poor or absence of iChloc expression. The cells

also showed time specific activation. For example, some of the cells were activated during the texture presentation time and others during the response period (Lick or No Lick).

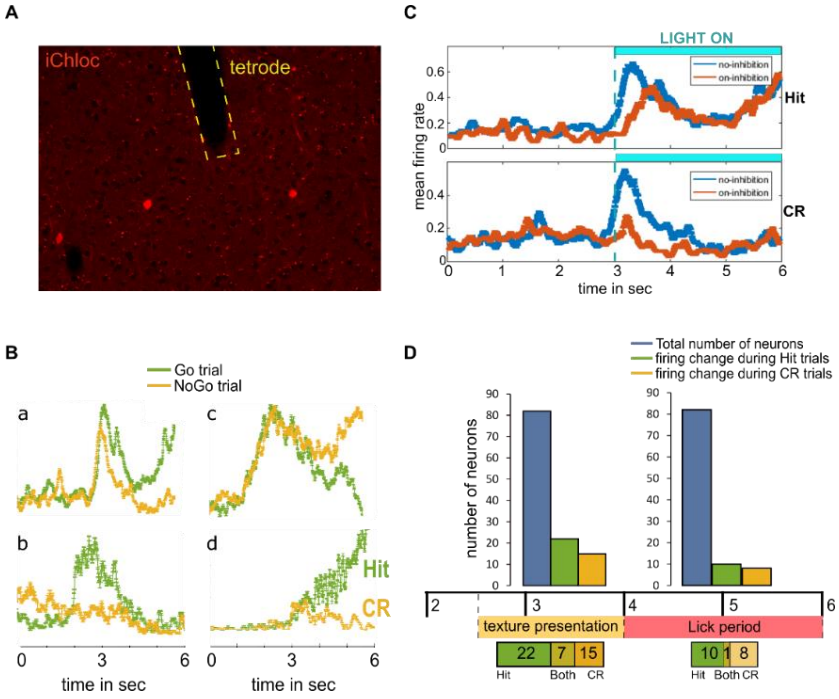

Figure 38. Optotetrode recordings and measurements. ***A)*** *Confocal image showing the fiber tip and the cells (in red) labelled with iChloc.* ***B)*** *Distinct neuronal behaviour during the texture discrimination task without inhibition.* ***(a)*** *a neuron showing similar activation pattern during both Go and NoGo trials.* ***(b)*** *Single unit which is active during texture presentation (2.5 s- 4 s) in Go trials. The same unit shows no activity during this period* ***(c)*** *Another neuron which is positively activated during the texture presentation in both Go and NoGo trials and then shows an increased activation in CR trials during lick period (4 s- 6 s). This neuron shows a decrease in activity just after entering the lick period* ***(d)*** *Example of a single unit showing increased activation in Go trials during lick period. The same neuron showed a diminished activity during CR trials.* ***C)*** *Spiking activity of a single unit to Hit and CR trials before and after the inhibition.* ***D)*** *The graph shows inhibition driven neuronal modulations during Go (hit) and NoGo (CR) trials. A few cells are modulated during texture presentation time and a few other cells are changed their firing during lick period (Wilcoxon rank sum test, $p < 0.05$).*

We obtained single unit responses and their modulations before and after the inhibition trials (**Fig 38, C**). A total of 82 cells were recorded in M1. With the help of Rank sum test, we compared the neuronal activity during Go and NoGo trials with and without inhibition. With

the help of pValues obtained we defined modulation. That is a single unit showing $P < 0.05$ was considered as a modulated neuron. Out of 82 cells recorded, A group of cells (n = 37) were modulated their activity significantly during inhibition across texture presentation period (2.5 s- 4 s). Cells (n = 22) changed their activity during Go trials and 15 cells were modulated during CR trials. 7 cells significantly modulated in both Go and NoGo trials. Another subset of cells (n = 18) showed significant modulation across lick period (4 s- 6 s). 10 cells demonstrated significant difference in their activity during Go trials and 8 cells exhibited modulation during NoGo trials. Only one cell modulated during both Go and NoGo trials in lick period (**Fig 38, D**).

13.2.7 INHIBITION OF M1→ S1-BF PATHWAY HAD NO EFFECT ON WHISKER ANGLE AND THE LICK RATE

Primary motor cortex controls and coordinates different motor activities in the brain. Inhibition of M1 could reduce the whisker movements or the lick rate of the animal. To test this, we analysed the whisker angle from the whisker recordings performed. Inhibition of M1 pyramidal neurons projecting to S1bf increased the FA response of the animal. So, we analysed the lick rate. The lick rate was extracted from the behaviour files recorded during the experiment. Interestingly inhibition did not affect whisker movement or lick rate of the animal. Further comparison showed that the animals did not show any difference in whisker angle or lick across correct (Hit) and incorrect (FA) lick trials (**Fig 39, A, B, C, D**).

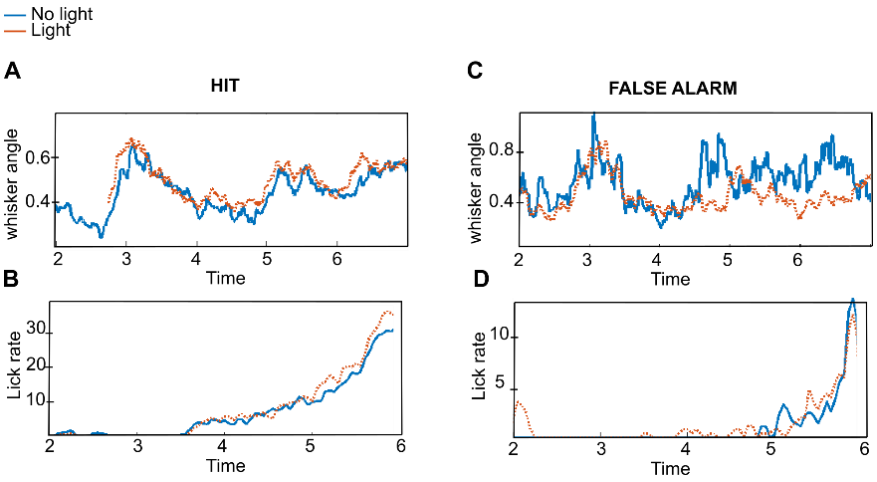

Figure 39. Whisker movement and Lick rate during inhibition. ***A****) Whisker angle during 'Hit' before and after the inhibition.* ***B****) Lick rate of the animal for Hit trials.* ***C****) Whisker envelope during 'False alarm' with and without inhibition.* ***D****) Lick rate during false alarm.*

13.3CONCLUDING REMARKS

Fragile X syndrome is a genetic condition that causes a range of developmental problems. Also, fragile X mental retardation protein regulates pathways and processes governing connectivity. It is important to study the systematic brain wide mapping of neuronal circuits. A combination of the different opsins to excite and inhibit specific neuronal populations and pathways coupled with imaging, physiological and behavioral approaches can give a better understanding of neuronal circuit function under healthy condition and its alteration in diseases. The behavior defects in FXS can be a contribution of perceptual alterations. To tackle such questions, we need to combine neuronal activity, genetic tools and behavior. Functional measurements using 2-photon imaging and GECIs) and manipulative approaches (using optogenetics) can provide genetically and anatomically high-yield circuit level access.

To understand how cellular and circuit level alterations impact on behavioral outcome in *Fmr*1$^{-/y}$ mice, I performed optogenetics in awake WT mice performing a complex sensory-based behavior task. Specifically, the animal must choose two different textures according to the reward and punishment that they receive (Chen, JL et al 2013). During the task, specific pathways projecting to S1 were inhibited. To do this, we used sophisticated viral approaches and validated the inhibition/ excitation effect of various injected opsins using optotetrodes (**Fig, 30- 36**) (Wietek, J et al 2015). We also analyzed multi-neuronal activities. We found that inhibition of local circuits (M1, S1) via enhancement of interneurons not direct inhibition of pyramidal neurons significantly reduced the performance of the mouse in the task. We also found that pathway specific inhibitions (M1→S1) significantly decreased the performance of the animal. We demonstrated that both false alarm rate (FA) and miss rate (Miss) were significantly modified with local inhibitions (via interneuron activation) of M1 or S1. Even though M1→ S1 pathway inhibition reduced the overall performance of the animals, only false

alarm rate is significantly modified. In these animals miss rate remain constant before and after the inhibition (**Fig 37-39**).

We will next investigate performance of *Fmr*1$^{-/y}$ mice in this discrimination paradigm. In parallel to this behavioral task, I will perform anatomical tracing (Haberl et al., 2015) using retrograde viral tracers (injected into S2, M1 or S1), brain clearing and 3D visualization and mapping approaches (Renier et al 2016).

Even though this is a preliminary data, we presume that a combination of the texture discrimination task, optogenetics and 2-photon imaging will help us to identify structural and functional connectivity impairment in *Fmr*1$^{-/y}$ mice.

CHAPTER 6

14 COLLABORATIVE PROJECT

14.1 DYSFUNCTIONAL AUTISM RISK GENES CAUSE CIRCUIT-SPECIFIC CONNECTIVITY DEFICITS WITH DISTINCT DEVELOPMENTAL TRAJECTORIES (PMID: 29901787)

14.2OUTLINE

This chapter includes a collaborative project that I completed during my PhD. In this work, in collaboration with Dr. Valerio Zerbi and Prof. Dr. Nicole Wenderoth (ETH Zurich) I performed neuronal tracing using modified retrograde Rabies virus. Structural connectivity data obtained from this project strengthened the data obtained with MRI showing a functional hypoconnectivity deficits in *Fmr*1$^{-/y}$ mice.

14.3METHODS

14.3.1 RETROGRADE TRACING USING GLYCOPROTEIN-DELETED RABIES VIRUS

14.3.1.1 VIRUS PRODUCTION

SAD ΔG-mCherry (a kind gift from Prof. K-K- Conzlemann, Ludwig-Maximillian University, Munich) pseudotyped with its native glycocoprotein was amplified and purified as described previously by (Haberl et al. 2015).

14.3.1.2 STEREOTAXIC INJECTIONS AND SLICE PREPARATION

Stereotaxic injections were performed in 12-week-old *Fmr1*−/y and wild-type littermate mice using protocols approved by the Ethics Committee of Bordeaux (CE50). Mice were anesthetized with isoflurane (4%) and maintained under isoflurane anesthesia (2%) throughout the procedure. Mice were placed in stereotaxic frame and purified viral particles injected in the right caudate putamen using a 10 µL glass syringe equipped with a 34G beveled needle (Nanofil, World Precision Instruments); coordinates with respect to bregma: -0.88 mm anterior/posterior, +3mm lateral/medial. Injections of 500 nl each were performed at two positions dorsal/ventral: -2.8mm and -3mm (with respect to pia). Injection volume and speed (50 nL/ min) were monitored using an Ultra Micro Pump (World Precision Instruments) as

described in (Haberl et al. 2017). Mice were perfused one week after injection and the brains were sectioned as described by Haberl et al. 2015.

14.3.1.3 FLUORESCENCE MICROSCOPY AND ANALYSIS

Red fluorescent protein (mCherry) expression in neurons in selected fore-brain regions was used to quantify the projection density. We used a scanning mosaic wide-field fluorescence acquisition system (NanoZoomer, Hamamatsu) equipped with a 20× 0.75 numerical aperture objective to acquire the images. Labelled neurons were mapped using the Allen Mouse Brain Atlas (Allen Institute for Brain Science). We used NDP.view2 (Hamamatsu) and manually counted labeled neurons within manually drawn regions of interest.

OXFORD

Cerebral Cortex, July 2018;28: 2495–2506

doi: 10.1093/cercor/bhy046
Advance Access Publication Date: 18 April 2018
Original Article

ORIGINAL ARTICLE

Dysfunctional Autism Risk Genes Cause Circuit-Specific Connectivity Deficits With Distinct Developmental Trajectories

Valerio Zerbi [1], Giovanna D. Ielacqua[2], Marija Markicevic[1], Matthias Georg Haberl[3], Mark H. Ellisman[3,4], Arjun A-Bhaskaran[5,6], Andreas Frick[5,6], Markus Rudin[2,7,8] and Nicole Wenderoth[1,7]

[1]Neural Control of Movement Lab, HEST, ETH Zürich, Winterthurerstrasse 190, 8057 Zurich, Switzerland, [2]Institute for Biomedical Engineering, University and ETH Zurich, Wolfgang-Pauli-Str. 27, 8093 Zurich, Switzerland, [3]National Center for Microscopy and Imaging Research, University of California, San Diego, La Jolla, CA 92093, USA, [4]Department of Neurosciences, University of California, San Diego, La Jolla, CA 92093, USA, [5]INSERM, Neurocentre Magendie, Physiopathologie de la Plasticité Neuronale, U1215, 33077 Bordeaux, France, [6]University of Bordeaux, Neurocentre Magendie, Physiopathologie de la Plasticité Neuronale, 33077 Bordeaux, France, [7]Neuroscience Center Zurich, University and ETH Zurich, Winterthurerstrasse 190, 8057 Zurich, Switzerland and [8]Institute of Pharmacology and Toxicology, University of Zurich, Winterthurerstrasse 190, 8057 Zurich, Switzerland

Address correspondence to Dr Valerio Zerbi, Neural Control of Movement Lab, Department of Health Sciences and Technology, ETH Zurich, Winterthurerstrasse 190, 8057 Zuerich, Switzerland. Email: valerio.zerbi@hest.ethz.ch orcid.org/0000-0001-7984-9565

Abstract

Autism spectrum disorders (ASD) are a set of complex neurodevelopmental disorders for which there is currently no targeted therapeutic approach. It is thought that alterations of genes regulating migration and synapse formation during development affect neural circuit formation and result in aberrant connectivity within distinct circuits that underlie abnormal behaviors. However, it is unknown whether deviant developmental trajectories are circuit-specific for a given autism risk-gene. We used MRI to probe changes in functional and structural connectivity from childhood to adulthood in Fragile-X ($Fmr1^{-/y}$) and contactin-associated ($CNTNAP2^{-/-}$) knockout mice. Young $Fmr1^{-/y}$ mice (30 days postnatal) presented with a robust hypoconnectivity phenotype in corticocortico and corticostriatal circuits in areas associated with sensory information processing, which was maintained until adulthood. Conversely, only small differences in hippocampal and striatal areas were present during early postnatal development in $CNTNAP2^{-/-}$ mice, while major connectivity deficits in prefrontal and limbic pathways developed between adolescence and adulthood. These findings are supported by viral tracing and electron micrograph approaches and define 2 clearly distinct connectivity endophenotypes within the autism spectrum. We conclude that the genetic background of ASD strongly influences which circuits are most affected, the nature of the phenotype, and the developmental time course of the associated changes.

Key words: autism, brain connectivity, CNTNAP2, FMR1, resting-state functional MRI

Introduction

Autism spectrum disorders (ASD) are among the most prevalent neurodevelopmental disorders with no currently available cure. While there are a large number of genetic risk factors associated with ASD (Ronald and Hoekstra 2011), only a few genetic variants are causal, as is the case in the neurodevelopmental syndrome Fragile-X (FXS), which has a higher than expected comorbidity with autism. It is critical to note, however, that variations in ASD risk genes do not directly affect behavior. Rather they affect molecular pathways that influence the development of neurons and synapses that, in turn, affect brain connectivity and function at the system level. Defective synaptic function leading to an excitation–inhibition (E/I) imbalance is commonly invoked as one possible explanation for ASD (Rubenstein and Merzenich 2003), and is supported by evidence in humans and rodents (Yizhar et al. 2011; Hashemi et al. 2017; Selimbeyoglu et al. 2017). According to this theory, E/I imbalance affects molecular mechanisms harnessing neuroplasticity, which is essential for brain development and experience-dependent learning at all ages. Early disruptions of E/I balance have been linked to long-lasting alterations in structural and functional connectivity within specific brain circuits, leading to a variety of clinical symptoms in ASD (Courchesne 2002; Belmonte et al. 2004; Vasa et al. 2016). Indeed, many functional magnetic resonance imaging (fMRI) studies have identified aberrant functional connectivity in individuals with ASD (Alaerts et al. 2014, 2015, 2016; Balsters et al. 2016; Balsters, Apps, et al. 2017; Balsters, Mantini, et al. 2017), even when tested during the resting state. However, the regional patterns of ASD-specific hypoconnectivity or hyperconnectivity vary considerably across studies and patient cohorts, suggesting that connectivity examined at a single developmental stage is only a moderate predictor of the pathology (Kassraian-Fard et al. 2016; Abraham et al. 2017). By contrast, a recent imaging study (Hazlett et al. 2017) in ASD infants suggests that aberrant developmental trajectories within circuits underlying abnormal behaviors might be sensitive markers of the disease. Yet to date, no longitudinal study has been performed that compares the developmental trajectory of brain connectivity between ASD and control subjects. This leaves many fundamental questions unanswered: (1) Which factors drive the pathological trajectory? (2) At which developmental stage does abnormal connectivity manifest itself in subjects with ASD? (3) Are certain brain circuits more susceptible to disrupted neural development than others?

We addressed these questions by measuring resting-state connectivity in 2 well-characterized mouse models exhibiting an Autism phenotype, in which E/I imbalance has been linked with both functional connectivity defects and phenotypical ASD-like behavior in adulthood (Haberl, Zerbi, et al. 2015; Garcia-Pino et al. 2017; Lee et al. 2017; Liska et al. 2017; Selimbeyoglu et al. 2017). Specifically, loss of the Fragile X mental retardation protein leads to excessive excitatory compared with inhibitory inputs in the sensory cortical system (Garcia-Pino et al. 2017), while in CNTNAP2 deficient mice a decreased ratio of GABA to glutamate is seen in the medial prefrontal cortex (Selimbeyoglu et al. 2017), a finding paralleling results in autism patients (Harada et al. 2011).

In order to assess how pathological brain connectivity develops from childhood to adulthood, here we used a longitudinal design starting our measurements immediately after weaning. Specifically, we tested the hypothesis that the genetic background is an important factor determining when delayed or abnormal development of brain circuits become manifest in resting state connectivity measurements. We investigate the developmental trajectory of functional and structural connectivity in Fragile X mental retardation 1 knockout ($Fmr1^{-/y}$) and contactin-associated protein 2 knockout ($CNTNAP2^{-/-}$) mice using MRI techniques (Grandjean et al. 2014; Zerbi et al. 2014, 2015). FMR1 plays a pivotal role in early embryotic neurodevelopment (Hinds et al. 1993) whereas the physiological expression of CNTNAP2 begins at around E14 but peaks during adulthood (P56) (Penagarikano et al. 2011). Because of the divergent expression profile of these 2 genes, we hypothesized that the emergence of circuit deficits would become apparent at different developmental stages: we expected to find strong differences in $Fmr1^{-/y}$ mice compared with wildtype littermates during childhood, whereas $CNTNAP2^{-/-}$ are expected to exhibit connectivity abnormalities at a later age.

Materials and Methods

Mice

All experiments were performed in accordance with the Swiss federal guidelines for the use of animals in research, and under licensing from the Zürich Cantonal veterinary office. Second-generation Fmr1 knockout ($Fmr1^{-/y}$) (Mientjes et al. 2006) and $CNTNAP2^{-/-}$ strains (Jackson laboratory, Maine, USA) were bred at the ETH animal facility (EPIC, Zürich, Switzerland) and kept on C57Bl/6j background for at least 6 generations. Animals were caged in standard housing, with food and water ad libitum, and a 12 h day/night cycle. The experimenter was blind to the genotype for all experiments. Only male Fmr1 mice were used, consistent with previous studies on this mouse model. In addition, the FMR1 gene, which is impaired in the human disorder, is carried on the X-chromosome leading to a strong penetrance of the mutation in males. Due to the random nature of the X-chromosome inactivation, females are mosaic rather than homozygous, which leads to a more subtle manifestation of symptoms (Hagerman and Hagerman 2016).

Magnetic Resonance Imaging

$Fmr1^{-/y}$ and $CNTNAP2^{-/-}$ mice were longitudinally evaluated during early development (juvenile stage: 34 ± 4 days postnatal, young-adult stage: 58 ± 5 days postnatal, adult stage: 112 ± 11 days postnatal). There was no difference in age and bodyweight between groups at each time point. Data acquisition was performed on a Biospec 70/16 small animal MR system (Bruker BioSpin MRI, Ettlingen, Germany) with a cryogenic quadrature surface coil (Bruker BioSpin AG, Fällanden, Switzerland). A standard gradient-echo echo planar imaging sequence (GE-EPI, repetition time TR = 1000 ms, echo time TE = 15 ms, in-plane resolution RES = 0.22 × 0.2 mm^2, number of slice NS = 20, slice thickness ST = 0.4 mm, slice gap SG = 0.1 mm) was applied to acquire 2000 volumes in 38 min. In addition, we acquired anatomical T2-weighted images (FLASH sequence, in-plane resolution of 0.05 × 0.02 mm^2, TE = 3.51, TR = 522 ms) and diffusion weighted images (DWI, multi-shot SE-EPI sequence, 4 segments, TR = 2000 ms, TE = 22 ms, RES = 0.2 × 0.2 mm^2, NS = 28, ST = 0.4 mm, SG = 0 mm, *b*-values = 1000–2000 s/mm^2, 90 directions encoding, for a total scan time of 18 min). The levels of anesthesia and mouse physiological parameters were monitored following an established protocol to obtain a reliable measurement of functional connectivity (Zerbi et al. 2015) (see Supplementary Material for details).

Data Preprocessing and Statistics

Rs-fMRI

Resting state fMRI datasets were preprocessed using an existing pipeline for removal of unwanted confounds from the time series (Zerbi et al. 2015), with modifications (Sethi et al. 2017). After artifact removal (see Supplementary Material) and despiking (Patel et al. 2014), datasets were band-pass filtered (0.01–0.3 Hz), coregistered to the skull-stripped T2-weighted images and normalized to the AMBMC template (www.imaging.org.au/AMBMC) using ANTs v2.1 (picsl.upenn.edu/ANTS).

Diffusion Tensor Parameter Estimation

After individual realignment of the diffusion images, eddy current correction and tensor estimation was performed (for further details, see Zerbi et al. 2013), then fractional anisotropy (FA) and mean diffusivity (MD) maps were calculated (see Supplementary Material). The resulting volumes were spatially normalized to the AMBMC template.

Transmission Electron Microscopy

After careful tissue preparation (see Supplementary Material) areas of interest from the corpus callosum were isolated and mounted onto dummy acrylic blocks with cyanoacrylic adhesive. Ultrathin sections (70 nm thick) were prepared using an ultramicrotome. Electron micrographs were recorded using a FEI Spirit transmission electron microscope operated at 120 kV.

Retrograde Tracing Using Glycoprotein-Deleted Rabies Virus

Virus Production

SAD ΔG-mCherry (a kind gift from Prof. K.-K. Conzlemann, Ludwig-Maximillian University, Munich) pseudotyped with its native glycocoprotein was amplified and purified as described previously by Haberl, Viana da Silva, et al. (2015).

Stereotaxic Injections and Slice Preparation

Sterotaxic injections were performed in 12-week-old Fmr1$^{-/y}$ and wildtype littermate mice using protocols approved by the Ethics Committee of Bordeaux (CE50). Purified viral particles were injected in the right caudate putamen (stereotactic coordinates with respect to Bregma: −0.88 mm anterior/posterior, +3 mm lateral/medial). Injections of 500 nL each were performed at 2 positions dorsal/ventral: −2.8 and −3 mm (with respect to pia). Injection volume and rate of injection (50 nL/min) were monitored using an Ultra Micro Pump (World Precision Instruments) as described in Haberl et al. (2017). Mice were perfused after a week of injection and the brains were sectioned as described by Haberl, Viana da Silva, et al. (2015).

Fluorescence Microscopy and Analysis

Red fluorescent protein (mCherry) expression in neurons at various brain regions were used to quantify the projection density. We used a scanning mosaic wide-field fluorescence acquisition system (NanoZoomer, Hamamatsu) equipped with a 20 × 0.75 numerical aperture objective to acquire the images. Images were arranged using the mouse brain atlas (Allen Brain Atlas). We used NDP.view2 (Hamamatsu) and manually counted 46 467 neurons labeled with the red fluorescent protein and further plotted them into different groups according to the genotype and brain areas.

Results

Using a longitudinal design, we compared 2 knockout mouse strains, Fmr1$^{-/y}$ (n = 13) and CNTNAP2$^{-/-}$ (n = 14) to their own control littermates (Fmr1$^{+/y}$: n = 12, CNTNAP2$^{+/+}$: n = 12), at 3 different stages of postnatal development, p32 (juvenile), p58 (young adult) and p112 (adult). Both males and females CNTNAP2 mice were included in the study, whilst heterozygous mice were excluded. Overall, CNTNAP2 males and females were similarly distributed between subgroups (CNTNAP2$^{-/-}{}_{\text{females}}$ = 5; CNTNAP2$^{+/+}{}_{\text{females}}$ = 5; CNTNAP2$^{-/-}{}_{\text{males}}$ = 9; CNTNAP2$^{+/+}{}_{\text{males}}$ = 7). The differences in bodyweight between males and females at each age-point were not significant (P = 0.524) and both groups showed a significant increase in bodyweight over time (P = 0.001). Gender was considered as a covariate in all of the following statistical analyses.

Development of Functional Connectivity Networks

We first employed a data-driven independent component analysis (ICA) approach across all animals (124 rs-fMRI datasets) and identified 16 meaningful resting-state networks (RSNs), which were named according to the ontological area of their maximum Z-score intensity (Fig. 1). For each of these RSN, we estimated a surrogate measure coupling strength at the voxel level using a dual regression approach (Filippini et al. 2009). We found an overall genotype effect: Fmr1$^{-/y}$ mice differed from their wildtype littermates mainly in lateral striatum and auditory/associative cortical networks. The only differences between CNTNAP2$^{-/-}$ and control littermates were found in small clusters in the ventral striatum and ventral hippocampus (Fig. 2A–C).

Next, we derived an index of coupling strength at the network level by averaging the Z-scores from the group-mean RSN masks (threshold at the 75th percentile, Fig. 1B) to identify interactions between genotype and developmental trajectories. Irrespective of their age, Fmr1$^{y/-}$ mice exhibited reduced network coupling compared with controls (Genotype main effect) in the dorsolateral striatum (P_{FDR} = 0.016) and the auditory/associative network (P_{FDR} = 0.016) throughout postnatal development (Fig. 2B). By contrast, for CNTNAP2$^{-/-}$ mice we observed a significant genotype × age interaction (P_{FDR} = 0.038) in the ventral striatum indicative of a deviation from the developmental trajectory. Pairwise comparisons showed that this effect is driven by an increase in network strength during adulthood in CNTNAP2$^{-/-}$ mice (postnatal day, p112). In line with the results at the voxel level, we observed an overall reduction in ventral hippocampus connectivity strength, although it did not survive FDR correction (P_{FDR} = 0.062) (Fig. 2D).

Development of Functional Connectome

To further probe which specific functional connections showed group differences we used a network-based statistics method (NBS) (Zalesky et al. 2010). Briefly, BOLD time series were extracted using the Allen Reference Atlas ontology (Oh et al. 2014) and their connectivity couplings were measured using regularized Pearson's correlation coefficients (FSLNets). Only macroareas that were fully covered by the field of view used for rs-fMRI acquisition were included in the analysis (isocortex, hippocampal formation, cortical subplate, striatum, pallidum, thalamus, hypothalamus, and midbrain) and consisted of 65 ROIs in each hemisphere. In order to remove spurious connections from the NBS analysis, matrices were given an arbitrary sparsity threshold, retaining only the top-10% of connections

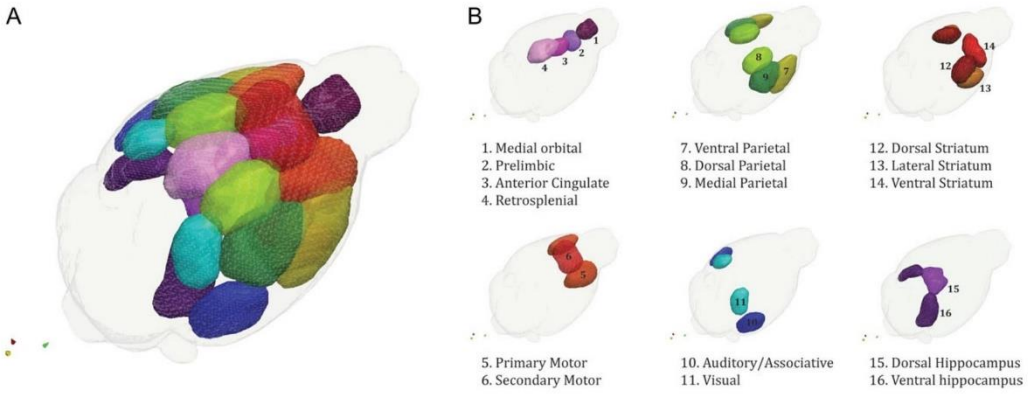

Figure 1. Selected brain networks. From a group-level independent component analysis of all our 124 resting-state fMRI datasets we selected 16 meaningful networks, many of which bear a striking resemblance to analogous human networks underscoring the high translational value of rs-fMRI across different species. Brain networks are overlaid with an anatomical template in a graphical 3D representations (*A*) and split according to their macroscopic ontology (*B*).

(Supplementary Fig. S1). A general linear model was used to model overall genotype differences, and genotype × age interactions. Permutation testing, using unpaired *t*-tests, was performed with 5000 permutations. A test statistic was then computed for each connection and a threshold applied ($t = 2.3$) to produce a set of suprathreshold connections, thereby identifying anatomical networks that show significant differences in structural connectivity between groups.

In $Fmr1^{-/y}$ mice, permutation testing for genotype differences identified one large and symmetric network with reduced coupling strength ($P = 0.033$). This network comprises bilateral sensory-related cortices, caudoputamen (CP), insula, and amygdala. These differences were seen in both juvenile and adult mice, confirming our original hypothesis that in $Fmr1^{-/y}$ mice functional connectivity deficits occur within 30 days of birth (Fig. 3A). To provide a plausible anatomical cause for these functional results, we injected retrograde viral tracer into the CP of $Fmr1^{-/y}$ mice and found that projections from somatosensory cortices, agranular insular, and visceral cortices were reduced by up to ~25% compared with wildtype littermates (Supplementary Fig. S2). These results strongly suggest that in $Fmr1^{-/y}$ mice, the reduced functional connectivity within the somatosensory RSN is directly coupled with a loss of long-range anatomical connections.

In $CNTNAP2^{-/-}$ mice, several genotype × age interactions were found. Specifically, at p112 3 networks showed significantly reduced functional connectivity (Fig. 3B). The first mainly involves connections from the anterior cingulate cortex (ACA) to other prefrontal cortical areas (prelimbic, Infralimbic, and orbitofrontal), retrosplenial cortices and superior colliculus (N1, $P = 0.015$). Interestingly a similar reduction in functional coupling between these regions was also observed by Liska and colleagues in adult $CNTNAP2^{-/-}$ mice, which highlight the strength and reproducibility of rs-fMRI phenotyping to characterize connectivity deficits in this model. Reduced neural projections in the cingulate cortex were also observed (Liska et al. 2017), suggesting a contribution of defective mesoscale axonal wiring to the observed functional impairments.

A reduction of connectivity during adulthood (p112) was also seen in a network comprising the right entorhinal cortex (ENT), temporal association area (TEa), presubiculum (PRE) and perirhinal areas (PERI) (N2, $P = 0.026$), and in several nodes of the ventral hippocampus (N3, $P = 0.026$). All these results were confirmed by mixed-model statistics, using the averaged network strength as a dependent variable. The only overall genotype difference, regardless of age, was driven by increased coupling strength in one symmetric network located in the ventral striatum (N4, $P = 0.001$). This network included bilateral nucleus accumbens (ACB), pallidum (PAL), hypothalamus (HY), thalamus (polymodal association cortex related, DORpm) and fundus of the striatum (FS). Mixed-model analysis of this network revealed an age-dependent effect, with the strongest deviation from the wildtype values seen during adulthood (Fig. 3C).

Development of Structural Connectivity

Structural integrity of major axon bundles was quantified by extracting FA values from 7 major white matter structures identified by the Allen Mouse Brain atlas (Fig. 4). All white matter tracts exhibited a marked increase in FA values with age ($P_{FDR} < 0.01$), which was independent of genotype and possibly reflects increased myelination and coherent alignment of fiber bundles during development (Lebel et al. 2008).

However, similar to previous human and rodent studies (Hashimoto et al. 2011; Haberl, Zerbi, et al. 2015), we found a marked FA reduction in $Fmr1^{-/y}$ mice compared with wildtype at all time points in the anterior commissure ($P_{FDR} < 0.01$), corpus callosum ($P_{FDR} < 0.01$), cingulum ($P_{FDR} = 0.01$) and internal capsule ($P_{FDR} = 0.02$) (Fig. 4B).

$CNTNAP2^{-/-}$ mice deviated from the developmental trajectory of controls during adulthood exhibiting a clear reduction of structural integrity in the cingulum (genotype × age: $P_{FDR} = 0.01$), a white matter tract projecting from the cingulate area to the entorhinal cortex, allowing for communication between components in the limbic system (Fig. 4C). This age-dependent structural abnormality corroborates with the functional connectivity changes observed, thus supporting the idea that both structural and functional deficits in these mice become apparent only later in life, and affect primarily the limbic system. An FA reduction was also observed in the corpus callosum of $CNTNAP2^{-/-}$ mice, but did not survive FDR correction for multiple comparisons ($P = 0.032$, uncorrected).

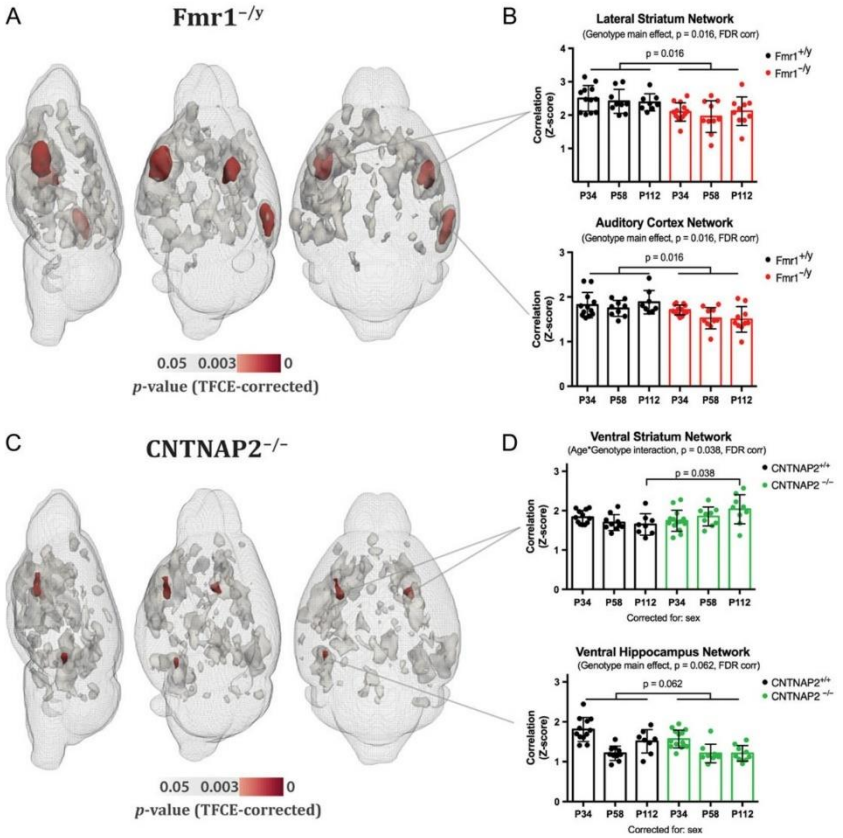

Figure 2. Genotype-dependent differences in resting state network strength. (*A*, *C*) Voxel-wise statistical analyses revealed significant genotype differences in resting-state network strength in both Fmr1$^{-/y}$ and CNTNAP2$^{-/-}$ models (shown in red). Other clusters that represent significant differences in Z-scores but did not survive Bonferroni correction (0.05/16 networks) are shown in gray. (*B*, *D*) Mixed linear models showed significant network strength reduction in lateral striatum and auditory/associative cortex in Fmr1$^{-/y}$ mice (for both networks: $P_{FDR} = 0.016$). A similar reduction was observed in the prelimbic and posterior parietal networks, although it did not reach significance after FDR correction (both networks, $P_{FDR} = 0.087$). In CNTNAP2$^{-/-}$ mice, overall genotype differences were identified in small clusters in the ventral striatum and ventral hippocampus. A genotype × age interaction was found in ventral striatum with a mixed linear model; pairwise analysis revealed an increase of ventral striatal connectivity in CNTNAP2$^{-/-}$ mice compared with littermates only during adulthood ($P_{FDR} = 0.038$). In the ventral hippocampus, the strength of network connectivity was reduced at all time points, although it did not survive FDR correction for multiple comparisons ($P_{FDR} = 0.062$). The genotype × age interaction almost reached significance ($P_{FDR} = 0.053$) in anterior cingulate, one of the main nodes comprising the default-mode network in mice (Sforazzini et al. 2014; Zerbi et al. 2015) and an important region for social cognition (Apps et al. 2016). In this case, however, connectivity was reduced in the CNTNAP2$^{-/-}$ compared with nontransgenic littermates at p112 (not shown). Data represent mean ± std. deviation.

To improve our understanding of the biological underpinnings of white matter abnormalities revealed by diffusion weighted imaging, we determined the ultrastructure of callosal axons from electron micrographs at Bregma −2.46 mm in Fmr1$^{-/y}$ and CNTNAP2$^{-/-}$ and their respective littermates (Fig. 5). We segmented the inner and outer axonal areas and calculated their circular equivalent diameters to determine the axon and myelin thickness. We further calculated the G-ratio (i.e., the ratio between the inner axonal diameter to the total outer axonal diameter), which is a robust measure for assessing degree of axonal myelination. We found significantly reduced G-ratios ($P < 0.001$) in both disease models, Fmr1$^{-/y}$ and CNTNAP2$^{-/-}$ mice, compared to their respective wild-type littermates (Fmr1$^{-/y}$: 0.634 ± 0.005 vs. Fmr1$^{+/y}$: 0.682 ± 0.008 and CNTNAP2$^{-/-}$ 0.607 ± 0.005 vs. CNTNAP2$^{+/+}$ 0.651 ± 0.008). In the CNTNAP2$^{-/-}$ mice this reduction was caused by a reduction in the axonsize (0.372 ± 0.006 in CNTNAP2$^{-/-}$ and 0.460 ± 0.017 in CNTNAP2$^{+/+}$), while the myelin thickness was unaltered (CNTNAP2$^{+/+}$: 0.121 ± 0.044 vs. CNTNAP2$^{-/-}$: 0.120 ± 0.037). In the Fmr1$^{-/y}$ mice the axon diameter was also reduced ($P < 0.001$; 0.3904 ± 0.010 vs. 0.4422 ± 0.013 in Fmr1$^{+/y}$), however, the myelin thickness was slightly elevated in the Fmr1$^{-/y}$ mice (0.112 ± 0.003 vs. 0.1026 ± 0.004 in Fmr1$^{+/y}$), which might in fact further exacerbate the G-ratio decrease seen in the Fmr1$^{-/y}$ mice.

Discussion

Previous research in humans and rodent models has led to the hypothesis that variations in ASD risk genes affect different aspects of the brain's development trajectory, resulting in the establishment of aberrant functional and/or structural long-range

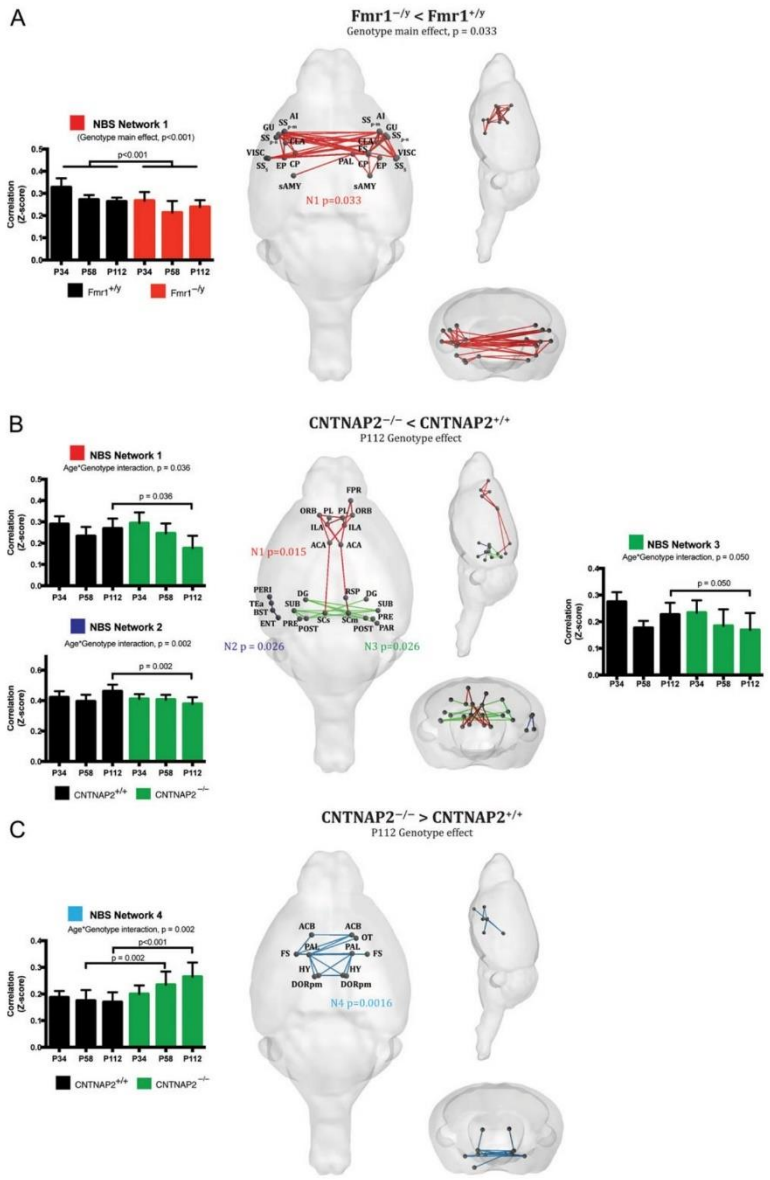

Figure 3. Genotype specific functional connectome analysis. Rs-fMRI connectome analysis combined with network-based statistics (NBS) detected characteristic and distinct pathways of aberrant connectivity in the 2 models. (*A*) $Fmr1^{-/y}$ mice show severe underconnectivity in bilateral corticocortico and corticostriatal circuits responsible for sensory processing, regardless of age. (*B*, *C*) In $CNTNAP2^{-/-}$ mice we detected significant genotype × age interactions in prefrontal-retrosplenial circuits (N1), left associative areas (N2), hippocampus (N3) and ventral striatum-pallidum-hypothalamus (N4). Our analysis shows that under- and overconnectivity profiling are detected only in adult mice, with the exception of the ventral striatum network detected at p58, demonstrating the gradual emergence of circuit-specific pathology over time.

connectivity. Here, we tested this hypothesis by applying longitudinal MRI-based connectivity mapping in 2 knockout mouse models commonly used in ASD research, $Fmr1^{-/y}$ and $CNTNAP2^{-/-}$ mice, during 3 critical developmental periods between childhood and adulthood. We found deviant functional and structural connectivity in both mouse models though the specific developmental and anatomical pattern depended on the genetic background. Remarkably, we found that from 30 days after birth $Fmr1^{-/y}$ mice

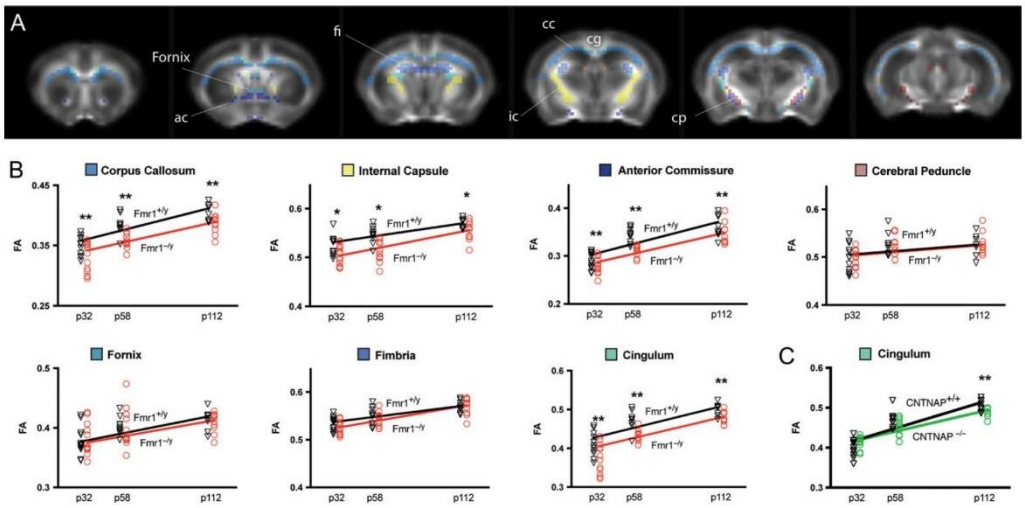

Figure 4. Fractional anisotropy of white matter in Fmr1$^{-/-}$ and CNTNAP2$^{-/-}$ mice. (*A*) Fractional anisotropy (FA) was assessed by diffusion tensor imaging in Fmr1$^{y/-}$ and CNTNAP2$^{-/-}$ mice and quantified in 7 large white matter structures. (*B*) At different developmental periods, Fmr1$^{y/-}$ mice had significantly lower FA in 4 major white-matter structures, including corpus callosum, internal capsule, anterior commissure and cingulum. (*C*) In CNTNAP2$^{-/-}$ an overall reduction of FA was found in the corpus callosum, although it did not survive FDR correction ($P_{FDR} = 0.056$). However, a strong genotype × age interaction was observed in the cingulum, with a marked reduction of FA only during adulthood. $^{*}P_{FDR} < 0.05$. $^{**}P_{FDR} < 0.01$.

exhibited pronounced reduction of functional coupling between sensory-processing areas, indicating that the developmental delay occurred during early childhood. By contrast, CNTNAP2$^{-/-}$ mice developed gradually deviating connectivity patterns in prefrontal and ventral striatal areas between adolescence and adulthood suggesting that related phenotypes became increasingly pronounced later in life. Interestingly, the time point of the aberrant functional and structural connectivity coincides with the expression profile of the knockout genes, suggesting that the timing in which ASD risk-genes are functionally active is critical for the development of aberrant connectivity patterns and possibly behavioral symptoms later in life. The conduction velocity of nerve fibers is influenced by the myelin and axon thickness. Thicker axonal diameters trigger thickening of myelin sheaths and elongation of the internodal segment and therefore lead to an increased internodal conduction velocity of action potentials. We conclude that the overlap of both disease models is a reduced G-ratio and a reduced axon diameter, which could impact the internodal conduction velocity and the overall reliability in signal transmission.

This work supports the growing notion that genetic etiologies may affect different phenotypes and brain circuits (Ellegood et al. 2015; Connor et al. 2016; Huang et al. 2016; Wang et al. 2016). In addition, we emphasize that measuring the developmental trajectory of functional connectivity deficits in ASD models is useful to understand the factors driving the pathology progress and may be crucial when planning a treatment approach.

Functional and Structural Changes in Fmr1 Knockout are Anatomically Located in Brain Areas Processing Sensory Information and are Detectable at a Young Age

Fragile X syndrome (FXS) is the most common syndromic form of ASD, with an estimated 25–50% of children diagnosed with FXS meeting the criteria for ASD (Klusek et al. 2014). Although FXS represents only a small fraction (~2%) of ASD patients, work on FXS has been particularly beneficial for improving our understanding of ASD. Indeed, FXS and ASD are intertwined at the molecular level (Parikshak et al. 2013), suggesting that several common pathways and cellular mechanisms are shared amongst these 2 disorders. Abnormal methylation of the fragile X mental retardation 1 (FMR1) gene observed in FXS patients leads to a complete or partial absence of fragile-X mental retardation protein (FMRP) (Pieretti et al. 1991). FMRP is highly expressed in the brain and acts as translational repressor of several signaling pathways at the synaptic level (Willemsen et al. 2011). Specifically, FMRP is required for the normal developmental progression of synaptic maturation, and loss of this important RNA binding protein impacts on synaptic plasticity in late embryonic stages and during the first postnatal days (Harlow et al. 2010). Behavioral symptoms include tactile defensiveness, sensory avoidance, and enhanced responses to stimuli of various sensory modalities (Rotschafer and Razak 2014). Symptom severity was found to correlate both with FMR1 activity and FMRP levels (Tassone et al. 1999; Dyer-Friedman et al. 2002; Loesch et al. 2004). As such, hypersensitivity to sensory stimuli—one of the most prominent features of FXS and ASD patients (Baron-Cohen et al. 2009; Gallagher and Hallahan 2012)—has been also described in Fmr1$^{-/y}$ mice (Rotschafer and Razak 2013; Zhang et al. 2014). This defect has been recently attributed to reduced and dysfunctional dendritic ion channels (Zhang et al. 2014), which alters the excitation/inhibition ratio in areas processing sensory information and affects neural plasticity in early postnatal developmental periods (Gibson et al. 2008; Goncalves et al. 2013). Compatible with an earlier study on functional connectivity in Fmr1$^{-/y}$ mice (Haberl, Zerbi, et al. 2015), our data show that the absence of FMRP translates into a hypoconnectivity phenotype at the network level. Thanks to our novel whole-brain data-driven approach, we found this effect specifically for brain networks and pathways associated with sensorial processing and perception (i.e., somatosensory–striatal connections) with strong analogies to symptoms

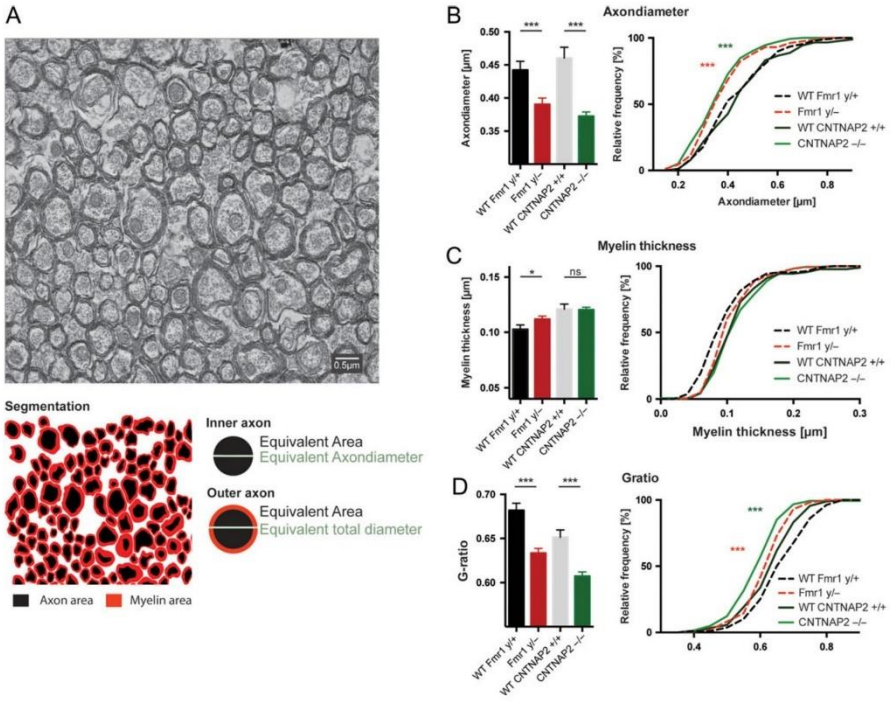

Figure 5. Electron micrograph. (*A*) Electron micrograph of axons in the corpus callosum. (*B*) Both, the Fmr1$^{-/y}$ and the CNTNAP2$^{-/-}$ animals have a smaller axon diameter compared with their respective wildtype littermates; the axon diameter distribution confirmed a shift towards smaller axon sizes (KS test). (*C*) Only minor changes were seen in myelin thickness between the groups, with the Fmr1$^{-/y}$ showing a slight increase compared with their wildtype littermates; however, there were no differences in their cumulative distribution. (*D*) Both, the Fmr1$^{-/y}$ and the CNTNAP2$^{-/-}$ animals show significant lower G-ratio, calculated as the ratio of the outer to inner equivalent axonal diameters and differ significantly in their distribution (KS test). with a shift towards axons with lower G-ratios. Data represent mean ± standard error.

typical for human FXS patients (Hall et al. 2013; Wilson 2014; Reig and Silberberg 2016). These findings were robust and consistent from 30 days after birth until adulthood, and were observed in both network-based and region-of-interest analyses. Reduction of functional connectivity was paralleled by structural deficits, with DWI revealing severe fiber coherence reductions in corticocortico and corticostriatal pathways. Our finding of lower FA values, which are also often observed in FXS patients (Grigsby 2016), reflect a reduction in axial diffusivity. Further, with electron microscopy we were able to show that the reduction in axial diffusivity was related to a reduction in the inner diameter of the axons, unveiling the microstructural basis for the aberrant functional connectivity patterns.

CNTNAP2 Knockout Mice Display Dysregulation of Connectivity in Prefrontal Cortical Areas

CNTNAP2 is a member of the Neurexin superfamily of transmembrane molecules and affects neuron-glia interactions, thus modulating brain connectivity during early brain maturation. In this neurodevelopmental phase, Caspr2, the protein encoded by *CNTNAP2*, is thought to assist in interactions important for cellular migration and subsequent laminar organization, indicating a role for *CNTNAP2* in the construction of neural circuits (Strauss et al. 2006). *CNTNAP2* has been identified as an ASD risk gene affecting primarily frontal lobe connectivity (Arking et al. 2008; Scott-Van Zeeland et al. 2010). *CNTNAP2*-KO mice have a reduced number of GABAergic interneurons and impaired migration of cortical projection neurons, which likely cause a higher incidence of seizures and abnormal behaviors such as impaired social interactions and elevated repetitive self-grooming (Penagarikano et al. 2011). In line with these previous observations and a recent functional study (Liska et al. 2017), we report here that the absence of the CNTNAP2 gene is associated with an underconnectivity profile in hippocampal and cortical prefrontal areas linked to reward-guided behavior (Rushworth et al. 2011; Neubert et al. 2015), which match earlier reports in subjects with the CNTNAP2 polymorphism (Scott-Van Zeeland et al. 2010; Dennis et al. 2011). In our connectome analysis, we found that the strongest age-dependent reduction in functional connectivity occurred between nodes that are part of the rodent default-mode network (DMN) (i.e., orbitofrontal, anterior cingulate, and retrosplenial cortices) (Lu et al. 2012; Zerbi et al. 2015; Gozzi and Schwarz 2016). Deactivation of the brain's DMN is often regarded as suppression of endogenous activity to support exogenous task-related processes (Hu et al. 2013). At the same time, reduced activation of the DMN during rest has been associated with a series of pathological conditions, including ASD. Interestingly, in children with ASD, internodal DMN functional connectivity failed to develop during

adolescence (11–13 years) but not during childhood (6–9 years) (Washington et al. 2014). In line with these observations, our results indicate that the connectivity deficits in CNTNAP2$^{-/-}$ mice within the DMN occur as a result of a lack of developmental strengthening of connectivity within this network during adolescence. These findings support the "developmental disconnection model" of the DMN in ASD, which could be related to the reduced number of GABAergic interneurons in these same regions (Scott-Van Zeeland et al. 2010) However, despite sharing some common structural/functional properties (Stafford et al. 2014), there is still no general agreement upon the functional role of this network as a real homologue to the human DMN. Therefore, the translational aspect of these results in the human condition should be taken carefully.

In CNTNAP2$^{-/-}$ mice, we also observed an increase functional coupling between several nodes of the ventral striatum. The ventral striatum is a complex structure that receives and integrates projections from several midbrain regions and across different neurotransmitter systems, including dopamine from ventral tegmental area and substantia nigra, oxytocin from the periventricular nucleus of hypothalamus and noradrenaline from locus coeruleus. In humans, increase functional connectivity between nodes of the ventral striatum has been reported in addiction, anxiety, lack of social motivation, and even obsessive-compulsive disorder (OCD) (Harrison et al. 2009; Sakai et al. 2011; Caldwell 2012). Both OCD and addiction have been related to nucleus accumbens dysfunction during reward processing (Figee et al. 2011; Hommer et al. 2011). Recent studies using optogenetic stimulation found that also frontal cortical areas play a key role in top-down modulation of striatal response to dopaminergic stimuli (Ferenczi et al. 2016). Thus, while activation of the prefrontal cortex and ventral striatum is related to healthy reward processing (Knutson et al. 2001), the disrupted prefrontal coupling and increased connectivity between ventral striatum/pallidum areas found in adult CNTNAP2$^{-/-}$ mice may reflect a shift from healthy goal-directed behavior towards compulsive habits. Although our experiment cannot prove a direct cause–effect relationship, we have shown a time-dependent relationship between the altered connectivity in prefrontal and ventral striatal networks that may be related to the imbalanced excitation/inhibition in mPFC of CNTNAP2$^{-/-}$ mice (Selimbeyoglu et al. 2017).

Notably, we found that deficits in these specific brain circuits gradually emerge during postnatal development and are observable only during adulthood. This age-dependent effect was also found in our structural data, in which a reduction of fiber coherence in the cingulum was observed in adult CNTNAP2 mice compared with wildtype littermates. Anatomically, this single observation is particularly interesting, as it strengthens the idea that structural and functional deficits in these mice primarily affect the limbic system. Furthermore, in CNTNAP2$^{-/-}$ mice we found a reduction in the axonal inner diameter in the corpus callosum, suggesting the presence of an underlying white-matter pathology. Taken together, these data strongly indicate a role for CNTNAP2 in shaping connectivity, particularly between areas of the limbic system, which may have important implications for the appearance of ASD-like behavioral features later in life (Penagarikano and Geschwind 2012).

Interpretational Issues

Measuring brain structural and functional connectivity in mice has high translational value, but both conceptual and methodological interpretational issues may arise when generalizing these findings to the human condition. At the conceptual level, it is unclear how the functional architecture of the mouse brain relates to functional circuits of the human brain. However, in recent years a number of studies have emerged demonstrating rodent–human analogies for basic structural and functional properties in networks of high translational importance, such as the default-mode network (Stafford et al. 2014) and striatocortical circuits (Balleine and O'Doherty 2010). While more work needs to be done in this direction, it is envisaged that connectivity measurements may serve the role of an important bridging measurement between human and rodent models, enabling predictions about how specific genetic and molecular alterations observed in mice might be expressed in macroscopic measurements that can be performed in humans (Stafford et al. 2014).

At the methodological level, it is important to consider that our results were collected in a lightly anesthetized state. As previously demonstrated in rats (Bettinardi et al. 2015) and monkeys (Barttfeld et al. 2015), modulating the depth of anesthesia correlates with changes in BOLD variability and reduces the overall connectivity strength. Thus, data acquired with any level of anesthesia cannot be fully generalized to the awake state, although it may have the positive effect of removing confounding BOLD fluctuation due to the environment or unconstrained cognitive shifts while awake. In this study, we took several measures to ensure that the levels of anesthesia were kept as consistent and low as possible, that is, we used mechanical ventilation to maintain the same tidal volume and blood oxygenation throughout the experiment, combined with continuous intravenous infusion of medetomidine and low dose of isoflurane (0.5%), optimized from our previous studies (Grandjean et al. 2014). This allowed us to overcome issues related to high-dose medetomidine (Akeju et al. 2014) and isoflurane accumulation over time (Chuang and Nasrallah 2017). With this protocol, we previously demonstrated that bilateral brain networks are readily detected as compared with other anesthesia protocols (Grandjean et al. 2014) and resemble the anatomical connectome obtained with viral tracer data, up to 90% for corticocortico and corticostriatal circuits (Grandjean et al. 2017). The light-anesthesia regime also minimizes the possibility that the mapped changes are the results of different brain states reflecting genotype-dependent sensitivity to anesthesia, as it was previously suggested for Fmr1$^{-/y}$ mice (Goncalves et al. 2013). Importantly, our results show functional connectivity defects in both Fmr1$^{-/y}$ and CNTNAP2$^{-/-}$ mice that are circuit-specific. A higher or lower sensitivity to the anesthesia in one group would have instead resulted in an increased or reduced connectivity in all the identified networks or pathways. Furthermore, our results are consistent with 2 other independent studies, which used different anesthesia setups (isoflurane-only and urethane). Because these agents act on different neurotransmitter systems (Hara and Harris 2002; Chuang and Nasrallah 2017) it is unlikely that common genotype × anesthesia effects would fully explain the findings of both studies. Finally, we present evidence that functional deficits are paired with structural deficits in the same anatomical locations, either by viral tracer, EM, or diffusion data.

It is important to mention that all between-groups comparisons were performed between matched strain-, age-, gender-, and bodyweight conditions; this experimental design is of critical importance to avoid confounding systematic variations in rs-fMRI parameters. Given that the physiological (and statistically significant) increase in bodyweight over time may systematically confound the anesthesia dosage, here we took a conservative position when interpreting effects arising from changes of rs-fMRI parameters as a function of age.

Conclusions

MRI-based connectivity mapping has become the method of choice for investigating hyperconnected and hypoconnected pathways at the systems level and across the whole brain. Applied to a suitable disease model system such as the mouse, it turns into a powerful translational tool to study gene-to-neural circuits interactions while minimizing the influence of environmental heterogeneity. In this study, we investigated developmental changes in 2 animal models for ASD. We demonstrated that mutations in ASD risk genes, which are known to alter cell and synaptic functioning, cause aberrant structural and functional connectivity within specific circuits. We also show that deviations from the normal developmental trajectory might be powerful markers of ASD, though the genetic background determines at which time point such deviations manifest themselves. Interestingly, these time points appear to correspond to the temporal expression profile of proteins encoded by the affected gene. The anatomical specificity of our measurements allowed for the detection of robust group-level brain connectivity profiles that can act as "fingerprints" to accurately identify the genetic contribution to the connectome shape and strength, and opens new perspectives for using this technique as a translational tool between animal models and humans. In summary, our results provide important evidence that measuring developmental changes in the functional and structural brain architecture using neuroimaging might reveal disease markers of clinical utility.

Supplementary Material

Supplementary material is available at *Cerebral Cortex* online.

Funding

ETH Career Seed Grant (SEED-42 16-1) to V.Z. Erasmus Mundus/ENC-Network to A.A.B.

Notes

Fmr1 knockout ($Fmr1^{-/y}$) breeders were generously donated by the laboratory of Prof. David L. Nelson, Baylor College of Medicine (Houston, TX, USA). We thank Dr. M. Ginger for production of purified RABV ΔG mcherry, Prof. K.-K. Conzelmann and Dr A. Ghanem for the RABV ΔG mcherry starter stock and Dr K. Le Corf for assistance with the stereotaxic injections. Some data were acquired using Bordeaux Imaging Center equipment, a service unit of the CNRS-INSERM and Bordeaux University. The authors thank the animal- and genotyping facilities of the Neurocentre Magendie (supported by INSERM and LabEX-BRAIN ANR-10-LABX-43) and Dr Jonathan Ward of the ETH Phenomic Center Zurich (EPIC). Finally, we thank Dr Daniel Woolley for proofreading the article and Daniele Tolomeo for assistance during scanning. *Conflict of Interest*: The authors have no conflict of interest to declare.

References

Abraham A, Milham MP, Di Martino A, Craddock RC, Samaras D, Thirion B, Varoquaux G. 2017. Deriving reproducible biomarkers from multi-site resting-state data: an autism-based example. Neuroimage. 147:736–745.

Akeju O, Loggia ML, Catana C, Pavone KJ, Vazquez R, Rhee J, Contreras Ramirez V, Chonde DB, Izquierdo-Garcia D, Arabasz G, et al. 2014. Disruption of thalamic functional connectivity is a neural correlate of dexmedetomidine-induced unconsciousness. Elife. 3:e04499.

Alaerts K, Geerlings F, Herremans L, Swinnen SP, Verhoeven J, Sunaert S, Wenderoth N. 2015. Functional organization of the action observation network in autism: a graph theory approach. PLoS One. 10:e0137020.

Alaerts K, Swinnen SP, Wenderoth N. 2016. Sex differences in autism: a resting-state fMRI investigation of functional brain connectivity in males and females. Soc Cogn Affect Neurosci. 11:1002–1016.

Alaerts K, Woolley DG, Steyaert J, Di Martino A, Swinnen SP, Wenderoth N. 2014. Underconnectivity of the superior temporal sulcus predicts emotion recognition deficits in autism. Soc Cogn Affect Neurosci. 9:1589–1600.

Apps MA, Rushworth MF, Chang SW. 2016. The anterior cingulate gyrus and social cognition: tracking the motivation of others. Neuron. 90:692–707.

Arking DE, Cutler DJ, Brune CW, Teslovich TM, West K, Ikeda M, Rea A, Guy M, Lin S, Cook EH, et al. 2008. A common genetic variant in the neurexin superfamily member CNTNAP2 increases familial risk of autism. Am J Hum Genet. 82:160–164.

Balleine BW, O'Doherty JP. 2010. Human and rodent homologies in action control: corticostriatal determinants of goal-directed and habitual action. Neuropsychopharmacology. 35:48–69.

Balsters JH, Apps MA, Bolis D, Lehner R, Gallagher L, Wenderoth N. 2017. Disrupted prediction errors index social deficits in autism spectrum disorder. Brain. 140:235–246.

Balsters JH, Mantini D, Apps MA, Eickhoff SB, Wenderoth N. 2016. Connectivity-based parcellation increases network detection sensitivity in resting state fMRI: an investigation into the cingulate cortex in autism. Neuroimage Clin. 11:494–507.

Balsters JH, Mantini D, Wenderoth N. 2017. Connectivity-based parcellation reveals distinct cortico-striatal connectivity fingerprints in Autism Spectrum Disorder. Neuroimage. pii: S1053-8119(17)30123-4 [Epub ahead of print].

Baron-Cohen S, Ashwin E, Ashwin C, Tavassoli T, Chakrabarti B. 2009. Talent in autism: hyper-systemizing, hyper-attention to detail and sensory hypersensitivity. Philos Trans R Soc Lond B Biol Sci. 364:1377–1383.

Barttfeld P, Uhrig L, Sitt JD, Sigman M, Jarraya B, Dehaene S. 2015. Signature of consciousness in the dynamics of resting-state brain activity. Proc Natl Acad Sci USA. 112:887–892.

Belmonte MK, Allen G, Beckel-Mitchener A, Boulanger LM, Carper RA, Webb SJ. 2004. Autism and abnormal development of brain connectivity. J Neuroscience. 24:9228–9231.

Bettinardi RG, Tort-Colet N, Ruiz-Mejias M, Sanchez-Vives MV, Deco G. 2015. Gradual emergence of spontaneous correlated brain activity during fading of general anesthesia in rats: evidences from fMRI and local field potentials. Neuroimage. 114:185–198.

Caldwell HK. 2012. Neurobiology of sociability. Adv Exp Med Biol. 739:187–205.

Chuang KH, Nasrallah FA. 2017. Functional networks and network perturbations in rodents. Neuroimage. 163:419–436.

Connor SA, Ammendrup-Johnsen I, Chan AW, Kishimoto Y, Murayama C, Kurihara N, Tada A, Ge Y, Lu H, Yan R, et al. 2016. Altered cortical dynamics and cognitive function upon haploinsufficiency of the autism-linked excitatory synaptic suppressor MDGA2. Neuron. 91:1052–1068.

Courchesne E. 2002. Abnormal early brain development in autism. Mol Psychiatry. 7(Suppl 2):S21–S23.

Dennis EL, Jahanshad N, Rudie JD, Brown JA, Johnson K, McMahon KL, de Zubicaray GI, Montgomery G, Martin NG, Wright MJ, et al. 2011. Altered structural brain connectivity

in healthy carriers of the autism risk gene, CNTNAP2. Brain Connect. 1:447–459.
Dyer-Friedman J, Glaser B, Hessl D, Johnston C, Huffman LC, Taylor A, Wisbeck J, Reiss AL. 2002. Genetic and environmental influences on the cognitive outcomes of children with fragile X syndrome. J Am Acad Child Adolesc Psychiatry. 41:237–244.
Ellegood J, Anagnostou E, Babineau BA, Crawley JN, Lin L, Genestine M, DiCicco-Bloom E, Lai JK, Foster JA, Penagarikano O, et al. 2015. Clustering autism: using neuroanatomical differences in 26 mouse models to gain insight into the heterogeneity. Mol Psychiatry. 20:118–125.
Ferenczi EA, Zalocusky KA, Liston C, Grosenick L, Warden MR, Amatya D, Katovich K, Mehta H, Patenaude B, Ramakrishnan C, et al. 2016. Prefrontal cortical regulation of brainwide circuit dynamics and reward-related behavior. Science. 351:aac9698.
Figee M, Vink M, de Geus F, Vulink N, Veltman DJ, Westenberg H, Denys D. 2011. Dysfunctional reward circuitry in obsessive-compulsive disorder. Biol Psychiatry. 69:867–874.
Filippini N, MacIntosh BJ, Hough MG, Goodwin GM, Frisoni GB, Smith SM, Matthews PM, Beckmann CF, Mackay CE. 2009. Distinct patterns of brain activity in young carriers of the APOE-epsilon4 allele. Proc Natl Acad Sci USA. 106:7209–7214.
Gallagher A, Hallahan B. 2012. Fragile X-associated disorders: a clinical overview. J Neurol. 259:401–413.
Garcia-Pino E, Gessele N, Koch U. 2017. Enhanced excitatory connectivity and disturbed sound processing in the auditory brainstem of fragile X mice. J Neurosci. 37:7403–7419.
Gibson JR, Bartley AF, Hays SA, Huber KM. 2008. Imbalance of neocortical excitation and inhibition and altered UP states reflect network hyperexcitability in the mouse model of fragile X syndrome. J Neurophysiol. 100:2615–2626.
Goncalves JT, Anstey JE, Golshani P, Portera-Cailliau C. 2013. Circuit level defects in the developing neocortex of fragile X mice. Nat Neurosci. 16:903–909.
Gozzi A, Schwarz AJ. 2016. Large-scale functional connectivity networks in the rodent brain. Neuroimage. 127:496–509.
Grandjean J, Schroeter A, Batata I, Rudin M. 2014. Optimization of anesthesia protocol for resting-state fMRI in mice based on differential effects of anesthetics on functional connectivity patterns. Neuroimage. 102(Pt 2):838–847.
Grandjean J, Zerbi V, Balsters JH, Wenderoth N, Rudin M. 2017. Structural basis of large-scale functional connectivity in the mouse. J Neurosci. 37:8092–8101.
Grigsby J. 2016. The fragile X mental retardation 1 gene (FMR1): historical perspective, phenotypes, mechanism, pathology, and epidemiology. Clin Neuropsychol. 30:815–833.
Haberl MG, Ginger M, Frick A. 2017. Dual anterograde and retrograde viral tracing of reciprocal connectivity. Methods Mol Biol. 1538:321–340.
Haberl MG, Viana da Silva S, Guest JM, Ginger M, Ghanem A, Mulle C, Oberlaender M, Conzelmann KK, Frick A. 2015. An anterograde rabies virus vector for high-resolution large-scale reconstruction of 3D neuron morphology. Brain Struct Funct. 220:1369–1379.
Haberl MG, Zerbi V, Veltien A, Ginger M, Heerschap A, Frick A. 2015. Structural-functional connectivity deficits of neocortical circuits in the Fmr1 (–/y) mouse model of autism. Sci Adv. 1: e1500775.
Hagerman RJ, Hagerman P. 2016. Fragile X-associated tremor/ataxia syndrome—features, mechanisms and management. Nat Rev Neurol. 12:403–412.
Hall SS, Jiang H, Reiss AL, Greicius MD. 2013. Identifying large-scale brain networks in fragile X syndrome. JAMA Psychiatry. 70:1215–1223.
Hara K, Harris RA. 2002. The anesthetic mechanism of urethane: the effects on neurotransmitter-gated ion channels. Anesth Analg. 94:313–318. , table of contents.
Harada M, Taki MM, Nose A, Kubo H, Mori K, Nishitani H, Matsuda T. 2011. Non-invasive evaluation of the GABAergic/glutamatergic system in autistic patients observed by MEGA-editing proton MR spectroscopy using a clinical 3 tesla instrument. J Autism Dev Disord. 41:447–454.
Harlow EG, Till SM, Russell TA, Wijetunge LS, Kind P, Contractor A. 2010. Critical period plasticity is disrupted in the barrel cortex of FMR1 knockout mice. Neuron. 65:385–398.
Harrison BJ, Soriano-Mas C, Pujol J, Ortiz H, Lopez-Sola M, Hernandez-Ribas R, Deus J, Alonso P, Yucel M, Pantelis C, et al. 2009. Altered corticostriatal functional connectivity in obsessive-compulsive disorder. Arch Gen Psychiatry. 66:1189–1200.
Hashemi E, Ariza J, Rogers H, Noctor SC, Martinez-Cerdeno V. 2017. The number of parvalbumin-expressing interneurons is decreased in the medial prefrontal cortex in autism. Cereb Cortex. 27:1931–1943.
Hashimoto R, Srivastava S, Tassone F, Hagerman RJ, Rivera SM. 2011. Diffusion tensor imaging in male premutation carriers of the fragile X mental retardation gene. Mov Disord. 26: 1329–1336.
Hazlett HC, Gu H, Munsell BC, Kim SH, Styner M, Wolff JJ, Elison JT, Swanson MR, Zhu H, Botteron KN, et al, IBIS Network; Clinical Sites; Data Coordinating Center; Image Processing Core; Statistical Analysis. 2017. Early brain development in infants at high risk for autism spectrum disorder. Nature. 542:348–351.
Hinds HL, Ashley CT, Sutcliffe JS, Nelson DL, Warren ST, Housman DE, Schalling M. 1993. Tissue specific expression of FMR-1 provides evidence for a functional role in fragile X syndrome. Nat Genet. 3:36–43.
Hommer DW, Bjork JM, Gilman JM. 2011. Imaging brain response to reward in addictive disorders. Ann NY Acad Sci. 1216:50–61.
Hu Y, Chen X, Gu H, Yang Y. 2013. Resting-state glutamate and GABA concentrations predict task-induced deactivation in the default mode network. J Neurosci. 33:18566–18573.
Huang WC, Chen Y, Page DT. 2016. Hyperconnectivity of prefrontal cortex to amygdala projections in a mouse model of macrocephaly/autism syndrome. Nat Commun. 7:13421.
Kassraian-Fard P, Matthis C, Balsters JH, Maathuis MH, Wenderoth N. 2016. Promises, pitfalls, and basic guidelines for applying machine learning classifiers to psychiatric imaging data, with autism as an example. Front Psychiatry. 7:177.
Klusek J, Martin GE, Losh M. 2014. Consistency between research and clinical diagnoses of autism among boys and girls with fragile X syndrome. J Intellect Disabil Res. 58:940–952.
Knutson B, Fong GW, Adams CM, Varner JL, Hommer D. 2001. Dissociation of reward anticipation and outcome with event-related fMRI. Neuroreport. 12(17):3683–3687.
Lebel C, Walker L, Leemans A, Phillips L, Beaulieu C. 2008. Microstructural maturation of the human brain from childhood to adulthood. Neuroimage. 40:1044–1055.
Lee E, Lee J, Kim E. 2017. Excitation/inhibition imbalance in animal models of autism spectrum disorders. Biol Psychiatry. 81:838–847.
Liska A, Bertero A, Gomolka R, Sabbioni M, Galbusera A, Barsotti N, Panzeri S, Scattoni ML, Pasqualetti M, Gozzi A. 2017. Homozygous loss of autism-risk gene CNTNAP2 results in reduced local and long-range prefrontal functional connectivity. Cereb Cortex. doi: 10.1093/cercor/bhx022. [Epub ahead of print].
Loesch DZ, Huggins RM, Hagerman RJ. 2004. Phenotypic variation and FMRP levels in fragile X. Ment Retard Dev Disabil Res Rev. 10:31–41.

Lu H, Zou Q, Gu H, Raichle ME, Stein EA, Yang Y. 2012. Rat brains also have a default mode network. Proc Natl Acad Sci USA. 109:3979–3984.

Mientjes EJ, Nieuwenhuizen I, Kirkpatrick L, Zu T, Hoogeveen-Westerveld M, Severijnen L, Rife M, Willemsen R, Nelson DL, Oostra BA. 2006. The generation of a conditional Fmr1 knock out mouse model to study Fmrp function in vivo. Neurobiol Dis. 21:549–555.

Neubert FX, Mars RB, Sallet J, Rushworth MF. 2015. Connectivity reveals relationship of brain areas for reward-guided learning and decision making in human and monkey frontal cortex. Proc Natl Acad Sci USA. 112:E2695–E2704.

Oh SW, Harris JA, Ng L, Winslow B, Cain N, Mihalas S, Wang Q, Lau C, Kuan L, Henry AM, et al. 2014. A mesoscale connectome of the mouse brain. Nature. 508:207–214.

Parikshak NN, Luo R, Zhang A, Won H, Lowe JK, Chandran V, Horvath S, Geschwind DH. 2013. Integrative functional genomic analyses implicate specific molecular pathways and circuits in autism. Cell. 155:1008–1021.

Patel AX, Kundu P, Rubinov M, Jones PS, Vertes PE, Ersche KD, Suckling J, Bullmore ET. 2014. A wavelet method for modeling and despiking motion artifacts from resting-state fMRI time series. Neuroimage. 95:287–304.

Penagarikano O, Abrahams BS, Herman EI, Winden KD, Gdalyahu A, Dong H, Sonnenblick LI, Gruver R, Almajano J, Bragin A, et al. 2011. Absence of CNTNAP2 leads to epilepsy, neuronal migration abnormalities, and core autism-related deficits. Cell. 147:235–246.

Penagarikano O, Geschwind DH. 2012. What does CNTNAP2 reveal about autism spectrum disorder? Trends Mol Med. 18:156–163.

Pieretti M, Zhang FP, Fu YH, Warren ST, Oostra BA, Caskey CT, Nelson DL. 1991. Absence of expression of the FMR-1 gene in fragile X syndrome. Cell. 66:817–822.

Reig R, Silberberg G. 2016. Distinct corticostriatal and intracortical pathways mediate bilateral sensory responses in the striatum. Cereb Cortex. 26:4405–4415.

Ronald A, Hoekstra RA. 2011. Autism spectrum disorders and autistic traits: a decade of new twin studies. Am J Med Genet B Neuropsychiatr Genet. 156B:255–274.

Rotschafer S, Razak K. 2013. Altered auditory processing in a mouse model of fragile X syndrome. Brain Res. 1506: 12–24.

Rotschafer SE, Razak KA. 2014. Auditory processing in fragile x syndrome. Front Cell Neurosci. 8:19.

Rubenstein JL, Merzenich MM. 2003. Model of autism: increased ratio of excitation/inhibition in key neural systems. Genes, Brain Behav. 2:255–267.

Rushworth MF, Noonan MP, Boorman ED, Walton ME, Behrens TE. 2011. Frontal cortex and reward-guided learning and decision-making. Neuron. 70:1054–1069.

Sakai Y, Narumoto J, Nishida S, Nakamae T, Yamada K, Nishimura T, Fukui K. 2011. Corticostriatal functional connectivity in non-medicated patients with obsessive-compulsive disorder. Eur Psychiatry. 26:463–469.

Scott-Van Zeeland AA, Abrahams BS, Alvarez-Retuerto AI, Sonnenblick LI, Rudie JD, Ghahremani D, Mumford JA, Poldrack RA, Dapretto M, Geschwind DH, et al. 2010. Altered functional connectivity in frontal lobe circuits is associated with variation in the autism risk gene CNTNAP2. Sci Transl Med. 2:56ra80.

Selimbeyoglu A, Kim CK, Inoue M, Lee SY, Hong ASO, Kauvar I, Ramakrishnan C, Fenno LE, Davidson TJ, Wright M, et al. 2017. Modulation of prefrontal cortex excitation/inhibition balance rescues social behavior in CNTNAP2-deficient mice. Sci Transl Med. 9:eaah6733.

Sethi SS, Zerbi V, Wenderoth N, Fornito A, Fulcher BD. 2017. Structural connectome topology relates to regional BOLD signal dynamics in the mouse brain. Chaos. 27:047405.

Sforazzini F, Schwarz AJ, Galbusera A, Bifone A, Gozzi A. 2014. Distributed BOLD and CBV-weighted resting-state networks in the mouse brain. Neuroimage. 87:403–415.

Stafford JM, Jarrett BR, Miranda-Dominguez O, Mills BD, Cain N, Mihalas S, Lahvis GP, Lattal KM, Mitchell SH, David SV, et al. 2014. Large-scale topology and the default mode network in the mouse connectome. Proc Natl Acad Sci USA. 111: 18745–18750.

Strauss KA, Puffenberger EG, Huentelman MJ, Gottlieb S, Dobrin SE, Parod JM, Stephan DA, Morton DH. 2006. Recessive symptomatic focal epilepsy and mutant contactin-associated protein-like 2. N Engl J Med. 354:1370–1377.

Tassone F, Hagerman RJ, Ikle DN, Dyer PN, Lampe M, Willemsen R, Oostra BA, Taylor AK. 1999. FMRP expression as a potential prognostic indicator in fragile X syndrome. Am J Med Genet. 84:250–261.

Vasa RA, Mostofsky SH, Ewen JB. 2016. The disrupted connectivity hypothesis of autism spectrum disorders: time for the next phase in research. Biol Psychiatry Cogn Neurosci Neuroimaging. 1:245–252.

Wang X, Bey AL, Katz BM, Badea A, Kim N, David LK, Duffney LJ, Kumar S, Mague SD, Hulbert SW, et al. 2016. Altered mGluR5-Homer scaffolds and corticostriatal connectivity in a Shank3 complete knockout model of autism. Nat Commun. 7:11459.

Washington SD, Gordon EM, Brar J, Warburton S, Sawyer AT, Wolfe A, Mease-Ference ER, Girton L, Hailu A, Mbwana J, et al. 2014. Dysmaturation of the default mode network in autism. Hum Brain Mapp. 35:1284–1296.

Willemsen R, Levenga J, Oostra BA. 2011. CGG repeat in the FMR1 gene: size matters. Clin Genet. 80:214–225.

Wilson CJ. 2014. The sensory striatum. Neuron. 83:999–1001.

Yizhar O, Fenno LE, Prigge M, Schneider F, Davidson TJ, O'Shea DJ, Sohal VS, Goshen I, Finkelstein J, Paz JT, et al. 2011. Neocortical excitation/inhibition balance in information processing and social dysfunction. Nature. 477:171–178.

Zalesky A, Fornito A, Bullmore ET. 2010. Network-based statistic: identifying differences in brain networks. Neuroimage. 53:1197–1207.

Zerbi V, Grandjean J, Rudin M, Wenderoth N. 2015. Mapping the mouse brain with rs-fMRI: an optimized pipeline for functional network identification. Neuroimage. 123:11–21.

Zerbi V, Kleinnijenhuis M, Fang X, Jansen D, Veltien A, Van Asten J, Timmer N, Dederen PJ, Kiliaan AJ, Heerschap A. 2013. Gray and white matter degeneration revealed by diffusion in an Alzheimer mouse model. Neurobiol Aging. 34:1440–1450.

Zerbi V, Wiesmann M, Emmerzaal TL, Jansen D, Van Beek M, Mutsaers MP, Beckmann CF, Heerschap A, Kiliaan AJ. 2014. Resting-state functional connectivity changes in aging apoE4 and apoE-KO mice. J Neurosci. 34:13963–13975.

Zhang Y, Bonnan A, Bony G, Ferezou I, Pietropaolo S, Ginger M, Sans N, Rossier J, Oostra B, LeMasson G, et al. 2014. Dendritic channelopathies contribute to neocortical and sensory hyperexcitability in Fmr1(–/y) mice. Nat Neurosci. 17:1701–1709.

Supplements

Detailed methods and material

Magnetic resonance imaging.

Fmr1$^{-/y}$ and CNTNAP2$^{-/-}$ mice were longitudinally evaluated during early development. There were no significant weight differences between the strains or between the genotypes, however, there was a significant Age effect (p-value<0.001) denoting a physiological increase in bodyweight over time in all models. MRI scanning was performed to evaluate brain structural and functional connectivity changes in comparison to their respective wildtype littermates. The levels of anesthesia and mouse physiological parameters were monitored following an established protocol to obtain a reliable measurement of functional connectivity (Zerbi V et al. 2015). Briefly, anesthesia was induced with 4% isoflurane and the animals were endotracheally intubated and the tail vein cannulated. Mice were positioned on a MRI-compatible cradle, and artificially ventilated at 80 breaths per minute, 1:4 O_2 to air ratio, and 1.8 ml/h flow (CWE, Ardmore, USA). A bolus injection of medetomidine 0.05 mg/kg and pancuronium bromide 0.2 mg/kg was administered, and isoflurane was reduced to 1.5%. After 5 min, an infusion of medetomidine 0.1 mg/kg/h and pancuronium bromide 0.4 mg/kg/h was administered, and isoflurane was further reduced to 0.5%. The animal temperature was monitored using a rectal thermometer probe, and maintained at 36.5 °C ± 0.5 during the measurements with a water heating system in the cradle. The preparation of the animals did not exceed 20 minutes.

Data acquisition was performed on a Pharmascan 7.0 small animal MR system operating at 300 MHz (Bruker BioSpin MRI, Ettlingen, Germany). A high SNR receive-only cryogenic coil (Bruker BioSpin AG, Fällanden, Switzerland) was used in combination with a linearly polarized room temperature volume resonator for transmission. Images were acquired using Paravision 6 software. After standard adjustments, shim gradients were optimized using mapshim protocol, with an ellipsoid reference volume covering the whole brain. Resting-state fMRI was performed with gradient-echo echo planar images that were acquired with repetition time TR = 1000 ms, echo time TE = 15 ms, flip angle = 60°, matrix size MS = 90 × 50, in-plane resolution RES = 0.22 × 0.2 mm^2, number of slice NS = 20, slice thickness ST = 0.4 mm, slice gap SG = 0.1 mm, and 2000 volumes, for a total scan time of 38 min. Anatomical T2-weighted images were acquired using a FLASH sequence with the same orientation as the GE-EPI, but with an in-plane resolution of 0.05 × 0.02 mm (TE = 3.51, TR = 522 ms, flip angle 30°). Diffusion weighted imaging (DWI) scans were acquired with multi-shot SE-EPI sequence, 4 segments, TR = 2000 ms, TE = 22 ms, FA = 90°, MS = 90 × 50, FOV = 20 × 17.5 mm^2, RES = 0.2 × 0.2 mm^2, NS = 28, ST = 0.4 mm, SG = 0 mm, 5 volumes acquired with b = 0 s/mm^2, b-values = 1000-2000 s/mm^2, 90 directions encoding, for a total scan time of 18 min.

Upon completion of the third MRI measurement (112 days post-natal), mice were transcardially perfused with phosphate-buffered saline (PBS, pH 7.4), followed by 4% buffered paraformaldehyde (PFA; pH 7.4) for fixation.

MRI data pre-processing.

Rs-fMRI

Resting state fMRI datasets were preprocessed using an existing pipeline for removal of unwanted confounds from the time-series (Zerbi V *et al.* 2015), with modifications (Sethi SS et al. 2017). Briefly, each rs-fMRI dataset was fed into MELODIC (Multivariate Exploratory Linear Optimized Decomposition of Independent Components (Beckmann CF and SM Smith 2004)) to perform a within-subject spatial-ICA with a fixed dimensionality estimation (number of components set to 100). This included correction for head motion using MCFLIRT (Jenkinson M et al. 2002) and in-plane smoothing with a 0.3 × 0.3 mm kernel. We applied FSL-FIX with a study-specific classifier obtained from an independent dataset of 15 mice and used a 'conservative' removal of the variance of the artifactual components (for more details, see (Griffanti L et al. 2014)). Thereafter, FIX-cleaned datasets were despiked (Patel AX et al. 2014), band-pass filtered (0.01-0.3 Hz), coregistered to the skull-stripped T2-weighted images and normalized to the AMBMC template (www.imaging.org.au/AMBMC) using ANTs v2.1 (picsl.upenn.edu/ANTS).

Diffusion tensor parameter estimation

Through measurement of water diffusivity in multiple directions, diffusion tensor MRI reconstructs an ellipsoid to model the diffusion in every voxel. The pre-processing steps consisted of individual realignment of the diffusion images, followed by eddy current correction and tensor estimation (Zerbi V et al. 2013). Briefly, the diffusion tensor was estimated for every voxel using the PATCH algorithm (Zwiers MP 2010). This method incorporates motion correction and is robust against both regional artifacts (e.g. cardiac motion) and slice-wise artifacts (e.g. bulk motion) by providing a weight for every voxel that reflects the probability of being an outlier in the tensor fitting. From the eigenvalues of the diffusion tensor, fractional anisotropy (FA) and mean diffusivity (MD) maps were calculated. The resulting volumes were spatially normalized to the AMBMC template using linear affine and non-linear elastic transformations in ANTs.

Transmission electron microscopy tissue preparation.

The brains were sectioned in 60 µm sections in 0.15 M cacodylate buffer + 2 mM $CaCl_2$ using a vibratome held at 4°C. Slices were washed 5 x 5 minutes in ice cold 0.15 M cacodylate buffer + 2 mM $CaCl_2$. Slices were postfixed in 2% OsO_4 in 0.15 M cacodylate buffer + 2 mM $CaCl_2$ for 1.5 hours. The sections were rinsed in ice cold double distilled water (DDW) 5 x 5 minutes and placed in 2% uranyl acetate in DDW at 4°C for 16 hours. Tissue was rinsed in ice cold DDW 3 x 3 minutes. The sections were then dehydrated in ethanol at 50%, 70%, 90%, 100% for 5 minutes each on ice, completed with dehydration using 100% ethanol 2 x 5 minutes at room temp and 100% acetone for 5 minutes. Slices were infiltrated with 50% acetone and 50% Durcupan ACM resin (Sigma-Aldrich, St. Louis, MO) for 16 hours at room temperature. Slices were changed to 100% Durcupan resin, with 3 subsequent changes into fresh resin for the next 2 days. The slices were flat-embedded and placed in a 60°C vacuum oven for 48 hours. The areas of interest from the corpus callosum were isolated and mounted onto dummy acrylic blocks with cyanoacrylic adhesive. Ultrathin sections (70 nm thick) were prepared using an ultramicrotome. Electron micrographs were recorded using a FEI Spirit transmission electron microscope operated at 120 kV.

Retrograde tracing using glycoprotein-deleted rabies virus

Stereotaxic injections and slice preparation

Mice were anesthetized with isoflurane (4%) and maintained under isoflurane anesthesia (2%) throughout the procedure. Mice were placed in stereotaxic frame and purified viral particles injected in the right caudate putamen using a 10 µL glass syringe equipped with a 34 G beveled needle (Nanofil, World Precision Instruments); coordinates with respect to bregma: -0.88 mm anterior/posterior, +3 mm lateral/medial. Injections of 500 nl each were performed at two positions dorsal/ventral: -2.8 mm and -3 mm (with respect to pia). Injection volume and speed (50 nL/min) were monitored using an Ultra Micro Pump (World Precision Instruments) as described in Haberl et al. 2016 (Haberl MG et al. 2017). Mice were perfused after a week of injection and the brains were sectioned as described by (Haberl MG et al. 2015). We have maintained a set of standards to make the result highly reliable.

1. We used a similar titer of virus throughout the experiments (maintained titer by keeping the virus in -80 degrees until prior to the experiment). This helped us to maintain the infection rate.
2. We maintained the volume of injection using an automated precise ultra-micro pump. It also helped us to limit the diffusion of the virus with a controlled slower uniform injection rate.
3. In order to avoid or reduce the infection of cells along the needle track, we extended the time interval between injection and removal of the needle.
4. We performed perfusion exactly 7 days after the injection to avoid a decline in the number of infected cells due to cytotoxicity.
5. Each quantification was verified by a second person to avoid bias.

Data analysis and Statistics:

Functional Connectivity: network analysis

Rs-fMRI examines the temporal correlations of slow fluctuations of the blood oxygen level dependent (BOLD) signal across the brain during rest, i.e. without overt perceptual inputs or motor output typically present in traditional fMRI studies. These fluctuations form spatial patterns of correlated activity (also called resting-state networks, RSNs) that unfold along long-range axonal connections of the brain revealing its intrinsic functional architecture (Zhang D and ME Raichle 2010). One common way to analyze functional connectivity data when no a-priori anatomical hypotheses are available is to perform a data-driven analysis of these RSNs. To derive robust RSNs in the mouse that are unbiased by genotype or age groups, we used all 124 pre-processed rs-fMRI datasets (see Materials & Methods section for details) to perform a group-level independent component analysis (ICA) using FSL Melodic. A variable number of components (30-60-100) were pre-set and the results compared and classified according to recent published criteria (Griffanti L et al. 2016). We selected sixteen meaningful RSNs that were identified in all analyses and named them according to the ontological area of their maximum Z-score intensity.

In our ICA approach, within-network connectivity analysis was performed using a dual regression approach implemented in FSL (Zuo XN et al. 2010). In short, this approach consists of two stages: (1) a spatial regression of the data is calculated to identify the time course of a RSN; and (2) a temporal

regression with those time courses is determined to get the subject specific map of the RSN. This is done for each RSN.

The resulting subject-specific component map was then masked by the 75th percentile group mean RSN map. The mean value of the parameter estimates within this region was extracted for each subject. The average of this parameter estimate can be seen as a measure of the average coupling strength (i.e. temporal synchronicity) of functional connectivity within each RSN. This analysis was performed for each RSN separately."

A dual-regression approach was used to identify subject-specific time courses and spatial maps of the mouse resting-state networks. The parameter estimates of the dual regression are a surrogate measure of synchronicity (i.e. coupling strength) within the RSN under investigation. Two types of statistical analyses were performed on these data to compare the influence of genotype on RSNs connectivity; first, we employed an exploratory voxel-based analysis to describe overall genotype differences between our models and their control with the highest possible spatial resolution. We performed nonparametric permutation testing with 5000 permutations, using family-wise error correction with threshold-free cluster enhancement (TFCE). Statistical significance was defined as $p < 0.05$ divided by the number of RSNs (16) to correct for multiple comparisons.

In the second analysis, we delineated the interaction between genotype and developmental trajectories at the network level. We therefore derived an index of "network strength" by averaging the Z-scores from the group-mean RSNs masks (thresholded at the 75th percentile). Group level statistics were performed in SPSS v22 using a Linear Mixed-Model, with the fixed factors Genotype and Age (3-levels, repeated measure), and with the individual mice as the random factor. Corresponding contrasts were used for post-hoc pairwise comparisons (LSD) while gender (in CNTNAP2 mice only) was kept as a covariate of no interest. *P*-values were considered significant at $p<0.05$ after False Discovery Rate (FDR) correction for multiple comparisons between RSNs. Age main effects are not reported because anesthesia-dependent effects can modulate the absolute strength of connectivity (Barttfeld P et al. 2015; Bettinardi RG et al. 2015), and may not scale linearly with body-weight. Instead we focused on Genotype and Genotype×Age effects.

Diffusion tensor imaging

In order to characterize the presence of structural differences in our models, at each scan-session all mice were imaged with a diffusion-weighted sequence. The resulting datasets were pre-processed and each voxel modeled as a tensor using established protocols (Zerbi V *et al.* 2013) to obtain whole-brain fractional anisotropy (FA) and mean diffusivity (MD) maps. FA measures the coherence of water diffusion along the main fiber orientation, giving indirect information on the structural integrity of a white-matter bundle. MD measures the overall diffusivity in a given voxel, and gives information on the amount of restricted isotropic diffusion, which is particularly relevant in gray matter areas. FA and MD maps were normalized to the AMBMC template; mean FA values were extracted from seven major white matter structures taken from the Allen Mouse Brain atlas (Figure 4A), while mean MD were obtained from each RSNs mask, and analyzed using a Linear Mixed-Model with FDR correction. Since the dosage of anesthesia

does not influence the brain structural proprieties, Age was considered as a repeated fixed factor as well as estimated marginal mean of the fitted models.

When required, FDR correction was carried out in Matlab by applying a linear-step up (LSU) procedure originally introduced by Benjamini and Hochberg (1995). In the ICA network-analysis statistics, *p*-values from all 16 RSNs were pooled in one vector and the correction was then applied. The same procedure was done for the FA analysis (pooling p-values from seven ROIs) and NBS (pooling p-values from the identified networks in each contrast). FDR correction was applied separately for overall genotype differences, and for genotype × age interactions.

Supplementary figures

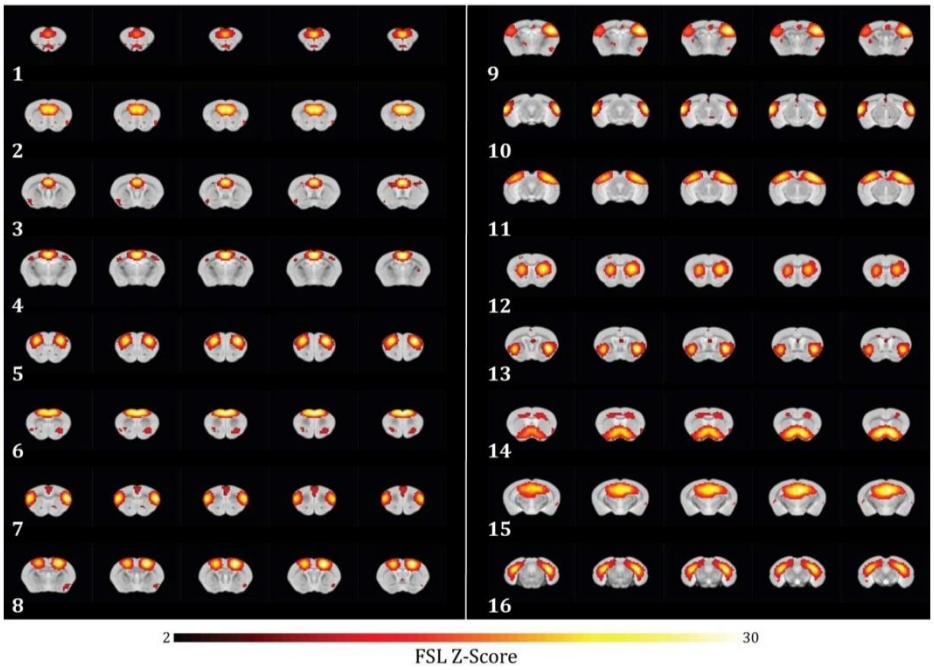

Figure S1. Selected mouse brain networks

The selected 16 brain networks are displayed as Z-scores overlaid with an anatomical template in two-dimensional coronal sections

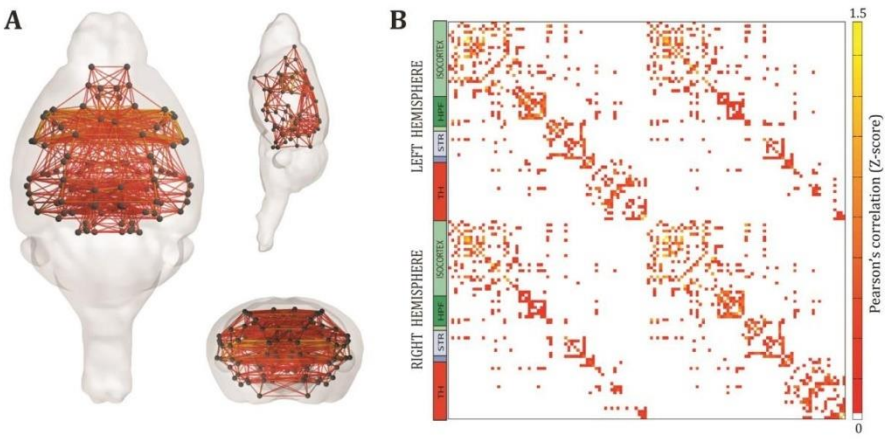

Figure S2. Mouse brain functional connectome.

Graphical (A) and matrix (B) representation of the whole-brain functional connectome in the mouse brain, obtained from the average of 124 datasets. The averaged connectivity matrix (130x130 nodes) was thresholded at 10% sparsity, resulting in an adjacency matrix of 1430 connections. Only these connections are included in the Network Based Statistics to test for group differences.

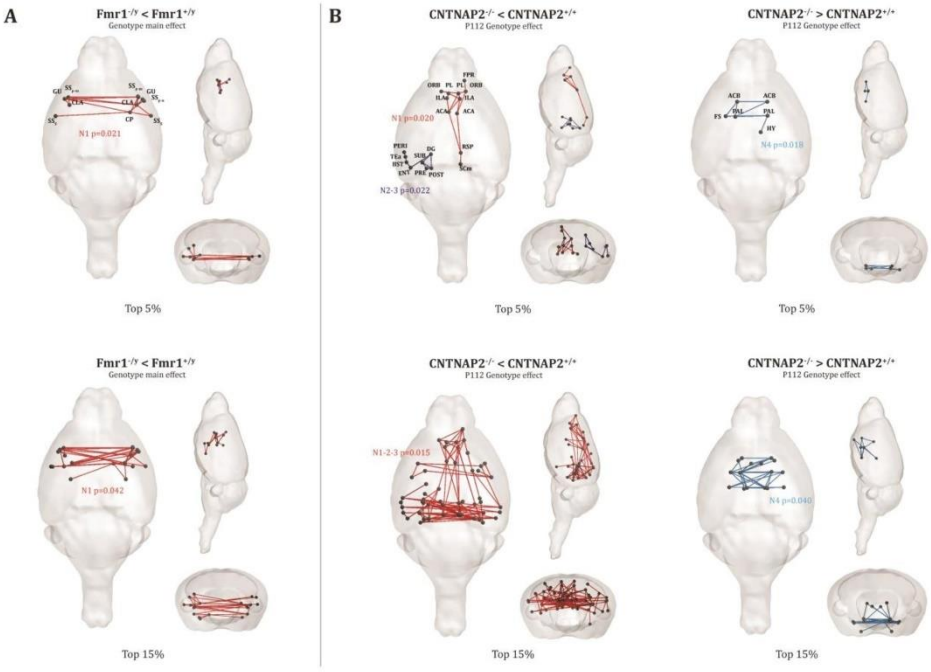

Figure S3. Network Based Statistics with different matrix-sparsity levels.

Rs-fMRI connectome analysis combined with network based statistics (NBS) using a lower (5%) and a higher (15%) sparsity levels compared to what reported in the main text (10%). **A)** Consistent with our main analysis, Fmr1$^{-/y}$ mice show severe underconnectivity in bilateral cortico-cortico and cortico-striatal circuits at both thresholds. **B)** In CNTNAP2$^{-/-}$ mice using the 5% sparsity we detected significant reduced connectivity in prefrontal-retrosplenial circuits (N1), left associative areas and left hippocampus (N2-3). Using the top-15% sparsity, all these previously identified networks are now merged in one single network, which is likely to occur when the connectivity matrix is too dense and therefore NBS fails to separate the data into distinct networks. At both thresholds, adult CNTNAP2$^{-/-}$ mice showed an increased connectivity in a network comprising ventral striatum-pallidum-hypothalamus (N4). As expected, the overall number of significant edges/nodes was less using the top-5% threshold and higher using the top-15% threshold.

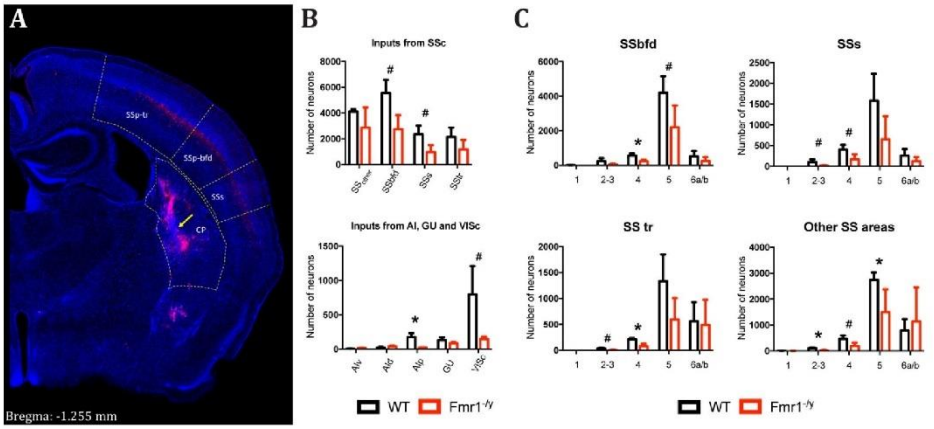

Figure S4. Retrograde viral tracing in Fmr1-/y mice.

Reduced inputs to CP of Fmr1-/y mice. **A)** Image showing the RABV ΔG (expressing mCherry) injection site in CP (indicated with a white arrow) and the retrograde labeled cells in cortical regions. **B)** Reduction of labeled projection neurons from somatosensory cortices and AI, GU and Visceral cortices. The neuronal projections from barrel field, dorsal cortex (SSbfd, pValue = 0.05, Bonferroni corrected) and parietal agranular insular cortices (AIp, pValue = 0.02, Bonferroni corrected) showed significant hypo-connectivity. **C)** In particular, projection neurons within layers 4 were most strongly affected for SSp-bfd and SSp-tr (pValue = 0.01, Bonferroni corrected).

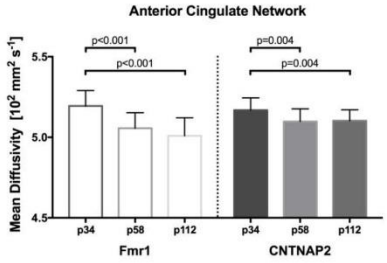

Figure S5. Mean diffusivity in Fmr1$^{-/y}$ and CNTNAP2$^{-/-}$ mice.

MD measures the overall diffusivity in a given voxel and gives information on amount of restricted isotropic diffusion, which is particularly relevant in gray matter areas. MD differences in Fmr1$^{-/y}$ and CNTNAP2$^{-/-}$ mice were negligible, and despite a few commonly observed Genotype and Genotype×Age interactions e.g. in anterior motor and anterior parietal areas, nothing survived FDR correction. However, robust and consistent Age effects were seen in both models in almost all RSNs (p-value<0.01, FDR corrected), with the exceptions of medial orbital and posterior motor areas. In all cases, MD in juvenile mice (p34) was higher compared to both young adult (p58) and adult (p112) mice. This early reduction in MD reflects the physiological brain maturation observed in typical developing children until middle childhood, at which time a plateau is generally reached and maintained until the elderly stages of life (Snook L et al. 2005; Lebel C et al. 2008). Mean Diffusivity in both mouse models showed a characteristic reduction throughout aging, also seen in human children. There were, however, no differences in mean diffusivity between animal groups.

References

Barttfeld P, Uhrig L, Sitt JD, Sigman M, Jarraya B, Dehaene S. 2015. Signature of consciousness in the dynamics of resting-state brain activity. Proc Natl Acad Sci U S A 112:887-892.

Beckmann CF, Smith SM. 2004. Probabilistic independent component analysis for functional magnetic resonance imaging. IEEE Trans Med Imaging 23:137-152.

Bettinardi RG, Tort-Colet N, Ruiz-Mejias M, Sanchez-Vives MV, Deco G. 2015. Gradual emergence of spontaneous correlated brain activity during fading of general anesthesia in rats: Evidences from fMRI and local field potentials. Neuroimage 114:185-198.

Griffanti L, Douaud G, Bijsterbosh J, Evangelisti S, Alfaro-Almagro F, Glasser MF, Duff EP, Fitzgibbon S, Westphal R, Carone D, Beckmann CF, Smith SM. 2016. Hand classification of fMRI ICA noise components. Neuroimage.

Griffanti L, Salimi-Khorshidi G, Beckmann CF, Auerbach EJ, Douaud G, Sexton CE, Zsoldos E, Ebmeier KP, Filippini N, Mackay CE, Moeller S, Xu J, Yacoub E, Baselli G, Ugurbil K, Miller KL, Smith SM. 2014. ICA-based artefact removal and accelerated fMRI acquisition for improved resting state network imaging. Neuroimage 95:232-247.

Haberl MG, Ginger M, Frick A. 2017. Dual Anterograde and Retrograde Viral Tracing of Reciprocal Connectivity. Methods Mol Biol 1538:321-340.

Haberl MG, Viana da Silva S, Guest JM, Ginger M, Ghanem A, Mulle C, Oberlaender M, Conzelmann KK, Frick A. 2015. An anterograde rabies virus vector for high-resolution large-scale reconstruction of 3D neuron morphology. Brain Struct Funct 220:1369-1379.
Jenkinson M, Bannister P, Brady M, Smith S. 2002. Improved optimization for the robust and accurate linear registration and motion correction of brain images. Neuroimage 17:825-841.
Lebel C, Walker L, Leemans A, Phillips L, Beaulieu C. 2008. Microstructural maturation of the human brain from childhood to adulthood. Neuroimage 40:1044-1055.
Patel AX, Kundu P, Rubinov M, Jones PS, Vertes PE, Ersche KD, Suckling J, Bullmore ET. 2014. A wavelet method for modeling and despiking motion artifacts from resting-state fMRI time series. Neuroimage 95:287-304.
Sethi SS, Zerbi V, Wenderoth N, Fornito A, Fulcher BD. 2017. Structural connectome topology relates to regional BOLD signal dynamics in the mouse brain. Chaos 27:047405.
Snook L, Paulson LA, Roy D, Phillips L, Beaulieu C. 2005. Diffusion tensor imaging of neurodevelopment in children and young adults. Neuroimage 26:1164-1173.
Zerbi V, Grandjean J, Rudin M, Wenderoth N. 2015. Mapping the mouse brain with rs-fMRI: An optimized pipeline for functional network identification. Neuroimage 123:11-21.
Zerbi V, Kleinnijenhuis M, Fang X, Jansen D, Veltien A, Van Asten J, Timmer N, Dederen PJ, Kiliaan AJ, Heerschap A. 2013. Gray and white matter degeneration revealed by diffusion in an Alzheimer mouse model. Neurobiology of aging 34:1440-1450.
Zhang D, Raichle ME. 2010. Disease and the brain's dark energy. Nature reviews Neurology 6:15-28.
Zuo XN, Kelly C, Adelstein JS, Klein DF, Castellanos FX, Milham MP. 2010. Reliable intrinsic connectivity networks: test-retest evaluation using ICA and dual regression approach. Neuroimage 49:2163-2177.
Zwiers MP. 2010. Patching cardiac and head motion artefacts in diffusion-weighted images. Neuroimage 53:565-575.

15 BIBLIOGRAPHY

Abraira, V.E., and Ginty, D.D. (2013). The Sensory Neurons of Touch. Neuron 79, 618–639.

Aguilar, J., Morales-Botello, M., and Foffani, G. (2008). Tactile responses of hindpaw, forepaw and whisker neurons in the thalamic ventrobasal complex of anesthetized rats. Eur J Neurosci 27, 378–387.

Akins, M.R., LeBlanc, H.F., Stackpole, E.E., Chyung, E., and Fallon, J.R. (2012). Systematic mapping of fragile X granules in the mouse brain reveals a potential role for presynaptic FMRP in sensorimotor functions. The Journal of Comparative Neurology 520, 3687–3706.

Aloisi, E., Corf, K., Dupuis, J., Zhang, P., and Nature …, G.M. (2017). Altered surface mGluR5 dynamics provoke synaptic NMDAR dysfunction and cognitive defects in *Fmr1* knockout mice.

Amatrudo, J.M., Weaver, C.M., Crimins, J.L., Hof, P.R., Rosene, D.L., and Luebke, J.I. (2012). Influence of Highly Distinctive Structural Properties on the Excitability of Pyramidal Neurons in Monkey Visual and Prefrontal Cortices. The Journal of Neuroscience 32, 13644–13660.

Andreas Frick, Melanie Ginger, Lynda El-Hassar, Leonard K. Kaczmarek. (2017). Ion channel dysfunction and FXS. Fragile X syndrome from genetics to targeted treatment. Book chapter, 323-334.

Annangudi, S.P., Luszpak, A.E., Kim, S., Ren, S., Hatcher, N.G., Weiler, I., Thornley, K.T., Kile, B.M., Wightman, M.R., Greenough, W.T., et al. (2010). Neuropeptide Release Is Impaired in a Mouse Model of Fragile X Mental Retardation Syndrome. ACS Chemical Neuroscience 1, 306–314.

Antar, L.N., Afroz, R., Dictenberg, J.B., Carroll, R.C., and Bassell, G.J. (2004). Metabotropic Glutamate Receptor Activation Regulates Fragile X Mental Retardation Protein and *Fmr1* mRNA Localization Differentially in Dendrites and at Synapses. The Journal of Neuroscience 24, 2648–2655.

Antar, L.N., Li, C., Zhang, H., Carroll, R.C., and Bassell, G.J. (2006). Local functions for FMRP in axon growth cone motility and activity-dependent regulation of filopodia and spine synapses. Molecular and Cellular Neuroscience 32, 37–48.

Arieli, A., Sterkin, A., Grinvald, A., and Aertsen, A. (1996). Dynamics of Ongoing Activity: Explanation of the Large Variability in Evoked Cortical Responses. Science 273, 1868–1871.

Arnett, M.T., Herman, D.H., and McGee, A.W. (2014). Deficits in Tactile Learning in a Mouse Model of Fragile X Syndrome. PLoS ONE 9, e109116.

Arsenault, J., Gholizadeh, S., Niibori, Y., Pacey, L.K., Halder, S., Koxhioni, E., Konno, A., Hirai, H., and Hampson, D. (2016). FMRP Expression Levels in Mouse CNS Neurons Determine Behavioral Phenotype. Human Gene Therapy.

August, G.J., and Lockhart, L.H. (1984). Familial autism and the fragile-X chromosome. Journal of Autism and Developmental Disorders 14, 197–204.

Bailey, D., Hatton, D., Mesibov, G., and of autism and …, A.N. (2000). Early development, temperament, and functional impairment in autism and fragile X syndrome.

Baker, K., Wray, S., Ritter, R., Mason, S., Lanthorn, T., and Savelieva, K.V. (2010). Male and female *Fmr1* knockout mice on C57 albino background exhibit spatial learning and memory impairments. Genes, Brain and Behavior 9, 562–574.

Bakker, C.E., Verheij, C., Willemsen, R., van Helm, R. der, Oerlemans, F., Vermey, M., Bygrave, A., Hoogeveen, A., Oostra, B.A., Reyniers, E., et al. (1994). *Fmr1* knockout mice: A model to study fragile X mental retardation. Cell 78, 23–33.

Baranek, G.T., David, F.J., Poe, M.D., Stone, W.L., and Watson, L.R. (2006). Sensory Experiences Questionnaire: discriminating sensory features in young children with autism, developmental delays, and typical development. J Child Psychol Psyc 47, 591–601.

Barnea-Goraly, N., Eliez, S., Hedeus, M., Menon, V., White, C.D., Moseley, M., and Reiss, A.L. (2003). White matter tract alterations in fragile X syndrome: Preliminary evidence from diffusion tensor imaging. American Journal of Medical Genetics Part B: Neuropsychiatric Genetics 118B, 81–88.

Barth, A.L., and Poulet, J. (2012). Experimental evidence for sparse firing in the neocortex. Trends in Neurosciences 35, 345–355.

Bassell, G.J., and Warren, S.T. (2008). Fragile X Syndrome: Loss of Local mRNA Regulation Alters Synaptic Development and Function. Neuron 60, 201–214.

Bear, M.F., Huber, K.M., and Warren, S.T. (2004). The mGluR theory of fragile X mental retardation. Trends in Neurosciences 27, 370–377.

Beltramo, R., D'Urso, G., Maschio, M., Farisello, P., Bovetti, S., Clovis, Y., Lassi, G., Tucci, V., Tonelli, D., and Fellin, T. (2013). Layer-specific excitatory circuits differentially control recurrent network dynamics in the neocortex. Nature Neuroscience 16, 227–234.

Benoit, P., and Mambrini, J. (1970). Modification of transmitter release by ions which prolong the presynaptic action potential. J Physiology 210, 681–695.

Berry-Kravis, E., and Ciurlionis, R. (1998). Overexpression of fragile X gene (FMR-1) transcripts increases cAMP production in neural cells.

Berwick, J., Redgrave, P., Jones, M., Hewson-Stoate, N., Martindale, J., Johnston, D., and Mayhew, J.E.W. (2004). Integration of neural responses originating from different regions of the cortical somatosensory map. Brain Res 1030, 284–293.

Berzhanskaya, J., Phillips, M.A., Gorin, A., Lai, C., Shen, J., and Colonnese, M.T. (2017). Disrupted Cortical State Regulation in a Rat Model of Fragile X Syndrome. Cerebral Cortex 27, 1386–1400.

Bhakar, A.L., Dölen, G., and Bear, M.F. (2012). The pathophysiology of fragile X (and what it teaches us about synapses). Annual Review of Neuroscience 35, 417–443.

Bolt, T., Anderson, M.L., and Uddin, L.Q. (2017). Beyond the evoked/intrinsic neural process dichotomy. Netw Neurosci 2, 1–44.

Bonasera, S., Chaudoin, T., Goulding, E., Mittek, M., and Dunaevsky, A. (2017). Decreased home cage movement and oromotor impairments in adult *Fmr1*-KO mice. Genes, Brain and Behavior 16, 564–573.

Bontekoe, C.J., McIlwain, K.L., Nieuwenhuizen, I.M., Yuva-Paylor, L.A., Nellis, A., Willemsen, R., Fang, Z., Kirkpatrick, L., Bakker, C.E., McAninch, R., et al. (2002). Knockout mouse model for Fxr2: a model for mental retardation. Hum Mol Genet 11, 487–498.

Boone, C.E., Davoudi, H., Harrold, J.B., and Foster, D.J. (2018). Abnormal Sleep Architecture and Hippocampal Circuit Dysfunction in a Mouse Model of Fragile X Syndrome. Neuroscience.

Bouet, V., Boulouard, M., Toutain, J., Divoux, D., Bernaudin, M., Schumann-Bard, P., Freret, T., 2009. The adhesive removal test: a sensitive method to assess sensorimotor deficits in mice. Nature Protocols 4, 1560–1564.

Boulle, K., Verkerk, A., Reyniers, E., Vits, L., Hendrickx, J., Roy, B., Bos, F., de Graaff, E., Oostra, B.A., and Willems, P.J. (1993). A point mutation in the FMR-1 gene associated with fragile X mental retardation. Nature Genetics 3, 31–35.

Boyd, B.A., Baranek, G.T., Sideris, J., Poe, M.D., Watson, L.R., Patten, E., and Miller, H. (2010). Sensory features and repetitive behaviors in children with autism and developmental delays. Autism Res 3, 78–87.

Brown MR, Kronengold J, Gazula V-R, Chen Y, Strumbos JG, Sigworth FJ et al. Fragile X mental retardation protein controls gating of the sodium-activated potassium channel Slack. Nat Neurosci 2010; **13**: 819.

Brown, T.W., Jenkins, E.C., Friedman, E., Brooks, J., Wisniewski, K., Raguthu, S., and French, J. (1982). Autism is associated with the fragile-X syndrome. Journal of Autism and Developmental Disorders 12, 303–308.

Brown, V., Jin, P., Ceman, S., Darnell, J.C., O'Donnell, W.T., Tenenbaum, S.A., Jin, X., Feng, Y., Wilkinson, K.D., Keene, J.D., et al. (2001). Microarray Identification of FMRP-Associated Brain mRNAs and Altered mRNA Translational Profiles in Fragile X Syndrome. Cell 107, 477–487.

Bruno, J., Hosseini, H.S., Saggar, M., Quintin, E.-M., Raman, M., and Reiss, A.L. (2017). Altered Brain Network Segregation in Fragile X Syndrome Revealed by Structural Connectomics. Cereb Cortex 27, 2249–2259.

Budimirovic, D.B., and Kaufmann, W.E. (2011). What Can We Learn about Autism from Studying Fragile X Syndrome? Developmental Neuroscience 33, 379–394.

Budimirovic, D.B., Bukelis, I., Cox, C., Gray, R.M., Tierney, E., and Kaufmann, W.E. (2006). Autism spectrum disorder in Fragile X syndrome: Differential contribution of adaptive socialization and social withdrawal. American Journal of Medical Genetics Part A 140A, 1814–1826.

Bureau, I., Shepherd, G.M., and Svoboda, K. (2008). Circuit and Plasticity Defects in the Developing Somatosensory Cortex of *Fmr1* Knock-Out Mice. The Journal of Neuroscience 28, 5178–5188.

Bureau, I., von Paul, F., and Svoboda, K. (2006). Interdigitated Paralemniscal and Lemniscal Pathways in the Mouse Barrel Cortex. Plos Biol 4, e382.

Burton, H., and Sinclair, R. (2000). Attending to and Remembering Tactile Stimuli: A Review of Brain Imaging Data and Single-Neuron Responses. Journal of Clinical Neurophysiology 17, 575.

Carlson, M., and Burton, H. (1988). Recovery of tactile function after damage to primary or secondary somatic sensory cortex in infant Macaca mulatta. J Neurosci 8, 833–859.

Carr, M.F., Karlsson, M.P., and Frank, L.M. (2012). Transient Slow Gamma Synchrony Underlies Hippocampal Memory Replay. Neuron 75, 700–713.

Casas-Torremocha, D., Clascá, F., and Núñez, Á. (2017). Posterior Thalamic Nucleus Modulation of Tactile Stimuli Processing in Rat Motor and Primary Somatosensory Cortices. Frontiers in Neural Circuits 11, 69.

Cascio, C.J. (2010). Somatosensory processing in neurodevelopmental disorders. Journal of Neurodevelopmental Disorders 2, 62–69.

Casten, K.S., Gray, A.C., and Burwell, R.D. (2011). Discrimination learning and attentional set formation in a mouse model of Fragile X. Behavioral Neuroscience 125, 473.

Castrén, M., Tervonen, T., Kärkkäinen, V., Heinonen, S., Castrén, E., Larsson, K., Bakker, C.E., Oostra, B.A., and Åkerman, K. (2005). Altered differentiation of neural stem cells in fragile X syndrome. Proceedings of the National Academy of Sciences of the United States of America 102, 17834–17839.

Cembrowski, M.S., and Menon, V. (2018). Continuous Variation within Cell Types of the Nervous System. Trends in Neurosciences.

Chabrol, F.P., Arenz, A., Wiechert, M.T., Margrie, T.W., and DiGregorio, D.A. (2015). Synaptic diversity enables temporal coding of coincident multisensory inputs in single neurons. Nature Neuroscience 18, nn.3974.

Charman, T., Pickles, A., Simonoff, E., Chandler, S., Loucas, T., and Baird, G. (2010). IQ in children with autism spectrum disorders: data from the Special Needs and Autism Project (SNAP). Psychol Med 41, 619–627.

Cheetham, C.E., Hammond, M.S., McFarlane, R., and Finnerty, G.T. (2008). Altered Sensory Experience Induces Targeted Rewiring of Local Excitatory Connections in Mature Neocortex. J Neurosci 28, 9249–9260.

Chen, J.L., Carta, S., Soldado-Magraner, J., Schneider, B.L., and Helmchen, F. (2013). Behaviour-dependent recruitment of long-range projection neurons in somatosensory cortex. Nature 499, 336.

Chen, J.L., Margolis, D.J., Stankov, A., Sumanovski, L.T., Schneider, B.L., and Helmchen, F. (2015). Pathway-specific reorganization of projection neurons in somatosensory cortex during learning. Nat Neurosci 18, 1101–1108.

Cheng, G.-R.R., Li, X.-Y.Y., Xiang, Y.-D.D., Liu, D., McClintock, S.M., and Zeng, Y. (2017). The implication of AMPA receptor in synaptic plasticity impairment and intellectual disability in fragile X syndrome. Physiological Research 66, 715–727.

Choi, I., Lee, J.-Y., and Lee, S.-H. (2018). Bottom-up and top-down modulation of multisensory integration. Current Opinion in Neurobiology 52, 115–122.

Chuong, A.S., Miri, M.L., Busskamp, V., Matthews, G.A., Acker, L.C., Sørensen, A.T., Young, A., Klapoetke, N.C., Henninger, M.A., Kodandaramaiah, S.B., et al. (2014). Noninvasive optical inhibition with a red-shifted microbial rhodopsin. Nat Neurosci 17, 1123–1129.

Clemens, A.M., Delgado, Y., Mehlman, M.L., Mishra, P., and Brecht, M. (2018). Multisensory and Motor Representations in Rat Oral Somatosensory Cortex. Sci Rep-Uk 8, 13556.

Contet, C., Goulding, S., Kuljis, D., and Barth, A. (2016). BK Channels in the Central Nervous System. International Review of Neurobiology 128, 281–342.

Contractor, A., Klyachko, V.A., and Portera-Cailliau, C. (2015). Altered Neuronal and Circuit Excitability in Fragile X Syndrome. Neuron 87, 699–715.

Cornish, K.M., Munir, F., and Cross, G. (1999). Spatial Cognition in Males with Fragile-X Syndrome: Evidence for a Neuropsychological Phenotype. Cortex 35, 263–271.

Crochet, S., and Petersen, C. (2009). Cortical Dynamics by Layers. Neuron 64, 298–300.

Crochet, S., Poulet, J., Kremer, Y., and Petersen, C. (2011). Synaptic Mechanisms Underlying Sparse Coding of Active Touch. Neuron 69, 1160–1175.

Dahlhaus, R. (2018). Of Men and Mice: Modeling the Fragile X Syndrome. Frontiers in Molecular Neuroscience 11, 41.

Dahlhaus, R., and El-Husseini, A. (2010). Altered neuroligin expression is involved in social deficits in a mouse model of the fragile X syndrome. Behavioural Brain Research 208, 96–105.

Darnell, J. (2011). Defects in translational regulation contributing to human cognitive and behavioral disease. Current Opinion in Genetics & Development 21, 465–473.

del Pino, I., Rico, B., and Marín, O. (2018). Neural circuit dysfunction in mouse models of neurodevelopmental disorders. Current Opinion in Neurobiology 48, 174–182.

Deng P-Y, Rotman Z, Blundon JA, Cho Y, Cui J, Cavalli V et al. FMRP Regulates Neurotransmitter Release and Synaptic Information Transmission by Modulating Action Potential Duration via BK Channels. Neuron 2013; **77**: 696–711.

Desai, N.S., Casimiro, T.M., Gruber, S.M., and Vanderklish, P.W. (2006). Early Postnatal Plasticity in Neocortex of *Fmr1* Knockout Mice. Journal of Neurophysiology 96, 1734–1745.

Deng, P.-Y., Rotman, Z., Blundon, J.A., Cho, Y., Cui, J., Cavalli, V., Zakharenko, S.S., and Klyachko, V.A. (2013). FMRP Regulates Neurotransmitter Release and Synaptic Information Transmission by Modulating Action Potential Duration via BK Channels. Neuron 77, 696–711.

Devys, D., Lutz, Y., Rouyer, N., Bellocq, J., and Mandel, J. (1993). The FMR-1 protein is cytoplasmic, most abundant in neurons and appears normal in carriers of a fragile X premutation. Nature Genetics 4, 335–340.

Ding, Q., Sethna, F., and Wang, H. (2014). Behavioral analysis of male and female *Fmr1* knockout mice on C57BL/6 background. Behavioural Brain Research 271, 72–78.

Dobkin, C., Rabe, A., Dumas, R., Idrissi, A., Haubenstock, H., and Brown, T.W. (2000). *Fmr1* knockout mouse has a distinctive strain-specific learning impairment. Neuroscience 100, 423–429.

Doll, C.A., Vita, D.J., and Broadie, K. (2017). Fragile X Mental Retardation Protein Requirements in Activity-Dependent Critical Period Neural Circuit Refinement. Current Biology: CB 27, 2318-2330.e3.

Domanski. A, J. T. Isaac, P. C. Kind. Abnormal thalamocortical activation of somatosensory cortex in the young Fmr1-KO mouse model of Fragile X Syndrome.Proceedings of The Physiological Society. 37th Congress of IUPS (Birmingham, UK) (2013) Proc 37th IUPS, SA214

Eadie, B.D., Zhang, W.N., Boehme, F., Gil-Mohapel, J., Kainer, L., Simpson, J.M., and Christie, B.R. (2009). *Fmr1* knockout mice show reduced anxiety and alterations in neurogenesis that are specific to the ventral dentate gyrus. Neurobiology of Disease 36, 361–373.

Ebrahimi-Fakhari, D., and Sahin, M. (2015). Autism and the synapse: emerging mechanisms and mechanism-based therapies. Current Opinion in Neurology 28, 91.

Eliez, S., Blasey, C.M., Freund, L.S., Hastie, T., and Reiss, A.L. (2001). Brain anatomy, gender and IQ in children and adolescents with fragile X syndrome. Brain 124, 1610–1618.

Eliez, S., Blasey, C.M., Freund, L.S., Hastie, T., and Reiss, A.L. (2001). Brain anatomy, gender and IQ in children and adolescents with fragile X syndrome. Brain 124, 1610–1618.

Ethridge, L., White, S., Mosconi, M., Wang, J., Byerly, M., and Sweeney, J. (2016). Reduced habituation of auditory evoked potentials indicates cortical hyper-excitability in Fragile X Syndrome. Translational Psychiatry 6, e787.

Ethridge, L.E., White, S.P., Mosconi, M.W., Wang, J., Pedapati, E.V., Erickson, C.A., Byerly, M.J., and Sweeney, J.A. (2017). Neural synchronization deficits linked to cortical hyper-excitability and auditory hypersensitivity in fragile X syndrome. Molecular Autism 8, 22.

Faber, L.E., and Sah, P. (2003a). Ca2+-activated K+ (BK) channel inactivation contributes to spike broadening during repetitive firing in the rat lateral amygdala. J Physiology 552, 483–497.

Faber, L.E., and Sah, P. (2003b). Calcium-Activated Potassium Channels: Multiple Contributions to Neuronal Function. Neurosci 9, 181–194.

Faisal, A.A., Selen, L.P., and Wolpert, D.M. (2008). Noise in the nervous system. Nat Rev Neurosci *9*, nrn2258.

Fata, G., Gärtner, A., Domínguez-Iturza, N., Dresselaers, T., Dawitz, J., Poorthuis, R.B., Averna, M., Himmelreich, U., Meredith, R.M., Achsel, T., et al. (2014). FMRP regulates multipolar to bipolar transition affecting neuronal migration and cortical circuitry. Nature Neuroscience 17, nn.3870.

Fatemi, H.S., and Folsom, T.D. (2011). The role of fragile X mental retardation protein in major mental disorders. Neuropharmacology 60, 1221–1226.

Feinstein, C., and Reiss, A.L. (1998). Autism: the point of view from fragile X studies.

Ferron L, Nieto-Rostro M, Cassidy JS, Dolphin AC. Fragile X mental retardation protein controls synaptic vesicle exocytosis by modulating N-type calcium channel density. Nature Communications 2014; **5**. doi:10.1038/ncomms4628.

Ferron L. Fragile X mental retardation protein controls ion channel expression and activity. The Journal of physiology 2016; **594**: 5861–5867.

Filippini, A., Bonini, D., Lacoux, C., Pacini, L., Zingariello, M., Sancillo, L., Bosisio, D., Salvi, V., Mingardi, J., Via, L., et al. (2017). Absence of the Fragile X Mental Retardation Protein results in defects of RNA editing of neuronal mRNAs in mouse. RNA Biology 1–12.

Finelli, P., Pueschel, and of Neurology …, P.-M.T. (1985). Neurological findings in patients with the fragile-X syndrome.

Fishell, G., and Heintz, N. (2013). The Neuron Identity Problem: Form Meets Function. Neuron 80, 602–612.

Frangeul, L., Kehayas, V., Sanchez-Mut, J.V., Fièvre, S., Krishna-K, K., Pouchelon, G., Telley, L., Bellone, C., Holtmaat, A., Gräff, J., et al. (2017). Input-dependent regulation of excitability controls dendritic maturation in somatosensory thalamocortical neurons. Nature Communications 8, 2015.

Frankland, P., Dockstader, C., and nald, R. (1998). Discriminative and nondiscriminative contextual fear conditioning potentiate the acoustic startle response. Psychobiology 26, 267–274.

Frick, A., and Johnston, D. (2005). Plasticity of dendritic excitability. J Neurobiol 64, 100–115.

Friefeld, S.J., and Macgregor, D. (1994). Sensorimotor coordination in boys with fragile X syndrome. Occupational Therapy International 1, 174–182.

Frigon, A. (2017). The neural control of interlimb coordination during mammalian locomotion. J Neurophysiol 117, 2224–2241.

Fryns, J., Jacobs, J., and genetics, K.A. (1984). The psychological profile of the fragile X syndrome.

Fu, Y.-H., Kuhl, D., Pizzuti, A., Pieretti, M., Sutcliffe, J.S., Richards, S., Verkert, A., Holden, J., Fenwick, R.G., Warren, S.T., et al. (1991). Variation of the CGG repeat at the fragile X site results in genetic instability: Resolution of the Sherman paradox. Cell 67, 1047–1058.

Galarreta, M., and Hestrin, S. (2001). Electrical synapses between Gaba-Releasing interneurons. Nat Rev Neurosci 2, 35077566.

Galvez, R., Gopal, A.R., and Greenough, W.T. (2003). Somatosensory cortical barrel dendritic abnormalities in a mouse model of the fragile X mental retardation syndrome. Brain Research 971, 83–89.

Galvez, R., Smith, R., and Greenough, W.T. (2005). Olfactory bulb mitral cell dendritic pruning abnormalities in a mouse model of the Fragile-X mental retardation syndrome: Further support for FMRP's involvement in dendritic development. Developmental Brain Research 157, 214–216.

Garcia-Pino, E., Gessele, N., and Koch, U. (2017). Enhanced Excitatory Connectivity and Disturbed Sound Processing in the Auditory Brainstem of Fragile X Mice. The Journal of Neuroscience 37, 7403–7419.

Gatto, C.L., and Broadie, K. (2008). Temporal requirements of the fragile X mental retardation protein in the regulation of synaptic structure. Development 135, 2637–2648.

Gauducheau, M., Lemaire-Mayo, V., D'Amato, F.R., Oddi, D., Crusio, W.E., and Pietropaolo, S. (2017). Age-specific autistic-like behaviors in heterozygous *Fmr1*-KO female mice. Autism Research 10, 1067–1078.

Geschwind, D.H. (2008). Autism: Many Genes, Common Pathways? Cell 135, 391–395.

Ghosh, A., Michalon, A., Lindemann, L., Fontoura, P., and Santarelli, L. (2013). Drug discovery for autism spectrum disorder: challenges and opportunities. Nat Rev Drug Discov 12, nrd4102.

Gibson, J.R., Bartley, A.F., Hays, S.A., and Huber, K.M. (2008). Imbalance of Neocortical Excitation and Inhibition and Altered UP States Reflect Network Hyperexcitability in the Mouse Model of Fragile X Syndrome. J Neurophysiol 100, 2615–2626.

Gilbert, C.D., and Sigman, M. (2007). Brain States: Top-Down Influences in Sensory Processing. Neuron 54, 677–696.

Gonçalves, T.J., Anstey, J.E., Golshani, P., and Portera-Cailliau, C. (2013). Circuit level defects in the developing neocortex of Fragile X mice. Nature Neuroscience 16, nn.3415.

Green, J., Charman, T., Pickles, A., Wan, M.W., Elsabbagh, M., Slonims, V., Taylor, C., McNally, J., Booth, R., Gliga, T., et al. (2015). Parent-mediated intervention versus no intervention for infants at high risk of autism: a parallel, single-blind, randomised trial. Lancet Psychiatry 2, 133–140.

Greicius, M.D., Boyett-Anderson, J.M., Menon, V., and Reiss, A.L. (2004). Reduced basal forebrain and hippocampal activation during memory encoding in girls with fragile X syndrome. NeuroReport 15, 1579.

Groh, A., Meyer, H.S., Schmidt, E.F., Heintz, N., Sakmann, B., and Krieger, P. (2010). Cell-Type Specific Properties of Pyramidal Neurons in Neocortex Underlying a Layout that Is Modifiable Depending on the Cortical Area. Cerebral Cortex 20, 826–836.

Gross, C., Hoffmann, A., Bassell, G.J., and Berry-Kravis, E.M. (2015). Therapeutic Strategies in Fragile X Syndrome: From Bench to Bedside and Back. Neurotherapeutics 12, 584–608.

Gu, Y., McIlwain, K., and of …, W.E. (2002). Impaired conditioned fear and enhanced long-term potentiation inFmr2 knock-out mice.

Güçlü, B., Tanidir, C., Mukaddes, N., and Ünal, F. (2009). Tactile sensitivity of normal and autistic children. Somatosens Mot Res 24, 21–33.

Guo, W., Allan, A.M., Zong, R., Zhang, L., Johnson, E.B., Schaller, E.G., Murthy, A.C., Goggin, S.L., Eisch, A.J., Oostra, B.A., et al. (2011). Ablation of Fmrp in adult neural stem cells disrupts hippocampus-dependent learning. Nature Medicine 17, 559–565.

Guo, W., Ceolin, L., Collins, K.A., Perroy, J., and Huber, K.M. (2015). Elevated CaMKIIα and Hyperphosphorylation of Homer Mediate Circuit Dysfunction in a Fragile X Syndrome Mouse Model. Cell Reports 13, 2297–2311.

Haas, B.W., Ea-Goraly, N., Lightbody, A.A., Patnaik, S.S., Hoeft, F., Hazlett, H., Piven, J., And Reiss, A.L. (2009). Early white-matter abnormalities of the ventral frontostriatal pathway in fragile X syndrome. Developmental Medicine & Child Neurology 51, 593–599.

Haberl, M., da Silva, S., Guest, J.M., Ginger, M., Ghanem, A., Mulle, C., Oberlaender, M., Conzelmann, K.-K., and Frick, A. (2015a). An anterograde rabies virus vector for high-resolution large-scale reconstruction of 3D neuron morphology. Brain Structure and Function 220, 1369–1379.

Haberl, M., Ginger, M., and and, F.A. (2017). Dual anterograde and retrograde viral tracing of reciprocal connectivity.

Haberl, M.G., Zerbi, V., Veltien, A., Ginger, M., Heerschap, A., and Frick, A. (2015). Structural-functional connectivity deficits of neocortical circuits in the *Fmr1*−/y mouse model of autism. Science Advances 1, e1500775.

Hagerman, R.J., Berry-Kravis, E., Hazlett, H.C., Bailey, D.B., Moine, H., Kooy, R., Tassone, F., Gantois, I., Sonenberg, N., Mandel, J.L., et al. (2017). Fragile X syndrome. Nature Reviews. Disease Primers 3, 17065.

Hagerman, R.J., Berry-Kravis, E., Kaufmann, W.E., Ono, M.Y., Tartaglia, N., Lachiewicz, A., Kronk, R., Delahunty, C., Hessl, D., Visootsak, J., et al. (2009). Advances in the Treatment of Fragile X Syndrome. Pediatrics 123, 378–390.

Hall, S., Lightbody, A., and on Mental, R.A. (2008). Compulsive, self-injurious, and autistic behavior in children and adolescents with fragile X syndrome.

Hall, S.S., Dougherty, R.F., and Reiss, A.L. (2016). Profiles of aberrant white matter microstructure in fragile X syndrome. NeuroImage: Clinical 11, 133–138.

Hallmayer, J., Cleveland, S., Torres, A., Phillips, J., Cohen, B., Torigoe, T., Miller, J., Fedele, A., Collins, J., Smith, K., et al. (2011). Genetic Heritability and Shared Environmental Factors Among Twin Pairs with Autism. Arch Gen Psychiat 68, 1095–1102.

Hanson, D., Jackson, A., and of …, H.R. (1986). Speech disturbances (cluttering) in mildly impaired males with the Martin-Bell/fragile X syndrome.

Hanson, J.E., and Madison, D.V. (2007). Presynaptic *Fmr1* Genotype Influences the Degree of Synaptic Connectivity in a Mosaic Mouse Model of Fragile X Syndrome. The Journal of Neuroscience 27, 4014–4018.

Happé, F., Ronald, A., and Plomin, R. (2006). Time to give up on a single explanation for autism. Nat Neurosci 9, nn1770.

Harrison, C., Jack, E., Allen, T., and of medical genetics, H.R. (1983). The fragile X: a scanning electron microscope study.

Hartmann, M.J. (2011). A night in the life of a rat: vibrissal mechanics and tactile exploration. Ann Ny Acad Sci 1225, 110–118.

Hays, S.A., Huber, K.M., and Gibson, J.R. (2011). Altered Neocortical Rhythmic Activity States in *Fmr1-/-y* Mice Are Due to Enhanced mGluR5 Signaling and Involve Changes in Excitatory Circuitry. J Neurosci 31, 14223–14234.

He, C.X., Cantu, D.A., Mantri, S.S., Zeiger, W.A., Goel, A., and Portera-Cailliau, C. (2018). Tactile Defensiveness and Impaired Adaptation of Neuronal Activity in the Fmr1 Knock-Out Mouse Model of Autism. J Neurosci 37, 6475–6487.

He, Q., Arroyo, E.D., Smukowski, S.N., Xu, J., Piochon, C., Savas, J.N., Portera-Cailliau, C., and Contractor, A. (2018). Critical period inhibition of NKCC1 rectifies synapse plasticity in the somatosensory cortex and restores adult tactile response maps in fragile X mice. Molecular Psychiatry 1–16.

He, Q., Nomura, T., Xu, J., and Contractor, A. (2014). The Developmental Switch in GABA Polarity Is Delayed in Fragile X Mice. The Journal of Neuroscience 34, 446–450.

Higgins, L.S., and Cordell, B. (1995). Genetically Engineered Animal Models of Human Neurodegenerative Diseases. Neurodegeneration 4, 117–129.

Hinton, V., Brown, W., and of …, W.K. (1991). Analysis of neocortex in three males with the fragile X syndrome.

Hinton, V., Brown, W., and of …, W.K. (1991). Analysis of neocortex in three males with the fragile X syndrome.

Hirasawa, N., Yamada, K., and Murayama, M. (2016). Brief hind paw stimulation is sufficient to induce delayed somatosensory discrimination learning in C57BL/6 mice. Behavioural Brain Research 301, 102–109.

Hirst, M., Grewal, P., Flannery, A., Slatter, R., Maher, E., Barton, D., Fryns, J., and Davies, K. (1995). Two new cases of FMR1 deletion associated with mental impairment. Am J Hum Genet 56, 67–74.

Hodges, S.L., Nolan, S.O., Taube, J.H., and Lugo, J.N. (2017). Adult Fmr1 knockout mice present with deficiencies in hippocampal interleukin-6 and tumor necrosis factor-[alpha] expression. NeuroReport Publish Ahead of Print, 1.

Hodkinson, D.J., Veggeberg, R., Kucyi, A., van Dijk, K.R., Wilcox, S.L., Scrivani, S.J., Burstein, R., Becerra, L., and Borsook, D. (2016). Cortico-Cortical Connections of Primary Sensory Areas and Associated Symptoms in Migraine. Eneuro 3, ENEURO.0163-16.2016.

Hoeft, F., Carter, J.C., Lightbody, A.A., Hazlett, H., Piven, J., and Reiss, A.L. (2010). Region-specific alterations in brain development in one- to three-year-old boys with fragile X syndrome. Proceedings of the National Academy of Sciences 107, 9335–9339.

Holsen, L.M., lton, K., Johnstone, T., and Davidson, R.J. (2008). Prefrontal social cognition network dysfunction underlying face encoding and social anxiety in fragile X syndrome. NeuroImage 43, 592–604.

Huber, K.M., Gallagher, S.M., Warren, S.T., and Bear, M.F. (2002). Altered synaptic plasticity in a mouse model of fragile X mental retardation. Proceedings of the National Academy of Sciences 99, 7746–7750.

Humanes-Valera, D., Foffani, G., and Aguilar, J. (2014). Increased cortical responses to forepaw stimuli immediately after peripheral deafferentation of hindpaw inputs. Scientific Reports 4, 7278.

Iliff, A.J., Renoux, A.J., Krans, A., Usdin, K., Sutton, M.A., and Todd, P.K. (2013). Impaired activity-dependent FMRP translation and enhanced mGluR-dependent LTD in Fragile X premutation mice. Hum Mol Genet 22, 1180–1192.

Imlach, W.L., Finch, S.C., Dunlop, J., Meredith, A.L., Aldrich, R.W., and Dalziel, J.E. (2008). The Molecular Mechanism of "Ryegrass Staggers," a Neurological Disorder of K+ Channels. J Pharmacol Exp Ther 327, 657–664.

Irwin, S.A., Galvez, R., and Greenough, W.T. (2000). Dendritic Spine Structural Anomalies in Fragile-X Mental Retardation Syndrome. Cerebral Cortex 10, 1038–1044.

Irwin, S.A., Idupulapati, M., Gilbert, M.E., Harris, J.B., Chakravarti, A.B., Rogers, E.J., Crisostomo, R.A., Larsen, B.P., Mehta, A., Alcantara, C.J., et al. (2002). Dendritic spine and dendritic field characteristics of layer V pyramidal neurons in the visual cortex of fragile-X knockout mice. American Journal of Medical Genetics 111, 140–146.

Irwin, S.A., Patel, B., Idupulapati, M., Harris, J.B., Crisostomo, R.A., Larsen, B.P., Kooy, F., Willems, P.J., Cras, P., Kozlowski, P.B., et al. (2001). Abnormal dendritic spine characteristics in the temporal and visual cortices of patients with fragile-X syndrome: A quantitative examination. Am J Med Genet 98, 161–167.

Irwin, S.A., Swain, R.A., Christmon, C.A., Chakravarti, A., Weiler, I., and Greenough, W.T. (2000). Evidence for Altered Fragile-X Mental Retardation Protein Expression in Response to Behavioral Stimulation. Neurobiology of Learning and Memory 73, 87–93.

Jeste, S.S., and Geschwind, D.H. (2014). Disentangling the heterogeneity of autism spectrum disorder through genetic findings. Nat Rev Neurol 10, nrneurol.2013.278.

Jia, H., Rochefort, N.L., Chen, X., and Konnerth, A. (2010). Dendritic organization of sensory input to cortical neurons in vivo. Nature 464, nature08947.

Jiang, X., Shen, S., Cadwell, C.R., Berens, P., Sinz, F., Ecker, A.S., Patel, S., and Tolias, A.S. (2015). Principles of connectivity among morphologically defined cell types in adult neocortex. Science 350, aac9462.

Jin, P., Zarnescu, D.C., Ceman, S., Nakamoto, M., Mowrey, J., Jongens, T.A., Nelson, D.L., Moses, K., and Warren, S.T. (2004). Biochemical and genetic interaction between the fragile X mental retardation protein and the microRNA pathway. Nat Neurosci 7, 113–117.

Johnston, D., Frick, A., Poolos, N. (2016) Dendrites and disease. Oxford University Press, USA, 3rd Edition. Editors: Greg Stuart, Nelson Spruston, Michael Haeuser: Chapter 24, 677-702.Jørgensen, O., Nielsen, K., and Psychiatrica …, I.T. (1984). Fragile X-chromosome among child psychiatric patients with disturbances of language and social relationships.

Juczewski, K., von Richthofen, H., Bagni, C., Celikel, T., Fisone, G., and Krieger, P. (2016). Somatosensory map expansion and altered processing of tactile inputs in a mouse model of fragile X syndrome. Neurobiology of Disease 96, 201–215.

Just, M., Cherkassky, V.L., Keller, T.A., and Minshew, N.J. (2004). Cortical activation and synchronization during sentence comprehension in high-functioning autism: evidence of underconnectivity. Brain 127, 1811–1821.

Kaas, J.H. (1997). Topographic Maps are Fundamental to Sensory Processing. Brain Res Bull 44, 107–112.

Kaila, K., Price, T.J., Payne, J.A., Puskarjov, M., and Voipio, J. (2014). Cation-chloride cotransporters in neuronal development, plasticity and disease. Nat Rev Neurosci 15, 637–654.

Kalmbach, B.E., Johnston, D., and Brager, D.H. (2015). Cell-Type Specific Channelopathies in the Prefrontal Cortex of the fmr1-/y Mouse Model of Fragile X Syndrome. Eneuro 2, ENEURO.0114-15.2015.

Kandler, S., Mao, D., McNaughton, B.L., and Bonin, V. (2018). Encoding of Tactile Context in the Mouse Visual Cortex. Biorxiv 199364.

Kanner, L. (1968). Autistic disturbances of affective contact. Acta Paedopsychiatr 35, 100–136.

kanth Ramaswamy, and Muller, E.B. (2015). Cell-type specific modulation of neocortical UP and DOWN states. Frontiers in Cellular Neuroscience 9, 370.

Katz, L., and Shatz, C. (1996). Synaptic Activity and the Construction of Cortical Circuits. Science 274, 1133–1138.

Kaufmann, W.E., Abrams, M.T., Chen, W., and Reiss, A.L. (1999). Genotype, molecular phenotype, and cognitive phenotype: Correlations in fragile X syndrome. Am J Med Genet 83, 286–295.

Kayser, C., Petkov, C.I., Augath, M., and Logothetis, N.K. (2005). Integration of Touch and Sound in Auditory Cortex. Neuron 48, 373–384.

Kazdoba, T.M., Leach, P.T., Silverman, J.L., and Crawley, J.N. (2014). Modeling fragile X syndrome in the Fmr1 knockout mouse. Intractable & Rare Diseases Research 3, 118–133.

Khandjian, E., Corbin, F., Woerly, S., and Rousseau, F. (1996). The fragile X mental retardation protein is associated with ribosomes. Nature Genetics 12, 91–93.

Klusek, J., Martin, G., and Losh, M. (2014). Consistency between research and clinical diagnoses of autism among boys and girls with fragile X syndrome. J Intell Disabil Res 58, 940–952.

Knoth, I., Vannasing, P., Major, P., Michaud, J.L., and Lippé, S. (2014). Alterations of visual and auditory evoked potentials in fragile X syndrome. International Journal of Developmental Neuroscience 36, 90–97.

Kock, D., Bruno, R., Spors, H., and Sakmann, B. (2007). Layer- and cell-type-specific suprathreshold stimulus representation in rat primary somatosensory cortex. The Journal of Physiology 581, 139–154.

Koga, K., Liu, M.-G., Qiu, S., Song, Q., O'Den, G., Chen, T., and Zhuo, M. (2015). Impaired Presynaptic Long-Term Potentiation in the Anterior Cingulate Cortex of Fmr1 Knock-out Mice. The Journal of Neuroscience 35, 2033–2043.

Kogan, C., Bertone, A., Cornish, K., Boutet, I., Kaloustian, D.V., Andermann, E., Faubert, J., and Chaudhuri, A. (2004). Integrative cortical dysfunction and pervasive motion perception deficit in fragile X syndrome. Neurology 63, 1634–1639.

Komotar, R.J., Kim, G.H., Sughrue, M.E., Otten, M.L., Rynkowski, M.A., Kellner, C.P., Hahn, D.K., Merkow, M.B., Garrett, M.C., arke, R., et al. (2007). Neurologic assessment of somatosensory dysfunction following an experimental rodent model of cerebral ischemia. Nat Protoc 2, nprot.2007.359.

Kootz, J.P., Marinelli, B., and Cohen, D.J. (1981). Sensory Receptor Sensitivity in Autistic Children: Response Times to Proximal and Distal Stimulation. Archives of General Psychiatry 38, 271–273.

Kooy, F.R. (2003). Of mice and the fragile X syndrome. Trends in Genetics 19, 148–154.

Kooy, R., D'Hooge, R., and of …, R.E. (1996). Transgenic mouse model for the fragile X syndrome.

Kooy, R.F., Willemsen, R., and Oostra, B.A. (2000). Fragile X syndrome at the turn of the century. Molecular Medicine Today 6, 193–198.

Kramvis, I., Mansvelder, H.D., Loos, M., and Meredith, R. (2013). Hyperactivity, perseveration and increased responding during attentional rule acquisition in the Fragile X mouse model. Frontiers in Behavioral Neuroscience 7, 172.

Krueger, D.D., Osterweil, E.K., Chen, S.P., Tye, L.D., and Bear, M.F. (2011). Cognitive dysfunction and prefrontal synaptic abnormalities in a mouse model of fragile X syndrome. Proceedings of the National Academy of Sciences 108, 2587–2592.

Kwan, K.Y., Lam, M., Johnson, M.B., Dube, U., Shim, S., Rašin, M.-R., Sousa, A., Fertuzinhos, S., Chen, J.-G., Arellano, J.I., et al. (2012). Species-Dependent Posttranscriptional Regulation of NOS1 by FMRP in the Developing Cerebral Cortex. Cell 149, 899–911.

Lane, A.E., Young, R.L., Baker, A.E., and Angley, M.T. (2010). Sensory Processing Subtypes in Autism: Association with Adaptive Behavior. J Autism Dev Disord 40, 112–122.

Lee, A.K., and Brecht, M. (2018). Elucidating Neuronal Mechanisms Using Intracellular Recordings during Behavior. Trends in Neurosciences.

Lee, J.J., Wedow, R., Okbay, A., Kong, E., Maghzian, O., Zacher, M., Nguyen-Viet, T.A., Bowers, P., Sidorenko, J., Linnér, R.K., et al. (2018a). Gene discovery and polygenic prediction from a genome-wide association study of educational attainment in 1.1 million individuals. Nat Genet 50, 1112–1121.

Lemaire-Mayo, V., Subashi, E., Henkous, N., Beracochea, D., and Pietropaolo, S. (2017). Behavioral effects of chronic stress in the *Fmr1* mouse model for fragile X syndrome. Behavioural Brain Research 320, 128–135.

Li, J., Ma, Z., Shi, M., Malty, R.H., Aoki, H., Minic, Z., Phanse, S., Jin, K., Wall, D.P., Zhang, Z., et al. (2015). Identification of Human Neuronal Protein Complexes Reveals Biochemical Activities and Convergent Mechanisms of Action in Autism Spectrum Disorders. Cell Syst 1, 361–374.

Li, J., Pelletier, M.R., Velazquez, J.-L., and Carlen, P.L. (2002). Reduced Cortical Synaptic Plasticity and GluR1 Expression Associated with Fragile X Mental Retardation Protein Deficiency. Molecular and Cellular Neuroscience 19, 138–151.

Lima-Cabello, E., Garcia-Guirado, F., Calvo-Medina, R., el Bekay, R., Perez-Costillas, L., Quintero-Navarro, C., Sanchez-Salido, L., and de Diego-Otero, Y. (2016). An Abnormal Nitric Oxide Metabolism Contributes to Brain Oxidative Stress in the Mouse Model for the Fragile X Syndrome, a Possible Role in Intellectual Disability. Oxidative Medicine and Cellular Longevity 2016, 1–12.

Lin, J.-W., and Faber, D.S. (2002). Modulation of synaptic delay during synaptic plasticity. Trends in Neurosciences 25, 449–455.

Liska, A., Bertero, A., Gomolka, R., Sabbioni, M., Galbusera, A., Barsotti, N., Panzeri, S., Scattoni, M.L., Pasqualetti, M., and Gozzi, A. (2017). Homozygous Loss of Autism-Risk Gene CNTNAP2 Results in Reduced Local and Long-Range Prefrontal Functional Connectivity. Cerebral Cortex (New York, N.Y. : 1991) 1–13.

Liu, Z.-H., and Smith, C. (2009). Dissociation of social and nonsocial anxiety in a mouse model of fragile X syndrome. Neuroscience Letters 454, 62–66.

London, M., and Häusser, M. (2005). DENDRITIC COMPUTATION. Annu Rev Neurosci 28, 503–532.

Lubs, H. (1969). A marker X chromosome. Am J Hum Genet 21, 231–244.

Lumaban, J.G., and Nelson, D.L. (2015). The Fragile X proteins Fmrp and Fxr2p cooperate to regulate glucose metabolism in mice. Human Molecular Genetics 24, 2175–2184.

Luque, A.M., Beltran-Matas, P., Marin, C.M., Torres, B., and Herrero, L. (2017). Excitability is increased in hippocampal CA1 pyramidal cells of Fmr1 knockout mice. PLOS ONE 12, e0185067.

Mainen, Z., and Sejnowski, T. (1995). Reliability of spike timing in neocortical neurons. Science *268*, 1503–1506.

Mainen, Z.F., and Sejnowski, T.J. (1996). Influence of dendritic structure on firing pattern in model neocortical neurons. Nature 382, 382363a0.

Manita, S., Suzuki, T., Homma, C., Matsumoto, T., Odagawa, M., Yamada, K., Ota, K., Matsubara, C., Inutsuka, A., Sato, M., et al. (2015). A Top-Down Cortical Circuit for Accurate Sensory Perception. Neuron 86, 1304–1316.

Marco, E.J., and Skuse, D.H. (2006). Autism-lessons from the X chromosome. Social Cognitive and Affective Neuroscience 1, 183–193.

Marco, E.J., Hinkley, L., Hill, S.S., and Nagarajan, S.S. (2011). Sensory Processing in Autism: A Review of Neurophysiologic Findings. Pediatr Res 69, 48R.

Martin, P.J., and Bell, J. (1943). A pedigree of mental defect showing sex-linkage. J Neurology Psychiatry 6, 154–157.

Marx, M., Günter, R.H., Hucko, W., Radnikow, G., and Feldmeyer, D. (2012). Improved biocytin labeling and neuronal 3D reconstruction. Nature Protocols 7, nprot.2011.449.

Matsubara, J.A., Chase, R., and Thejomayen, M. (1996). Comparative morphology of three types of projection-identified pyramidal neurons in the superficial layers of cat visual cortex. J Comp Neurol 366, 93–108.

McKinney, B.C., Grossman, A.W., Elisseou, N.M., and Greenough, W.T. (2005). Dendritic spine abnormalities in the occipital cortex of C57BL/6 Fmr1 knockout mice. American Journal of Medical Genetics Part B: Neuropsychiatric Genetics 136B, 98–102.

McNaughton, C.H., Moon, J., Strawderman, M.S., Maclean, K.N., Evans, J., and Strupp, B.J. (2008). Evidence for social anxiety and impaired social cognition in a mouse model of fragile X syndrome. Behavioral Neuroscience 122, 293.

Medini, P. (2011). Cell-type–specific sub- and suprathreshold receptive fields of layer 4 and layer 2/3 pyramids in rat primary visual cortex. Neuroscience 190, 112–126.

Meijer, H., de Graaff, E., Merckx, D., Jongbloed, R., de Die-Smulders, C., Engelen, J., Fryns, J., Curfs, P., and Oostra (1994). A deletion of 1.6 kb proximal to the CGG repeat of the FMR1 gene causes the clinical phenotype of the fragile X syndrome. Hum Mol Genet 3, 615–620.

Merenstein, S.A., Sobesky, W.E., Taylor, A.K., Riddle, J.E., Tran, H.X., and Hagerman, R.J. (1996). Molecular-clinical correlations in males with an expanded FMR1 mutation. Am J Med Genet 64, 388–394.

Meryash, D.L., Szymanski, L.S., and Gerald, P.S. (1982). Infantile autism associated with the Fragile-X syndrome. Journal of Autism and Developmental Disorders 12, 295–301.

Mientjes, E.J., Nieuwenhuizen, I., Kirkpatrick, L., Zu, T., Hoogeveen-Westerveld, M., Severijnen, L., Rifé, M., Willemsen, R., Nelson, D.L., and Oostra (2006). The generation of a conditional *Fmr1* knock out mouse model to study Fmrp function in vivo. Neurobiology of Disease 21, 549–555.

Mikkelsen, M., Wodka, E.L., Mostofsky, S.H., and Puts, N. (2018). Autism spectrum disorder in the scope of tactile processing. Dev Cogn Neurosci 29.

Milenkovic, N., Zhao, W.-J., Walcher, J., Albert, T., Siemens, J., Lewin, G.R., and Poulet, J.F. (2014). A somatosensory circuit for cooling perception in mice. Nat Neurosci 17, 1560–1566.

Mineur, Y.S., Sluyter, F., de Wit, S., Oostra, B.A., and Crusio, W.E. (2002). Behavioral and neuroanatomical characterization of the *Fmr1* knockout mouse. Hippocampus 12, 39–46.

Mo, A., Mukamel, E.A., Davis, F.P., Luo, C., Henry, G.L., Picard, S., Urich, M.A., Nery, J.R., Sejnowski, T.J., Lister, R., et al. (2015). Epigenomic Signatures of Neuronal Diversity in the Mammalian Brain. Neuron 86, 1369–1384.

Mo, C., Petrof, I., Viaene, A.N., and Sherman, M.S. (2017). Synaptic properties of the lemniscal and paralemniscal pathways to the mouse somatosensory thalamus. Proc National Acad Sci 114, E6212–E6221.

Molholm, S., Ritter, W., Murray, M.M., Javitt, D.C., Schroeder, C.E., and Foxe, J.J. (2002). Multisensory auditory–visual interactions during early sensory processing in humans: a high-density electrical mapping study. Cognitive Brain Res 14, 115–128.

Moore, B., Glover, T., Kaiser-McCaw, B., and Hecht, F. (1982). Fragile X-linked mental retardation of macro-orchidism. The Western Journal of Medicine 137, 278–281.

Morales-Botello, M., Aguilar, J., and Foffani, G. (2012). Imaging the Spatio-Temporal Dynamics of Supragranular Activity in the Rat Somatosensory Cortex in Response to Stimulation of the Paws. PLoS ONE 7, e40174.

Moy, S., and Nadler, J. (2008). Advances in behavioral genetics: mouse models of autism. Molecular Psychiatry 13, 4–26.

Munir, F., Cornish, K., and Neuropsychologia, W.J. (2000). A neuropsychological profile of attention deficits in young males with fragile X syndrome.

Nair, A., Treiber, J.M., Shukla, D.K., Shih, P., and Müller, R.-A. (2013). Impaired thalamocortical connectivity in autism spectrum disorder: a study of functional and anatomical connectivity. Brain 136, 1942–1955.

Nelson, S.B., Sugino, K., and Hempel, C.M. (2006). The problem of neuronal cell types: a physiological genomics approach. Trends Neurosci 29, 339–345.

Neuhofer, D., Henstridge, C.M., Dudok, B., Sepers, M., Lassalle, O., Katona, I., and Manzoni, O.J. (2015). Functional and structural deficits at accumbens synapses in a mouse model of Fragile X. Frontiers in Cellular Neuroscience 9, 100.

Nicolelis, M.A., Ghazanfar, A.A., Stambaugh, C.R., Oliveira, L.M., Laubach, M., Chapin, J.K., Nelson, R.J., and Kaas, J.H. (1998). Simultaneous encoding of tactile information by three primate cortical areas. Nature Neuroscience 1, 621–630.

Nolan, S.O., and Lugo, J.N. (2018). Reversal learning paradigm reveals deficits in cognitive flexibility in the *Fmr1* knockout male mouse. F1000research 7, 711.

Nolan, S.O., Reynolds, C.D., Smith, G.D., Holley, A.J., Escobar, B., Chandler, M.A., Volquardsen, M., Jefferson, T., Pandian, A., Smith, T., et al. (2017). Deletion of *Fmr1* results in sex-specific changes in behavior. Brain and Behavior 7, e00800.

Noto, V., Harrity, C., Walsh, D., and Marron, K. (2016). The impact of FMR1 gene mutations on human reproduction and development: a systematic review. J Assist Reprod Gen 33, 1135–1147.

O'Riordan, M., and Passetti, F. (2006). Discrimination in Autism Within Different Sensory Modalities. Journal of Autism and Developmental Disorders 36, 665–675.

Oberle, I., Rousseau, F., Heitz, D., Kretz, C., Devys, D., Hanauer, A., Boue, J., Bertheas, M., and Mandel, J. (1991). Instability of a 550-base pair DNA segment and abnormal methylation in fragile X syndrome. Science 252, 1097–1102.

O'Donnell, C., and van Rossum, M.C. (2014). Systematic analysis of the contributions of stochastic voltage gated channels to neuronal noise. Front Comput Neurosc *8*, 105.

Oddi, D., Crusio, W.E., D'Amato, F.R., and Pietropaolo, S. (2013). Monogenic mouse models of social dysfunction: Implications for autism. Behav Brain Res 251, 75–84.

Oddi, D., Subashi, E., Middei, S., Bellocchio, L., Lemaire-Mayo, V., Guzmán, M., Crusio, W.E., D'Amato, F.R., and Pietropaolo, S. (2015). Early Social Enrichment Rescues Adult Behavioral and Brain Abnormalities in a Mouse Model of Fragile X Syndrome. Neuropsychopharmacology 40, 1113–1122.

Olcese, U., Iurilli, G., and Medini, P. (2013). Cellular and Synaptic Architecture of Multisensory Integration in the Mouse Neocortex. Neuron 79, 579–593.

Orefice, L.L., Zimmerman, A.L., Chirila, A.M., Sleboda, S.J., Head, J.P., and Ginty, D.D. (2016). Peripheral Mechanosensory Neuron Dysfunction Underlies Tactile and Behavioral Deficits in Mouse Models of ASDs. Cell 166, 299–313.

Padmashri, R., Reiner, B.C., Suresh, A., Spartz, E., and Dunaevsky, A. (2013). Altered Structural and Functional Synaptic Plasticity with Motor Skill Learning in a Mouse Model of Fragile X Syndrome. The Journal of Neuroscience 33, 19715–19723.

Palmer, L.M., hulz, J., Murphy, S.C., Ledergerber, D., Murayama, M., and Larkum, M.E. (2012). The Cellular Basis of GABAB-Mediated Interhemispheric Inhibition. Science 335, 989–993.

Parikshak, N.N., Luo, R., Zhang, A., Won, H., Lowe, J.K., Chandran, V., Horvath, S., and Geschwind, D.H. (2013). Integrative Functional Genomic Analyses Implicate Specific Molecular Pathways and Circuits in Autism. Cell 155, 1008–1021.

Paul, R., Dykens, E., Leckman, J.F., Watson, M., Breg, R.W., and Cohen, D.J. (1987). A comparison of language characteristics of mentally retarded adults with fragile X syndrome and those with nonspecific mental retardation and autism. Journal of Autism and Developmental Disorders 17, 457–468.

Penagarikano, O., Mulle, J.G., and Warren, S.T. (2007). The Pathophysiology of Fragile X Syndrome. Annual Review of Genomics and Human Genetics 8, 109–129.

Pereira, A., Ribeiro, S., Wiest, M., Moore, L.C., Pantoja, J., Lin, S.-C., and Nicolelis, M.A. (2007). Processing of tactile information by the hippocampus. Proceedings of the National Academy of Sciences 104, 18286–18291.

Petersen C, Crochet S. Synaptic computation and sensory processing in neocortical layer 2/3. Neuron 2013.

Petersen, C.C., Grinvald, A., and Sakmann, B. (2003). Spatiotemporal dynamics of sensory responses in layer 2/3 of rat barrel cortex measured in vivo by voltage-sensitive dye imaging combined with whole-cell voltage recordings and neuron reconstructions. The Journal of Neuroscience: The Official Journal of the Society for Neuroscience 23, 1298–1309.

Petersen, C.C., Hahn, T.T., Mehta, M., Grinvald, A., and Sakmann, B. (2003). Interaction of sensory responses with spontaneous depolarization in layer 2/3barrel cortex. Proceedings of the National Academy of Sciences 100, 13638–13643.

Pfeiffer, B.E., and Foster, D.J. (2015). Autoassociative dynamics in the generation of sequences of hippocampal place cells. Science 349, 180–183.

Pfeiffer, B.E., and Huber, K.M. (2007). Fragile X Mental Retardation Protein Induces Synapse Loss through Acute Postsynaptic Translational Regulation. The Journal of Neuroscience 27, 3120–3130.

Pieretti, M., Zhang, F., Fu, Y.-H., Warren, S.T., Oostra, B.A., Caskey, C.T., and Nelson, D.L. (1991). Absence of expression of the FMR-1 gene in fragile X syndrome. Cell 66, 817–822.

Pilpel, Y., Kolleker, A., Berberich, S., Ginger, M., Frick, A., Mientjes, E., Oostra, B.A., and Seeburg, P.H. (2009). Synaptic ionotropic glutamate receptors and plasticity are developmentally altered in the CA1 field of *Fmr1* knockout mice. The Journal of Physiology 587, 787–804.

Pueschel, S.M., Herman, R., and Groden, G. (1985). Brief report: Screening children with autism for fragile-X syndrome and phenylketonuria. Journal of Autism and Developmental Disorders 15, 335–338.

Puts, N.A., Wodka, E.L., Tommerdahl, M., Mostofsky, S.H., and Edden, R.A. (2014). Impaired tactile processing in children with autism spectrum disorder. J Neurophysiol *111*, 1803–1811.

Pyronneau, A., He, Q., Hwang, J.-Y., Porch, M., Contractor, A., and Zukin, S.R. (2017). Aberrant Rac1-cofilin signaling mediates defects in dendritic spines, synaptic function, and sensory perception in fragile X syndrome. Sci. Signal. 10, eaan0852.

Qin, M., Kang, J., Burlin, T.V., Jiang, C., and Smith, C. (2005). Postadolescent Changes in Regional Cerebral Protein Synthesis: An In Vivo Study in the *Fmr1* Null Mouse. The Journal of Neuroscience 25, 5087–5095.

Qin, M., Schmidt, K.C., Zametkin, A.J., Bishu, S., Horowitz, L.M., Burlin, T.V., Xia, Z., Huang, T., Quezado, Z.M., and Smith, C. (2013). Altered Cerebral Protein Synthesis in Fragile X Syndrome: Studies in Human Subjects and Knockout Mice. Journal of Cerebral Blood Flow & Metabolism 33, 499–507.

Qin, M., Xia, Z., Huang, T., and Smith, C.B. (2011). Effects of chronic immobilization stress on anxiety-like behavior and basolateral amygdala morphology in *Fmr1* knockout mice. Neuroscience 194, 282–290.

Rague, L., Caravella, K., Tonnsen, B., Klusek, J., and Roberts, J. (2017). Early gesture use in fragile X syndrome. Journal of Intellectual Disability Research.

Reiss, A., Abrams, M., Greenlaw, R., Freund, L., and Denckla (1995). Neurodevelopmental effects of the FMR-1 full mutation in humans. Nature Medicine 1, 159–167.

Reiss, A.L., and Dant, C.C. (2003). The behavioral neurogenetics of fragile X syndrome: Analyzing gene–brain–behavior relationships in child developmental psychopathologies. Dev Psychopathol 15, 927–968.

Riley, C., and Wheeler, A. (2017). Assessing the Fragile X Syndrome Newborn Screening Landscape. Pediatrics 139, S207–S215.

Renier, N., Adams, E.L., Kirst, C., Wu, Z., Azevedo, R., Kohl, J., Autry, A.E., Kadiri, L., Venkataraju, K.U., Zhou, Y., Wang, V.X., Tang, C.Y., Olsen, O., Dulac, C., Osten, P., Tessier-Lavigne, M., 2016. Mapping of Brain Activity by Automated Volume Analysis of Immediate Early Genes. Cell 165, 1789–1802.

Rensen, E., Bertelsen, F., Weikop, P., ovborg, M., Banke, T., Drasbek, K.R., and Scheel-Krüger, J. (2015). Hyperactivity and lack of social discrimination in the adolescent *Fmr1* knockout mouse. Behavioural Pharmacology 26, 733.

Restivo, L., Ferrari, F., Passino, E., Sgobio, C., Bock, J., Oostra, B.A., Bagni, C., and Ammassari-Teule, M. (2005). Enriched environment promotes behavioral and morphological recovery in a mouse model for the fragile X syndrome. Proceedings of the National Academy of Sciences of the United States of America 102, 11557–11562.

Reyniers, E., Martin, J., and of …, C.P. (1999). Postmortem examination of two fragile X brothers with an FMR1 full mutation.

Robertson, C.E., and Baron-Cohen, S. (2017). Sensory perception in autism. Nature Reviews Neuroscience 18, nrn.2017.112.

Rohe, T., and Noppeney, U. (2016). Distinct Computational Principles Govern Multisensory Integration in Primary Sensory and Association Cortices. Curr Biol 26, 509–514.

Ronesi, J.A., Collins, K.A., Hays, S.A., Tsai, N.-P., Guo, W., Birnbaum, S.G., Hu, J.-H., Worley, P.F., Gibson, J.R., and Huber, K.M. (2012). Disrupted Homer scaffolds mediate abnormal mGluR5 function in a mouse model of fragile X syndrome. Nature Neuroscience 15, 431–440.

Rotschafer, S., and Razak, K. (2013). Altered auditory processing in a mouse model of fragile X syndrome. Brain Research 1506, 12–24.

Rotschafer, S.E., and Razak, K.A. (2014). Auditory Processing in Fragile X Syndrome. Frontiers in Cellular Neuroscience 8, 19.

Routh, B.N., Rathour, R.K., Baumgardner, M.E., Kalmbach, B.E., Johnston, D., and Brager, D.H. (2017). Increased transient Na+ conductance and action potential output in layer 2/3 prefrontal cortex neurons of the fmr1−/y mouse. The Journal of Physiology 595, 4431–4448.

Roy, S., Zhao, Y., Allensworth, M., Farook, M.F., LeDoux, M.S., Reiter, L.T., and Heck, D.H. (2011). Comprehensive motor testing in *Fmr1*-KO mice exposes temporal defects in oromotor coordination. Behavioral Neuroscience 125, 962.

Rudelli, R., Brown, W., Wisniewski, K., Jenkins, E., Laure-Kamionowska, M., Connell, F., and Wisniewski, H. (1985). Adult fragile X syndrome. Acta Neuropathol 67, 289–295.

Saffary, R., and Xie, Z. (2011). FMRP Regulates the Transition from Radial Glial Cells to Intermediate Progenitor Cells during Neocortical Development. The Journal of Neuroscience 31, 1427–1439.

Sailer, C.A., Kaufmann, W.A., Kogler, M., Chen, L., Sausbier, U., Ottersen, O., Ruth, P., Shipston, M.J., and Knaus, H. (2006). Immunolocalization of BK channels in hippocampal pyramidal neurons. Eur J Neurosci 24, 442–454.

Schauder, K.B., Park, W., Tadin, D., and Bennetto, L. (2017). Larger Receptive Field Size as a Mechanism Underlying Atypical Motion Perception in Autism Spectrum Disorder. Clin Psychological Sci 5, 827–842.

Schmeisser, M.J., Ey, E., Wegener, S., Bockmann, J., Stempel, V.A., Kuebler, A., Janssen, A.-L., Udvardi, P.T., Shiban, E., Spilker, C., et al. (2012). Autistic-like behaviours and hyperactivity in mice lacking ProSAP1/Shank2. Nature 486, nature11015.

Schroeter, A., Grandjean, J., Schlegel, F., Saab, B.J., and Rudin, M. (2016). Contributions of structural connectivity and cerebrovascular parameters to functional magnetic resonance imaging signals in mice at rest and during sensory paw stimulation. Journal of Cerebral Blood Flow & Metabolism 37, 2368–2382.

Schütt, J., Falley, K., Richter, D., Kreienkamp, H.-J., and Kindler, S. (2009). Fragile X Mental Retardation Protein Regulates the Levels of Scaffold Proteins and Glutamate Receptors in Postsynaptic Densities. Journal of Biological Chemistry 284, 25479–25487.

Schwarzkopf, S.D., Anderson, E.J., de Haas, B., White, S.J., and Rees, G. (2014). Larger Extrastriate Population Receptive Fields in Autism Spectrum Disorders. J Neurosci 34, 2713–2724.

Scott, K.E., Schormans, A.L., Pacoli, K., Oliveira, C., Allman, B.L., and Schmid, S. (2018). Altered auditory processing, filtering, and reactivity in theCntnap2knockout rat model for neurodevelopmental disorders. J Neurosci 0759–18.

Scotto-Lomassese, S., Nissant, A., Mota, T., Néant-Féry, M., Oostra, B.A., Greer, C.A., Lledo, P.-M., Trembleau, A., and Caillé, I. (2011). Fragile X Mental Retardation Protein Regulates New Neuron Differentiation in the Adult Olfactory Bulb. The Journal of Neuroscience 31, 2205–2215.

Senkowski, D., Schneider, T.R., Foxe, J.J., and Engel, A.K. (2008). Crossmodal binding through neural coherence: implications for multisensory processing. Trends Neurosci 31, 401–409.

Sethna, F., Feng, W., Ding, Q., Robison, A.J., Feng, Y., and Wang, H. (2017). Enhanced expression of ADCY1 underlies aberrant neuronal signalling and behaviour in a syndromic autism model. Nature Communications 8, 14359.

Shadlen, M.N., and Newsome, W.T. (1998). The Variable Discharge of Cortical Neurons: Implications for Connectivity, Computation, and Information Coding. J Neurosci 18, 3870–3896.

Shang, Y., Wang, H., Mercaldo, V., Li, X., Chen, T., and Zhuo, M. (2009). Fragile X mental retardation protein is required for chemically-induced long-term potentiation of the hippocampus in adult mice. Journal of Neurochemistry 111, 635–646.

Sharpee, T.O. (2014). Toward Functional Classification of Neuronal Types. Neuron 83, 1329–1334.

Shimaoka, D., Harris, K.D., and Carandini, M. (2018). Effects of Arousal on Mouse Sensory Cortex Depend on Modality. Cell Reports 22, 3160–3167.

Sidorov, M.S., Auerbach, B.D., and Bear, M.F. (2013). Fragile X mental retardation protein and synaptic plasticity. Molecular Brain 6, 1–11.

Simons, D.J., and Land, P.W. (1987). Early experience of tactile stimulation influences organization of somatic sensory cortex. Nature 326, 326694a0.

Sinclair, D., Oranje, B., Razak, K., Siegel, S., and Schmid, S. (2017). Sensory processing in autism spectrum disorders and Fragile X syndrome-From the clinic to animal models. Neuroscience and Biobehavioral Reviews 76, 235–253.

Smalley, S.L. (1998). Autism and Tuberous Sclerosis. J Autism Dev Disord 28, 407–414.

Sourial, M., and Doering, L.C. (2017). Abnormal neural precursor cell regulation in the early postnatal Fragile X mouse hippocampus. Brain Research 1666, 58–69.

Sporns, O., Tononi, G., and Edelman, G.M. (2000). Theoretical Neuroanatomy: Relating Anatomical and Functional Connectivity in Graphs and Cortical Connection Matrices. Cereb Cortex 10, 127–141.

Sreenivasan V, Kyriakatos A, Mateo C, Jaeger D, Petersen C. Parallel pathways from whisker and visual sensory cortices to distinct frontal regions of mouse neocortex. Neurophotonics 2017; **4**: 031203–031203.

Sugino, K., Clark, E., Schulmann, A., Shima, Y., Wang, L., Hunt, D.L., Hooks, B.M., Trankner, D., Chandrashekar, J., Picard, S., et al. (2017). The Transcriptional Logic of Mammalian Neuronal Diversity. Biorxiv 208355.

Sunamura, N., Iwashita, S., Enomoto, K., Kadoshima, T., and Isono, F. (2018). Loss of the fragile X mental retardation protein causes aberrant differentiation in human neural progenitor cells. Sci Reports 8, 11585.

Suvrathan, A., Hoeffer, C.A., Wong, H., Klann, E., and Chattarji, S. (2010). Characterization and reversal of synaptic defects in the amygdala in a mouse model of fragile X syndrome. Proceedings of the National Academy of Sciences 107, 11591–11596.

Sych, Y., Chernysheva, M., Sumanovski, L., and Helmchen, F. (2018). High-density multi-fiber photometry for studying large-scale brain circuit dynamics. Biorxiv 422857.
Szlapczynska. M, Audrey Bonnan, Melanie Ginger and Andreas Frick. (2014). Plasticity and Pathology of Dendritic Intrinsic Excitability. In: Horizons in Neuroscience Research 14, 41-88.

Tabet, R., Moutin, E., Becker, J.A., Heintz, D., Fouillen, L., Flatter, E., Krężel, W., Alunni, V., Koebel, P., Dembélé, D., et al. (2016). Fragile X Mental Retardation Protein (FMRP) controls diacylglycerol kinase activity in neurons. Proceedings of the National Academy of Sciences 113, E3619–E3628.

Talbot, Z., Sparks, F., Dvorak, D., Curran, B., Alarcon, J., and Fenton, A. (2018). Normal CA1 Place Fields but Discoordinated Network Discharge in a Fmr1-Null Mouse Model of Fragile X Syndrome. Neuron.

Tang, B., Wang, T., Wan, H., Han, L., and of the …, Q.X. (2015). *Fmr1* deficiency promotes age-dependent alterations in the cortical synaptic proteome.

Tasic, B., Menon, V., Nguyen, T.N., Kim, T.K., Jarsky, T., Yao, Z., Levi, B., Gray, L.T., Sorensen, S.A., Dolbeare, T., et al. (2016). Adult mouse cortical cell taxonomy revealed by single cell transcriptomics. Nature Neuroscience 19, 335–346.

Tassone, F., Hagerman, R.J., Iklé, D.N., Dyer, P.N., Lampe, M., Willemsen, R., Oostra, B.A., and Taylor, A.K. (1999). FMRP expression as a potential prognostic indicator in fragile X syndrome. Am J Med Genet 84, 250–261.

Tavassoli, T., Miller, L., Schoen, S.A., Brout, J., Sullivan, J., and Baron-Cohen, S. (2018). Sensory reactivity, empathizing and systemizing in autism spectrum conditions and sensory processing disorder. Developmental Cognitive Neuroscience 29. Adusei, D.C., Pacey, L., Chen, D., and Hampson, D.R. (2010). Early developmental alterations in GABAergic protein expression in fragile X knockout mice. Neuropharmacology 59, 167–171.

Theobald, T., Hay, D., and of …, J.C. (1987). Individual variation and specific cognitive deficits in the fra (X) syndrome.

Tian, Y., Yang, C., Shang, S., Cai, Y., Deng, X., Zhang, J., Shao, F., Zhu, D., Liu, Y., Chen, G., et al. (2017). Loss of FMRP Impaired Hippocampal Long-Term Plasticity and Spatial Learning in Rats. Frontiers in Molecular Neuroscience 10, 269.

Till, S.M., Asiminas, A., Jackson, A.D., Katsanevaki, D., Barnes, S.A., Osterweil, E.K., Bear, M.F., Chattarji, S., Wood, E.R., Wyllie, D., et al. (2015). Conserved hippocampal cellular pathophysiology but distinct behavioural deficits in a new rat model of FXS. Human Molecular Genetics 24, 5977–5984.

Till, S.M., Li, H.-L., Miniaci, M., Kandel, E.R., and Choi, Y.-B. (2011). A presynaptic role for FMRP during protein synthesis–dependent long-term plasticity in Aplysia. Learning & Memory 18, 39–48.

Till, S.M., Wijetunge, L.S., Seidel, V.G., Harlow, E., Wright, A.K., Bagni, C., Contractor, A., Gillingwater, T.H., and Kind, P.C. (2012). Altered maturation of the primary somatosensory cortex in a mouse model of fragile X syndrome. Human Molecular Genetics 21, 2143–2156.

Todd, P.K., and Mack, K.J. (2000). Sensory stimulation increases cortical expression of the fragile X mental retardation protein in vivo. Molecular Brain Research 80, 17–25.

Tomasi, D., and Volkow, N.D. (2017). Reduced Local and Increased Long-Range Functional Connectivity of the Thalamus in Autism Spectrum Disorder. Cerebral Cortex (New York, N.Y. : 1991).

Tomchek, S., and Dunn, W. (2007). Sensory Processing in Children With and Without Autism: A Comparative Study Using the Short Sensory Profile. American Journal of Occupational Therapy 61, 190–200.

Toro, L., Wallner, M., Meera, P., and Tanaka, Y. (1998). Maxi-K(Ca), a Unique Member of the Voltage-Gated K Channel Superfamily. News Physiological Sci Int J Physiology Prod Jointly Int Union Physiological Sci Am Physiological Soc 13, 112–117.

Tripathy, S.J., Padmanabhan, K., Gerkin, R.C., and Urban, N.N. (2013). Intermediate intrinsic diversity enhances neural population coding. Proc National Acad Sci 110, 8248–8253.

Trottier, G., vastava, L., and of and, W.C. (1999). Etiology of infantile autism: a review of recent advances in genetic and neurobiological research.

Uchida, I., Freeman, V., and journal of …, J.H. (1983). Additional evidence for fragile X activity in heterozygous carriers.

Uhlhaas, P.J., and Singer, W. (2006). Neural Synchrony in Brain Disorders: Relevance for Cognitive Dysfunctions and Pathophysiology. Neuron 52, 155–168.

Uljarević, M., Hedley, D., Alvares, G.A., Varcin, K.J., and Whitehouse, A.J. (2017). Relationship between early motor milestones and severity of restricted and repetitive behaviors in children and adolescents with autism spectrum disorder. Autism Res 10, 1163–1168.

van Atteveldt, N., Murray, M.M., Thut, G., and Schroeder, C.E. (2014). Multisensory Integration: Flexible Use of General Operations. Neuron 81, 1240–1253.

van der Molen, M.J., Stam, C.J., and van der Molen, M.W. (2014). Resting-State EEG Oscillatory Dynamics in Fragile X Syndrome: Abnormal Functional Connectivity and Brain Network Organization. Plos One 9, e88451.

van Padje, S., Engels, B., Blonden, L., Severijnen, L.-A., Verheijen, F., Oostra, B.A., and Willemsen, R. (2005). Characterisation of Fmrp in zebrafish: evolutionary dynamics of the *Fmr1* gene. Development Genes and Evolution 215, 198–206.

Veenema, H., Veenema, T., and of medical genetics, G.J. (1987). The fragile X syndrome in a large family. II. Psychological investigations.

Verkerk, A., Pieretti, M., Sutcliffe, J., Fu, Y., and Cell, D. (1991). Identification of a gene (FMR-1) containing a CGG repeat coincident with a breakpoint cluster region exhibiting length variation in fragile X syndrome.

Viaene, A.N., Petrof, I., and Sherman, M.S. (2011). Properties of the thalamic projection from the posterior medial nucleus to primary and secondary somatosensory cortices in the mouse. Proceedings of the National Academy of Sciences 108, 18156–18161.

Villalon-Reina, J., Jahanshad, N., Beaton, E., Toga, A.W., Thompson, P.M., and Simon, T.J. (2013). White matter microstructural abnormalities in girls with chromosome 22q11.2 deletion syndrome, Fragile X or Turner syndrome as evidenced by diffusion tensor imaging. Neuroimage 81, 441–454.

Vislay, R.L., Martin, B.S., Olmos-Serrano, J., Kratovac, S., Nelson, D.L., Corbin, J.G., and Huntsman, M.M. (2013). Homeostatic Responses Fail to Correct Defective Amygdala Inhibitory Circuit Maturation in Fragile X Syndrome. The Journal of Neuroscience 33, 7548–7558.

Wallace, M., Roberson, G., Hairston, W., Stein, B., Vaughan, J., and Schirillo, J. (2004). Unifying multisensory signals across time and space. Exp Brain Res 158, 252–258.

Wallingford, J., Scott, A.L., Rodrigues, K., and Doering, L.C. (2017). Altered Developmental Expression of the Astrocyte-Secreted Factors Hevin and SPARC in the Fragile X Mouse Model. Frontiers in Molecular Neuroscience 10, 268.

Wang, H., Wu, L.-J., Kim, S.S., Lee, F., Gong, B., Toyoda, H., Ren, M., Shang, Y.-Z., Xu, H., Liu, F., et al. (2008). FMRP Acts as a Key Messenger for Dopamine Modulation in the Forebrain. Neuron 59, 634–647.

Wang, J., Ethridge, L.E., Mosconi, M.W., White, S.P., Binder, D.K., Pedapati, E.V., Erickson, C.A., Byerly, M.J., and Sweeney, J.A. (2017). A resting EEG study of neocortical hyperexcitability and altered functional connectivity in fragile X syndrome. Journal of Neurodevelopmental Disorders 9, 11.

Wang, X., Zorio, D.A., Schecterson, L., Lu, Y., and Wang, Y. (2018). Postsynaptic FMRP regulates synaptogenesisin vivoin the developing cochlear nucleus. The Journal of Neuroscience 0665–18.

Watson, C., Hoeft, F., Garrett, A.S., Hall, S.S., and Reiss, A.L. (2008). Aberrant Brain Activation During Gaze Processing in Boys with Fragile X Syndrome. Archives of General Psychiatry 65, 1315–1323.

Weiler, I., and Greenough, W. (1999). Synaptic synthesis of the Fragile X protein: possible involvement in synapse maturation and elimination. American Journal of Medical Genetics 83, 248–252.

Wietek, J., Beltramo, R., Scanziani, M., Hegemann, P., Oertner, T.G., and Wiegert, S.J. (2015). An improved chloride-conducting channelrhodopsin for light-induced inhibition of neuronal activity in vivo. Scientific Reports 5, srep14807.

Wigham, S., Rodgers, J., South, M., McConachie, H., and Freeston, M. (2015). The Interplay Between Sensory Processing Abnormalities, Intolerance of Uncertainty, Anxiety and Restricted and Repetitive Behaviours in Autism Spectrum Disorder. J Autism Dev Disord 45, 943–952.

Winnubst, J., Cheyne, J.E., Niculescu, D., and Lohmann, C. (2015). Spontaneous Activity Drives Local Synaptic Plasticity In Vivo. Neuron 87, 399–410.

Wisniewski, K., French, J., and neurology, F.S. (1985). Fragile X syndrome: associated neurological abnormalities and developmental disabilities.

Yun, S.-W., Platholi, J., Flaherty, M., Fu, W., Kottmann, A.H., and Toth, M. (2006). Fmrp is required for the establishment of the startle response during the critical period of auditory development. Brain Research 1110, 159–165.

Zaitsev, A., Povysheva, N., Gonzalez-Burgos, G., and Lewis, D. (2012). Electrophysiological classes of layer 2/3 pyramidal cells in monkey prefrontal cortex. Journal of Neurophysiology 108, 595–609.

Zangenehpour, S., Cornish, K.M., and Chaudhuri, A. (2009). Whole-brain expression analysis of FMRP in adult monkey and its relationship to cognitive deficits in fragile X syndrome. Brain Research 1264, 76–84.

Zeng, H., and Sanes, J.R. (2017). Neuronal cell-type classification: challenges, opportunities and the path forward. Nature Reviews Neuroscience 18, 530–546.

Zerbi, V., Ielacqua, G.D., Markicevic, M., Haberl, M., Ellisman, M.H., A-Bhaskaran, A., Frick, A., Rudin, M., and Wenderoth, N. (2018). Dysfunctional Autism Risk Genes Cause Circuit-Specific Connectivity Deficits with Distinct Developmental Trajectories. Cerebral Cortex 28, 2495–2506.

Zhang, L., Liang, Z., Zhu, P., Li, M., Yi, Y.-H., Liao, W.-P., and Su, T. (2016). Altered intrinsic properties and bursting activities of neurons in layer IV of somatosensory cortex from Fmr-1 knockout mice. Experimental Neurology 280, 60–69.

Zhang, Y., Bonnan, A., Bony, G., Ferezou, I., Pietropaolo, S., Ginger, M., Sans, N., Rossier, J., Oostra, B., LeMasson, G., et al. (2014). Dendritic channelopathies contribute to neocortical and sensory hyperexcitability in Fmr1-/y mice. Nature Neuroscience 17, 1701–1709.

Zhao, S., Ting, J.T., Atallah, H.E., Qiu, L., Tan, J., Gloss, B., Augustine, G.J., Deisseroth, K., Luo, M., Graybiel, A.M., et al. (2011). Cell type–specific channelrhodopsin-2 transgenic mice for optogenetic dissection of neural circuitry function. Nat Methods 8, 745.

Zorio, D., Jackson, C., and of …, L.Y. (2017). Cellular distribution of the fragile X mental retardation protein in the mouse brain.

16 ANNEXE

16.1 PROPERTIES AND VALUES MEASURED

PROPERTIES MEASURED (MEAN ± SD)	**ANIMAL GENOTYPE**			
SPONTANEOUS PROPERTIES	**WT- NR**	**WT-R_{sub}**	**KO-NR**	**KO-R_{sub}**
Downstate (Vm) in mV	-76.60 ± 6.53	-75.05 ± 8.77	-74.4 ± 6.64	-78.89 ± 5.79
Upstate (Vm) in mV	-71.28 ± 3.42	-71.16±7.75	-70.17 ± 5.91	-74.16 ± 5.50
Up-threshold in mV	2.09 ±1.49	1.383 ± 0.62	1.75 ± 1.03	1.87 ± 1.16
Up-frequency in Hz	1.13 ± 0.16	1.039 ± 0.20	1.136 ± 0.197	1.05 ± 0.316
Up-duration in ms	418.64 ± 116.02	357.09 ± 81.8	403.59 ± 88.6	380.65 ± 68.85
Spontaneous firing rate in Hz	0.0185 ± 0.012	0.011 ± 0.005	0.019 ± 0.015	0.293 ± 0.273
INTRINSIC PROPERTIES	**WT- NR**	**WT-R_{sub}**	**KO-NR**	**KO-R_{sub}**
AP-threshold in mV	38.17 ± 14.24	40.49 ± 7.27	39.26 ± 12.32	37.96 ± 13.42
AP-amplitude in mV	45.83 ± 7.62	58.53 ± 12.6	51.96 ± 11.75	2.315 ± 0.72
AP-halfwidth in ms	2.395 ± 1.01	1.82 ± 0.43	2.019 ± 0.43	2.315 ± 0.72
Max firing rate (Hz)	20.63 ± 10.6	18.59 ± 5.45	23.15 ± 8.20	23.60 ± 6.5
2 times rheobase (n)	7.47 ± 4.73	8.52 ± 3.66	7.85 ± 3.91	8.69 ± 4.99
ADP-halfwidth ratio (3/1)	-	1.00 ± 0.01	-	1.02 ± 0.014
ADP-amplitude (mV)	-	1.149 ± 1.23	-	2.44 ± 0.616
MORPHOLOGY	**WT- NR**	**WT-R_{sub}**	**KO-NR**	**KO-R_{sub}**
Apical dendrites				

Mean length (µm)	32.95 ± 3.99	46.43 ± 9.38	35.65 ± 14.07	21.3 ± 3.59
Total length (µm)	1148.03 ± 8.26	790.04 ± 165.6	825 ± 569.9	445.7 ± 223.34
Number of endings (n)	11.71 ± 8.26	12.8 ± 3.11	13.5 ± 10.88	6 ± 3.95
Number of nodes (n)	10.14 ± 6.69	10 ± 2.55	7.13 ± 3.72	4.67 ± 3.83
Basal dendrites				
Mean length (µm)	83.34 ± 28.29	84.54 ± 12.46	69.77 ± 15.06	64.97 ± 10.32
Total length (µm)	789.34 ± 82.38	1439.02 ± 578.3	876.39 ± 346.6	904.55 ± 497.39
Number of endings (n)	17.88 ± 8.74	27.4 ± 8.85	14.5 ± 4.85	20.57 ± 4.58
Number of nodes (n)	12.13 ± 8.49	17.8 ± 8.41	8.75 ± 4.29	13 ± 5.03
EPSP PARAMETERS	**WT-R_{sub}**	**KO-R_{sub}**		
Peak amplitude in mV	6.11 ± 2.95	9.39 ± 4.38		
Half-amplitude duration in ms	29.96 ± 6.52	43.85 ± 16.84		
Rise slope (20-80 %) in mV.ms	0.32 ± 0.202	0.43 ± 0.33		
Peak latency in ms	49.68 ± 14.4	43.73 ± 12.8		
Onset latency in ms	25.5 ± 13.5	28.31 ± 19.08		
Standard deviation (noise) in mV	0.97 ± 0.466	1.689 ± 0.956		
Signal to noise ratio	13.76 ± 5.45	13.93 ± 6.93		
EVOKED AP PARAMETER	**WT-R_{supra}**	**KO-R_{supra}**		

Average pre-stimulus AP (within 200 ms before stimulus onset)	0.007 ± 0.012	0.095 ± 0.158		
Average post-stimulus AP (within 200 ms after stimulus onset)	0.332 ± 0.77	0.77 ± 0.35		
Evoked AP per stimulus	0.325 ± 0.23	0.675 ± 0.33		
Coefficient of variation	1.72 ± 0.739	0.886 ± 0.52		
Total number of APs fired	13.29 ± 9.27	30.8 ± 14		
THALAMIC STIMULATION	**WT-R_{sub}**	**KO-R_{sub}**		
EPSP parameters				
Peak amplitude in mV	2.98 ± 2.27	8.59 ± 3.43		
Half-amplitude duration in ms	21.19 ± 9.32	19.25 ± 4.63		
Rise slope (20-80 %)	0.343 ± 0.102	0.7 ± 0.358		
Area under the curve (mV/ ms)	183.63 ± 121.69	131.59 ± 81.28		
IPSP parameters				
Peak amplitude in mV	1.072 ± 0.133	3.68 ± 1.98		
Half-amplitude duration in ms	14.65 ± 8.97	32.58 ± 17.95		
Rise slope (20-80 %)	0.183 ± 0.074	0.276 ± 0.143		

Area under the curve (mV/ ms)	199.62 ± 145. 01	554.69 ± 324.34		
ADHESIVE REMOVAL TEST	**WT MICE**	**KO-MICE**	**WT MICE**	**KO-MICE**
	1st paw	1st paw	2nd paw	2nd paw
First contact (s)	146.93 ± 56.14	168.7 ± 70.21	110.67 ± 49.69	122.91 ± 107.72
Start removal (s)	136.83 ± 35.30	192.11 ± 72.57	115.83 ± 40.02	129 ± 94.71
End removal (s)	220.29 ± 101.54	301.29 ± 189.18	209.77 ± 114.25	377.5 ± 189.18
Total duration (s)	83.87 ± 91.61	109.38 ± 102.02	39.8 ± 27.64	225.5 ± 258.02
BMS-KO	**KO-NR - BMS**	**KO-R_{sub}- BMS**		
SPONTANEOUS PROPERTIES				
Downstate (Vm) in mV	-73.15 ± 8.07	-70.04 ± 4.5		
Upstate (Vm) in mV	-66.16 ± 9.70	-63.57 ± 7.89		
Upstate threshold in mV	2.11 ± 1.07	2.18 ± 1.5		
Upstate frequency (Hz)	1.183 ± 0.14	1.35 ± 0.13		
Upstate duration (ms)	416.58 ± 83.2	345.63 ± 53.7		
Spontaneous firing rate (Hz)	0.027 ± 0.05	0.002 ± 0.004		
BMS-KO	**KO-NR - BMS**	**KO-R_{sub}- BMS**		
INTRINSIC PROPERTIES				
AP- amplitude (mV)	53.95 ± 11.61	49.58 ± 10.55		
AP- halfwidth (ms)	1.99 ± 0.445	1.896 ± 0.28		
Max firing rate (Hz)	23.27 ± 5.91	25.67 ± 4.08		

2 times rheobase (n)	9.06 ± 4.15	9.86 ± 2.45		

16.2 MANUSCRIPT 1: SENSORY STIMULUS EVOKED RESPONSES IN LAYER 2/3 PYRAMIDAL NEURONS OF THE HIND PAW RELATED MOUSE PRIMARY SOMATOSENSORY CORTEX.

Title: Sensory stimulus evoked responses in layer 2/3 pyramidal neurons of the hind paw-related mouse primary somatosensory cortex

Author: Guillaume Bony[1,2], Arjun A-Bhaskaran[1,2], Katy Le Corf,[1,2] & Andreas Frick[1,2]

Affiliations:

[1]INSERM, Neurocentre Magendie, Physiopathologie de la plasticité neuronale, U1215, 33077 Bordeaux Cedex, France.

[2]Univ. Bordeaux, Neurocentre Magendie, Physiopathologie de la plasticité neuronale, U1215, 33077 Bordeaux Cedex, France.

Key words: sensory processing, tactile stimulus, patch-clamp in vivo

Corresponding author:

Name: Dr. Andreas Frick

Postal address: INSERM U862, Neurocentre Magendie, 146 Rue Léo Saignat, 33077 Bordeaux Cedex, France

Email: andreas.frick@inserm.fr

Running title: Hind paw responses in L2/3 neurons

Table of contents

Key points

- Electrical hind-paw stimulation activates the layer 2/3 pyramidal neurons of the primary somatosensory cortex in about 23 ms.
- These pyramidal neurons show a low spontaneous firing rate and a sparse action potential coding of evoked activity.
- The vast majority of layer 2/3 pyramidal neurons respond to prolonged hind-paw stimulation with both on- and off-responses.
- Most of our knowledge regarding information processing in the primary somatosensory cortex comes from studies of the whisker-related barrel cortex.
- These results help us understand sensory information processing in the layer 2/3 of the neocortex and the regional differences.

Abstract

The mouse primary somatosensory cortex (S1) processes tactile sensory information, and is the largest neocortex area emphasizing the importance of this sensory modality for rodent behavior. Most of our knowledge regarding information processing in S1 stems from studies of the whisker-related barrel cortex (S1–BC), yet the processing of tactile inputs from the hind-paws is poorly understood. We used *in vivo* whole-cell patch-clamp recordings from layer (L) 2/3 pyramidal neurons (PN) of the S1 hind-paw (S1-HP) region of anaesthetized mice to investigate their evoked sub- and supra-threshold activity, intrinsic properties, and spontaneous activity. Approximately 45% of these L2/3-PN responded to contralateral HP stimulation in a subthreshold manner, ~5% fired action potentials, and ~50% of L2/3-PN did not respond at all. The evoked subthreshold responses had long onset- (23 ms) and peak-latencies (61 ms). The majority (86%) of L2/3-PN responded to prolonged HP stimulation with both on- and off-responses. L2/3-PN displayed up- and down-states, and low spontaneous firing rates (~0.1 Hz). HP stimulation responsive L2/3-PN had a greater intrinsic excitability compared to non-responsive ones, reflected in an increase in the action potential firing as a function of current injected. Our findings support a sparse coding scheme of operation for S1–HP L2/3-PN.

Abbreviations: AHP, after hyperpolarization; AP, action potentials; APhw, AP half-width; FP, forepaw; L2/3, layer 2/3 of the neocortex; NR-cells, non-responding cells; PN, pyramidal neurons; R-cells, responding cells; RMP, resting membrane potential; R_N, input resistance; S1, primary somatosensory cortex; S1-BC, whisker-related barrel cortex of S1; S1-HP, hindpaw-related S1; UDS, up and down states.

Introduction

The sense of touch facilitates exploration, recognition of the environment, object discrimination, and social interaction. In rodents, the primary somatosensory cortex (S1) processing this tactile sensory information is — with a surface area of ~25% of the neocortex — the largest sensory neocortex area, highlighting the importance of this sensory modality for rodent behavior (Catania & Remple, 2002; Seelke *et al.*, 2012). Tactile signals are generated by activation of various types of cutaneous receptors (Roudaut *et al.*, 2012; Zimmerman *et al.*, 2014) and reach the neocortex mainly through the dorsal column pathway after passing the synapses in the brainstem and the thalamus (Gilman, 2002). The processing of this sensory modality in the neocortex has been extensively studied for the whisker-related barrel cortex (S1-BC; reviewed in (Brecht, 2007; Feldmeyer, 2012; Petersen & Crochet, 2013) system. Knowledge of the processing of tactile information derived from the hind-paws (HPs), however, is largely lacking. In rodents, the HPs are involved in several behaviors, such as grooming, postural reflexes, walking, and swimming (Whishaw *et al.*, 1999).

Within layer (L) 2/3 of the S1, sensory information spreads horizontally and vertically, both within the home, and across neighboring columns (reviewed in (Feldmeyer, 2012). Thus, L2/3 pyramidal neurons (PN) are in the position to integrate the activity of several cortical columns. Previous studies about S1-HP processing showed the spatio-temporal dynamic and area connectivity of L2/3-PN activity with voltage-sensitive dye imaging (Lim *et al.*, 2012; Morales-Botello *et al.*, 2012). It has also been shown that S1–BC L2/3-PN fire few action potentials (APs) in response to a given sensory stimulus (e.g. (Margrie *et al.*, 2002; Brecht *et al.*, 2003; de Kock *et al.*, 2007; de Kock & Sakmann, 2009; Crochet *et al.*, 2011). Here, we explored whether sensory processing features in L2/3-PN such as the latencies, and on-/off- components of the paw related information are unique for this tactile modality or more broadly applicable. Further, we asked if neurons that respond to sensory stimulus and those that do not could be distinguished based on their intrinsic properties. A sparse firing rate has been suggested to be a general landmark of L2/3-PN of primary sensory cortices (Barth & Poulet, 2012), but this has never been shown for S1-HP. We addressed these questions by performing whole-cell patch-clamp recordings together with HP stimulation in anesthetized mice.

Methods

Ethical approval

All experimental procedures were performed in accordance with the EU directive 2010/63/EU and French law following procedures approved by the Bordeaux Ethics Committee (CE2A50). Wildtype mice from our transgenic breeding program (as described in (Zhang *et al.*, 2014) were used in these experiments. These mice were generated by backcrossing 129/Sv/C57Bl/6J/FVB founders into a C57Bl/6J background (6 generations). These mice were chosen to permit comparison with transgenic mice for a companion study and to spare the number of mice used in the two studies.

Animal preparation and hind paw stimulation

Male mice (P24–32) were anaesthetized with a mixture of ketamine (100 $mg.kg^{-1}$) and xylazine (10 $mg.kg^{-1}$) injected intraperitoneally and supplemented as necessary throughout the procedure. Mice were head-fixed using non-puncture ear-bars and a nose-clamp (SR-6M, Narishige). Temperature was maintained at 37°C, although some recordings at 35 °C are included but they do not show different properties. A small craniotomy was made above the S1-HP (1 mm posterior, 1.5 mm lateral from Bregma) using a dental drill (World Precision Instruments). The stereotaxic coordinates were assessed in a set of control experiments using intrinsic optical imaging (data not shown).

Sensory responses were evoked by applying current pulses (2 ms or 200 ms, 100 V, 0.5–30 mA) via conductive adhesive strips (~1 cm^2) placed on top of, and below the HP, as described previously (Palmer *et al.*, 2012). These electrodes cover the entire paw (toes and palm, both glabrous and hairy skin). We repeated the stimulation protocol 40 times with at least 3 sec of interval (~0.3 Hz).

In vivo whole-cell patch-clamp recordings

Blind whole-cell patch-clamp recordings were performed from L2/3 pyramidal neurons of anaesthetized mice (average sub-pial depth 207 ± 60 µm, n = 83 neurons in 68 mice), as described previously (Margrie *et al.*, 2002). Pipettes with an open-tip resistance of 4–6 MΩ were pulled from borosilicate glass using a PC-10 puller (Narishige) and filled with (in mM): 130 K-methanesulphonate, 10 Hepes, 7 KCl, 0.05 EGTA, 2 Na_2ATP, 2 MgATP, 0.5 Na_2GTP; pH 7.28 (adjusted with KOH). In a

subset of experiments, biocytin (3 mg/mL) or a mammalian expression plasmid encoding eGFP (150 ng/µL; as described in (Rancz *et al.*, 2011) was added to the recording solution for *post-hoc* neuronal identification. The intracellular solution was filtered using a 0.22-µm pore-size centrifuge filter (Costar Spin-X). Signals were acquired using a Multiclamp 700B amplifier and Clampex 10.4 software (Axon Instruments). Data were low-pass filtered at 3 kHz and sampled at 20 kHz.

Staining of neuronal morphology and neocortical barrels

Following biocytin filling of the recorded neurons, the brains were fixed by transcardial perfusion with 4% paraformaldehyde in PBS, and post-fixed 2h. Subsequently, 80-µm-thick tangential slices were cut using a vibratome (Leica), and biocytin was detected using streptavidin-Alexa Fluor 555 (1:1,000, 2h at RT). To reconstruct the S1 barrels, we performed immunostaining against GAD67 (Meyer *et al.*, 2011) using the following protocol: MOM blocking/permeabilization (0.3% triton X-100, 4% NGS, and 3% BSA in PBS) for 30 min; primary antibody (Mouse anti-GAD67 clone 1G10.2; 1:1,500; Millipore) overnight at 4°C; secondary antibody (Goat anti-Mouse IgG2A Alexa 488; 1: 500; Life technologies) 2h at RT. The images were acquired with a confocal microscope (Leica) or a slide scanner (Nanozoomer, Hamamatsu). The S1 reconstructions were performed with ImageJ software (NIH).

Data analysis

To measure input resistance we injected 500-ms-long hyperpolarizing (-100 pA) current and measured the membrane potential deflection at 300 ms relative to baseline after bridge balance correction. To determine the AP threshold, we measured the membrane potential at the beginning of the rising phase of the first AP occurring during the IV curve protocol. AP half-width was determined by measuring the duration of these first APs at half-amplitude (from threshold to the peak) (see Fig. 1*D*). We determined average up- and down-state membrane potentials by plotting the distribution of membrane potential values. Up-state frequency and duration analysis were adapted from Beltramo et al. 2013. Briefly, the spontaneous down- to up-state transitions were identified as membrane depolarization crossing a threshold set at 1/3 of the amplitude down- to up-state. Only transitions in which the signal

remained for more than 150 ms above the threshold were considered. Parameters of evoked sub-threshold synaptic potentials were calculated from an averaged trace of 40 successive trials. Latency was determined by measuring the time point after HP stimulation where the Gaussian fit of the response's rising phase crosses the baseline. The duration of the synaptic responses was calculated by measuring the width of the averaged response at half-maximal amplitude. The calculation of evoked supra-threshold responses and their coefficient of variation were adapted from (de Kock *et al.*, 2007). Briefly, the number of APs was quantified within a 200-ms-long time window following the stimulus onset and averaged over 40 stimulus trials. The average spontaneous activity (0–200 ms window before stimulus) was then subtracted from this value. The coefficient of variation was calculated by dividing the number of APs within 200 ms following the stimulus by the standard deviation on a trial-by-trial basis. To measure on- and off-responses we used a 200-ms-long stimulation (30 mA, 100 V). All analysis was performed using Clampfit 10.4 software (Axon Instruments).

Statistical analysis

Data are given as means ± SD unless otherwise stated. Statistical analysis was performed using two-tailed unpaired or paired *t* tests to evaluate the difference between two groups of data. For repeated measures, data were analyzed by two-way ANOVA (GraphPad Software). P values < 0.05 were considered significant (* $P < 0.05$, ** $P < 0.01$, *** $P < 0.001$). Boxplots indicate the median value (middle line), the 25th and 75th percentiles (box), and the highest and lowest values (whiskers).

Results

We performed whole-cell patch-clamp recordings from individual L2/3 pyramidal neurons of the S1–HP in anesthetized mice (Figure 1A-C) at an age (P24–32) when gait is considered mature (Clarke & Still, 2001). We distinguished pyramidal neurons (~84%) from putative interneurons (~16%; Figure 1A) based on their intrinsic properties, and subsequently focused our analysis on pyramidal neurons (Figure 1C). We could clearly identify fast-spiking interneurons based on their intrinsic properties (Figure 1D; Table 1; n = 7), and in particular the input resistance (R_N), action potential half-width

(APhw), after hyperpolarization (AHP), and maximum firing rate were significantly different from pyramidal neurons (Table 1). However, non-fast spiking interneuron cannot be easily distinguished from excitatory neurons (Gentet *et al.*, 2010; Gentet *et al.*, 2012) and we therefore discarded the recordings whenever we saw a large after-hyperpolarization, high firing rate following current injection, and/or short action potential half-width (n = 9).

HP stimulation evoked responses in L2/3 pyramidal neurons

We applied current pulses via conductive adhesive strips placed above and below the HP to measure the sub- and supra-threshold responses of S1-HP L2/3-PN evoked by sensory HP stimulation. Importantly, we performed multiple recordings with HP stimulation in 15 mice and we recorded both R- and NR-cells in 6 mice (13 neurons in total, 6 R-cells and 7 NR-cells). To rule out a mislocalization of our recordings we also performed contralateral forepaw (FP) stimulation in a subset of experiments (n = 42), and we found that few neurons were responding to FP (7/42 neurons) with only 4 neurons belonging to the NR-cells (~9%). These neurons, perhaps located in S1-FP, were discarded from the analysis. Stimulation of the contralateral HP evoked sub- and supra-threshold responses in ~51% of the L2/3-PN (42/83 neurons), while ~49% of the neurons (41/83 neurons) failed to respond (Figure 1E,F). Both 'responders' (R-cells) and 'non-responders' (NR-cells) were pyramidal cells recorded at an equivalent depth from the pia (R-cells: ~194 µm; NR-cells: ~218 µm) located within S1-HP, as confirmed by *posthoc* staining of their morphology and GAD67 staining of the S1 barrel pattern (Meyer *et al.*, 2011). An example for a NR-cell is given in Figure 1B,C.

One explanation for this high rate of NR-cells could be that the stimulation intensity was below the threshold for evoking a response. To examine this possibility, we measured the minimum stimulus intensity required to elicit a response in responding neurons. On average this threshold intensity was ~12 mA (range 0.5–30 mA, n = 16) and therefore far below the intensity (i.e. 30 mA) used for our analysis. It is therefore unlikely that a low stimulus intensity is the reason for the absence of a response in the majority of NR-cells, and rather that other factors such as the anatomical connectivity patterns of these two populations determine their different functional role within S1-HP.

We performed a detailed characterization of HP-related sensory responses using the maximum stimuli previously applied (i.e. 30 mA; Figure 2) and the average response over 40 trials. At the population level for R-cells, the average amplitude of the subthreshold responses was 8.98 ± 5.05 mV (median 7.71 mV), ranging from 2.53 mV to 21.72 mV (n = 33) (Figure 2C). The amplitude of the sub-threshold response was correlated with the membrane potential (Figure 2D), and was significantly smaller during up-states as compared to down-states (Regression analysis, R square = 0.3499, $P < 0.001$). On average, the half-amplitude duration of the responses was 98.21 ± 76.23 ms, the onset latency was 21.88 ± 8.91 ms, and the peak latency 58.82 ± 30.76 ms (n = 36) (Figure 2E). Interestingly, the onset latency is substantially longer than that reported for whisker stimulation in mice (Crochet & Petersen, 2006; Crochet *et al.*, 2011), and may reflect the functional role of HP information for the animal (see Discussion). On average, the slope of rise (measured at 20-80% of the amplitude) was 0.589 ± 0.508 mV.ms and the area of the response was 833.05 ± 560.39 mV.ms (n = 30; data not shown).

We detected supra-threshold responses in approximately 5% of all recorded pyramidal neurons (4/83 neurons) (Example in Figure 2F). These neurons responded with a single AP to HP stimulation in 42.5% of the trials (range: 20.0%-77.5%) and with a sub-threshold depolarization in the other trials (Figure 2F-I). Interestingly, we could identify an inhibitory component for the trials with an AP response (grand average in Figure 2G; 4 cells, 160 trials), suggestive of either feedback or feedforward inhibition. Both mechanisms are thought to sharpen the sensory response (Isaacson & Scanziani, 2011).

Off responses in L2/3 pyramidal neurons

In rodents, the paws are mostly used for sensory/discriminative aspects and for locomotive behavior involving their synchronized movement (Whishaw *et al.*, 1999). Locomotion can be divided into different phases — stance (when the paw is in contact with the floor) and swing (when the paw is moving forward to a new position), and the timing of each phase can vary depending on the animal's speed. In mice, the average stance phase duration is ~200 ms (Clarke & Still, 1999). To mimic the stimulation received during the stance phase of locomotion, we performed a subset of experiments in

which a 200 ms-long stimulus was applied to the plantar surface of the HP. The subsequent responses recorded in L2/3-PN are expected to follow the activity pattern of skin receptors modulated by neocortical processing. Interestingly, a majority of R-cells responded to both the onset and offset of the stimulus (on only: 14%; on and off: 86%; n = 14) (Fig. 3*A*), with the membrane potential remaining slightly depolarized during the time course of the stimulation (Fig. 3*B,C*). The presence of onset and offset peaks could reflect either the activation of fast adapting receptors in the skin or it could be a property of neocortical circuits (see Discussion). In an attempt to describe sensory integration during stance and swing phases, we compared the on- and off-responses (Fig. 3D). Peak latency (on: 50.57 ± 21.44 ms, n = 7; off: 62.35 ± 15.47 ms, n = 7) and half-amplitude duration (on: 62.86 ± 15.01 ms, n = 7; off: 89.43 ± 36.64 ms, n = 7) were substantially longer for off-responses, but these differences did not reach statistical significance ($P = 0.13$ and $P = 0.08$, respectively). On- and off-responses had also similar amplitude (on: 7.88 ± 5.25 mV, n = 7; off: 6.89 ± 3.18 mV, n = 7). In contrast, we found that the onset latency was significantly longer for off- compared to on-responses (on: 22.14 ± 10.37 ms, n = 7; off: 27.5 ± 9.22 ms, n = 7; $P = 0.0242$), which highlights different processing for these two sensory signals.

Given the presence of this anatomically similar, but physiologically heterogenous population, we asked whether R-cells and NR-cells could be distinguished based on their intrinsic excitability properties (Fig. 4). An analysis of the integrative properties revealed that most parameters were comparable between the two groups. The resting membrane potential (RMP) during down-states (R-cells: –72.26 ± 8.43 mV; NR-cells: –71.69 ± 7.48 mV; $P = 0.7438$) and up-states (R-cells: –63.01 ± 11.3 mV; NR-cells: –61.94 ± 10.24 mV; $P = 0.692$), and the input resistance (R_N) in down-states (R-cells: 99.78 ± 48.84 MΩ; NR-cells: 89.48 ± 65.38 MΩ; $P = 0.4424$) were similar between both groups. In agreement with recordings from L2/3-PN of S1–BC, there was no sag response in either group (Fig. 4*A*). Similarly, the properties of single APs (Figure 4B), including threshold (R-cells: –28.57 ± 11.09 mV; NR-cells: –27.58 ± 11.7 mV; $P = 0.711$), half-width (R-cells: 2.12 ± 0.49 ms; NR-cells: 2.2 ± 0.69 ms; $P = 0.5805$), and rheobase (R-cells: 195.1 ± 89.3 pA; NR-cells: 211.9 ± 123.4 pA; $P =$

0.4807) were, for the most part, equivalent between the two groups. However, the number of APs triggered as a function of current injected was larger in R- as compared to NR-cells ($P = 0.0172$) (Fig. 4*C*). Accordingly, at two times rheobase the number of APs was significantly larger for R-cells compared to NR-cells (R-cells: 8.14 ± 4.04, NR-cells: 5.7 ± 4; $P = 0.0175$; n = 35 and 30). These findings suggest that the R-cell population might be distinguishable from the NR-cell population based on differences in their intrinsic excitability.

Spontaneous firing activity and up-states

The aforementioned differences in intrinsic excitability might be expected to contribute to an alteration in spontaneous activity. Surprisingly, however, we found a similar level of non-evoked activity in the two populations (Fig. 5). Specifically, ~48% of R-cells and ~51% of NR-cells spontaneously fired APs (together 33/66 of L2/3-PN), and the spontaneous firing rate was equivalent between the two groups (Fig. 5*A*,*B*) (R-cells: 0.1 ± 0.23 Hz, NR-cells: 0.2 ± 0.24 Hz; $P = 0.2470$). Of note, these values are in good agreement with the sparse spontaneous firing activity of L2/3-PN previously reported for the primary sensory cortices (Barth & Poulet, 2012; Palmer *et al.*, 2014). During sleep, and under anesthesia, neocortical activity is characterized by slow oscillations that are accompanied by up- and down- states (UDS) in the membrane potential of neocortical neurons (reviewed in Castro-Alamancos 2009). Up-states represent brief episodes of increased neocortical activity resulting in strong depolarization of the neurons. The presence of these ongoing network patterns could interact with the neuronal intrinsic excitability to determine the neurons' responses to sensory stimulation. In our recordings, these up-states had on average a duration of 527.54 ± 194.07 ms (n = 52) and occurred with a frequency of 0.98 ± 0.27 Hz (n = 55) (Fig. 5*A*), in good agreement with findings from a recent study in rats (Palmer *et al.*, 2014). Similar to the spontaneous firing rate, there was no significant difference in either the duration (R-cells: 588.99 ± 208.22 ms, NR-cells: 488.16 ± 175.4 ms; $P = 0.0814$) or frequency (R-cells: 0.89 ± 0.25 Hz, NR-cells: 1.01 ± 0.24 Hz; $P = 0.119$) of up-states between R- and NR-cells (Fig. 5*C*). These results suggest that UDS-related firing is not a criterion for distinguishing R- from NR-cells.

Discussion

In the work described herein, we provide a detailed description of the intrinsic properties, spontaneous activity, and sensory stimulus evoked responses of layer 2/3 pyramidal neurons of the hind paw-related primary somatosensory cortex in anesthetized mice. Specifically, we report a sparse spontaneous firing, the identification of two discrete populations (based on sensory stimulus-induced responses and intrinsic properties), long response latency to tactile stimulus, and the presence of a novel on-/off- response.

Tactile sensory processing has been extensively described for the S1-BC. One striking feature that we found for stimulus-evoked responses of L2/3 pyramidal neurons of the S1-HP region was their long latency. Whisker stimulation evokes a fast depolarizing response with ~9 ms latency (Brecht *et al.*, 2003; Petersen *et al.*, 2003; Higley & Contreras, 2005; de Kock *et al.*, 2007), in coherence with the role for the whiskers in fine environmental sensing. Tactile information from paw stimulation on the other hand has a substantially slower latency (23 ms for HP stimulation as shown here) likely reflecting the different functional role of the paw, whose primary function is locomotion. Based on our results, as well as those derived from forepaw stimulation experiments (Milenkovic *et al.*, 2014), we propose that locomotion, in particular the synchronization of limb movement involves sensory information processing on a different temporal scale from that required for whisker-related information. While a difference in the latency of responses exists for the S1-HP and S1-BC, the amplitude of the response was similar. Sensory evoked depolarization had an average amplitude of ~9 mV (Fig. 2*C*), which is consistent with the amplitude measured in L2/3 of S1-BC following whisker deflection in anaesthetized rats and awake mice (Brecht *et al.*, 2003; Higley & Contreras, 2005; Crochet *et al.*, 2011).

In the supragranular layers of S1, many studies have described a sparse activity in rodents (Brecht *et al.*, 2003; Kerr *et al.*, 2005; Crochet & Petersen, 2006; Kerr *et al.*, 2007; Greenberg *et al.*, 2008; Poulet & Petersen, 2008; de Kock & Sakmann, 2009). We found that the spontaneous activity was ~0.16 Hz for active cells, and that approximately 50% of the L2/3-PN remained silent during the recordings. This low spontaneous firing activity of S1-HP L2/3-PN is in general agreement with

previous reports concerning the activity of supragranular neurons of other sensory neocortical regions (primary visual, auditory, and somatosensory) in anaesthetized rodents (Brecht *et al.*, 2003; Kerr *et al.*, 2005; Greenberg *et al.*, 2008; Sakata & Harris, 2009). Similarly, our results regarding evoked responses support a sparse firing code (for a review about sparse firing, see (Barth & Poulet, 2012). Hindpaw stimulation elicited AP firing in only ~5% of L2/3-PN, and these APs occurred in less than 50% of the trials with a maximum of one AP per trial. It should be noted, that the level of spontaneous and evoked firing activity likely depends on the brain state (de Kock & Sakmann, 2008; Greenberg *et al.*, 2008; de Kock & Sakmann, 2009).

Similarly, the duration and frequency of up- and down-states – thought to be fundamental for modulating sensory responses – are comparable to those described in the literature for rodent sensory cortices (Chance *et al.*, 2002; Petersen *et al.*, 2003; Haider *et al.*, 2007; Hasenstaub *et al.*, 2007; Luczak *et al.*, 2009; Palmer *et al.*, 2014). We show that these up-states reduce S1-HP responses to brief tactile stimulation, similar to what has been described for S1-BC responses to whisker deflection in rodents (Petersen *et al.*, 2003; Sachdev *et al.*, 2004; Higley & Contreras, 2005). This suggests that sensory responses collide with up-state spontaneous activity in the entire S1. Interestingly, sensory responses are enhanced in the cat visual cortex during up-states (Haider *et al.*, 2007). Whether these opposing findings are modality-, area-, or species-specific features requires further investigation.

Our finding that the tactile stimulus used in our study triggered a response in only half of the L2/3-PN population within S1-HP supports the idea that L2/3 contains neuronal pyramidal populations with different functional roles during behavioral tasks (Chen *et al.*, 2013; Yamashita *et al.*, 2013; Peron *et al.*, 2015). For instance, some of these neurons in the S1-HP region might be activated by stimuli such as cold or hot temperature (see (Milenkovic *et al.*, 2014), alone or in combination with mechanical stimulation. Furthermore, differences in the stimulus evoked responses of these various L2/3 PN populations are likely correlated with their distinct specific connectivity matrix and intrinsic excitability properties (Chen *et al.*, 2013; Yamashita *et al.*, 2013). In agreement with these findings, we found that neurons that responded to hind-paw stimulation displayed an increased intrinsic excitability when compared to those that did not respond.

We found that the majority of R-cells responded to a prolonged paw stimulus with an on- and off component, reflecting the activation of the paw during the stance phase of locomotion. The off response could be a consequence of the activation of fast adaptive receptors in the glabrous skin of the HP when the stimulation ceases (Roudaut *et al.*, 2012). Pacinian and Meissner corpuscles are both rapidly adapting mechanoreceptors that could underlie the off response (Roudaut *et al.*, 2012).

Altogether, our data indicate that L2/3-PN of the S1-HP have both features that are common for different tactile modalities as well as those that are unique for the paw related information. This work opens new avenues to compare tactile sensory responses in L2/3-PN of WT mice, as recorded here, with mouse models of sensory processing defects or to explore developmental changes in sensory processing.

References

Barth AL & Poulet JF. (2012). Experimental evidence for sparse firing in the neocortex. *Trends in neurosciences* **35,** 345-355.

Brecht M. (2007). Barrel cortex and whisker-mediated behaviors. *Current opinion in neurobiology* **17,** 408-416.

Brecht M, Roth A & Sakmann B. (2003). Dynamic receptive fields of reconstructed pyramidal cells in layers 3 and 2 of rat somatosensory barrel cortex. *The Journal of physiology* **553,** 243-265.

Catania KC & Remple MS. (2002). Somatosensory cortex dominated by the representation of teeth in the naked mole-rat brain. *Proceedings of the National Academy of Sciences of the United States of America* **99,** 5692-5697.

Chance FS, Abbott LF & Reyes AD. (2002). Gain modulation from background synaptic input. *Neuron* **35,** 773-782.

Chen JL, Carta S, Soldado-Magraner J, Schneider BL & Helmchen F. (2013). Behaviour-dependent recruitment of long-range projection neurons in somatosensory cortex. *Nature* **499,** 336-340.

Clarke KA & Still J. (1999). Gait analysis in the mouse. *Physiology & behavior* **66,** 723-729.

Clarke KA & Still J. (2001). Development and consistency of gait in the mouse. *Physiology & behavior* **73,** 159-164.

Crochet S & Petersen CC. (2006). Correlating whisker behavior with membrane potential in barrel cortex of awake mice. *Nature neuroscience* **9,** 608-610.

Crochet S, Poulet JF, Kremer Y & Petersen CC. (2011). Synaptic mechanisms underlying sparse coding of active touch. *Neuron* **69,** 1160-1175.

de Kock CP, Bruno RM, Spors H & Sakmann B. (2007). Layer- and cell-type-specific suprathreshold stimulus representation in rat primary somatosensory cortex. *The Journal of physiology* **581,** 139-154.

de Kock CP & Sakmann B. (2008). High frequency action potential bursts (>or= 100 Hz) in L2/3 and L5B thick tufted neurons in anaesthetized and awake rat primary somatosensory cortex. *The Journal of physiology* **586,** 3353-3364.

de Kock CP & Sakmann B. (2009). Spiking in primary somatosensory cortex during natural whisking in awake head-restrained rats is cell-type specific. *Proceedings of the National Academy of Sciences of the United States of America* **106,** 16446-16450.

Feldmeyer D. (2012). Excitatory neuronal connectivity in the barrel cortex. *Frontiers in neuroanatomy* **6,** 24.

Gentet LJ, Avermann M, Matyas F, Staiger JF & Petersen CC. (2010). Membrane potential dynamics of GABAergic neurons in the barrel cortex of behaving mice. *Neuron* **65,** 422-435.

Gentet LJ, Kremer Y, Taniguchi H, Huang ZJ, Staiger JF & Petersen CC. (2012). Unique functional properties of somatostatin-expressing GABAergic neurons in mouse barrel cortex. *Nature neuroscience* **15,** 607-612.

Gilman S. (2002). Joint position sense and vibration sense: anatomical organisation and assessment. *Journal of neurology, neurosurgery, and psychiatry* **73,** 473-477.

Greenberg DS, Houweling AR & Kerr JN. (2008). Population imaging of ongoing neuronal activity in the visual cortex of awake rats. *Nature neuroscience* **11,** 749-751.

Haider B, Duque A, Hasenstaub AR, Yu Y & McCormick DA. (2007). Enhancement of visual responsiveness by spontaneous local network activity in vivo. *Journal of neurophysiology* **97,** 4186-4202.

Hasenstaub A, Sachdev RN & McCormick DA. (2007). State changes rapidly modulate cortical neuronal responsiveness. *The Journal of neuroscience : the official journal of the Society for Neuroscience* **27,** 9607-9622.

Higley MJ & Contreras D. (2005). Integration of synaptic responses to neighboring whiskers in rat barrel cortex in vivo. *Journal of neurophysiology* **93,** 1920-1934.

Isaacson JS & Scanziani M. (2011). How inhibition shapes cortical activity. *Neuron* **72,** 231-243.

Kerr JN, de Kock CP, Greenberg DS, Bruno RM, Sakmann B & Helmchen F. (2007). Spatial organization of neuronal population responses in layer 2/3 of rat barrel cortex. *The Journal of neuroscience : the official journal of the Society for Neuroscience* **27,** 13316-13328.

Kerr JN, Greenberg D & Helmchen F. (2005). Imaging input and output of neocortical networks in vivo. *Proceedings of the National Academy of Sciences of the United States of America* **102,** 14063-14068.

Lim DH, Mohajerani MH, Ledue J, Boyd J, Chen S & Murphy TH. (2012). In vivo Large-Scale Cortical Mapping Using Channelrhodopsin-2 Stimulation in Transgenic Mice Reveals Asymmetric and Reciprocal Relationships between Cortical Areas. *Frontiers in neural circuits* **6,** 11.

Luczak A, Bartho P & Harris KD. (2009). Spontaneous events outline the realm of possible sensory responses in neocortical populations. *Neuron* **62,** 413-425.

Margrie TW, Brecht M & Sakmann B. (2002). In vivo, low-resistance, whole-cell recordings from neurons in the anaesthetized and awake mammalian brain. *Pflugers Archiv : European journal of physiology* **444,** 491-498.

Meyer HS, Schwarz D, Wimmer VC, Schmitt AC, Kerr JN, Sakmann B & Helmstaedter M. (2011). Inhibitory interneurons in a cortical column form hot zones of inhibition in layers 2 and 5A. *Proceedings of the National Academy of Sciences of the United States of America* **108,** 16807-16812.

Milenkovic N, Zhao WJ, Walcher J, Albert T, Siemens J, Lewin GR & Poulet JF. (2014). A somatosensory circuit for cooling perception in mice. *Nature neuroscience* **17,** 1560-1566.

Morales-Botello ML, Aguilar J & Foffani G. (2012). Imaging the spatio-temporal dynamics of supragranular activity in the rat somatosensory cortex in response to stimulation of the paws. *PloS one* **7,** e40174.

Palmer LM, Schulz JM, Murphy SC, Ledergerber D, Murayama M & Larkum ME. (2012). The cellular basis of GABA(B)-mediated interhemispheric inhibition. *Science* **335,** 989-993.

Palmer LM, Shai AS, Reeve JE, Anderson HL, Paulsen O & Larkum ME. (2014). NMDA spikes enhance action potential generation during sensory input. *Nature neuroscience* **17,** 383-390.

Peron SP, Freeman J, Iyer V, Guo C & Svoboda K. (2015). A Cellular Resolution Map of Barrel Cortex Activity during Tactile Behavior. *Neuron* **86,** 783-799.

Petersen CC & Crochet S. (2013). Synaptic computation and sensory processing in neocortical layer 2/3. *Neuron* **78,** 28-48.

Petersen CC, Hahn TT, Mehta M, Grinvald A & Sakmann B. (2003). Interaction of sensory responses with spontaneous depolarization in layer 2/3 barrel cortex. *Proceedings of the National Academy of Sciences of the United States of America* **100,** 13638-13643.

Poulet JF & Petersen CC. (2008). Internal brain state regulates membrane potential synchrony in barrel cortex of behaving mice. *Nature* **454,** 881-885.

Rancz EA, Franks KM, Schwarz MK, Pichler B, Schaefer AT & Margrie TW. (2011). Transfection via whole-cell recording in vivo: bridging single-cell physiology, genetics and connectomics. *Nature neuroscience* **14,** 527-532.

Roudaut Y, Lonigro A, Coste B, Hao J, Delmas P & Crest M. (2012). Touch sense: functional organization and molecular determinants of mechanosensitive receptors. *Channels* **6,** 234-245.

Sachdev RN, Ebner FF & Wilson CJ. (2004). Effect of subthreshold up and down states on the whisker-evoked response in somatosensory cortex. *Journal of neurophysiology* **92,** 3511-3521.

Sakata S & Harris KD. (2009). Laminar structure of spontaneous and sensory-evoked population activity in auditory cortex. *Neuron* **64,** 404-418.

Seelke AM, Dooley JC & Krubitzer LA. (2012). The emergence of somatotopic maps of the body in S1 in rats: the correspondence between functional and anatomical organization. *PloS one* **7,** e32322.

Whishaw I, Haun F & Kolb B. (1999). Analysis of Behavior in Laboratory Rodents. In *Modern Techniques in Neuroscience Research*, ed. Windhorst U & Johansson H, pp. 1243-1275. Springer Berlin Heidelberg.

Yamashita T, Pala A, Pedrido L, Kremer Y, Welker E & Petersen CC. (2013). Membrane potential dynamics of neocortical projection neurons driving target-specific signals. *Neuron* **80,** 1477-1490.

Zhang Y, Bonnan A, Bony G, Ferezou I, Pietropaolo S, Ginger M, Sans N, Rossier J, Oostra B, LeMasson G & Frick A. (2014). Dendritic channelopathies contribute to neocortical and sensory hyperexcitability in Fmr1(-/y) mice. *Nature neuroscience* **17,** 1701-1709.

Zimmerman A, Bai L & Ginty DD. (2014). The gentle touch receptors of mammalian skin. *Science* **346,** 950-954.

Additional information

Competing interest

The authors declare that they have no competing interests.

Author contribution

GB and AAB carried out electrophysiological recording, data analysis and staining of neurons. KLC carried out staining of neurons. AF conceived the project and designed experiments. All authors wrote the manuscript and have approved its final version. All persons designated as authors qualify for authorship, and all those who qualify for authorship are listed.

Funding

This work was supported by the Institut National de la Santé et de la Recherche Médicale, the Conseil de la Région d'Aquitaine, and the Fondation pour la Recherche Médicale (SPF20130526794, ING20140129376), as well as the European Commission (European Erasmus Mundus Programme-ENC network).

Acknowledgements

We would like to thank Dr. M. Brecht for help with setting up the *in vivo* patch-clamp techniques in our laboratory. We are also grateful to Drs. X. Leinekugel and M. Ginger for fruitful discussions and feedback on the manuscript. The images were acquired using equipment of the Bordeaux Imaging Center.

Table 1

	RMP (mV)	Rin (MΩ)	APth (mV)	APhw (ms)	AHP (mV)	Rheobase (pA)	Max firing (Hz)
Pyramidal neurons (n = 83)	-71.86 ± 7.9	91.31 ± 54.3	-30.62 ± 9.51	2.12 ± 0.51	3.89 ± 2.02	203.66 ± 108.23	19.22 ± 7.46
Fast-spiking interneurons (n = 7)	-68.3 ± 12.67	134.19 ± 53.51	-34.71 ± 12.76	1.22 ± 0.28	12.78 ± 4.64	142.86 ± 93.22	59.43 ± 30.78
P-value	*P = 0.2796*	*P = 0.0495**	*P = 0.2972*	*P < 0.0001* ***	*P < 0.0001* ***	*P = 0.1536*	*P < 0.0001* ***

Figure Legends

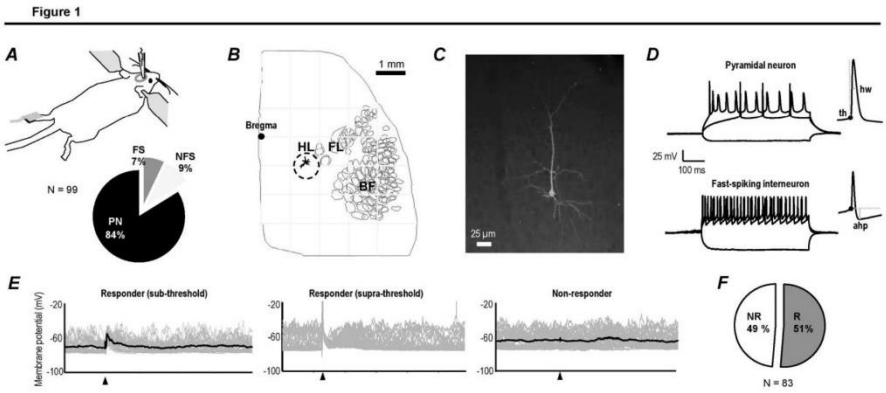

Figure 1. Physiological properties of L2/3-PN in S1-HP of anaesthetized mice. (*A*) Experimental design (left panel): Whole-cell recordings were made from S1-HP L2/3-PN to record their intrinsic properties and sensory responses to contra-lateral HP stimulation. (*B*) Example of a recorded and biocytin-filled L2/3-PN superimposed with the outline of the different S1 regions. The dashed circle shows the HP region based on the Allen Brain atlas and 3 immuno-staining. HL, hind-limb; FL, forelimb; BF, barrel field. (*C*) Image of a recorded L2/3-PN in S1-HP expressing eGFP from a plasmid that was introduced during the whole-cell recording. (*D*) Example traces from an I-V curve of

a pyramidal neuron and a fast-spiking interneuron. Illustration of AP threshold (th), half-width (hw) and afterhyperpolarization (ahp) analysis (inset). (*E*) Example traces of subthreshold responses over 40 trials (light color) superimposed with the average response (dark color) in an individual L2/3-PN (left); example of suprathreshold responses over 40 trials (middle); example of a non-responder cell over 40 trials (right). The arrowhead indicates the stimulation (2 ms, 30 mA). (*F*) Fraction of L2/3-PN responding to HP stimulation (responding neurons (R), n = 42; non-responding neurons (NR), n = 41).

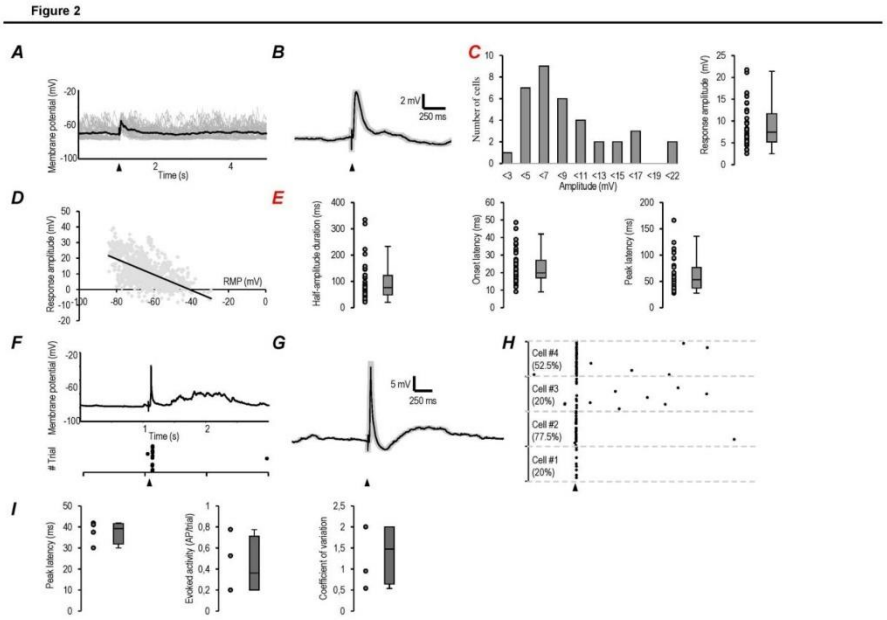

Figure 2. Sub- and supra-threshold responses to HP stimulation. (*A*) Example traces of subthreshold responses over 40 trials (light color) superimposed with the average response (dark color) in an individual L2/3-PN. The arrowhead indicates the stimulation (2 ms, 30 mA). (*B*) Average trace of subthreshold responses for all R-cells (n = 24, 960 trials) with s.e.m (gray). (*C*) Peak amplitudes of subthreshold response for the whole population in rank (left) and distribution (right). (*D*) Correlation between peak response amplitudes (Y-axis) and membrane potential (X-axis). (*E*) Distribution of half-amplitude duration (left), onset latency (middle) and peak latency (right) of subthreshold recordings (n = 36). The latencies were measured from the beginning of the stimulation.

(*F*) Example of suprathreshold recordings (single trial, up; and action potential timing over 40 trials, down). The arrowhead shows the stimulation onset. (*G*) Grand average of supra group response from 4 cells (160 trials) with s.e.m. (gray). (*H*) Overview of action potential timing in all neurons recorded from the supra group. The numbers in parenthesis indicate the percentage of trials with action potential response. (*I*) Distribution of peak latency (left), evoked activity (middle), and coefficient of variation (right). Box plot shows the median, interquartiles, range, and individual values.

Figure 3

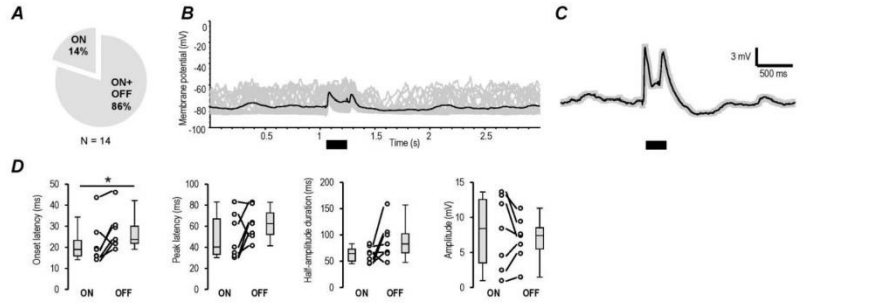

Figure 3. L2/3-PN show off-responses in S1-HP. (*A*) Fraction of L2/3-PN responding to HP stimulation at onset only (ON; n = 2) and both at onset and ending (ON+OFF; n = 12). (*B*) Example of ON+OFF over 40 trials (gray) with superimposed average (black). (*C*) Grand average of ON+OFF responses (8 cells, 320 trials) with s.e.m. (gray). (*D*) Distribution of onset latency, peak latency, half-amplitude duration, and amplitude (from left to right) of ON+OFF responses. Box plot shows the median, interquartiles, range, and individual values. Statistical significance was calculated by paired Student's *t* test. * $P < 0.05$.

Figure 4

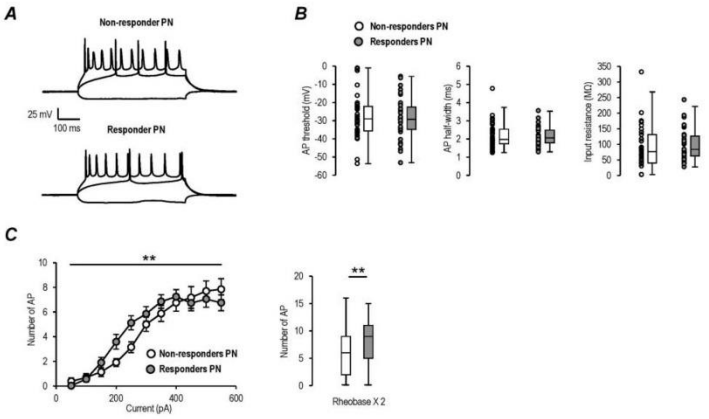

Figure 4. Intrinsic properties of L2/3-PN in S1-HP. (*A*) Example traces from an I-V curve of an R- and an NR-cell (–200 pA, rheobase, rheobase x 2). (*B*) Average AP threshold, half-width, and input resistance for R- (n = 37) and NR-cells (n = 35). (*C*) Average number of AP as a function of current injected for R- and NR-cells (left panel). Average number of AP at two times rheobase for R- (n = 35) and NR-cells (n = 30) (right panel). Box plots show the median, interquartiles, range, and individual values. Statistical significance was calculated by two-way ANOVA with repetition or unpaired Student's *t* test. * $P < 0.05$, *** $P < 0.001$ (R-cells compared to NR-cells).

Figure 5

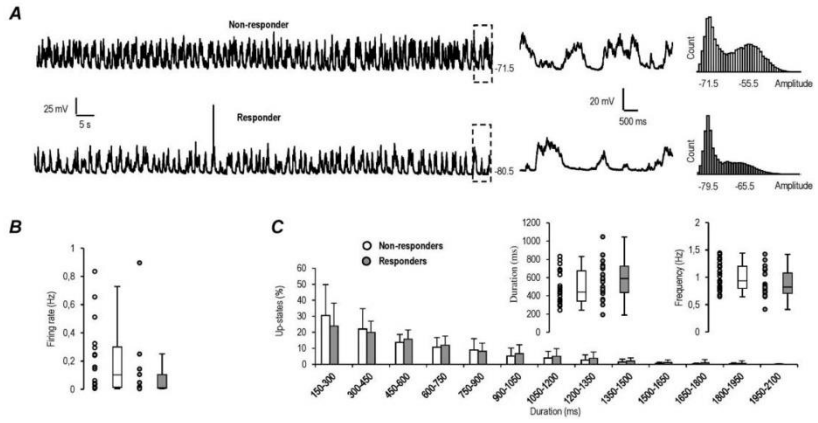

Figure 5. Spontaneous firing activity and slow wave oscillations in L2/3-PN. (*A*) Example of a 2-min continuous recording of spontaneous activity in an R- and NR-cells (left). Zoom-in of an 5-sec period of the examples shown in the left (middle). Plot of membrane potential of the example in left (right). (*B*) Spontaneous firing rate for active cells (both R- and NR-cells). (*C*) Population data for up-states. Plot of the fraction of the different up-state durations, as well as average duration and frequency (insets). Box plot shows the median, interquartiles, range, and individual values. Statistical significance was calculated by unpaired Student's *t* test.